MATERIALI IN TEHNOLOGIJE

MATERIALS AND TECHNOLOGY

4

MATER. TEHNOL. LETNIK VOLUME 51 ŠTEV. NO. 4 STR. P. 555-705 LJUBLJANA SLOVENIJA JUL.-AVG. JULY-AUG. 2017

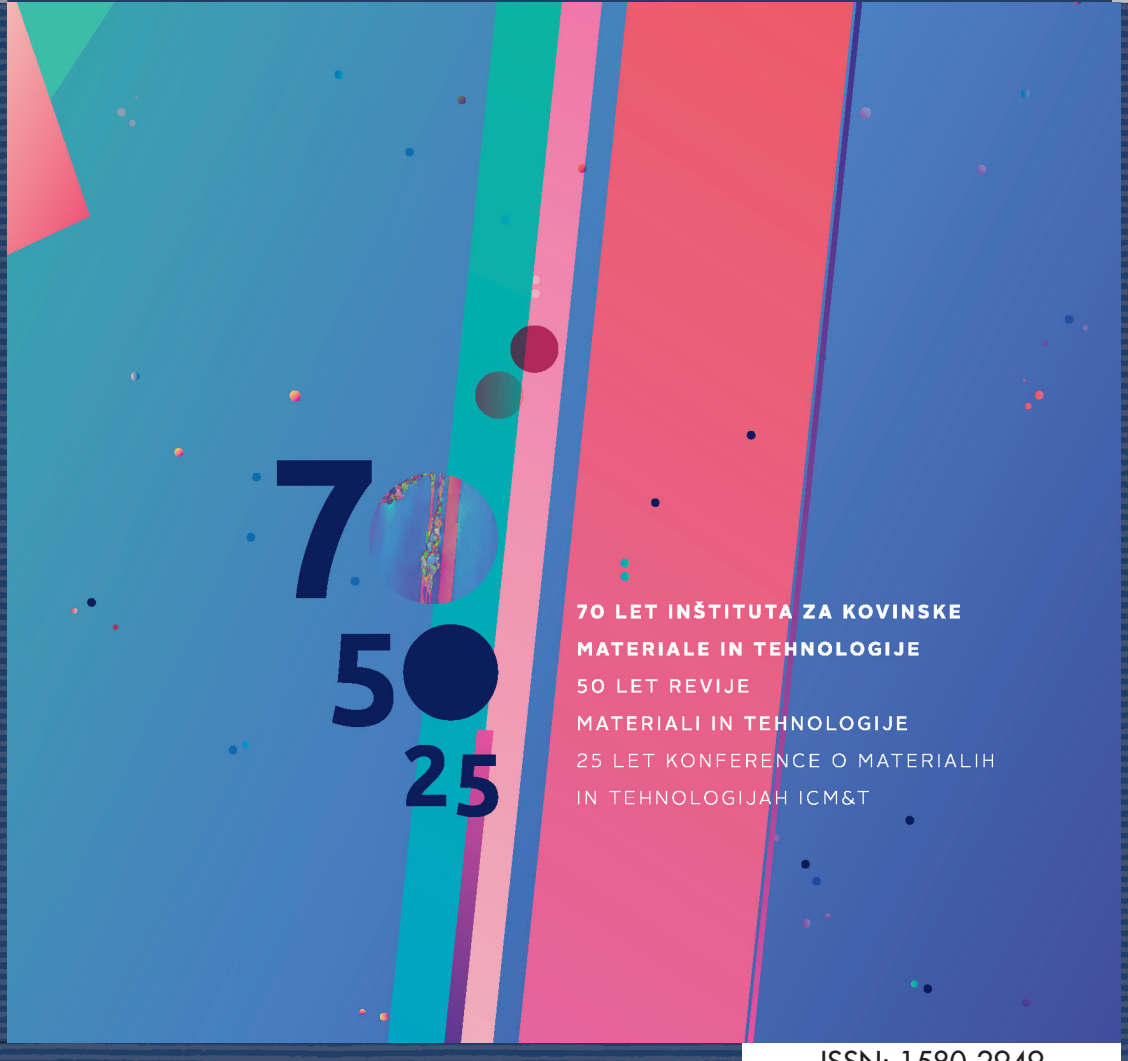

70 LET INŠTITUTA ZA KOVINSKE MATERIALE IN TEHNOLOGIJE

50 LET REVIJE MATERIALI IN TEHNOLOGIJE

25 LET KONFERENCE O MATERIALIH IN TEHNOLOGIJAH ICM&T

ISSN: 1580-2949
UDK: 669+666+678+53

MATERIALI IN TEHNOLOGIJE
MATERIALS AND TECHNOLOGY

4

MATER. TEHNOL. | LETNIK VOLUME 51 | ŠTEV. NO. 4 | STR. P. 555-705 | LJUBLJANA SLOVENIJA | JUL.-AVG. JULY-AUG. 2017

ISSN: 1580-2949
UDK: 669+666+678+53

MATERIALI IN TEHNOLOGIJE / MATERIALS AND TECHNOLOGY *so znanstvena serijska publikacija, ki objavlja izvirne in tudi pregledne znanstvene članke ter tehnične novice, ki obravnavajo teoretična in praktična vprašanja naravoslovnih ved in tehnologije na področjih kovinskih in anorganskih materialov, polimerov, vakuumske tehnike in v zadnjem času tudi nanomaterialov.*

The journal MATERIALI IN TEHNOLOGIJE / MATERIALS AND TECHNOLOGY *is a scientific journal, devoted to original scientific papers, reviewed scientific papers and technical news concerned with the areas of fundamental and applied science and technology. Topics of particular interest include metallic materials, inorganic materials, polymers, vacuum technique and lately nanomaterials.*

Izdajatelj (Published for):
Inštitut za kovinske materiale in tehnologije Ljubljana (IMT)

Soizdajatelji (Associated Publishers):
IMPOL Slovenska Bistrica, METAL Ravne, TALUM Kidričevo

Izdajanje **MATERIALI IN TEHNOLOGIJE** sofinancira: Javna agencija za raziskovalno dejavnost Republike Slovenije (ARRS)
(Journal **MATERIALS AND TECHNOLOGY** is financially supported by Slovenian Research Agency (ARRS))

Članki revije Materiali in tehnologije so indeksirani v/Articles published in Materials and Technology are indexed in: SCIENCE CITATION INDEX EXPANDED, MATERIALS SCIENCE CITATION INDEX® AND JOURNAL CITATION REPORTS/ SCIENCE EDITION.
Po bazi podatkov JCR15 ima Materiali in Tehnologije dejavnik vpliva 0,439. / In JCR15 Database Mater. Tehnol. has an impact factor of 0.439.

Članki objavljeni v periodični publikaciji MATERIALI IN TEHNOLOGIJE so indeksirani v mednarodnih sekundarnih virih: (Articles published in journal are indexed in international secondary periodicals and databases):
– DOAJ (Directory of Open Access Journals)
– Google Scholar
– SCIRUS
– CA SEARCH® – Chemical Abstracts®
– METADEX®
– TEME – Technology and management
– Inside Conferences
– Engineered Materials Abstracts®
– Aluminium Industry Abstracts
– SCOPUS
– Civil Engineering Abstracts
– Ceramic Abstracts/World Ceramic Abstracts
– Corrosion Abstracts
– Mechanical & Transportation Engineering Abstracts
– CSA Aerospace & High Technology Database
– Solid State and Superconductivity Abstracts
– Materials Business File
– Referativnyj žurnal: Metallurgija
– COBIB

Izhajanje: 6 številk letno / **Published:** 6 issues per year
Naročnina / Subscription: 42 EUR – **tujina / abroad:** 85 EUR

Na INTERNET-u je revija MATERIALI IN TEHNOLOGIJE dosegljiva na naslovu (ELECTRONIC ACCESS): http://mit.imt.si

Naslov uredništva (Editorial Address):
MATERIALI IN TEHNOLOGIJE
IMT Ljubljana
Lepi pot 11
1000 Ljubljana, Slovenija
Telefon: +386 1 470 18 60
Telefax: +386 1 470 19 39
Podračun pri UJP št. 01100-6030344339

Elektronska pošta (E-mail): mit@imt.si

Oblikovanje ovitka (Design): Ignac Kofol
Oblikovanje plakata na naslovnici (Poster on the Cover): Ajda Schmidt
Računalniški prelom in tisk (Prepress and Printed by): NONPAREL grafične storitve d.o.o., Medvode
Naklada (Circulation): 400 izvodov/issues

ISSN 1580-2949
UDK 669+666+678+53 MTAEC9, 51(4)555–705(2017)

MATER. TEHNOL.	LETNIK VOLUME 51	ŠTEV. NO. 4	STR. P. 555–705	LJUBLJANA SLOVENIJA	JUL.–AVG. JULY–AUG. 2017

VSEBINA – CONTENTS

IZVIRNI ZNANSTVENI ČLANKI – ORIGINAL SCIENTIFIC ARTICLES

UDK 67.017.620.1:62-419:621.78
Original scientific article/Izvirni znanstveni članek

ISSN 1580-2949
MTAEC9, 51(4)557(2017)

MECHANICAL PROPERTIES OF LAMINATED STEEL-BASED COMPOSITE MATERIALS FABRICATED BY HOT ROLLING

MEHANSKE LASTNOSTI SLOJEV JEKLA, OSNOVANEGA NA KOMPOZITNIH MATERIALIH, IZDELANIH Z VROČIM VALJANJEM

Tomáš Kubina, Jan Nacházel

COMTES FHT a.s., Průmyslová 995, 334 41 Dobřany, Czech Republic
jan.nachazel@comtesfht.cz

Prejem rokopisa – received: 2015-07-15; sprejem za objavo – accepted for publication: 2017-01-16

doi:10.17222/mit.2015.227

The fabrication of laminated steel composites by hot rolling is described. Composite sandwiches were made from martensitic stainless tool steel with an increased nitrogen content and from standard AISI 304 steel using 3 to 7 layers. The maximum strength of the martensitic steel was 1370 MPa. The composite sheets had strengths in the range 950–1200 MPa, depending on the number of layers and the proportion of the steels. A metallographic observation of the fractures revealed that the first occurrence was fracture in the martensitic steel layers, followed by deformation of the layers of tough austenitic AISI 304 steel. The notch toughness values were the highest when the notch was oriented from the sheet surface to the sheet interior.

Keywords: laminated composite, steel sandwich, tension test, hot rolling, notch toughness

V delu je opisana izdelava laminiranih jeklenih kompozitov z vročim valjanjem. Kompozitni sestavi so bili narejeni iz martenzitnega nerjavečega orodnega jekla s povečano vsebnostjo dušika, in v skladu s standardom AISI 304 je bilo uporabljeno jeklo s 3 do 7 sloji. Maksimalna moč martenzitnega jekla je bila 1370 MPa. Moč kompozitnih slojev je bila med 950–1200 MPa, odvisno od števila slojev in proporcev jekla. Metalografska analiza zlomov je pokazala, da je najprej prišlo do zloma pri slojih martenzitnega jekla, sledila je deformacija slojev težkega avstenitnega jekla AISI 304. Vrednosti žilavosti v zarezah so bile najvišje, kjer je bila zareza usmerjena iz površine sloja v njegovo notranjost.

Ključne besede: laminirani kompozit, sestav jekla, napetostni preizkus, vroče valjanje, žilavost zareze

1 INTRODUCTION

Various fabrication methods can be used for making composite materials. For multi-layered laminated composites, pressure-based joining comes into consideration. In the review article by H. J. McQueen,[1] the differences between pressure-based joining, diffusion bonding and friction joining are explained. In terms of production efficiency, rolling is an advantageous method, which permits the pressure-based joining of two or more dissimilar materials.

Various combinations of dissimilar roll-bonded metallic materials have been described in the literature. These included, for instance, titanium alloy/steel,[2–3] aluminum alloy/aluminum alloy,[4] aluminum alloy/steel,[5] brass/steel,[6] steel/steel[7–9] and other possible combinations.[10]

Laminated metallic composites offer an abundance of topics for study, ranging from fabrication, where the flow of layers during deformation can be explored,[11–13] through their overall mechanical properties[14] measured, for instance, by conventional tension testing[10,15] or by three-point bend test;[16,17] used for mapping delamination during failure.[18] One can also investigate internal stresses on the interlayer interface, for instance, in a composite fabricated of martensitic and austenitic steels.[19] It is these two steel types, austenitic and martensitic steel, that receive attention in the present paper. The focus of the paper is conventional. It covers the fabrication of laminated composite sheets and a description of their fundamental properties.

2 EXPERIMENTAL PART

Two stainless steels with different properties upon heat treatment were chosen for the experiments. The first, soft constituent was AISI 304L austenitic steel. It is characterized by its relatively high ductility and by an average level of tensile strength. Martensitic stainless steels have an inverted combination of properties: high strength and very low elongation upon heat treatment.

The attention was focused on a carbon steel (mark as 55C15N) with a high nitrogen level. It was made for this particular purpose by melting in an electrical induction furnace using N_2 overpressure in the final melting stage. A round ingot was cast and rolled into a 7-mm-thick sheet. The chemical composition of the 55C15N steel obtained in this way is given in **Table 1**. It clearly shows that the 55C15N steel is a carbon tool steel, in which corrosion resistance was achieved by no other means than alloying with chromium. As opposed to normal practice, the carbon content has been reduced and a part

of the original carbon content has been substituted with an increased nitrogen content of 0.15 % of mass fraction.

Table 1: Chemical composition of the experimental steels in mass fractions (*w*/%)

Steel	C	Co	Cr	Mn	Mo	Si	S	P	Ni	N
AISI 304	0.08	-	18.20	2	-	0.75	0.03	0.045	8.6	
55C15N	0.52	0.007	13.628	0.56	0.03	0.185	0.003	0.007	0.07	0.15

The surface of the sheets was ground. Stacks were assembled from 55C15N steel blanks of 7 mm thickness and AISI 304 steel blanks of 3 mm thickness. The blank size was 65×250 mm^2. The stacks were assembled according to the schematic drawing in **Figure 1**.

The designation of the specimens and the numbers of layers of the individual sheets were as follows:

- S1 – 55C15N steel sheet,
- S3 – 1 sheet of 55C15N steel, 2 sheets of AISI 304 steel,
- S5 – 2 sheets of 55C15N steel, 3 sheets of AISI 304 steel,
- S7 – 3 sheets of 55C15N steel, 4 sheets of AISI 304 steel.

A verified method was employed to hold the stack together. It was GMAW welding along the entire circumference of the stack. The positions of the welds were such that in each case, a pair of sheets of different steels, i.e., 55C15N steel and AISI 304 steel, were joined by the weld.

The first pass in the rolling process involved a thickness reduction denoted as ε_h. It was approximately equal to 23 % engineering strain, as calculated from the actual stack height *h*. Additional passes involved thickness reductions of 27 %. All the specimens were rolled to a thickness of 4.1 mm. The soaking temperature and time were 1100 °C and 40–60 min, respectively. The rolling operations were carried out in the laboratory rolling mill at COMTES FHT a.s. The work rolls had a diameter of 550 mm. Upon rolling, the scale was removed by grinding to achieve the final thickness of 4 mm.

The S7 specimen was reheated upon the fifth pass using the soaking parameters: 1100 °C and 40 min. The rolled specimens were cooled in still air.

Given the limited width of the laminated rolled sheet, the orientation of the specimens for tension testing was chosen in the rolling direction.[21] The test pieces for impact testing with the dimensions of (4×4×25) mm^3 were

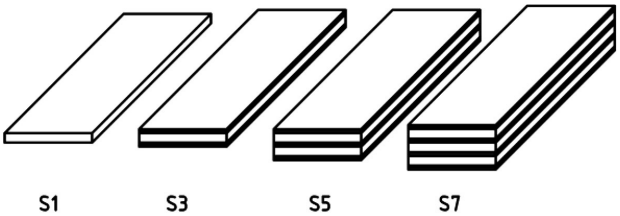

Figure 1: Configuration of sheets in stacks. Each white layer represents a 7-mm-thick sheet of 55C15N steel, each black layer represents a sheet of AISI 304 steel of 3 mm thickness

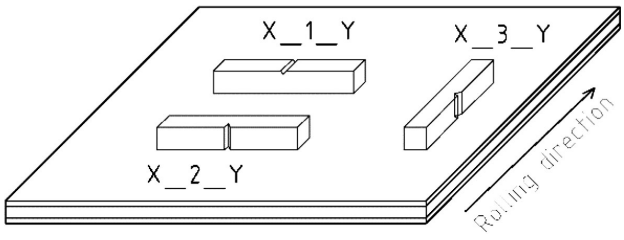

Figure 2: Schematic representation of samples taken from rolled sheets for Charpy impact test; X stands for the stack number and Y denotes the sequential number of the test piece

machined according to the sketch in **Figure 2**, which shows the orientation of the 1-mm-deep V notches.

The procedure for finding the appropriate heat-treating sequence is described in [21]. Considering the expected use of the 55C15N steel, the final hardness of this steel in the sandwich products was specified as 57 HRC. All the mechanical testing specimens were pre-treated as follows:

- sheets were painted with a protective coating,
- heating to 1050 °C and holding for 30 min,
- oil quenching,
- tempering at 175 °C for 2 h.

The specimens were then prepared using a standard metallographic procedure involving grinding and subsequent polishing.

The macro and microstructure in the ingots and rolled sheets of 55C15N steel were revealed by etching with nital, i.e., a 5 % solution of nitric acid.

The microstructure in the tension test pieces was revealed by etching with Marble's reagent (bringing out one constituent) and then with Beraha 2 (bringing out the other constituent). The un-etched microstructure and the microstructures upon consecutive etching steps were documented using a Carl Zeiss – Observer.Z1m optical microscope. The microscope workstation is equipped with AxioVision Rel. 4.8 digital image-processing software.

The fracture surfaces in tension and the impact test pieces were documented using a JEOL JSM 6380 scanning electron microscope (SEM), which is provided with an Oxford INCA X-sight EDX detector for measuring the local chemical composition.

3 RESULTS AND DISCUSSION

3.1 Sandwich fabrication by rolling

In the course of the sandwich rolling process, rolling forces, torque values, surface temperatures measured by pyrometers and the set rolled product thickness were recorded. An example of mean values measured and calculated for S3 specimen is given in **Table 2**. The first-pass rolling force *F* for all three stacks was around 630 MPa. Due to different initial heights, the torque values (*M*) were in the range from 20 kNm to 45 kNm. The strain rate ($\dot{e}$) in the first pass was 2.3–3.6 s^{-1}.

Table 2: Measured and calculated mean values of fundamental rolling parameters for S3 specimen

pass	h	ε_h	v_v	F	M	$\dot{e}$
	mm	-	ms^{-1}	kN	kNm	s^{-1}
0	14					
1	10.7	0.238	0.5	629	20.6	3.6
2	7.8	0.267	0.9	857	19.8	8.2
3	5.7	0.267	0.9	1283	29.8	9.6
4	4.2	0.267	0.9	1519	28.2	11.0

Considering the initial sandwich width of 65 mm, the rolling-force values are not high. They are normally below 2000 kN, despite the fact that the reductions ε_h in individual passes exceeded 25 %. The calculated strain rates ($\dot{e}$) were between 2 and 11 s^{-1}. The rolling speeds (v_v) were 0.5 and 0.9 $m \cdot s^{-1}$.

These rolling parameters were sufficient for adequate layer bonding within all the sandwiches. A joint in the S5 specimen is documented in **Figure 3**. A line of iron oxides on the interface can be seen. Similar structures were found in the S3 and S7 specimens.

Table 3: Layer-thickness ratios in individual sandwiches

specimen	Layer thickness ratios	
	Initial	Post-rolling
S3	1:2.33:1	1:2.614:1
S5	1:2.33:1: 2.33:1	1:2.59:0.93:2.59:1
S7	1:2.33:1:2.33:1:2.33:1	1:2.56:0.87:2.27:0.87:2.56:1

The layer thicknesses in specimens S3, S5 and S7 are given in **Table 3**. These post-rolling ratios were found by microstructure examination under an optical microscope. A detailed analysis of thickness evolution vs. rolling parameters, as reported in [11], was impossible, due to multiple passes having been carried out. Despite that, it was confirmed that the "soft" constituent, AISI 304L steel, undergoes larger reductions than the 55C15N steel.

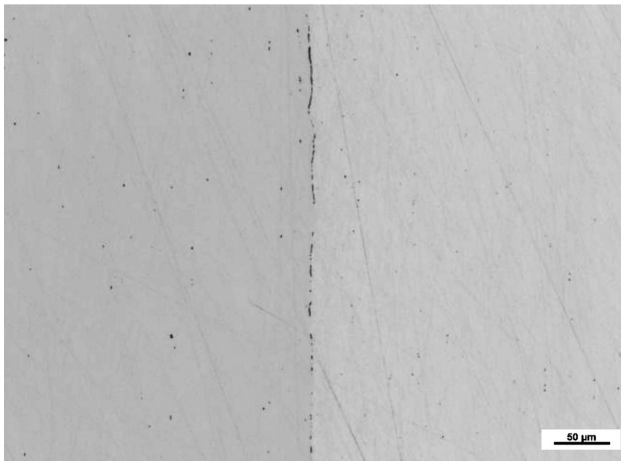

Figure 3: Joint between the 55C15N steel layer and AISI 304 steel layer; un-etched microstructure

3.2 Mechanical properties of rolled sandwiches

The test pieces used for the tension testing were oriented in the forming direction. Three specimens from each sandwich were tested. The test results plotted as engineering stress vs. strain curves are shown in **Figure 4**.

The specimen denoted as S1 represents the 55C15N steel upon heat treatment to a hardness of 57 HRC. The laminated composite sheets exhibit lower hardness values. Among the composites, the highest strength of 1210 MPa was found in the 7-layer sheet. This sheet contained the largest volume fraction of 55C15N steel. The AISI 304 steel had a strength of 580 MPa and elongation to fracture of more than 85 %. The pure 55C15N steel had a low ductility, which corresponds to the heat treatment procedure used. This is characteristic of tool steels. The micrographs of the fracture regions in the tension test pieces (**Figure 5**) show that the fractures were of the brittle type, initiating in the 55C15N steel layers. Then, the austenitic steel layers underwent large deformation and the fracture of the entire specimen occurred. This is in agreement with the behavior described in the review article by J. Wadsworth.[22]

Three different specimen orientations were used for taking samples for impact testing. No effect of the notch or specimen orientation was proved by the impact tough-

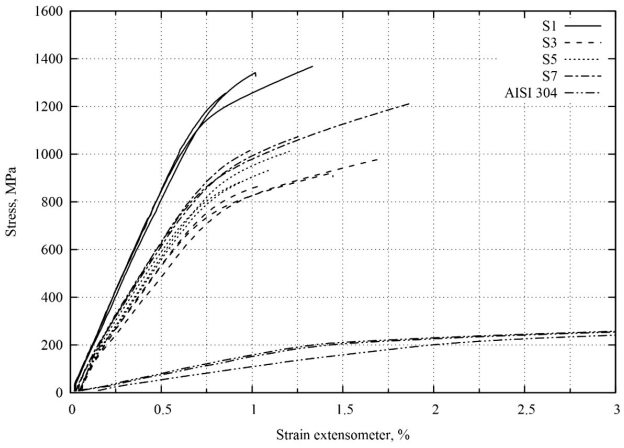

Figure 4: Engineering stress vs. strain plot of the sandwich sheet tension test

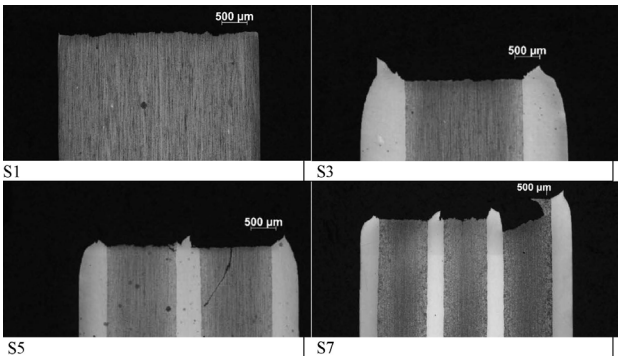

Figure 5: Micrographs of fractures in tension test pieces of sandwich sheets

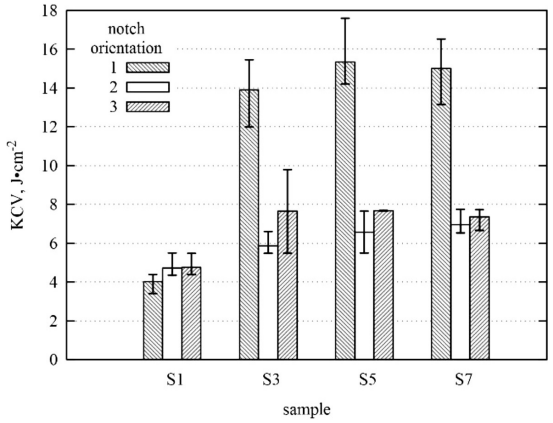

Figure 6: Impact energy KCV measured in heat-treated composite sheets

ness test of the material with a single 55C15N steel layer, as illustrated in **Figure 6**, specimen designation S1. For the specimens taken in the transverse direction with respect to the rolling direction and provided with notches in a direction oriented from the rolled sheet surface (the group denoted 1), the impact energy (13–15 Jcm^{-2}) approximately doubled when compared to the previous case. There is a clear effect of the AISI 304 steel layer, which retards the crack propagation. Neither the orientation of the notch across all the layers, nor the transverse or longitudinal orientation of the specimen has any effect, as evidenced by the minimal differences between impact energy levels. In the specimens made entirely of AISI 304 steel, the impact energy was 135 Jcm^{-2}.

The fracture surfaces in the tensile and impact test specimens were examined using scanning electron microscopy. In the fracture surfaces of the tension test pieces, inclusions were found in the 55C15N steel. They were identified by means of EDX analysis as complex aluminum oxides. Examples of the measured chemical composition of the inclusions are summarized in **Table 4**. **Figure 7** shows the fracture surface in the 55C15N steel layer in the seven-layer sandwich. In all cases, the fracture surfaces examined showed transgranular fracture morphology. In the fracture surfaces of the impact test pieces, no aluminum oxides were found.

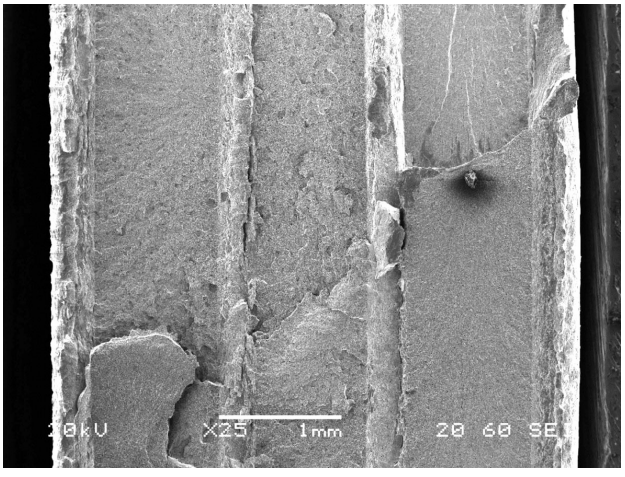

Figure 7: Fracture surface of S7 test piece

Table 4: Chemical composition of inclusions in mass fractions (*w*/%), measured by EDX

Elements	O	Al	Si	Cr	Mn	Fe + C
Inclusion 1	53.24	32.57	1.28	5.22	-	balance
Inclusion 2	42.77	40.82	-	3.64	-	balance
Inclusion 3	35.11	37.80	5.01	14.76	4.75	balance

4 CONCLUSIONS

A fabrication procedure for laminated composite materials was mastered, in which two different steels were joined by hot rolling. The resulting sandwiches containing martensitic stainless tool steel and austenitic steel were rolled to a thickness of 4 mm and heat-treated to a hardness of 57 HRC in the 55C15N steel layers. Oxides were found at the interface between the martensitic 55C15N and austenitic AISI 304 steels. They, however, had no impact on the delamination between the layers during the mechanical testing.

No contribution of austenitic AISI 304 steel to ductility enhancement was proved. It can be attributed to the small number of its layers. The impact energy value measured with impact tests suggests an increased resistance in cases where the notch is oriented from the sheet surface to its centerline, where the presence of the tough austenitic steel layers is beneficial.

Acknowledgements

The present paper was developed under the Development of the West Bohemian Centre of Materials and Metallurgy project, reg. No. LO1412, which was funded by the Ministry of Education of the Czech Republic.

5 REFERENCES

[1] H. J. McQueen, Pressure welding, solid state: role of hot deformation, Canadian Metallurgical Quarterly, 51 (**2012**) 3, 239–249, doi:10.1179/1879139512Y.0000000011

[2] K. Lee, D. Yoon, S. Lee, Y. Lee, The effect of thermomechanical treatment on the interface microstructure and local mechanical properties of roll bonded pure Ti/439 stainless steel multilayered materials, Procedia Engineering, 10 (**2011**), 3459–3464, doi:10.1016/j.proeng.2011.04.570

[3] J. C. Yan et al., Vacuum hot roll bonding of titanium alloy and stainless steel using nickel interlayer, Materials Science and Technology, 25 (**2009**) 7, 914–918, doi:10.1179/174328408X365766

[4] C. M. Cepeda-Jimenez et al., Influence of constituent materials on the impact toughness and fracture mechanisms of hot-roll-bonded aluminum multilayer laminates, Metallurgical and Materials Transactions A, 41A (**2010**) 1, 61–72, doi:10.1007/s11661-009-0069-x

[5] J. W. Yuan, Y. H. Pang, T. Li, Multilayer clad plate of stainless steel/aluminum/aluminum alloy, Journal of Wuhan University of Technology materials Science Edition, 26 (**2011**) 1, 111–113, doi:10.1007/s11595-011-0179-3

[6] H.-Y. Wu, S. Lee, J.-Y. Wang, Solid-state bonding of iron-based alloys, steel-brass, and aluminum alloys, Journal of Materials Processing Technology, 75 (**1998**) 1–3, 173–179, doi:10.1016/S0924-0136(97)00323-3

[7] F. X. Yin et al., Hot rolling bonded multilayered composite steels and varied tensile deformation behaviour, Materials Science and Technology, 28 (**2012**) 7, 783–787, doi:10.1179/1743284711Y.0000000116

[8] S. Nambu, M. Michiuchi, J. Inoue, T. Koseki, Effect of interfacial bonding strength on tensile ductility of multilayered steel composites, Composites Science and Technology, 69 (**2009**) 11-12, 1936–1941, doi:10.1016/j.compscitech.2009.04.013

[9] Q. X. Huang et al., Interface-correlated characteristics of stainless steel/carbon steel plate fabricated by AAWIV and hot rolling, Journal of Iron and Steel Research International, 21 (**2014**) 10, 931–937, doi:10.1016/S1006-706X(14)60164-3

[10] A. Cohades, A. Cetin, A. Mortensen, Designing laminated metal composites for tensile duktility, Materials & Design, 66 (**2015**) 412–420, doi:10.1016/j.matdes.2014.08.061

[11] G. P. Chaudhari, V. Acoff, Cold roll bonding of multi-layered bi-metal laminate composites, Composites Science and Technology, 69 (**2009**) 10, 1667–1675, doi:10.1016/j.compscitech.2009.03.018.

[12] Y.-M. Hwang, H.-H. Hsu, H.-J. Lee, Analysis of plastic instability during sandwich sheet rolling, International Journal of Machine Tools and Manufacture, 36 (**1996**) 1, 47–62, doi:10.1016/0890-6955(95)92628-C

[13] X. P. Zhang et al., Proposal of bond criterion for hot roll bonding and its application, Materials &Design, 32 (**2011**) 4, 2239–2245, doi:10.1016/j.matdes.2010.11.039

[14] D. R. Lesuer et al., Mechanical behaviour of laminated metal composites, International Materials Reviews, 41 (**1996**) 5, 169–197, doi:10.1179/imr.1996.41.5.169

[15] A. Cetin, C. Bernardi, A. Mortensen, An analysis of the tensile elongation to failure of laminated metal composites in the presence of strain-rate hardening, Acta Materialia, 60 (**2012**) 5, 2265–2276, doi:10.1016/j.actamat.2011.12.041

[16] J. Yanagimoto et al., Enhancement of bending formability of brittle sheet metal in multilayer metallic sheets, CIRP Annals – Manufacturing Technology, 59 (**2010**) 1, 287–290, doi:10.1016/j.cirp.2010.03.109

[17] E. Corona, T. Eisenhour, Wiping die bending of laminated steel, International Journal of Mechanical Sciences , 49 (**2007**) 3, 392–403, doi:10.1016/j.ijmecsci.2006.08.007

[18] M. Pozuelo, F. Carreno, O. A. Ruano, Delamination effect on the impact toughness of an ultrahigh carbon-mild steel laminate composite, Composites Science and Technology, 66 (**2006**) 15, 2671–2676, doi:10.1016/j.compscitech.2006.03.018

[19] R. I. Barabash et al., Interphase strain gradients in multilayered steel composite from microdi-ffraction, Metallurgical and Materials Transactions A, 45A (**2014**) 1, 98–108, doi:10.1007/s11661-013-2100-5

[20] ČSN EN ISO 6892-1 (420310). Metallic materials – Tensile testing – Part 1: Method of test at room temperature

[21] Š. Tománek, Preparation of composite plates from different tool steels and their mechanical properties (in czech), Diploma thesis. VŠB-Technical Univerzity of Ostrava, Faculty of Metallurgy and Materials Engineering, Department of Materials Forming, Ostrava (**2015**)

[22] J. Wadsworth, Ancient and modern steels and laminated composites containing steels, MRS Bulletin, 27 (**2002**) 12, 980–987, doi:10.1557/mrs2002.305

UDK 67.017:6:621.385.833:669.721
Original scientific article/Izvirni znanstveni članek

ISSN 1580-2949
MTAEC9, 51(4)563(2017)

PROPERTIES AND STRUCTURES OF BULK METALLIC GLASSES BASED ON MAGNESIUM

LASTNOSTI IN STRUKTURA MASIVNEGA KOVINSKEGA STEKLA NA OSNOVI MAGNEZIJA

Anna Kiljan, Ryszard Nowosielski, Rafał Babilas

Silesian University of Technology, Faculty of Mechanical Engineering, Institute of Engineering Materials and Biomaterials, Konarskiego Street 18A, 44-100 Gliwice, Poland
anna.kiljan@polsl.pl

Prejem rokopisa – received: 2015-09-19; sprejem za objavo – accepted for publication: 2016-11-11

doi:10.17222/mit.2015.300

Nowadays, Mg-based amorphous alloys are very attractive materials used in industries such as the automotive, aviation and medical industries. This group of bulk metallic glasses has specific properties such as corrosion resistance, strength and stiffness that are higher than those of crystalline ones. Also, Mg-based amorphous alloys are characterized by their high glass-forming ability, low density, good ductility, light weight, low cost, and good thermal and electrical conductivities. This work presents the basic information regarding metallic glasses. The project was focused on Mg-based bulk metallic glasses. The work shows the results of a differential thermal analysis (DTA), differential scanning calorimetry (DSC) and calorimetric surveys that determined the temperature at the beginning and at the end of crystallization. X-ray studies were performed and they confirmed the formation of the alloy's amorphous structure. The results of cross-sectional SEM and EDS were presented using a scanning electron microscope. This confirmed the homogeneity of the chemical composition and the structure of amorphous samples in the form of a plate with a thickness of 1 mm and a width of 5 mm. The value of the average sample microhardness is 295 HV.

Keywords: bulk metallic glasses, Mg-based amorphous alloys, SEM, XRD, microhardness

Dandanes so amorfne zlitine zelo atraktiven material, ki se uporablja v industriji, kot je npr.: avtomobilska, letalska ter medicinska industrija. Ta skupina kovinskega stekla ima specifične lastnosti, kot so npr.: odpornost proti koroziji, zdržljivost in togost, precej boljše kot kristalna skupina. Prav tako je za amorfne zlitine na osnovi Mg značilna njihova visoka sposobnost oblikovanja stekla, nizka gostota, dobra duktilnost, majhna teža, nizki stroški in dobre toplotne in električne prevodnosti. Delo predstavlja osnovno informacijo o kovinskih steklih. Projekt je bil fokusiran na masivnih kovinskih steklih na osnovi magnezija. Delo prikazuje rezultate diferencialne termalne analize (angl. DTA) in diferenčne dinamične kalorimetrije (angl. DSC), kolorimetričnimi analizami, ki so določile temperaturo na začetku in na koncu kristalizacije. Izvedene so bile rentgenske študije, ki so potrdile nastanek amorfne strukture zlitine. Rezultati prečnega prereza SEM in EDS so bile predstavljene s pomočjo skeniranja z elektronskim mikroskopom. To je potrdilo homogenost struktur kemijske sestave in amorfnih vzorcev v obliki plošče z debelino 1 mm in širine 5 mm. Vrednost mikrotrdote povprečnega vzorca je 295 HV.

Ključne besede: masivna kovinska stekla, amorfne zlitine na bazi Mg, SEM, XRD, mikrotrdota

1 INTRODUCTION

It is widely known that amorphous alloys, called bulk metallic glasses, are characterized by favorable properties due to their structural qualities. These properties include high resistance, high ductility, high corrosion resistance and surface quality. For the bulk metallic glasses based on La-, Mg-, Zr-, Pd-, Fe-, Ni-, Cu-, Co-, investigations were conducted, initiating wide application possibilities.[1,4] Due to the high glass-forming ability and excellent mechanical properties, especially low density, Mg-based BMGs are considered to be new, promising materials.[1–3]

Mg-based amorphous alloys are often prepared in an Mg-TM-RE system, in which TM is a transition metal, while RE is a rare-earth element. In 1991, Inoue, with his colleagues, generated an amorphous alloy of the following chemical composition: $Mg_{65}Cu_{25}Y_{10}$. For such alloys, the high cooling rate of amorphous samples with a 4-mm diameter was found to be about 102 K/s. Mg-based amorphous alloys are typically characterized with a better resistance to the ultimate tensile strength, crack resistance or compressive strength than their crystalline equivalents.[4]

There are various methods for producing bulk metallic glasses including the method of rapid cooling of crystalline alloys. Other methods for the production of bulk metallic glasses include: high-pressure die casting, copper-mold casting, the cap-cast technique and the suction-casting method. High-pressure die casting is the most popular and common method for producing bulk metallic glasses. The advantages of this method are: rapid molding, which can achieve a high cooling rate, and a good contact with the copper-alloy form, especially under the influence of high-pressure applications. However, a disadvantage of this method is that pores form as a result of shrinkage during the solidification of the liquid metal. This method is used for the production of complex shapes, where differently shaped molds allow the casting of the material in the forms of rods and

plates. This method was used by Inoue to produce BMGs in the Mg-Cu-Y alloy system.[5,6]

In this paper, the authors report their fabrication and investigation of the $Mg_{65}Cu_{25}Y_{10}$ alloy in the form of plates, which were prepared with the method of high-pressure die casting. The purpose of the investigation was to obtain amorphous plates that can be sintered in the future.

2 EXPERIMENTAL PART

2.1 Materials

Three samples with a composition of $Mg_{65}Cu_{25}Y_{10}$ were prepared using elemental cuts of magnesium (99.99 % purity), copper (99.95 % purity) and yttrium (99.99 % purity). Weight masses of individual elements (Mg, Cu, Y) are shown in **Table 1**.

Table 1: Characteristics of the elements utilized (Mg, Cu, Y)

Element	$Mg_{65}Cu_{25}Y_{10/30g}$	Melting temperature of the element
Mg	11.608 g	650 °C
Cu	11.7458 g	1085 °C
Y	6.5733 g	1522 °C

2.2 Research methodology

The studied alloy was made in two steps. The first step was the preparation of pure Cu and Y to obtain a binary alloy in an Al_2O_3 crucible by means of induction melting in an argon atmosphere. Then the Cu-Y alloy was melted with pure Mg in the Al_2O_3 crucible in an electric chamber furnace in an argon atmosphere.[2,7–9] The studied three samples were produced with the pressure-die-casting method in the form of plates with a thickness of 1 mm and a width of 5 mm (**Figure 1**).

By means of a differential thermal analysis (DTA), investigations were conducted on the thermal properties of the preliminary alloy $Mg_{65}Cu_{25}Y_{10}$, which was applied to the cast bulk metallic glasses in the form of plates. These investigations were conducted with a scanning calorimeter, Netzsch DSC 404C, in a temperature range of 200–800 °C. The heating rate was found to be 10 K/min and the measurements were conducted in the protective argon atmosphere. By means of the DSC (differential scanning calorimetry) method and the scanning calorimeter Netzsch DSC 404C, investigations of the crystallization process of the generated bulk metallic glasses in the form of plates, cast in a temperatures range of 100–600 °C, were conducted. The measurements were conducted in the protective argon atmosphere with a heating rate of 10 K/min. After the analysis of the obtained thermal results, the crystallization temperature and glass formation of the studied samples in the form of plates were established. The glass-forming temperatures were read at the inflection point of the DSC baseline towards the endothermic effect. The temperature of the crystallization beginning at T_x was set at the tangent intersection point with the line of the exothermic process. Meanwhile, the temperature of the crystallization peak represented the peak of the exothermic process T_p.[10]

An X-ray diffractometer, X'Pert Pro Panalytical, was used to study the structures of the fabricated plates. The data of diffraction lines were recorded using the step-scanning method in a 2θ range of 20–90° and with a 0.013° step.[11]

The particle size and shape of the $Mg_{65}Cu_{25}Y_{10}$ plate fractures were characterized using the scanning electron microscopy (SEM) SUPRA 25 ZEISS with a magnification of up to 2000×.[12]

Microhardness values of the samples were measured with a Vickers hardness-testing machine with automatic track measurement using the image analysis FUTURETECH FM-ARS 9000.[13] The microhardness measurements were made under a load of 100 g For each of the prepared samples, seven particles were tested.

3 RESULTS AND DISCUSSION

3.1 DTA

The DTA method was used to determine the onset (T_m) and end (T_L) melting temperatures of the $Mg_{65}Cu_{25}Y_{10}$ master alloy. The tests were carried out using the Netzsch DSC 404C calorimeter within the temperature range of 200–800 °C, at the heating rate of 10 K/min in an argon protective atmosphere. The T_m

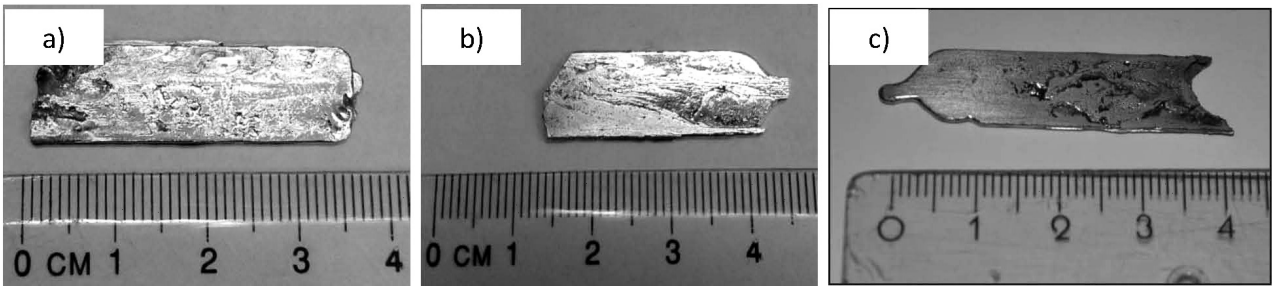

Figure 1: Three samples: a) sample 1, b) sample 2, c) sample 3, produced with the pressure-die-casting method

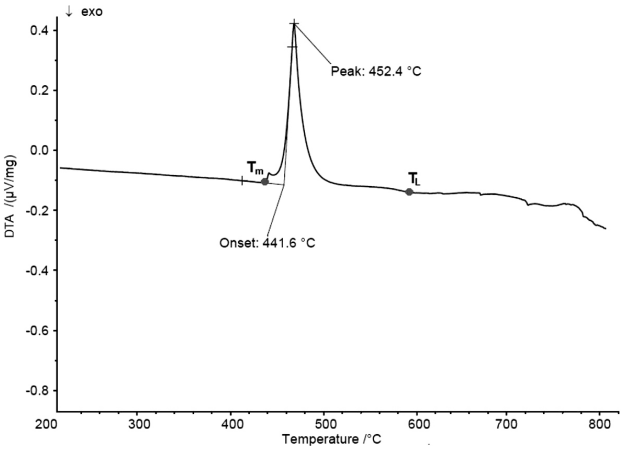

Figure 2: DTA curve for the $Mg_{65}Cu_{25}Y_{10}$ master alloy

temperature was 440 °C and the T_L temperature was 592 °C (**Figure 2**).

3.2 DSC

The DSC method was used to determine the glass-transition (T_g), onset-crystallization (T_x) and peak-crystallization (T_p) temperatures. The investigations were carried out using the Netzsch DSC 404C calorimeter in the temperature range of 100–400 °C. The measurements were carried out in an argon protective atmosphere and at the heating rate of 10 K/min.

The results of the calorimetric DSC investigations are presented in the **Table 2**.

Table 2: Results of the calorimetric DSC investigations

	T_g (°C)	T_x (°C)	T_p (°C)	ΔT_x (°C)
Sample 1	122	180	188	58
Sample 2	141	184	190	43
Sample 3	138	187	192	49
Average	134	184	190	50

The glass-forming temperature of the plates was within a range of 122–141 °C. The difference between the initial temperature and the crystallization peak was consecutively 8 °C, 6 °C and 5 °C. The value of the ΔT_x parameter for Sample 1 was – 58 °C, for Sample 2 – 43 °C, and for Sample 3 – 49 °C (**Figures 3a** to **3c**). The average value of the ΔT_x parameter was 50 °C. The

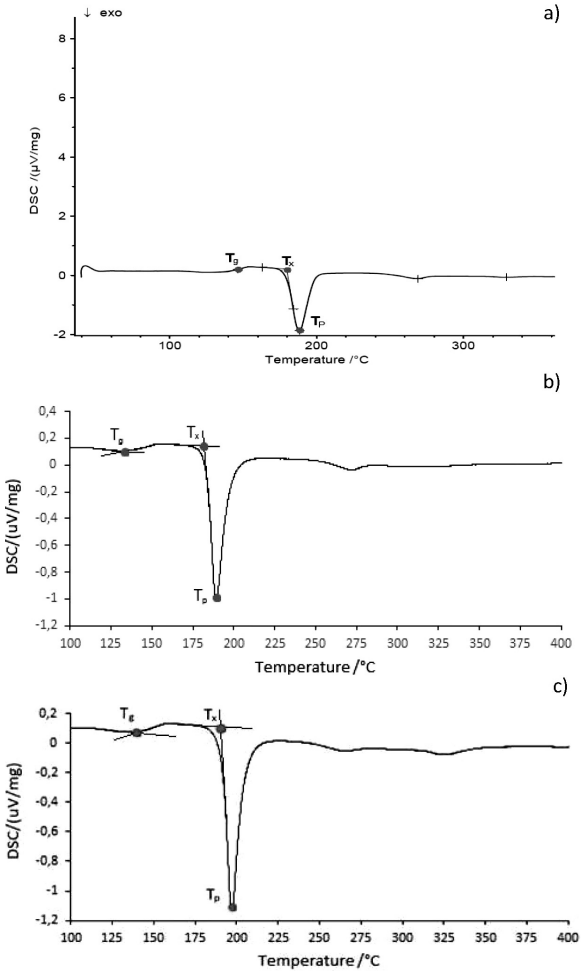

Figure 3: DSC curves: a) sample 1, b) sample 2, c) sample 3 of $Mg_{65}Cu_{25}Y_{10}$ metallic glasses

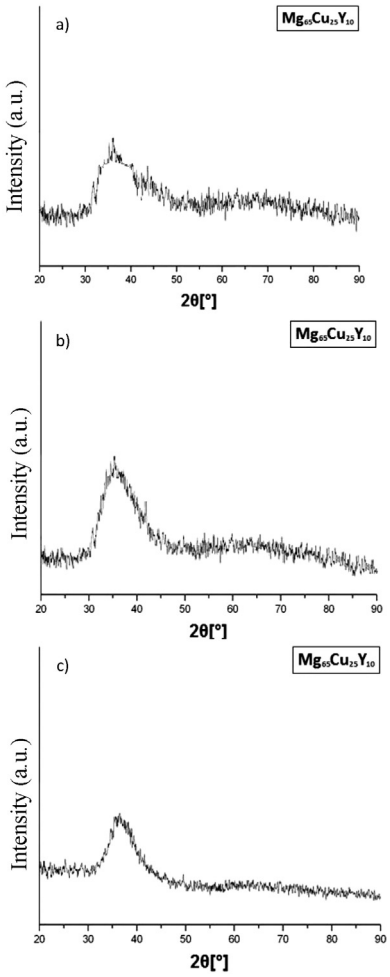

Figure 4: XRD patterns: a) sample 1, b) sample 2, c) sample 3 of $Mg_{65}Cu_{25}Y_{10}$ metallic glasses in the form of plates

higher the value of ΔT_x, the better was the glass-forming property of the material. ΔT_x is the difference between temperatures T_x and T_g.

For the $Mg_{65}Cu_{25}Y_{10}$ alloy, the value given in the literature is 65 °C.

3.2 XRD analysis

X-ray diffraction tests were carried out with an X-ray diffractometer X'Pert Pro with a cobalt anode. **Figures 4a–c** show that the test samples of the $Mg_{65}Cu_{25}Y_{10}$ alloy have an amorphous structure. The XRD patterns show a broad halo between 30–50°, which is typical for amorphous structures of magnesium alloys. Even more, a single diffraction peak (**Figure 4a**) can be observed on the amorphous halo, which might suggest the beginning of oxidation of the prepared sample.

3.3 Microstructure

Fractographic investigations of the sample fracture surfaces (**Figures 5** to **7**) revealed that they were characterized by a mixed-mode morphology. Selected areas were characterized by both "smooth" and "flake-like" fracture morphologies. The areas with the "flake-like" morphology are characteristic of hard and brittle alloys. These properties are characteristic of bulk metallic glasses based on magnesium. A photographic analysis showed that the investigated fracture surfaces had an appearance characteristic of an amorphous material.

3.4 Microhardness

Three samples in the form of $Mg_{65}Cu_{25}Y_{10}$ alloy plates were subjected to a microhardness investigation.

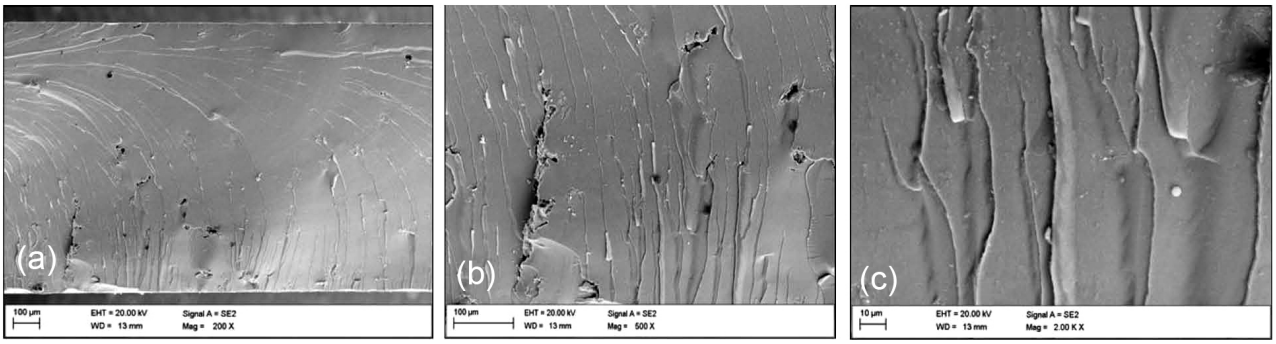

Figure 5: Fracture morphology of sample 1 of $Mg_{65}Cu_{25}Y_{10}$, SEM images with magnifications of: a) 200×, b) 500×, c) 2000×

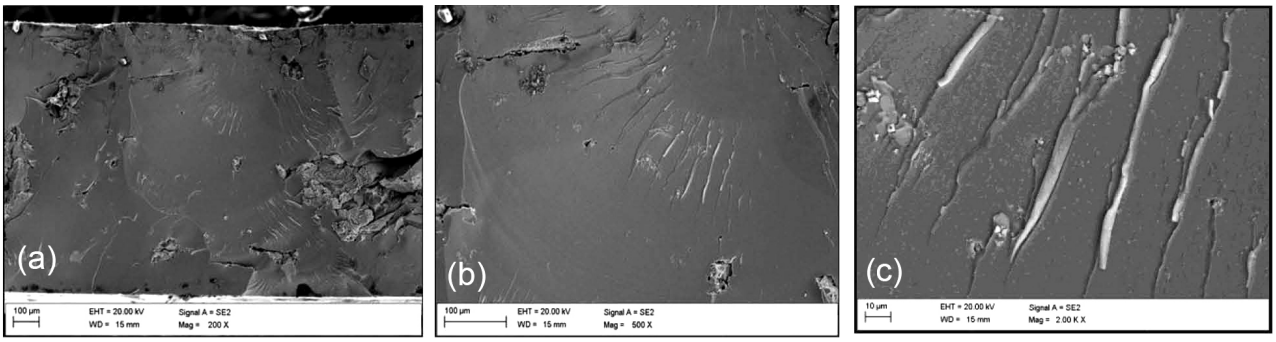

Figure 6: Fracture morphology of sample 2 of $Mg_{65}Cu_{25}Y_{10}$, SEM images with magnifications of: a) 200×, b) 500×, c) 2000×

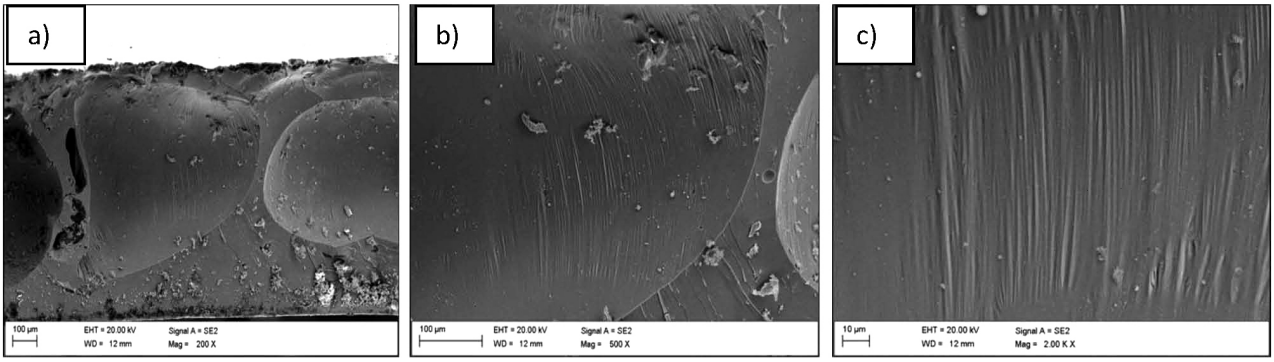

Figure 7: Fracture morphology of sample 3 of Mg65Cu25Y10, SEM images with magnifications of: a) 200×, b) 500×, c) 2000×

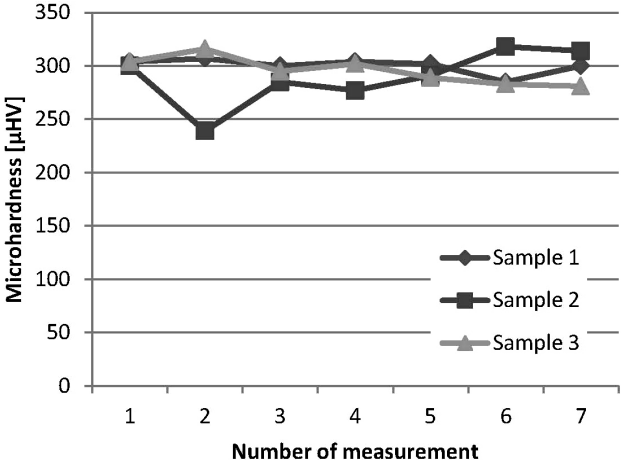

Figure 8: Results of the measured microhardness for three samples of $Mg_{65}Cu_{25}Y_{10}$

Seven measurements were performed for each sample, on random areas of the sample (**Table 3**). The obtained microhardness values for the amorphous plates of $Mg_{65}Cu_{25}Y_{10}$ alloys were found to be between 239 μHV and 318 μHV (**Figure 8**). The mean hardness was 295 μHV.

Table 3: Microhardness measurements of the samples

Measurement	Sample 1	Sample 2	Sample 3
	(μHV)	(μHV)	(μHV)
1	304	300	304
2	307	239	316
3	300	285	295
4	304	277	302
5	302	291	289
6	285	318	283
7	300	314	281
Average	300	289	296

4 CONCLUSIONS

Based on the conducted DTS, DSC, X-ray investigations, fracture-surface and microhardness investigations of the $Mg_{65}Cu_{25}Y_{10}$ samples, the following conclusions were formulated:

Samples of bulk metallic glass in the form of plates with a thickness of 1 mm and a width of 5 mm were created using the method of pressure casting.

X- ray investigations confirmed that the samples had an amorphous structure.

Calorimetric investigations allowed the establishment of the mean glass-forming temperature of T_g = 134 °C, the temperature at the beginning of crystallization of T_x = 184 °C, the crystallization peak temperature of T_p = 190 °C and the calculation of the parameter ΔT_x = 50 °C.

Fractographic investigations of fracture surfaces indicated the presence of a "flake-like" fracture morphology, which is characteristic of brittle materials and a property characteristic of Mg-based bulk metallic glasses.

Microhardness investigations allowed the determination of the mean hardness, which was 295 μHV.

5 REFERENCES

[1] G. B. Liu, P. Gao, Z. Xue, S. Q. Yang, M. L. Zhang, Study on the formation of new Mg–Cu–Ti–Y quaternary bulk metallic glasses with high mechanical strength, Journal of Non-Crystalline Solids, 358 (**2012**), 3084–3088

[2] R. Nowosielski, A. Lebuda, R. Babilas, P. Sakiewicz, Manufacturing of $Mg_{65}Cu_{25}Y_{10}$ bulk metallic glasses, XVI. International Student Scientific Session, Materials and Technologies of the XXI Century, Katowice, 2014

[3] C. Suryanarayana, A. Inoue, Bulk metallic glasses, Boca Raton, CRC Press, 2011

[4] R. Babilas, A. Zajączkowski, W. Głuchowski, R. Nowosielski, Preparation and glass-forming ability of Mg-based bulk amorphous alloys, Journal of Achievements in Materials and Manufacturing Engineering, 62 (**2013**) 2, 78–86

[5] L. Wang, K. Q. Qiu, J. H. You, Y. L. Ren, R. D. Li, Phase separation and sample size independence of fracture strength for (Mg0.585Cu0.305Y0.11)95Be5 bulk metallic glass, Journal of Non-Crystalline Solids, 370 (**2013**), 1–5

[6] R. Babilas, A. Lebuda, K. Cesarz-Andraczke, P. Sakiewicz, R. Nowosielski, Technology development of magnesium-based bulk amorphous alloys, Selected Engineering Problems, (**2013**) 4, 9–13

[7] X. Hui, R. Gao, G. L. Chen, S. L. Shang, Y. Wang, Z. K. Liu, Short-to-medium-range order in Mg65Cu25Y10 metallic glass, Physics Letters, A 372 (**2008**) 17, 3078–3084

[8] H. Ma, Q. Zhang, J. Xu, Y. Li, E. Ma, Doubling the critical size for bulk metallic glass formation in the Mg-Cu-Y ternary system, Journal of Materials Research, 20 (**2005**), 2252–2255

[9] R. Nowosielski, R. Babilas, A. Guwer, A. Gawlas-Mucha, A. Borowski, Fabrication of Mg65Cu25Y10 bulk metallic glasses, Archives of Materials Science and Engineering, 53 (**2012**) 2, 77–84

[10] L.-L. Shi, H. Xu, Mg based bulk metallic glasses: Glass transition temperature and elastic properties versus toughness, Journal of Non-Crystalline Solids, 357 (**2011**), 2

[11] M. Karolus, X-ray structure of the test method for amorphous and nanocrystalline materials, First edition, Katowice, 2011

[12] L. Klimek, The scanning electron microscope in biomedical engineering, Łódź University of Technology publishing, Łódź, 2012

[13] J. Q. Wang, P. Yu, H. Y. Bai, Minor addition induced enhancement of strength of Mg-based bulk metallic glass, Journal of Non-Crystalline Solids, 354 (**2008**), 5440–5443

UDK 67.017:620.168:620.3
Original scientific article/Izvirni znanstveni članek

ISSN 1580-2949
MTAEC9, 51(4)569(2017)

MECHANICAL AND TRIBOLOGICAL PROPERTIES OF NANOFILLED PHENOLIC-MATRIX LAMINATED COMPOSITES

MEHANSKE IN TRIBOLOŠKE LASTNOSTI FENOLNIH MATRIC V KOMPOZITIH, PRIDOBLJENIH Z NANOTEHNOLOGIJO

George Pelin[1,2], Cristina-Elisabeta Pelin[1], Adriana Ştefan[1], Ion Dincă[1], Ecaterina Andronescu[2], Anton Ficai[2], Roxana Truşcă[2]

[1]National Institute for Aerospace Research – Elie Carafoli, 220 Iuliu Maniu Blvd, 061126 Bucharest, Romania
[2]University Politehnica of Bucharest, Faculty of Applied Chemistry and Materials Science, 1-7 Gh. Polizu St., 011061 Bucharest, Romania
ban.cristina@incas.ro

Prejem rokopisa – received: 2016-01-17; sprejem za objavo – accepted for publication: 2016-10-24

doi:10.17222/mit.2016.013

Phenolic-resin composites have attractive properties for applications in various fields from the wood and adhesive industry to the automotive, aeronautics and aerospace industries. The paper presents the obtaining of SiC-nanofilled phenolic-resin-based composites reinforced with a bidimensional fabric. Different contents of nanometric silicon carbide (0.5, 1 and 2) % mass fractions) were dispersed into the phenolic-resin matrix, using the ultrasonication method, to ensure the optimum dispersion. Several layers of the bidimensional fabric were impregnated with the obtained mixtures and the final laminated composites were obtained using high-temperature pressing, followed by a multistage temperature program. The obtained laminated nanocomposites were characterized with FTIR spectroscopy and evaluated in terms of mechanical and tribological properties. After mechanical testing, fracture cross-sections were characterized with SEM and optical microscopy. The results highlight the positive effect of the nanometric silicon-carbide addition to the phenolic-resin matrix of the laminated composites, in terms of mechanical and tribological performance, improving their strength, stiffness and abrasive properties.

Keywords: laminated composites, tensile strength, flexural strength, nanometric silicon carbide, nanocomposites, friction coefficient

Kompoziti fenolnih smol imajo možnosti raznovrstne uporabe na različnih področjih, tako na področju lesne industrije, v industriji lepil, kot v avtomobilski in letalski industriji. Prispevek predstavlja pridobitev SiC fenolnih kompozitov na osnovi smole, ojačanih z bidimenzionalnimi vlakni. Različne vsebine nanosilicijevega karbida (0,5, 1 in 2) % masnega odstotka, so bile razpršene z uporabo ultrazvočne metode v matrici, pridobljeni s smolo, da je bila zagotovljena optimalna disperzija. Več plasti bidimenzionalnih vlaken je bilo impregniranih s pridobljenimi mešanicami in končni laminirani kompoziti so bili pridobljeni z visokotemperaturnim tlačnim pritiskanjem, kateremu je sledil večstopenjski temperaturni program. Pridobljeni laminirani kompoziti so bili preučevani s FTIR-spektroskopijo in ovrednoteni glede na mehanske in tribološke lastnosti. Presek zloma po mehanskem testiranju je bil preučevan s SEM-mikroskopijo in optično mikroskopijo. Rezultati kažejo pozitiven učinek dodatka nanometričnih silicijevih karbidov, s smolo pridobljenih matric v večplastnih kompozitih, zaradi njihovih mehanskih in triboloških lastnosti, in ker se tako izboljša moč, togost in abrazivne lastnosti.

Ključne besede: laminirani kompoziti, natezna trdnost, upogibna trdnost, nanosilicijevi karbidi, nanokompoziti, koeficient trenja

1 INTRODUCTION

Due to their high strength and rigidity combined with low density, fiber-reinforced polymeric composites (FRP) are extensively used in a wide variety of fields, from sports equipment[1–2] to the automotive, civil engineering,[3–5] military,[6–7] aeronautics and aerospace[8–10] industries. The oldest thermoset polymers are phenolic resins. This type of resins are mostly used as heat insulation in aerospace applications, due to their low cost and facile processability[11] as well as their attractive properties such as chemical, heat and friction resistance and superior thermal insulation characteristics.[12] They are generally used in combination with other materials such as powder fillers and short or long fiber reinforcements. Phenolic-resin-impregnated fibers (glass, carbon, aramid) result in phenolic-resin-laminated composites and are mostly formed with compression molding.[12–13] During the obtaining process of this kind of materials, volatile-compound management is crucial in producing high-quality laminates.[14] An efficient management of volatile compounds during the development stage of phenolic-resin/fiber laminates leads to void-free composites and, consequently, fewer stress-concentration sites that contribute to creating a stronger interface. The fiber/matrix interface is a decisive factor for the final mechanical and physical properties of the composite materials.[15]

Composite materials based on phenolic resins/carbon fibers have been used by NASA as the standard material for high-temperature applications. These composites have different micronic fillers added to the matrix for the stabilization of charred polymer during the combustion.[16] However, the use of nanofillers instead of the micronic ones allows a weight reduction in the aerospace systems, and it also leads to thinner protection layers with better ablative properties.[16] Studies show that mechanical, thermal and friction properties of phenolic-matrix/fiber com-

posites can be improved by adding nanometric fillers such as carbon nanotubes,[17–18] layered silicates (nanoclays),[19] POSS compounds,[20] silica[21–22] or silicon carbide[23–25] to the phenolic resin. In the case of carbon-phenolic composites with nanoclays, studies show that higher nanoclay contents decrease the erosion rate, surface temperature and insulation index,[26] and can improve some properties, such as the flexural strength, stiffness and glass-transition temperature.[27] On the contrary, there are studies that report a decrease in the flexural strength and stiffness.[16] Literature also presents studies that examine the effect of montmorillonite nanoclays on the mechanical and morphological characteristics of the glass-fiber-reinforced composites based on the novolac phenol- formaldehyde matrix, showing that a nanoclay addition enhances the mechanical properties when a strong matrix-fiber interface is observed.[11]

The other interesting nanofiller is silicon carbide (nSiC) that is mostly used to improve the thermo-oxidative resistance[25] and wear resistance[23–24] of carbon/phenolic ablative materials. However, literature reports no studies involving carbon- and/or glass-fiber-fabric-laminated composites based on the nSiC-modified phenolic resin. The aim of this study is the evaluation of the effect of a silicon-carbide nanofiller addition to the phenolic-resin matrix of carbon- and glass-fabric-reinforced composites, taking into consideration morphological, mechanical and tribological properties. The paper presents the obtaining of nanometric silicon-carbide-filled phenolic-resin-matrix composites reinforced with glass or carbon-fiber bidimensional fabric. The obtained laminates based on different nanofiller contents were characterized in terms of chemical, mechanical and tribological properties. The results highlighted the positive effect of nSiC on the laminated composites, when added in the optimum weight content relative to the phenolic-resin matrix.

2 EXPERIMENTAL PART

2.1 Materials

The matrix used was the resole-type phenolic resin ISOPHEN 215 SM 57 % (PR) provided by ISOVOLTA S.A. Bucharest, with a density of 1135 g/cm^3. The nanofiller used was the β-type nanometric silicon carbide (nSiC) purchased from Nanostructured & Amorphous Materials Inc., USA, with the following characteristics: a purity of 97.5 %, the average particle size of 45–55 nm, the specific surface area of 34-40 m^2/g and true density of 3.22 g/cm^3. The reinforcing materials were the carbon fiber (CARP/T 193, produced by Chemie Craft, France) and E-glass-fiber bidimensional fabrics.

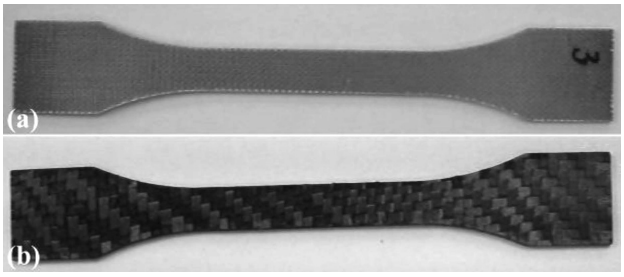

Figure 1: a) glass-fiber and b) carbon-fiber-PR-based composites; specimens for tensile tests

2.2 Method for obtaining nanofilled-laminated composites

The development of the nanofilled-laminated composites was a 3-stage process. The first stage consisted of nSiC additions of different contents (0, 0.5, 1 and 2) % of mass fractions to the phenolic resin (PR), bulk homogenization achieved with mechanical stirring for approx. 5 min and nanofiller dispersion carried out with the ultrasonication technique, using a Bandelin Sonopuls probe for 15 min. In the second stage, 5 layers of carbon fiber (CF) and glass fiber (GF), respectively, were impregnated with the obtained mixtures. The soaked layers were maintained at 25 °C for 30 h for a better impregnation, then they were subjected to methanol-solvent elimination at 70 °C for 30 min.[28] The final stage was the heat-curing process that took place under pressure using a CARVER hydraulic press. Along with pressing, the temperature was raised from 25 °C to 150 °C at a 30 °C/min heating rate, followed by a 30 min dwell period at 150 °C and cooling under pressure down to room temperature. Laminated composite plates were obtained; from them, dumbbell and rectangular specimens for mechanical and tribological tests were cut. **Figure 1** shows two of the specimens used for tensile tests, illustrating the dumbell geometry.

2.3 Characterization techniques

The phenolic-based nanocomposite laminates were subjected to a spectroscopy analysis using a Nicolet iS50 spectrometer (operated in the ATR mode) and scanning electron microscopy (SEM) using a QUANTA INSPECT F microscope with a field emission gun and 1.2 nm resolution, and an energy-dispersive X-ray spectrometer (EDS). The materials were tested in terms of mechanical performance with an INSTRON 5982 machine. The tensile tests carried out on dumbbell specimens were performed according to SR EN ISO 527-2[29] using a 5 mm/min tensile rate, while flexural (3-point bending) tests carried out on rectangular specimens were performed according to SR EN ISO 14125[30] using a 2 mm/min speed, conventional deflection and the nominal span length (16× the specimen thickness). Tribological tests were performed using CETR UMT 3 (Universal Macro Materials Tester) – the block-on ring module – on a 35 mm (diameter) × 11 mm (width) stamped steel roller (A4138 Timken outer rolling bearing ring), in the counterclockwise testing direction under a 10 N normal force, using samples with dimensions of 16 mm (length) × 6.5 mm (width) × 2 (thickness) mm. A

test was performed for 60 s using two different rotation speeds: 1000 min^{-1} (1.75 m/s) and 1500 min^{-1} (2.62 m/s). The tests were conducted on a minimum of 3 specimens per sample, at the standard atmospheric conditions, (25 °C and 45–55 % relative humidity).

3 RESULTS AND DISCUSSION

3.1 FTIR-spectroscopy

The nanofilled phenolic matrix of the laminated composites was subjected to FTIR spectroscopy analyses after polishing the analyzed area. The nanofilled-matrix-based laminated composite samples were compared with the control sample to evaluate the interactions between nSiC and the phenolic resin that could generate peak-position shifting and/or peak-intensity variations. **Figure 2** presents the spectra of the nSiC nanofiller powder and simple nSiC-filled phenolic resin from the laminated composites; all the composite samples present the characteristic peaks of the cured resin. The peak at 3290 cm^{-1} corresponds to the OH stretching from resole, the one at 2920 cm^{-1} is due to the CH_2 stretching, while the peaks in the 1600–1470 cm^{-1} range are due to the -C=C stretching in the aromatic ring. The CH_2 bending vibration generated the peaks at 1435 cm^{-1} and 1330 cm^{-1}, the C-O stretching at approximately 1190 cm^{-1} and the C-O-C stretching at 998 cm^{-1}.[31] The 3 peaks between 900–600 cm^{-1} are due to ortho-disubstituted, meta-disubstituted and monosubstituted benzenes.[31–32] The meta-disubstituted benzene peak at 815 cm^{-1} overlaps with the nSiC characteristic peak, assigned to the Si-C vibration that appears at approximately 800–815 cm^{-1} [33–34] so that the nSiC presence is more difficult to highlight. However, it is noticed that the peak intensity increases with the nSiC content in the PR matrix of the laminated composites, which could be due to the higher nSiC content interacting with the phenolic resin.[35] The absorption of a diamond crystal generates a noise between 1900–2300 cm^{-1}, which, therefore, must be ignored.

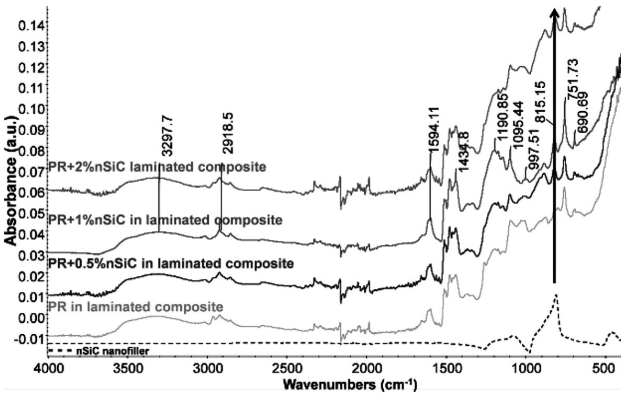

Figure 2: FTIR spectra of PR and nSiC/PR from the laminated composites

3.2 SEM analysis

A SEM analysis was performed on the fracture cross-sections of the mechanically tested laminated samples to evaluate the fiber/matrix interface at high magnification levels. SEM images of carbon and glass-fabric-based control samples (**Figure 3a** to **3c**) illustrate that the resin did not embed the entire surface of the fibers that the fabric is made of, and that the stress induced during the mechanical testing generated both a detachment of the polymer from the fibers as well as the matrix micro-cracking. In the case of the 1 % nSiC-filled matrix, it can be observed that the polymer layer covering the fibers is more compact, suggesting that the matrix was able to undergo the mechanical stress without being subjected to a detachment or micro-cracking. This could be due to the strengthening of the matrix caused by the nSiC presence that, along with a proper fiber/matrix interface, helps sustain a better mechanical load transfer within the composite. **Figure 4** illustrates high-magnification images of the samples with 1 % and 2 % nSiC contents added to the phenolic resin of the carbon-fiber-reinforced composites. A higher agglomeration tendency of the nanoparticles can be observed in the samples with a higher nSiC content. Also, in the case of 5CF/PR+1% nSiC (**Figure 4a**) the polymer layer uniformly covers the fiber surface, embedding the nanoparticles, while in the case of 5CF/PR+2% nSiC (**Figure 4b**) the agglomerated nanoparticles produce voids around that area. The areas composed of voids and agglomerated nanoparticles can act as stress-concentration sites, sustaining crack propagation, which influences the mechanical behavior.

3.3 Mechanical testing

The mechanical-performance evaluation was done through tensile and three-point bending tests. Mechani-

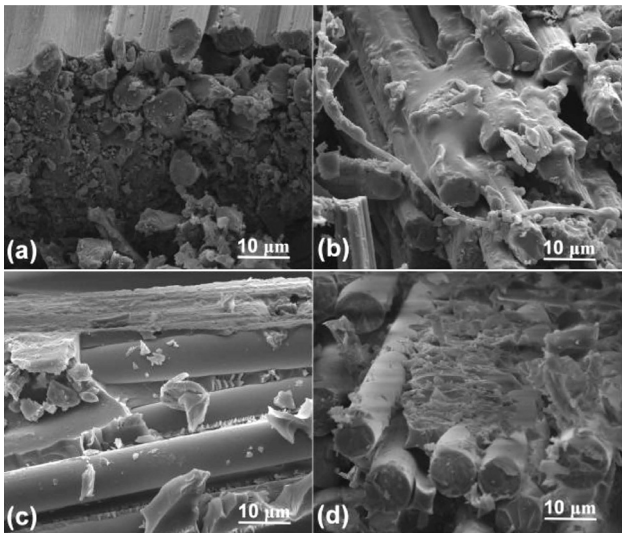

Figure 3: SEM images of: a) 5CF/PR, b) 5CF/PR+1% nSiC, c) 5GF/PR, d) 5GF/PR+1% nSiC

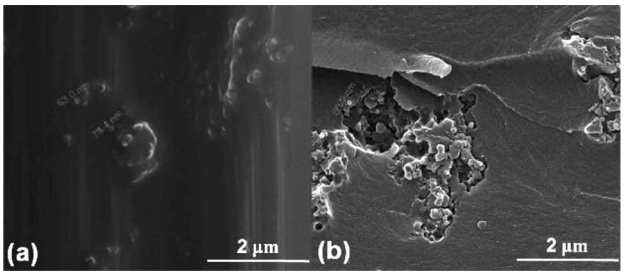

Figure 4: High-magnification SEM images of: a) 5CF/PR+1% nSiC, b) 5CF/PR+2% nSiC

cal test results (**Table 1**) show the fact that an nSiC addition to the phenolic-resin matrix significantly improves the mechanical performance of both carbon- and glass-fiber-reinforced laminated composites. Overall, all the nanofilled samples exhibited higher strength and stiffness compared with the control samples.

Table 1: Mechanical properties of nSiC-filled 5CF/PR and 5GF/PR laminated composites

nSiC (*w*/%)	Tensile strength (MPa)	Tensile modulus (GPa)	Tensile strain (%)	Flexural strength (MPa)	Flexural modulus (GPa)	Elongation (%)
5CF/PR based laminated composites						
0	318.0	47.8	0.8	382.1	43.9	1.22
0.5	344.5	50.5	0.75	420.3	48.6	1.09
1	384.5	68.6	0.7	458.0	56.3	1.04
2	331.9	52.9	0.48	440.2	45.0	1.02
5GF/PR based laminated composites						
0	300.3	22.0	2.02	350.7	27.4	2.41
0.5	314.3	27.1	0.83	363.2	32.7	1.29
1	342.5	37.5	0.77	423.6	34.6	1.23
2	293.3	22.1	0.71	352.0	33.3	1.17

The same trend was observed in both carbon- and glass-fiber laminates in terms of the nSiC-content effect. The highest results were exhibited by the samples based on the 1 % nSiC-filled matrix, in the case of 5CF/PR, where the 1 % content samples showed an increase of 20 % in the tensile and flexural strength and an increase of 30–40 % in the tensile and flexural modulus, while for 5GF/PR, the 1 % nanofiller led to an increase of 15–20 % in the tensile and flexural strength and an increase of 30–70 % in the tensile and flexural modulus. The nanoparticles embedded into the phenolic-resin matrix that covers the fibers (**Figure 4a**) could act as a crack-propagation hindering agent, enhancing the matrix strength and stiffness and, consequently, the mechanical properties of the laminated composite based on this matrix. This phenomenon was observed also in the case of phenolic-resin/nSiC nanocomposites presented in a previous study.[35] At higher contents (2 %), the properties decrease compared to 1 %, probably due to the existent nanofiller agglomeration, showed by SEM images (**Figure 4b**), that could lead to stress-concentration sites and/or crack-initiation sites that sustain earlier mechanical failures and contribute to the decrease in the mechanical-properties.

In both tensile and flexural tests, elongation decreases with the nSiC content increase due to the brittle nature of nSiC that enhances the composite rigidity.

3.4 Fractography

Fractography represents the fracture-mode analysis through light microscopy. Being an important tool in a material investigation related to a failure analysis and quality control,[36] light microscopy was the main method used to analyze the damage after the mechanical testing and to establish the failure mode type and mechanism. Light microscopy was the first method used to investigate the failure mode as it allows a visualization of the entire fractured area along the whole length of a sample. **Figure 5** illustrates the fractured areas of the representative specimens of laminated composite samples. Both carbon- and glass-fiber-based composites showed the same behavior as the nSiC content in the phenolic matrix. All the samples exhibited a certain degree of delamination, generated by crack propagation. While the control samples (**Figure 5a** and **5e**) and the PR-matrix laminates including 0.5 % nSiC (**Figure 5b** and **5f**) showed more extended delaminated areas, the 1 % nSiC-content-based sample showed the lowest delamination degree in both carbon and glass-fabric laminates

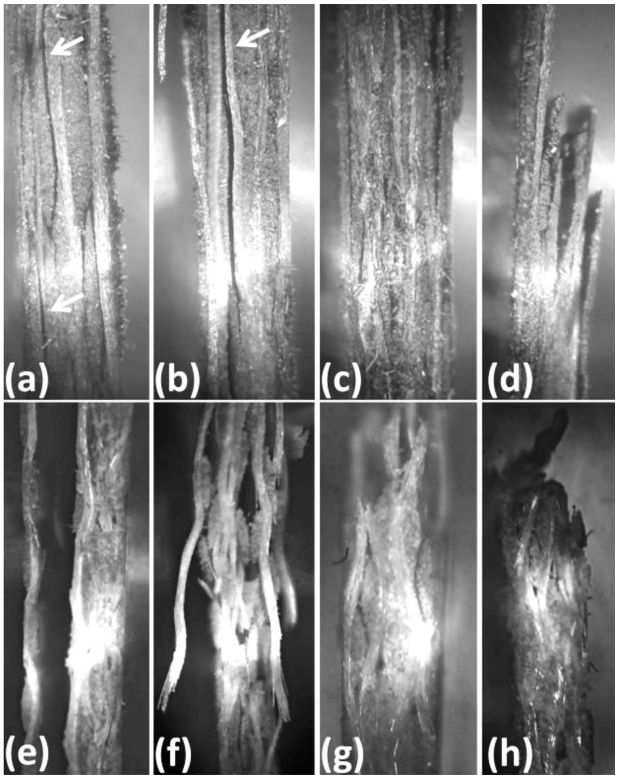

Figure 5: Optical-microscopy images of the tensile-test specimens: a), b), c), d) 5CF/PR+ 0; 0.5; 1; 2 % nSiC and e), f), g), h) 5GF/PR+ 0; 0.5; 1; 2 % nSiC

(**Figure 5c** and **5g**), where only the external layers exhibited detachment.

In the case of the 2 % nSiC laminates (**Figure 5d** and **5h**), all the fabric layers ruptured after the tensile testing, showing delaminated layers only in the fracture regions.

The optical-microscopy method was further supported with higher-magnification images of the fracture cross-sections, captured with SEM (**Figure 6**). Optical-microscopy images provide valuable information when choosing the most appropriate locations to be visualized with scanning electronic microscopy.[36] SEM images of the entire fracture cross-sections of the samples show that the control samples (**Figure 6a** and **6c**) were subjected to a higher damage extent; delaminated areas are still visible on the 0.5% nSiC-based sample (**Figure 6b**), while the image of the 1% nSiC sample (**Figure 6d**) suggests that the fabric-layer fracture occurred due to the strain and that the fibers broke on the same fracture section line.

3.5 Tribological testing

The positive effect of the nSiC addition was also reflected on the tribological test results. The laminated composites were tested at two speed rates: 1000 cm^{-1} (1.75 m/s) and 1500 cm^{-1} (2.62 m/s), on a minimum of three specimens per sample, over a short period of time (60 s) to evaluate the friction-coefficient trend at the initial stage of the friction-force action. **Figure 7** and **Figure *8*** illustrate the friction-coefficient function of the nSiC weight content in the matrix of the carbon- and glass-fabric-laminated composites. It can be observed that there is a significant increase in the friction coefficient with a nanofiller content increase in the matrix, where substantial increments are obtained at the higher testing speed.

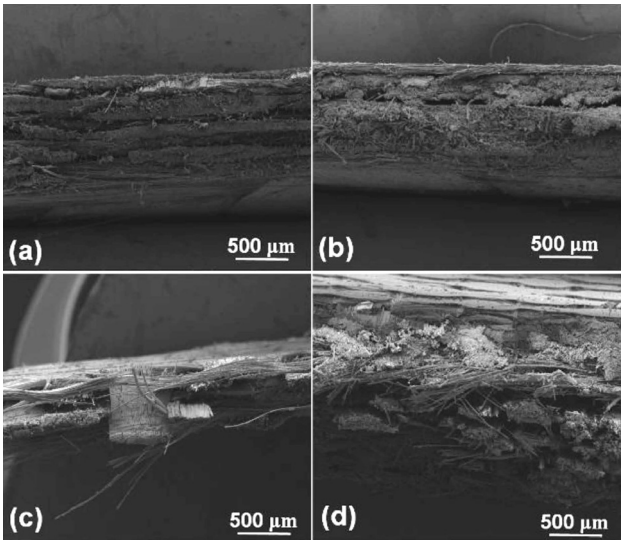

Figure 6: SEM images of fracture cross-sections of: a) 5CF/PR, b) 5CF/PR+0.5% nSiC, c) 5GF/PR, d) 5GF/PR+1% nSiC

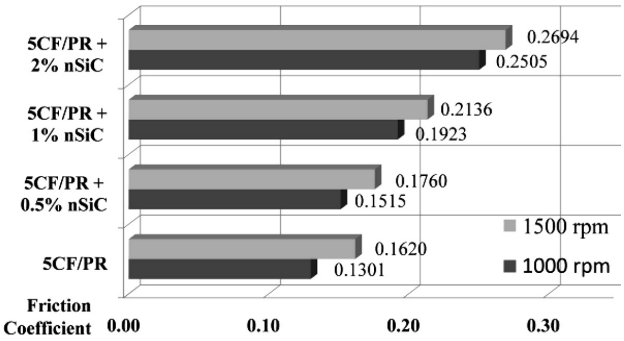

Figure 7: Friction-coefficient values for 5CF/PR/nSiC composites

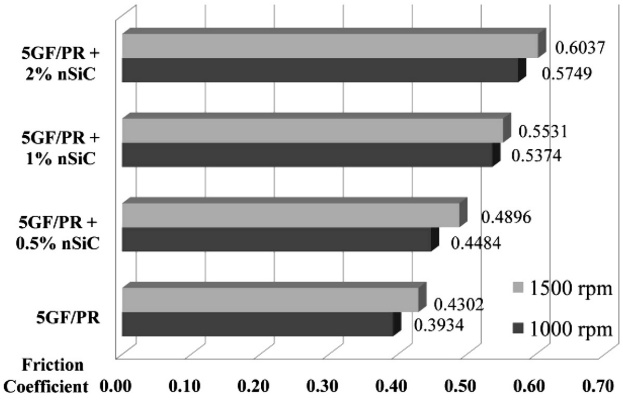

Figure 8: Friction-coefficient values for 5GF/PR/nSiC composites

In the case of carbon-fiber-based composites, the friction coefficient increases by approximately 10–16 % when adding 0.5 % nSiC, 30–50 % for 1 % nSiC and 70–90 % for the 2 % nanofiller compared with the control sample.

For glass-fiber-based composites, the friction-coefficient increments are not as significant as in the case of carbon fiber, as nSiC generates an increase of 14 % in the case of the 0.5 % addition, 30–37 % in the case of the 1 % addition and 40–45 % in the case of the 2 % addition.

The differences between the GF- and CF-based samples regarding the friction-coefficient values are due to different tribological characteristics of the two fiber types, where the carbon fiber is an anti-friction material[37], while the glass fiber promotes friction.[38]

4 CONCLUSIONS

The paper presents the obtaining and characterization of glass- or carbon-fiber bidimensional, reinforced composites based on the phenolic-resin matrix with different nSiC contents. The obtained results showed that the addition of nanometric silicon carbide improved the tensile and flexural strength and the modulus of the laminated composites, and that the best results were obtained with the 1 % mass fractions of the nanofiller contents for both carbon- and glass-fiber-reinforced composites. The ten-

sile and flexural strength increased by 15–20 % with the 1 % nSiC content in the PR matrix for both glass- and carbon-fiber-reinforced composites, while the tensile and flexural modulus increased by 30–40 % for the carbon-fiber and 20–30 % for the glass-fiber composites.

In terms of the tribological behavior, the friction coefficient increased with the nanofiller-content increase. For the glass-fiber-based composites, nSiC generated an increase of 30–37 % when the 1 % content was added and an increase of 40–45 % for the 2 % weight contents. In the case of the carbon-fiber-based composites, the control sample had a very low friction coefficient (0.13); therefore, the nanofilled sample's friction coefficient increased significantly: by 30–50 % for 1 % nSiC and by 70–90 % for the 2 % nanofiller. It was observed that higher speed rates led to higher friction-coefficient values.

The results highlight that 1 % nSiC by weight is the optimum content for phenolic/fabric composites in order to obtain both the maximum mechanical and tribological improvements as, at this content, the optimum nanoparticle embedment into the phenolic resin is achieved.

Acknowledgments

The work was funded by the Sectorial Operational Programme Human Resources Development 2007–2013 of the Ministry of European Funds through the Financial Agreement POSDRU/159/1.5/S/134398.

5 REFERENCES

[1] T. Johnson: Applications of carbon fiber – what products use carbon fiber today, Composite.about.com, http://composite.about.com/od/aboutcarbon/a/Applications-Of-Carbon-Fiber.htm, 27.10.2015

[2] T. Johnson, Carbon fiber in sports, Composite.about.com, http://composite.about.com/od/aboutcarbon/a/Carbon-Fiber-In-Sports.htm, 29.10.2015

[3] N. E. Chikh, B. Bousalem, M. Gahmous, N. Djebbar, T. Zarza, R. Renzaid, Use of FRP composites in civil engineering structural applications, Proc. du Colloque Méditerranéen sur les Matériaux, Cmedimat, Algeria, 2005

[4] D. R. Mertz, Application of fiber reinforced polymer composites to the highway infrastructure – Report 503, National Cooperative Highway Research Program, Washington, US, 2003, http://onlinepubs.trb.org/onlinepubs/nchrp/nchrp_rpt_503.pdf, 3.12.2015

[5] J. Bai, Advanced fibre-reinforced polymer (FRP) composites for structural applications, 1st ed., Woodhead Publishing, Oxford, 2013, 928

[6] P. K. Mallick, Introduction – aircraft and military application, in: Fiber-Reinforced Composites, Materials, Manufacturing, and Design, CRC Press Taylor & Francis Group, New York 2007, 24–29

[7] L. A. Pilato, M. J. Michno, Advanced Composite Materials, Springer Science & Business Media, Berlin 1994, 208

[8] J. Li, Effect of fiber surface treatment on wear characteristics of carbon fiber reinforced polyamide 6 composites, Iran. J. Chem. Chem. Eng., 29 (**2010**) 1, 141–147

[9] N. Chand, M. Fahim, An introduction to tribology of FRP materials, Allied Publishers, New Delhi, 2000, 299

[10] P. E. Irving, C. Soutis, Polymer composites in the aerospace industry, Woodhead Publishing, Cambridge, 2014, 536

[11] M. Eesaee, A. Shojaei, Effect of nanoclays on the mechanical properties and durability of novolac phenolic resin/woven glass fiber composite at various chemical environments, Compos. Part A, 63 (**2014**) August, 149–158, doi:10.1016/j.compositesa.2014.04.008

[12] N. Winya, S. Chankapoe, C. Kiriratnikom, Ablation, mechanical and thermal properties of fiber/phenolic matrix composites, International Journal of Chemical, Molecular, Nuclear, Materials and Metallurgical Engineering, 6 (**2012**) 9, 875–878, doi:10.1016/S1359-835X(01)00092-6

[13] N. Winya, A. Boonpan, K. Prapunkarn, Study of factors affecting the ablation rate of phenolic resin/fiber glass, International Journal of Chemical Engineering and Applications, 4 (**2013**) 4, 234–237, doi: 10.7763/IJCEA.2013.V4.302

[14] T. H. Hou, J. M. Bai, J. M. Baughman, Processing and properties of a phenolic composite system, NASA Technical Report LAR-16877-1, 2006, http://ntrs.nasa.gov/archive/nasa/casi.ntrs.nasa.gov/20080014267.pdf, 6.1.2016

[15] M. A. Hayat, S. M. A. Suliman, Mechanical and structural properties of glass reinforced phenolic laminates, Polym. Test., 17 (**1998**) 2, 79–97, doi: 10.1016/S0142-9418(97)00019-6

[16] L. Asaro, G. Rivero, L. B. Manfredi, V. A. Alvarez, E. S. Rodriguez, Development of carbon fiber/phenolic resin prepregs modified with nanoclays, J. Compos. Mater., 5 (**2015**), 1–14, doi:10.1177/0021998315590866

[17] M. Natali, M. Monti, D. Puglia, J. M. Kenny, L. Torre, Ablative properties of carbon black and MWNT/phenolic composites: a comparative study, Compos. Part A, 43 (**2012**) 1, 174–182, doi:10.1016/j.compositesa.2011.10.006

[18] M.-K. Yeh, N.-H. Tai, Y.-J. Lin, Mechanical properties of phenolic-based nanocomposites reinforced by multi-walled carbon nanotubes and carbon fibers, Compos. Part A, 39 (**2008**) 4, 677–684, doi:10.1016/j.compositesa.2007.07.010

[19] A. R. Bahramian, M. Kokabi, Ablation mechanism of polymer layered silicate nanocomposite heat shield, Hazardous Materials, 166 (**2009**) 1, 445–454, doi:10.1016/j.jhazmat.2008.11.061

[20] J. H. Koo, M. Natali, J. S. Tate, E. Allcorn, Polymer nanocomposites as ablative materials – a comprehensive review, International Journal of Energetic Materials and Chemical Propulsion, 12 (**2013**) 2, 119–162, doi:10.1615/IntJEnergeticMaterialsChemProp.2013005383

[21] M. Natali, M. Monti, J. Kenny, L. Torre, Synthesis and thermal characterization of phenolic resin/silica nanocomposites prepared with high shear rate-mixing technique, J. Appl. Polym. Sci., 120 (**2011**) 5, 2632–2640, doi:10.1002/app.33494

[22] I. Srikanth, A. Daniel, S. Kumar, N. Padmavathi, V. Singh, P. Ghosal, A. Kumar, G. R. Devi, Nano silica modified carbon-phenolic composites for enhanced ablation resistance, Scripta Mater., 63 (**2010**) 2, 200–203, doi:10.1016/j.scriptamat.2010.03.052

[23] M. Atarian, H. R. Salehi, M. Atarian, A. Shokuhfar, Effect of oxide and carbide nanoparticles on tribological properties of phenolic-based nanocomposites, Iran. Polym. J., 21 (**2012**) 5, 297–305, doi:10.1007/s13726-012-0038-x

[24] M. Nakada, Trends in engine technology and tribology, Tribol. Int., 27 (**1994**) 1, 3–8, doi:10.1016/0301-679X(94)90056-6

[25] P. H. Kang, H. S. Yang, Preparation of SiC/C composite sheet from polycarbosilane/carbon-based resin mixture, Korean. J. Chem. Eng., 15 (**1998**) 6, 580–584, doi:10.1007/BF02698981

[26] J. H. Koo, L. A. Pilato, G. E. Wissler, Polymer nanostructured materials for propulsion systems, J. Spacecraft Rockets, 44 (**2007**) 6, 1250–1262, doi:10.2514/1.26295

[27] G. Zhou, S. Movva, L. J. Lee, Nanoclay and long-fiber-reinforced composites based on epoxy and phenolic resins, J. Appl. Polym. Sci., 108 (**2008**) 6, 3720–3726, doi:10.1002/app.27886

[28] Physical Properties Of Methanol: CH_3OH, Cetiner Engineering Corporation (CEC Database), http://www.cetinerengineering.com/Properties.htm, 6.12.2015

[29] European Standard SR EN ISO 527: Plastics – Determination of tensile properties, 2003

[30] European Standard SR EN ISO 14125 Fibre-reinforced plastics composites – Determination of flexural properties, 2001

[31] P. S. Parameswaran, Modification of phenol formaldehyde resin for improved mechanical properties, PhD. Thesis, Department of Polymer Science & Rubber Technology, Cochin University of Science and Technology, India, 2010

[32] J. M. Perez, J. M. Echeverria, M. Oliet, M. V. Alonso, F. Rodriguez, Characterization of a novolac resin substituting phenol by ammonium lignosulfonate as filler or extender BioResources, 2 (**2007**) 2, 270–283

[33] S. Janz, Amorphous silicon carbide for photovoltaic applications, Masters Thesis, Fakultät für Physik, Universität Konstanz, Freiburg, 2006

[34] P. V. Prabhakaran, K. J. Sreejith B. Swaminathan, S. Packirisamy, K. N. Ninan, Silicon carbide wires of nano to sub-micron size from phenolfurfuraldehyde resin, J. Mater. Sci., 44 (**2009**) 2, 528–533, doi:10.1007/s10853-008-3087-y

[35] G. Pelin, C.-E. Pelin, A. Ştefan, I. Dincă, A. Ficai, E. Andronescu, R. Truşcă, Influence of nanometric silicon carbide on phenolic resin composites properties, Bulletin of Materials Science, 39 (**2016**) 3, 769–775, doi:10.1007/s12034-016-1185-z

[36] B. S. Hayes, L. M. Gammon, Optical Microscopy of Fiber-Reinforced Composites, ASM International, Ohio, 2010

[37] J. K. Lancaster, The effect of carbon fibre reinforcement on the friction and wear of polymers, J. Phys. D: Appl. Phys., 1 (**1968**) 5, 549–559, doi:10.1088/0022-3727/1/5/303

[38] N. Subramaniam, B. R. Sinha, F. D. Blum, Y.-R. Chen, L. R. Dharani, Glass fiber based friction materials, International Journal of Polymeric Materials and Polymeric Biomaterials, 15 (**1991**) 2, 93–102, doi:10.1080/00914039108031526

UDK 621.785.6:669.018:669.295:621.785.53
Original scientific article/Izvirni znanstveni članek

ISSN 1580-2949
MTAEC9, 51(4)577(2017)

MECHANISMS OF HARDNESS INCREASE FOR COMPOSITE SURFACE LAYERS DURING LASER GAS NITRIDING OF THE Ti6Al4V ALLOY

MEHANIZMI POVEČANJA TRDOTE POVRŠINSKIH SLOJEV KOMPOZITOV ZLITINE Ti6Al4V MED LASERSKO-PLINSKIM NITRIRANJEM

Aleksander Lisiecki

Silesian University of Technology, Faculty of Mechanical Engineering, Welding Department, Konarskiego 18A, 44-100 Gliwice, Poland
aleksander.lisiecki@polsl.pl

Prejem rokopisa – received: 2016-06-14; sprejem za objavo – accepted for publication: 2016-12-14

doi:10.17222/mit.2016.106

Titanium matrix composite (TMC) TiN_X/Ti surface layers characterized by high microhardnesses in a range from 1000 HV0.2 up to 2330 HV0.2 were produced by the Laser Gas Nitriding (LGN) of Ti6Al4V substrate in a pure nitrogen environment by a diode laser beam with unique characteristics. Despite the high hardness, crack-free surface layers were produced in a wide range of processing parameters. It was found that the maximum values of hardness and its depth profile on the cross-section of the surface layer should be considered in relation not only to the population and volume fraction of the dendritic precipitations of titanium nitrides TiN, but also in relation to the atomic ratio N/Ti in the TiN_X compounds. Conditions favorable for stoichiometric δ-TiN nitrides precipitation exist in the vicinity of the liquid/gaseous nitrogen boundary, because of the highest temperatures in this region of melt pool and the highest concentration of atomic nitrogen. Therefore, the population of stoichiometric titanium nitrides is the highest directly under the top surface.

Keywords: laser gas nitriding, titanium alloy, diode laser, metal-matrix composite, hardening

Nitriranje kompozita na osnovi titana (angl. TMC) TiN_X/Ti, za katere je značilna visoka mikrotrdota v območju med 1000 $HV_{0.2}$ in 2330 $HV_{0.2}$, je bilo izvedeno s plinskim laserskim nitriranjem (angl. LGN) na substratu zlitine Ti6Al4V s specialnim diodnim laserskim snopom. Kljub visoki trdoti, so površinske plasti proizvedene brez razpok v širokem območju procesnih parametrov. Ugotovljeno je bilo, da je potrebno upoštevati mejne vrednosti trdote in globino profila na preseku površinskega sloja v povezavi, ne samo s količino in volumskim deležem dendritov titanovih nitridov (TiN), pač pa tudi z atomskim razmerjem N/Ti v TiN_X spojinah. Najugodnejši pogoji za izločanje stehiometričnih δ-TiN nitridov obstajav bližini meje talina/plinasti dušik. Tam so najvišje temperature in zato nastaja bazenček staljene kovine v prisotnosti najvišje atomske koncentracije dušika. Zato je količina nastalih stehiometričnih titanovih nitridov najvišja tik pod površino.

Ključne besede: lasersko-plinsko nitriranje, titanova zlitina, diodni laser, kovinska kompozitna matrica, utrjevanje (kaljenje)

1 INTRODUCTION

Titanium and titanium alloys, in particular, show great mechanical properties, especially strength-to-weight ratio and corrosion resistance in different environments, compared to other advanced metallic or composite materials such advanced high-strength steels (AHSS), stainless steel, nickel- or cobalt-based superalloys, aluminium or magnesium alloys.[1–6] Titanium alloys also show good resistance to static, dynamic, and cyclic alternating loads (fatigue), such as in the case of vibrations.[7–11] One of the most commonly used two-phase titanium alloys is the $\alpha+\beta$ alloy Ti6Al4V, the properties of which can be controlled through a heat treatment used to adjust the amounts and types of phases.[12–16] However, the application of titanium alloys is often limited due to medium or even poor tribological properties.[1,3,17–22] For that reason different surface treatments or surface-modification methods are often applied to improve the surface characteristic of Ti alloys, such hardness, erosion, friction, cavitation wear resistance, or even to improve the corrosion resistance.[1,23–27] One of such methods is the Laser Gas Nitriding of a titanium substrate in the solid or liquid state, by Laser Surface Melting (LSM) in a nitrogen-rich atmosphere or in pure gaseous or even liquid nitrogen (cryogenic conditions).[1,24–27] In the field of Laser Gas Nitriding of titanium and its alloys, a lot of research has already been done. Laser nitriding of titanium substrate leads to the precipitation of hard titanium nitrides TiN in the metallic matrix, increasing hardness of the substrate surface. Additionally, the wear and also corrosion resistance of the substrate can be significantly increased, as shown by many studies and many researchers.[1,3,11–14,24–27] However, the main problem widely reported is cracking of hard nitrided layers due to excessive hardness and stresses, especially in the case of multi-bead surface layers, when the subsequent layers are produced by overlapping.[1,3,26–29] Thus, the control of hardness is crucial to ensure high quality and appropriate service properties of the laser nitrided surface layers.[1] S. Mridha and T. N. Baker[25] produced hard a surface layers with a maximum surface hardness of 1480 HV by laser

melting a Ti6Al4V substrate in pure nitrogen environment. They found that the hardness is related to the dendritic TiN population (concentration) in the layers. Additionally, they indicate that the microstructure and thus the surface hardness can be controlled by nitrogen flow rates and laser energy density. In turn, C. Hu and T. N. Baker[26] produced crack-free overlapped nitrided layers, and they indicate that the tendency to crack is related to the volume fraction of titanium nitrides formed in the melt. They point to the importance of preheating the substrate before nitriding, which can reduce the tendency to crack and improve the depth profile.[26] M. S. Selamat et al.[27] successfully produced crack-free overlapped nitrided surface layers on a Ti6Al4V substrate in a dilute nitrogen atmosphere comprising 20 % nitrogen and 80 % argon. However, the surface hardness was rather in the medium range, from only 500 HV to 800 HV.

In this study, a High Power Direct Diode Laser (HPDDL) with unique characteristics of the laser beam was applied for the surface melting of the Ti6Al4V alloy in a pure gaseous nitrogen environment at different scanning speeds and different laser output powers. Microhardness depth profiles were determined on the cross-section of the surface layers, while the structure, chemical and phase compositions were determined and analyzed.

2 EXPERIMENTAL PART

The tests of Laser Gas Nitriding were carried out on a substrate of the titanium alloy Ti6Al4V (Grade 5 according to ASTM B265), with the nominal chemical composition of 6.29 Al, 4.12 V, 0.14 C, 0.18 Fe in % of mass fractions and balance Ti. This titanium alloy is comprised of a hexagonal close-packed (hcp) α phase and a body-centered cubic (bcc) β phase, at room temperature, thanks the addition of vanadium that stabilizes the β phase. The desired properties of this Ti-alloy are shaped during the heat treatment. The samples prepared for nitriding tests were 3.0 mm thick and cut from a hot-rolled sheet into coupons of 40.0 mm × 70.0 mm. The whole surfaces of specimens were mechanically ground using 180-grade SiC paper to remove the surface oxide layers and to ensure uniform conditions for the absorption of laser radiation. Next the surfaces were decreased by acetone. The experimental setup was based on a fully automated and programmable positioning system coupled with a High Power Direct Diode Laser (HPDDL) with a rectangular beam spot. In the design of direct diode laser, the beam is emitted directly from the laser head, without the need to transmit a laser beam. In this case the generator of the laser radiation, shaping, and focusing optics are placed in a compact laser head. The laser head was mounted on a linear drive, set in a vertical position. The characteristic features of the specific HPDDL laser is a rectangular beam spot with dimensions of 1.8 mm × 6.8 mm, multimode energy distribution in the longitudinal direction, and a short wavelength of 808 nm, which is advantageous because of the high absorption coefficient on the surfaces of metals. The rectangular beam spot was focused on the top surface of a sample and set transversely to the scanning direction. Single stringer beads were produce as a result of surface melting in the pure gaseous nitrogen. Due to the width of 6.8 mm, the width of the stringer beads was in a range from approximately 6.0 mm to 6.5 mm wide. To provide stable and reproducible conditions of laser nitriding, and also to prevent the access of oxygen, or hydrogen from the ambient air, as well as the problem with degassing of the substrate a gas chamber was applied with a continuous flow of gaseous nitrogen at a pressure slightly higher than atmospheric pressure of about 1.0 bar. The gas chamber was first evacuated and next filled with gaseous nitrogen at room temperature. The nitrogen of 99.999 % purity was delivered by an inlet placed on a side wall, and the free flow of nitrogen was provided via the chamber and through the outlet placed on the opposite side wall. The nitrogen flow rate was kept at 10.0 L/min. The gas chamber was made of acrylic glass (PMMA), which is completely transparent for the 808 nm radiation, so the laser beam was delivered into the chamber through the cover glass (**Figure 1**).

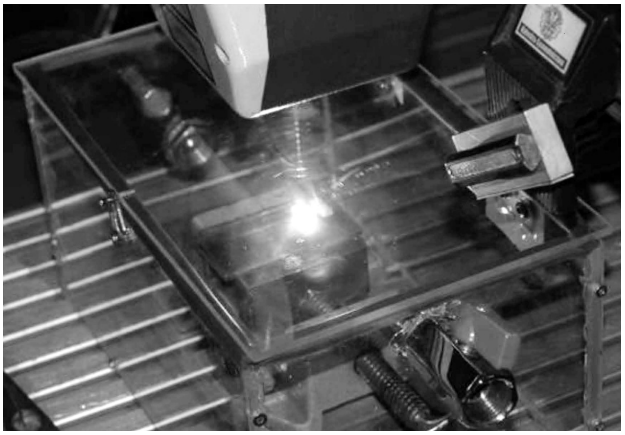

Figure 1: A view of laser melting of Ti6Al4V alloy substrate in the gas chamber filled with nitrogen by the HPDDL laser beam transmitted via the transparent cover made of acrylic glass (PMMA)

Table 1: Parameters of laser gas nitriding of the Ti6Al4V alloy by the HPDDL laser

Surface layer	Scanning speed (mm/min)	Laser output power (kW)	Energy input (J/mm)	Power density (W/cm^2)
SL1	400	1.8	270	1.5×10^4
SL2	1000	1.5	90	1.2×10^4
SL3	1500	1.5	60	1.2×10^4

Processing parameters were chosen based on previous investigations in such a way as to provide different penetration depth, different thermal conditions of nitriding, and thus different structures and morphologies

of the test surface layers. In general, the higher the energy input of the laser nitriding, the higher the penetration depth. Preliminary tests have shown that when using the HPDDL laser beam, preheating of the substrate is not required. The processing parameters and technological conditions are given in **Table 1**. After the nitriding trials, the samples were sectioned and grinded by 180 up to 1500 grit SiC abrasive papers and polished by 0.5 μm diamond paste. Kroll's reagent was applied to reveal the microstructure on polished cross-sections. The composition, crystal structure and microstructure of the test surface layers were analysed by optical microscopy (OM), scanning electron microscopy (SEM), energy-dispersive spectroscopy (EDS), electron backscatter diffraction (EBSD), and X-ray diffraction (XRD). Vickers microhardness was measured along the symmetry axis of cross-sections, and the microhardness depth profiles were determined. The hardness values in specific regions of surface layers were correlated with the microstructures. The results of the investigations are given in **Figures 2** to **8**.

3 RESULTS AND DISCUSSION

The surface layers produced by the HPDDL laser surface melting of Ti6Al4V substrate in a pure nitrogen environment are shiny and have a golden colour. The surface topography, depth of the fusion zone, and morphology are dependent on the processing parameters, such as scanning speed and the laser output power. Vickers microhardness depth profiles were determined with a load of 200 g on the cross-sections, starting from the subsurface region, through the fusion zone, heat affected zone, to the base metal, as shown in **Figure 2**. As can be seen, the maximum values of the microhardness were determined in the subsurface regions of every tested surface layer. However, the highest value of microhardness 2330 HV0.2 was measured for the surface layer (SL1) produced at the highest energy input 270 J/mm, and the lowest scanning speed 400 mm/min (**Table 1, Figure 2**). In this case the maximum depth of the fusion zone was estimated at approximately 1.6 mm. As can be seen in **Figures 3** to **5** the fusion zone is not homogeneous, and it can be divided into subregions. These results are consistent with the previous investigations described in [1]. The first subsurface region A extends to a depth of 150 μm and consists of densely packed dendrites perpendicular to the top surface (**Figure 3**). However, some of these dendrites reach deeper, up to a depth of 250 μm or even 300 μm, (**Figures 3, 4**). It is also worth nothing that the surface (SL1) is flat, as shown in **Figure 3a**. The surface is covered tightly by a

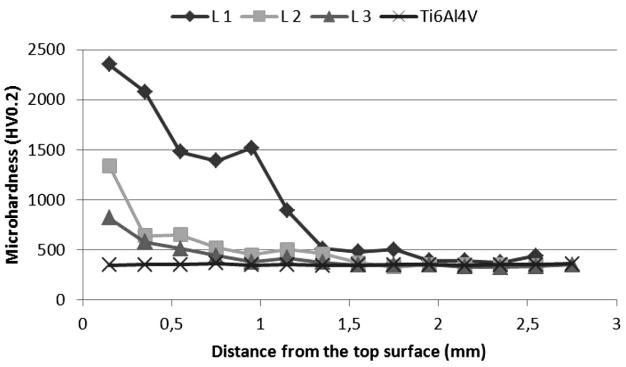

Figure 2: Microhardness profiles determined on cross-sections of nitrided surface layers compared to the substrate of Ti6Al4V alloy

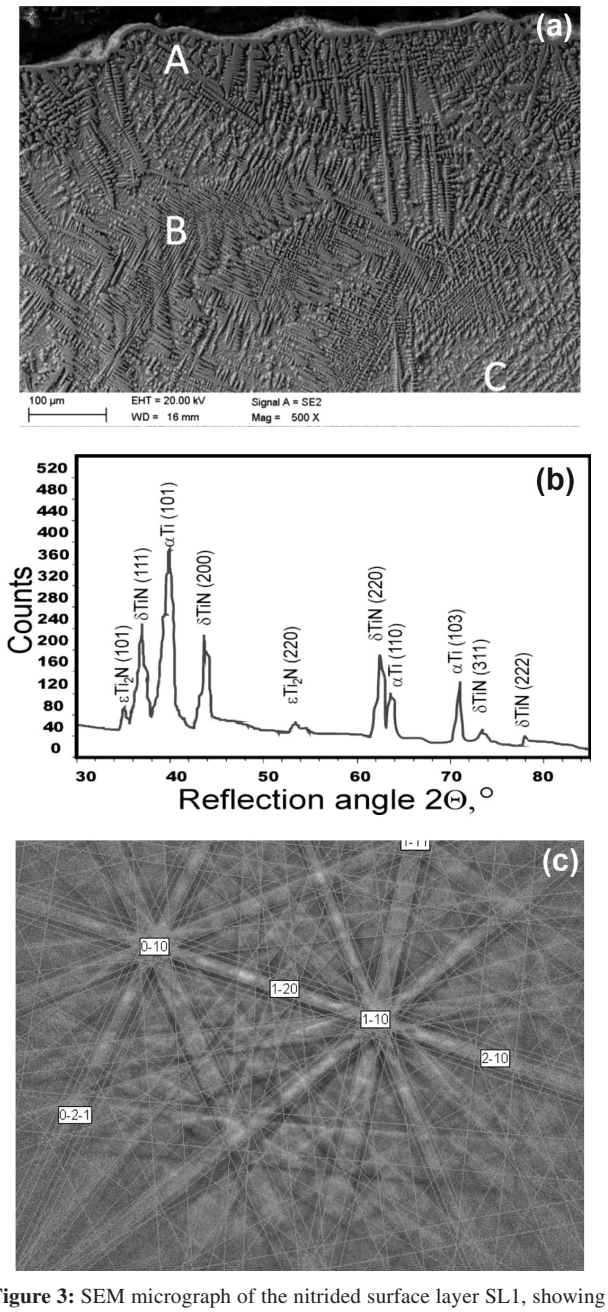

Figure 3: SEM micrograph of the nitrided surface layer SL1, showing the: a) composite structure consisting of TiN_x dendrites in metallic matrix and b) XRD pattern of the subsurface region A, and c) Kikuchi lines of EBSD analysis in the A region indicating TiN phase type of the composition N(50 % of amount fractions) and Ti(50 % of amount fractions)

homogenous layer with a thickness from 8 μm to a maximum 10 μm. An analysis of the chemical composition conducted on the depth profile of the cross-section of the surface layers LS1 indicates the presence of only nitrogen and titanium to a depth of approximately 8 μm, (**Figures 7, 8**). Despite the large scatter of results, the trend lines show that the nitrogen concentration in this region is up to 40 % (**Figure 7b**). The results of the XRD analysis show the presence of titanium nitrides δ-TiN in the subsurface region (**Figure 3b**). Additionally, the EBSD analysis indicates that the titanium nitrides have a stoichiometric atomic ratio N/Ti (50 % of N and 50 % of Ti), as show in **Figure 3c**. However, the nitrogen concentration decreases rapidly with the depth, as can be seen in **Figure 7b**. The structure in the middle region "B" of the surface layer SL1 shows different morphology (**Figures 3a, 4**). In this region the share of dendrites is considerably smaller, and the orientation of dendrites becomes random. Additionally, the interdendritic spaces are filled with needle-like phases, which were identified by XRD and EBSD analysis as the matrix of martensitic α'-Ti enriched in nitrogen (**Figures 3b, 4b**). The microhardness in this region falls down gradually to approximately 1400 HV0.2. The XRD spectrum taken from this region indicates presence of α'-Ti(N), δ-TiN, and also ε-Ti_2N nitrides. Detailed EBSD analysis confirmed the presence of ε-Ti_2N nitrides at the atomic ratio N/Ti 33.3 % of amount fractions of nitrogen and 66.7 % of amount fractions of titanium (**Figure 4b**). Additionally, the EBSD analysis revealed that the titanium nitrides TiN_X in this region do not have the stoichiometric composition. The precipitations of hard titanium nitrides TiN phase are particularly important because these phases responsible for the enhancement of hardness and wear characteristics of nitrided layers.[27] The titanium nitride at the stoichiometric ratio of N/Ti (equal to 1) has a face-centred cubic (fcc) structure with the lattice constant a = 0.4249 nm. However, the lattice parameter depends on the content of nitrogen, but the compound is stable over a wide range of atomic ratio N/Ti ($0.6 < N/Ti < 1.16$), as shown by M. S. Selamat et al.[27] Similarly the hardness of titanium nitride TiN_X depends on the atomic ratio N/Ti. That is why different values can be found in the literature. In general, Vickers microhardness values in a range from 2100 HV up to 2400 HV are often reported for the titanium nitride hard coating. However, in the case of coatings or thin films deposited on different substrates the range of microhardness reported in literature is significantly wider. Depending on the applied method of coating deposition, microstructure, especially grain size, columnar vs. equiaxed structure, the thickness of the film, the presence of voids,

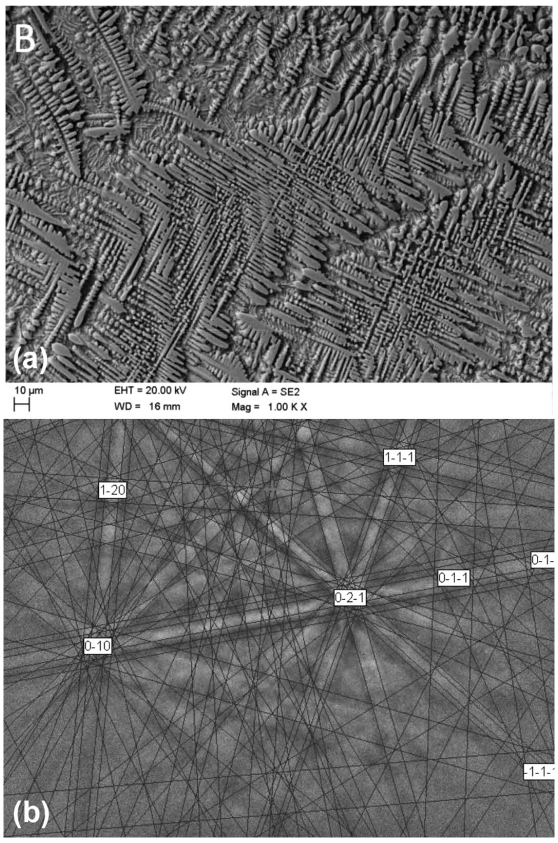

Figure 4: SEM micrograph of: a) the middle region B of the nitrided surface layer SL1 and b) Kikuchi lines of EBSD analysis in the B region indicating $TiN_{0.61}$ phase type of the composition N(37.9 % of amount fractions) and b) Ti(62.1 % of amount fractions)

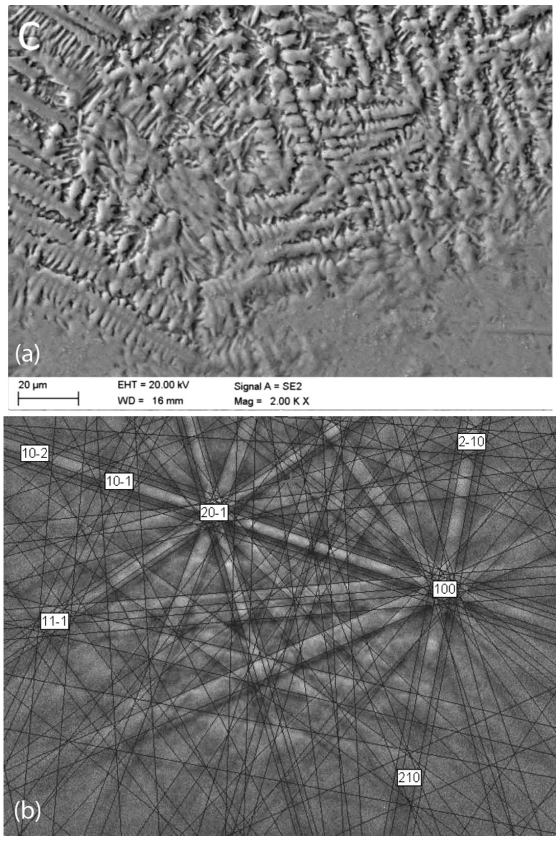

Figure 5: SEM micrograph of: a) the bottom region C of the nitrided surface layer SL1 and b) Kikuchi lines of EBSD analysis in the C region indicating Ti_2N phase type of the composition N (33.3 % of amount fractions) and Ti (66.7 % of amount fractions)

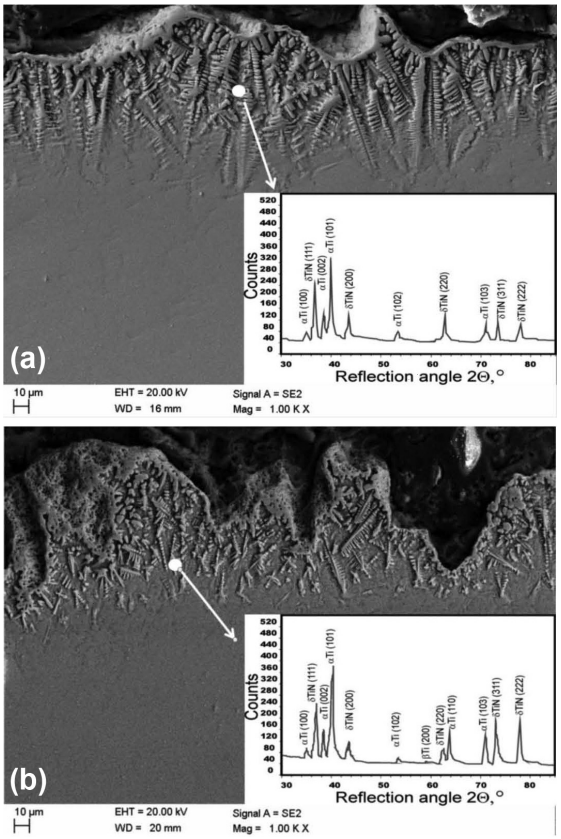

Figure 6: SEM micrographs and XRD patterns of the surface layers: a) SL2, b) SL3

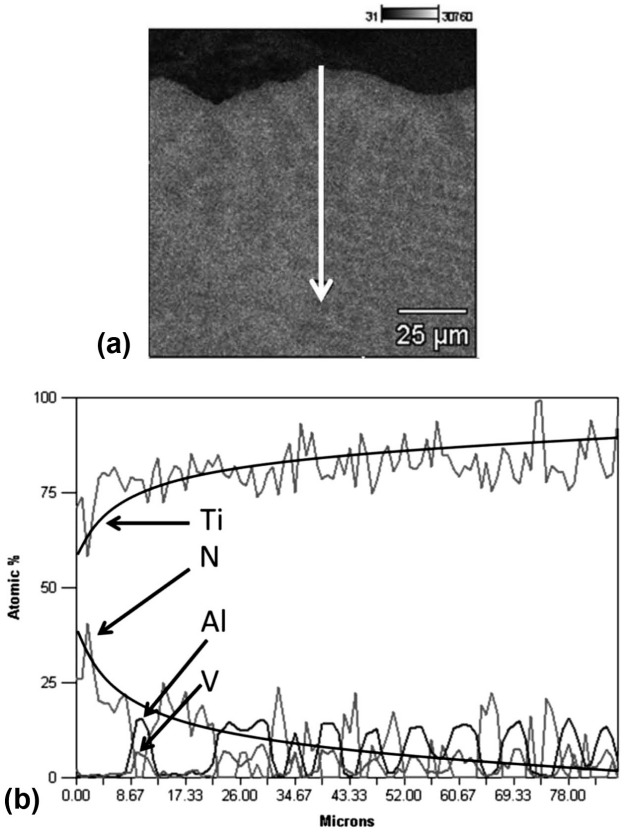

Figure 7: Analysis of the chemical composition on the depth of surface layers LS1 indicates the: a) the line along which the chemical composition was determined b) change in the composition of individual elements

purity, etc., and the microhardness can be significantly higher than 2400 HV. On the other hand, the results of hardness nanoindentation of nanocrystalline TiN presented in the literature show significant difference between the single crystal TiN (2900 HV) and the polycrystalline TiN (3200 HV).[26,27] In the case of the middle region (B) of the surface layer SL1 the atomic ratio of TiN_X dendrites was determined as 38 % of amount fractions of nitrogen and 62 % of amount fractions of titanium, so the $TiN_{0.61}$ phase was identified. Additionally, the quantity (volume fraction) of dendritic precipitations decreases with the depth. Thus, the microhardness changes should be considered in relation to both the share of titanium nitrides precipitations, as well as to the atomic ratio N/Ti of the TiN_X compounds. Since the stoichiometric titanium nitrides δ-TiN have the highest hardness, the share of these nitrides determines the maximum hardness of the surface layers. The third characteristic region C that can be distinguished in the surface layer SL1 is placed on the bottom, i.e., at the boundary of fusion zone and the heat-affected zone. In this specific region, the amount of titanium nitrides is very small, but the microhardness remains at a high level of about 510 HV0.2. This is because high cooling rates resulted in the formation of martensitic structure of α'-Ti(N). However, the titanium metal matrix is enriched in nitrogen, which is a strong α-phase stabilizer and its solubility in the α-Ti phase reaches 23 % of amount fractions at 1050 °C. Additionally, nitrogen is an interstitial element, which can be considered as strengthening element. The nitrogen distorts the lattice of α'-Ti matrix by occupying the available interstitial sites in the structure. Thus, during the laser gas nitriding in the liquid state the lattice parameter of α'-Ti phase is affected by both the rapid cooling rates and the nitrogen content dissolved in the titanium matrix. On the other hand, in the region of the heat-affected zone, which reaches the bottom surface of the 3.0-mm-thick sample, the microhardness is in a range from 450 HV0.2 to 500 HV0.2.

The surface layers SL2 and SL3, produced at significantly lower energy inputs of 90 J/mm and 60 J/mm, respectively, show a different morphology (**Figure 6**). The surface layer SL2 is covered by a homogenous layer of stoichiometric δ-TiN, but the layer is thinner compared to the surface layer SL1. In this case the thickness of the homogenous layer is from 2 µm up to 5 µm. Dendrites perpendicular to the top surface layer extend to a depth of approximately 100 µm. In contrast to the surface layer SL1, in this case the dendritic nitrides are embedded by the metallic matrix of α'-Ti(N) in the subsurface region (**Figure 6a**). Therefore, the maximum value of the microhardness measured in the subsurface region is just 1340 HV0.2. Next the microhardness falls

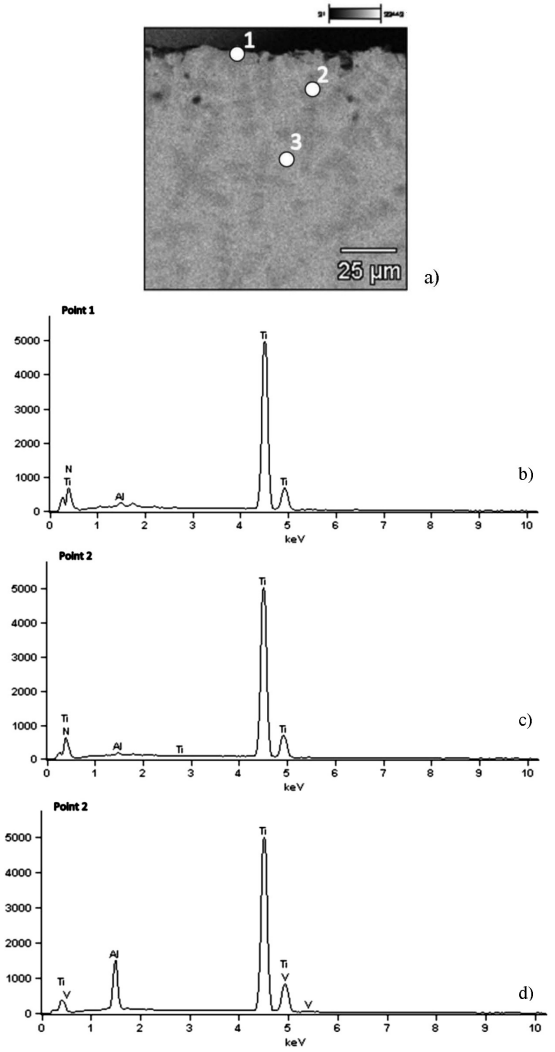

Figure 8: EDS analysis in the subsurface region of the surface layer SL1: a) points of EDS measurements on the cross-section, b) EDS in the point 1, c) EDS in the point 2, d) EDS in the point 3

down to approximately 550 HV0.2 and 400 HV0.2 in the heat-affected zone.

The surface layer SL3 produced at the lowest energy input is also covered by the characteristic golden layer; however, the surface layer is very thin and not tight (**Figure 6b**). The thickness of the layer is from 1 µm to 3 µm. The longest dendrites in the subsurface region have approximately 30 µm. Additionally, the share of titanium matrix α'-Ti(N) is significantly greater than the dendritic nitrides. Therefore, in this case the highest microhardness of just 820 HV0.2 was determined in the subsurface region, and next the microhardness decreased gradually to the value 500 HV0.2 characteristic for the heat-affected zone.

4 CONCLUSIONS

The morphology of surface layers produced by the HPDDL laser surface melting of the Ti6Al4V alloy in a pure nitrogen atmosphere are dependent on the laser processing conditions, such as laser power, beam power density, and scanning speed. However, the highest values of microhardness were measured directly under the top surface for each nitrided surface layer. Depth profiles of microhardness determined on the cross-sections indicate that the microhardness decreases gradually from the subsurface region to the base metal of the titanium alloy, having a microhardness of 330–350 HV.02. The highest value of the microhardness of approximately 2330 HV0.2 was determined in the subsurface region of the surface layer with the greatest depth of 1.6 mm, produced at the highest energy input of 270 J/mm. The subsurface region consists mainly of closely spaced dendrites oriented perpendicularly to the surface, and identified by XRD and EBSD analysis as titanium nitrides. Additionally, each nitrided surface is covered tightly by a homogenous layer having a thickness up to 10 µm. The top layer was also identified as the TiN phase at the stoichiometric or near stoichiometric atomic ratio of N/Ti. Below the subsurface region the orientation of dendrites becomes random, and additionally a needle-like phase occurs. The needle-like structure was identified as the matrix of martensitic α'-Ti(N) enriched in nitrogen. The share of the dendritic precipitations and the needle-like matrix structure changes with depth. Moreover, the dendrites concentration decreases with the depth. Thus, it is clear that value of the hardness or the microhardness is correlated with the share of dendritic titanium nitrides and the matrix. However, it was found that the atomic ratio N/Ti of the dendritic nitrides is not constant for the nitrided layers produced under different conditions, as well as within a single layer produced at the highest energy input. The EBSD results showed that the dendritic nitrides in the subsurface region of the thicker surface layer are mainly stoichiometric δ-TiN with the atomic ratio 50 % of N and 50 % of Ti. Since the stoichiometric titanium nitrides exhibit the highest hardness, the share of stoichiometric δ-TiN determines the maximum hardness of the surface layers. The share of stoichiometric δ-TiN decreases rapidly with the depth, which is why the highest microhardness of the composite TiN/Ti layers can be found directly under the top surface, and next the drop of microhardness can be observed.

5 REFERENCES

[1] A. Lisiecki, Titanium matrix composite Ti/TiN produced by diode laser gas nitriding, Metals, 5 (**2015**), 54–69, doi:10.3390/met5010054

[2] R. Burdzik, L. Konieczny, Z. Stanik, P. Folega, A. Smalcerz, A. Lisiecki, Analysis of impact of chosen parameters on the wear of camshaft, Arch. Metall. Mater., 59 (**2014**), 957–963, doi:10.2478/amm-2014-0161

[3] J. Kusiński, S. Kac, A. Kopia, A. Radziszewska, M. Rozmus-Górnikowska, B. Major, L. Major, J. Marczak, A. Lisiecki, Laser modification of the materials surface layer – a review paper, Bull. Pol. Acad. Sci. Tech. Sci., 60 (**2012**), 711–728, doi:10.2478/v10175-012-0083-9

[4] J. Górka, Weldability of thermomechanically treated steels having a high yield point, Arch. Metall. Mater., 60 (2015), 469–475

[5] A. Kurc-Lisiecka, W. Ozgowicz, W. Ratuszek, J. Kowalska, Analysis of deformation texture in AISI 304 steel sheets, Sol. St. Phenom., 203–204 (**2013**), 105–110, doi:10.4028/www.scientific.net/SSP.203-204.105

[6] K. Janerka, M. Pawlyta, J. Jezierski, J. Szajnar, D. Bartocha, Carburiser properties transfer into the structure of melted cast iron, J. Mat. Proc. Tech., 214 (**2014**) 4, 794–801

[7] L. Konieczny, R. Burdzik, B. Lazarz, Application of the vibration test in the evaluation of the technical condition of shock absorbers built into the vehicle, J. Vibroeng, 15 (**2013**) 4, 2042–2048

[8] A. Czuprynski, J. Górka, M. Adamiak, Examining properties of arc sprayed nanostructured coatings, Metalurgija, 55 (**2016**) 2, 173–176

[9] L. A. Dobrzański, W. Sitek, M. Krupiński, J. Dobrzański, Computer aided method for evaluation of failure class of materials working in creep conditions, J. Mat. Proc. Tech., 157 (**2004**), 102–106

[10] J. Bodzenta, A. Kaźmierczak, T. Kruczek, Analysis of thermograms based on FFT algorithm, J. Phys. IV, 129 (**2005**), 201–206

[11] G. Moskal, A. Grabowski, A. Lisiecki, Laser remelting of silicide coatings on Mo and TZM alloy, Sol. St. Phenom., 226 (**2015**), 121–126, doi:10.4028/www.scientific.net/SSP.226.121

[12] A. Lisiecki, Welding of thermomechanically rolled steel by Yb:Yag disk laser, Arch. Metall. Mater., 60 (**2015**), 2851–2859, doi:10.1515/amm-2015-0456

[13] A. Lisiecki, R. Burdzik, G. Siwiec, Ł. Konieczny, J. Warczek, P. Folęga, B. Oleksiak, Disk laser welding of car body zinc coated steel sheets, Arch. Metall. Mater., 60 (**2015**), 2913–2922, doi:10.1515/amm-2015-0465

[14] A. Lisiecki, Welding of thermomechanically rolled fine-grain steel by different types of lasers, Arch. Metall. Mater., 59 (**2014**), 1625–1631, doi:10.2478/amm-2014-0276

[15] R. Burdzik, T. Węgrzyn, Ł. Konieczny, A. Lisiecki, Research on influence of fatigue metal damage of the inner race of bearing on vibration in different frequencies, Arch. Metall. Mater., 59 (**2014**), 1275–1281, doi:10.2478/amm-2014-0218

[16] M. Staszuk, L. A. Dobrzański, T. Tański, W. Kwaśny, M. Musztyfaga-Staszuk, The effect of PVD and CVD coating structures on the durability of sintered cutting edges, Arch. Metall. Mater., 59 (**2014**), 269–274

[17] A. Grajcar, M. Różański, S. Stano, A. Kowalski, Microstructure characterization of laser-welded Nb-microalloyed silicon-aluminum TRIP steel, J. Mater. Eng. Perform., 23 (**2014**), 3400–3406

[18] T. Węgrzyn, J. Piwnik, D. Hadryś, R. Wieszała, Car body welding with micro-jet cooling, J.Arch. Mater. Sci. Eng., 49 (**2011**), 90–94

[19] A. Grajcar, M. Różański, S. Stano, A. Kowalski, B. Grzegorczyk, Effect of heat input on microstructure and hardness distribution of laser welded Si-Al TRIP-type steel, Adv. Mater. Sci. Eng., 2014 (**2014**), doi.org/10.1155/2014/658947

[20] B. Oleksiak, G. Siwiec, A. Blacha-Grzechnik, J. Wieczorek, The obtained of concentrates containing precious metals for pyro-metallurgical processing, Metalurgija 53 (**2014**), 605–608

[21] J. Slania, Influence of phase transformations in the temperature ranges of 1250–1000 °C and 650–350 °C on the ferrite content in austenitic welds made with T 23 12 LRM3 tubular electrode, Arch. Metall. Mater., 50 (**2005**), 757–767

[22] D. Janicki, Disk laser welding of Armor steel, Arch. Metall. Mater., 59 (**2014**), 1641–1646, doi:10.2478/amm-2014-0279

[23] B. Slazak, J. Słania, T. Węgrzyn, A. P. Silva, Process stability evaluation of manual metal arc welding using digital signals, Mater. Sci. Forum, 730–732 (**2013**), 847–852

[24] H. C. Man, Z. D. Cui, T. M. Yue, F. T. Cheng, Cavitation erosion behavior of laser gas nitrided Ti and Ti6Al4V alloy, Mat. Sci. Eng. A, 355 (**2003**), 167–173, doi:10.1016/S0921-5093(03)00062-5

[25] S. Mridha, T. N. Baker, Effects of nitrogen gas flow rates on the microstructure and properties of laser-nitrided IMI318 titanium alloy (Ti–4V–6Al), J. Mat. Proc. Tech., 77 (**1998**), 115–121, doi:10.1016/S0924-0136(97)00408-1

[26] C. Hu, T.N. Baker, The importance of preheat before laser nitriding a Ti-6Al-4V alloy, Mat. Sci. Eng. A, 265 (**1999**), 268–275, doi:10.1016/S0921-5093(98)01135-6

[27] M. S. Selamat, T. N. Baker, L. M. Watson, Study of the surface layer formed by the laser processing of Ti–6Al–4V alloy in a dilute nitrogen environment, J. Mat. Proc. Tech., 113 (**2001**), 509–515, doi:10.1016/S0924-0136(01)00595-7

[28] W. Pakieła, T. Tański, Z. Brytan, K. Labisz, The influence of laser alloying on the structure and mechanical properties of AlMg5Si2Mn surface layers, Appl. Phys. A, 122 (**2016**), 352, doi:10.1007/s00339-016-9834-z

[29] M. Bonek, The investigation of microstructures and properties of high speed steel HS6-5-2-5 after laser alloying, Arch. Metall. Mater., 59 (**2014**), 1647–1651, doi:10.2478/amm-2014-0280

UDK 67.017:621.9.025.6:621.78
Original scientific article/Izvirni znanstveni članek

ISSN 1580-2949
MTAEC9, 51(4)585(2017)

STUDY OF THE PROPERTIES AND STRUCTURE OF SELECTED TOOL STEELS FOR COLD WORK DEPENDING ON THE PARAMETERS OF HEAT TREATMENT

ŠTUDIJA LASTNOSTI IN STRUKTURE IZBRANIH ORODNIH JEKEL ZA HLADNO OBLIKOVANJE V ODVISNOSTI OD TOPLOTNE OBDELAVE

Martin Kuřík, Jakub Lacza, Tomáš Vlach, Jana Sobotová

Czech Technical University, Faculty of Mechanical Engineering, Karlovo námesti 13, 121 35 Prague 2, Czech Republic
martin.kurik@fs.cvut.cz

Prejem rokopisa – received: 2016-06-20; sprejem za objavo – accepted for publication: 2016-12-09

doi:10.17222/mit.2016.120

Tool steels produced with powder metallurgy (P/M) are perspective materials, although they are more expensive in comparison with tool steels produced with the conventional method. The work focuses on the study of mechanical properties and structure depending on the heat-treatment conditions for the two tool steels. These are the 1.2379 steel for cold work produced with classical metallurgy and high-speed P/M steel Vanadis 23. Both materials were heat treated in the conventional manner to achieve a hardness of 61 HRC. They were also exposed to a cryogenic treatment at temperatures of –90 °C and –196 °C for 4 h between the hardening and the tempering. We evaluated the hardness and strength using the three-point-bending test and the wear resistance using the pin-on-disk method.

Keywords: powder metallurgy, high-speed steels, heat treatment, cryogenic treatment, wear rate

Orodna jekla, proizvedena s postopki metalurgije v prahu (angl. P/M) so perspektivni materiali, kljub temu da so dražji od tistih izdelanih s konvencionalno metodo. Delo je osredotočeno na študijo mehanskih lastnosti in strukturo, v odvisnosti od pogojev toplotne obdelave za ti dve vrsti orodnih jekel. To so jekla 1.2379 za delo v hladnem, proizvedena s klasičnimi metalurškimi postopki in hitrorezno P/M jeklo Vanadis 23. Oba materiala sta bila toplotno obdelana s konvencionalnimi postopki, glede na njuno sestavo, tako, da sta dosegli trdnost 61 HRC. Bili sta tudi izpostavljeni obdelavi s podhlajevanjem pri temperaturah od –90 °C in –196 °C za 4 h med strjevanjem in temperiranjem. Trdnost je bila ocenjena pri tritočkovnem mehanskem testu (zvijanje) in s testom obrabe po metodi pin-on-disk.

Ključne besede: metalurgija prahov, visokorezna jekla, toplotna obdelava, obdelava s podhlajevanjem, stopnja obrabe

1 INTRODUCTION

It is well known that for tool steels at a given hardness, the wear resistance may vary depending on the parameters of heat treatment and also on the mode of load for the tool during its use in manufacturing. In addition, we can assume that the resulting wear resistance will also affect the method of producing the material itself. As most of the tool steels are produced in the metallurgical process based on the solidification of the melt, this method can be classified as conventional (C/M). This metallurgy causes undesirable segregation that negatively affects the primarily toughness. In the tool steels produced with powder metallurgy (P/M), we achieve, in comparison with C/M, a finer and more homogeneous structure exhibiting better mechanical properties of the tools, such as greater toughness and wear resistance at higher cutting speeds.[1] Although P/M tool steels are several times more expensive compared with C/M steels, they may be economically advantageous. The economic benefit of their use is particularly significant in the applications where the replacement of the tools is time consuming.

The present work deals with a comparison of the properties of selected tool steels for cold work with different primary-metallurgy steels, which were heat treated in a conventional manner (CHT), i.e., quenched and multiply tempered. Currently, the cryogenic treatment is increasingly used for tool steels.[1–5] The aim is to obtain the optimum ratio between contradictory properties, like hardness and toughness, providing for a greater wear resistance of the treated instruments.[5] Authors attribute this benefit of cryogenic treatment to the precipitation of very fine carbides and a reduction of the proportion of the residual austenite in the structure. Cryogenic treatment usually takes place between quenching and tempering; its main parameters are the temperature and the holding time. Cryogenic treatment is generally divided, according to the minimum temperature, into: shallow cryogenic treatment (SCT), which is generally performed in a temperature range from –80 °C to –140 °C and deep cryogenic treatment (DCT), which is generally performed at a temperature of –196 °C.[5] It can be said that, in the available literature, we can clearly find more publications dedicated to monitoring the effect of cryogenic treatment on the functional characteristics of

the C/M tool steel, compared with the publications that address the same issue for the P/M steel. There are only a few papers about the benefits of the cryogenic treatment of high-speed steels (HSS).[6,7] In the present work, we observe the influence of heat treatment on the properties of C/M tool steel 1.2379 and P/M HSS Vanadis 23. The work is part of the solution of a problem taken from practice, and the task is to find a more suitable material for a tool for cold forming and specify its heat treatment. A heat-treatment shop suggested to a customer to use cryogenically treated steel Vanadis 23 (1.3395) instead of steel 1.2379 (X153CrMoV12, AISI D2).

Steel 1.2379 is a C/M cold-work tool steel with high carbon and chromium contents. The steel is characterized with a high wear resistance, high compressive strength, good hardenability, high dimensional stability and good resistance to tempering. It is recommended for the tools that require a high wear resistance and sufficient toughness. The maximum hardness in the soft-annealed condition is 250 HBW. This steel is often used for cryogenic treatment as reported in references.[2–4] It is noted that the steel showed an improvement in the wear resistance after cryogenic processing. For example, Das et al. investigated the effect of cryogenic treatment including low-temperature quenching and low-temperature tempering on the structure and properties of the 1.2379 steel.[8,9] The authors conclude that both bulk hardness and apparent hardness of the matrix of the 1.2379 steel increase with the decreasing temperature of cryogenic treatments; however, this effect is more pronounced for the manifestation of the hardness of the matrix than of the bulk hardness.[8] Furthermore, the authors note that the wear resistance of the 1.2379 steel gets considerably enhanced due to cryogenic treatment, compared to that of the CHT one, irrespective of the holding time at –196 °C.

The extent of the improvement in the wear resistance monitored with a pin-on-disk tester, however, is dependent on the test condition (using the normal load and sliding velocity). The authors attribute this fact to the wear-test condition, controlling the active mechanisms and the mode of wear. It was found that the hardness of the 1.2379 steel increases marginally due to cryogenic treatment, in contrast to a significant increase in the wear resistance. The most suitable parameters of DCT were determined for the 1.2379 tool steel, which are –196 °C/36 h for obtaining the best combination of the desired microstructure and wear properties of the steel.[9] It is necessary to mention that at the used cooling and heating rate of 0.75 K/min during the cryogenic treatment, the total time is 46 hours for DCT. Generally, when the time is longer, the processing is more expensive. This fact must also be included in the design of the parameters of DCT for real tools.[10]

Vanadis 23 (1.3395) is a chromium-molybdenum-tungsten-vanadium-alloyed high-speed P/M steel which is characterized by an excellent combination of wear resistance and toughness, correct hardness for the application, very good dimensional stability during heat treatment and temper resistance. The maximum hardness in the soft-annealed condition is 260 HBW. It is especially suitable for blanking and forming thinner work materials where mixed (abrasive-adhesive) or abrasive types of the wear are encountered and where the risk for a plastic deformation of the working surface of a tool is high. We do not know of a research in the literature that would resolve the influence of heat-treatment conditions on the properties of this steel. However, C/M high-speed steel 1.3343 (AISI M2) is often used for cryogenic treatment according to references,[6,11–12] as it has low carbon and vanadium contents in comparison with the other type of steel. Reference[12] notes that no significant impact of DCT on the final hardness of steel 1.3343 was not proven, while its positive effect on the wear resistance was demonstrated. The wear resistance was observed to be greater by 44 % after DCT, in comparison with that obtained after CHT using laboratory tests.

The tool life of twist drills made of steel increased after DCT, depending on the cutting conditions, in a range of 65–343 %. Conversely, reference[11] notes that the hardness and also the wear resistance increase after DCT for steel 1.3343. A 6 % increase in the hardness and a 35 % increase in the wear resistance are established. It is stated in reference[6] that moderate increases in the hardness and fracture toughness after DCT for steel 1.3343 result in a better wear resistance than in the case when only one of the parameters is extremely high. However, reference[7] observes that the influence of DCT was not found for the hardness of P/M HSS Vanadis 30.

The aim of the present work was to investigate the effects of SCT and DCT taking place between quenching and tempering on the properties and structures of the two above-mentioned tool steels.

Table 1: Heat treatment of the experimental materials

Material	Quenching	Cryogenic treatment	Tempering	Designation of the regime
1.2379	1050 °C/30 min	–	2× 500 °C/2 h	CHT
1.2379	1050 °C/30 min	–90 °C/4 h	2× 500 °C/2 h	SCT
1.2379	1050 °C/30 min	–196 °C/4 h	2× 500 °C/2 h	DCT
Vanadis 23	1050 °C/5 min	–	3× 560 °C/1 h	CHT
Vanadis 23	1050 °C/5 min	–90 °C/4 h	3× 560 °C/1 h	SCT
Vanadis 23	1050 °C/5 min	–196 °C/4 h	3× 560 °C/1 h	DCT

2 EXPERIMENTAL PART

The experimental material included commercial C/M cold-work steel 1.2379 (X153CrMoV12, AISI D2), nominally containing (in mass fractions, *w*/%) 1,53 % C, 0,35 % Si, 0,45 % Mn, 12,00 % Cr, 0,85 % Mo, 0,85 % V and P/M HSS Vanadis 23 (1.3395) nominally containing (in mass fractions, *w*/%) 1,29 % C, 058 % Si, 0,29 % Mn, 0,024 % P, 0,014 % S, 4,02 % Cr, 4,91 % Mo, 6,13 % W, 2,97 % V. The choice of the materials was explained in the introduction. Samples for the three-point-bending test (10 × 10 × 100 mm with surface roughness of 0.2–0.3 μm) were made from the two materials. CHT consisted of the following steps for both materials: austenitizing, quenching and double or triple tempering. Cryogenic processing also included hardening and tempering of each material. The heat-treatment regime is shown in **Table 1**. Five samples of each series were processed.

The distance between supports was 80 mm during the three-point-bending test; the loading rate was 1 mm/min up to the moment of fracture. The average values and standard deviation were calculated from the measured values. Broken specimens were used for measuring the HRC hardness. The hardness was measured five times on each sample and the average values and standard deviation were calculated. One specimen whose strength was close to the average value was chosen from each series. These samples served for a metallographic analysis and the measurement of the wear resistance. A basic metallographic analysis was performed using light microscopy of cross-section samples. Metallographic samples were prepared in the standard way and etched with 2 % Nital.

SEM micrograhps were taken with a JOEL JSM7600F device. The wear resistance was determined with the pin-on-disk tester in line with the standard.[13] As the disk was used for testing the material, its surface was polished to a surface roughness better than 0.04 μm. The test was carried out under dry sliding conditions, performed at a room temperature of 22 °C and relatively humidity of 60 %. All the specimens were ultrasonically cleaned in ethanol and dried in air. An Al_2O_3 ball of ∅ 6 mm was used as the counterpart. The sliding speed was 6.4 cm/s, the total sliding distance was 100 m and the scratch radius was 4 mm. The width of scratches was evaluated with light microscopy using a Nis Elements image analyser, always at six locations. The average value was calculated and the wear rate was determined. Control measurements were performed in the transverse area of the scratches using a profilometer, recording a good range of the results.

3 RESULTS AND DISCUSSION

The bending strength for both materials is shown in **Figure 1**. As expected, the strength of steel Vanadis 23 is about 1000 MPa higher than that of steel 1.2379. As stated by the author in reference[14], the flexural strength is dependent, among other things, on the size and distribution of carbides. For steel Vanadis 23, a more uniform distribution of small carbides is expected than in the case of steel 1.2379. Fracture was always brittle to form two large parts and small fragments of the fracture surface. The measurement was conducted only for the purpose of comparison.

It can be concluded that the bending strength was almost identical depending on the heat treatment of both steels. This result is in good agreement with the results of previous works.[7,15] As expected, the hardness of steel Vanadis 23 is 1–2 HRC higher than the hardness of steel 1.2379 (**Figure 2**).

It seems that the hardness values slightly decreased for the two reference materials after cryogenic processing, which is in good agreement with the results of monitoring the impact of cryogenic treatment on the properties of P/M tool steel Vanadis 6.[15,16] On the contrary, D. Das[8] concluded that both the bulk hardness and the apparent hardness of the matrix increase with the decreasing temperature of cryogenic treatments of the C/M 1.2379 steel, and that the degree of influence of cryogenic treatment on the hardness is dependent on the parameters of the heat treatment (the temperature and time of austenizing and tempering) as well as the rate of cooling, depth of cryogenic treatment and holding time. However, it should be noted that in his case, low-temperature tempering was used.

The microstructures of steels 1.2379 and Vanadis 23 after CHT and DCT are shown in **Figure 3.** The microstructure of both steels consists of the matrix and carbides. The distribution and size of carbides differ, de-

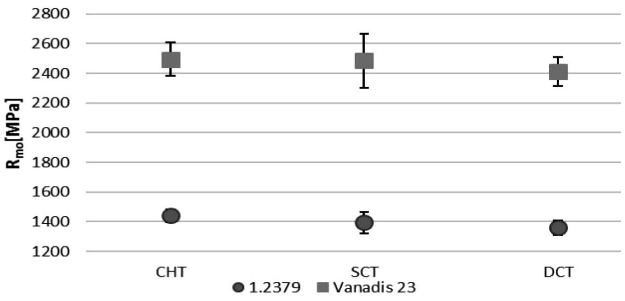

Figure 1: Influence of heat treatment on the bending strength of 1.2379 and Vanadis 23 steels

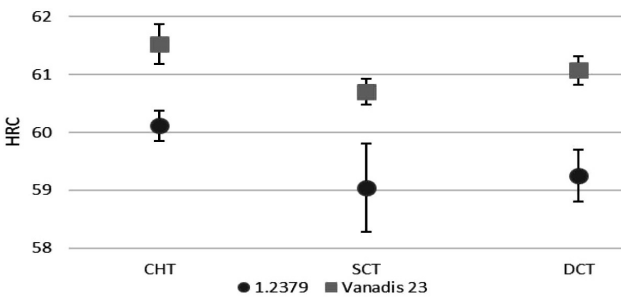

Figure 2: Influence of heat treatment on the hardness of 1.2379 and Vanadis 23 steels

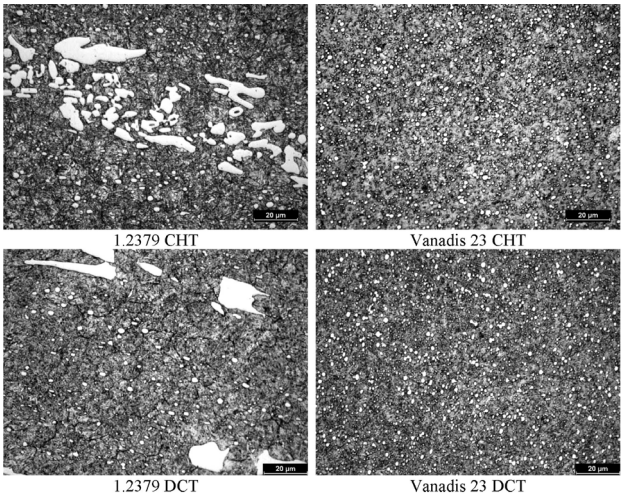

Figure 3: Microstructures of 1.2379 and Vanadis 23 steels after CHT and DCT

pending on the method of steelmaking (C/M or P/M). The banding carbides observed in steel 1.2379 confirm the measurement of the bending strength. In both cases, the matrix mainly contains tempered martensite. Minor phases include retained austenite. It can be expected that the amount of retained austenite and precipitated fine carbides is smaller after DCT than after CHT.[2–4]

The SEM analysis did not show any significant differences in the structure between CHT, SCT and DCT. No significant areas of residual austenite were observed, as illustrated in **Figure 4**. A TEM analysis was necessary for an accurate determination of the amount of residual austenite. In both cases, we observed small carbides with sizes smaller than 1 micron, but in the case of Vanadis 23, their amount was significantly larger. Moreover, its structure included carbides with sizes of 100–200 nm.

The wear rate was determined for both materials and monitored states (**Figure 5**). As expected, it is seen that

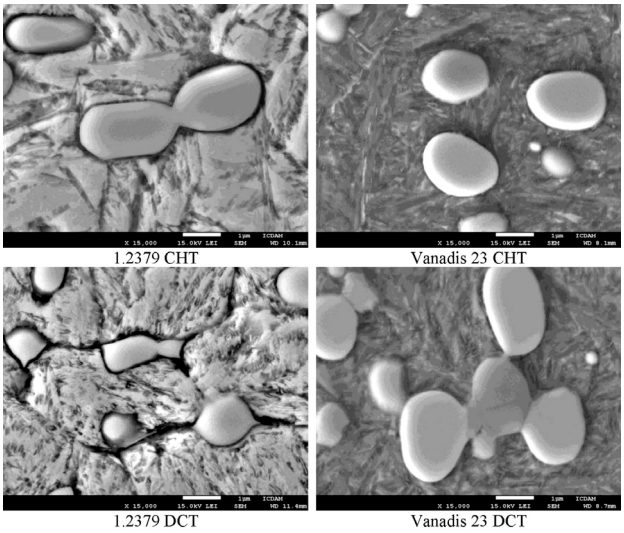

Figure 4: SEM micrographs of 1.2379 and Vanadis 23 steels after CHT and DCT

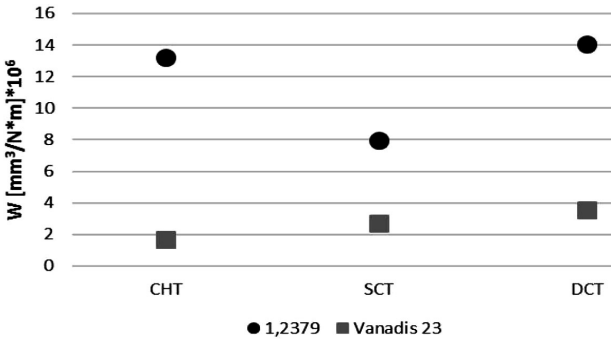

Figure 5: Influence of heat treatment on the wear rate of 1.2379 and Vanadis 23 steels

the wear-rate values are much lower for Vanadis 23 than for steel 1.2379. The wear rate of steel Vanadis 23 depends on the heat treatment, but it varies minimally. It was necessary to verify the value of the wear rate of steel 1.2379 after SCT. The existing results and the results from reference[9] do not indicate that the wear rate should be lower after SCT than after DCT of the 1.2379 steel. Based on these laboratory results, it is possible to believe that Vanadis 23 is a suitable material for the replacement of steel 1.2379 in the case of cold forming. Although the current results of the pin-on-disk test do not conform to our assumption, it can be assumed that the tools made of steel Vanadis 23 using DCT have better wear resistance than the tools after CHT. The results may be distorted because the formed wear-track width was between 200–300 microns, which is about 5 % of the diameter of the inserted Al_2O_3 ball. Based on this finding, it would be preferable to use a larger normal load for the pin-on-disc test for the wear-track width to be in a range of 20–80 % of the ball diameter. Yan[10] states that although the hardness and wear tests provided information on the properties of the cryogenically treated HSS, they may not properly represent the loads of real tools in the operating conditions. For this reason, the heat treatment of P/M HSS Vanadis 23 will be recommended after a durability test of real tools.

4 CONCLUSIONS

The obtained results and our pertinent discussion allow us to infer the following:

- The bending-strength values were almost identical after the conventional and cryogenic treatment of C/M tool steel 1.2379 and P/M HSS Vanadis 23. The strength of steel Vanadis 23 was about 1000 MPa higher than that of steel 1.2379 in all the modes of heat treatment.
- The hardness values for the two reference materials slightly decreased after the cryogenic processing. The hardness of steel Vanadis 23 was 1–2 HRC higher than the hardness of steel 1.2379.

- Light metallography is not appropriate for investigating structural changes after the cryogenic treatment of the 1.2379 and Vanadis 23 steel.
- The wear-rate values are much lower for Vanadis 23 than for steel 1.2379.
- Based on these laboratory results, Vanadis 23 is a suitable material for the replacement of steel 1.2379 in the case of cold forming.
- The inclusion of a cryogenic treatment in the conventional heat treatment of Vanadis 23 will be decided on after a durability test of real tools.

Acknowledgements

This work was supported by the Ministry of Education, Youth and Sport of the Czech Republic, programe NPU1, project No. LO1207 and by the Grant Agency of the Czech Technical University in Prague, grant No. SGS15/149/OHK2/2T/12.

5 REFERENCES

[1] S. Akincioğlu, H. Gökkaya, İ. Uygur, A review of cryogenic treatment on cutting tools, The Inter. J. of Advanced Manufacturing Technology, 78 (**2015**), 1609–1627, doi:10.1007/s00170-014-6755-x

[2] S. S. Gill, J. Singh, R. Singh, H. Singh, Metallurgical principles of cryogenically treated tool steels, A review on the current state of science, The International Journal of Advanced Manufacturing Technology, 54 (**2011**), 59–82, doi:10.1007/s00170-010-2935-5

[3] N. S. Kalsi, R. Sehgal, V. S. Sharma, Cryogenic Treatment of Tool Materials: A Review, Materials and Manufacturing Processes, 25 (**2010**), 1077–1100, doi:10.1080/10426911003720862

[4] P. F. Stratton, Optimising nano-carbide precipitation in tool steels, Materials Science and Engineering A, 449–451 (**2007**), 809–812, doi:10.1016/j.msea.2006.01.162

[5] P. Baldissera, C. Delprete, Deep Cryogenic Treatment: A Bibliographic Review, The Open Mechanical Engineering Journal, Benthham Science Publishers Ltd., 2 (**2008**), 1–11

[6] V. Leskovšek, M. Kalin, J. Vižintin, Influence of deep-cryogenic treatment on wear resistance of vacuum heat-treated HSS, Vacuum, 80 (**2006**) 6, 507–518, doi:10.1016/j.vacuum.2005.08.023

[7] J. Sobotová, M. Kuřík, J. Cejp, Influence of Heat Treatment Conditions on Properties of High-Speed P/M Steel Vanadis 30, Key Engineering Materials, 647 (**2015**), 17–22, doi: 10.4028/www.scientific.net/KEM.647.17

[8] D. Das, A. K. Dutta, K. K. Ray, Sub-zero treatments of AISI D2 steel: Part I, Microstructure and hardness, Materials Science and Engineering A, 527 (**2010**), 2182–2193, doi:10.1016/j.msea.2009.10.070

[9] D. Das, A. K. Dutta, K. K. Ray, Influence of varied cryotreatment on the wear behavior of AISI D2 steel, Wear, 266 (**2009**), 297–309, doi: 10.1016/j.wear.2008.07.001

[10] X. G. Yan, D. Y. Li, Effects of the sub-zero treatment condition on microstructure, mechanical behavior and wear resistance of W9Mo3Cr4V high speed steel, Wear, 302 (**2013**), 854–862, doi:10.1016/j.wear.2012.12.037

[11] A. Molinari, M. Pellizzari, S. Gialanella, Effect of deep cryogenics treatment on the mechanical properties of tool steels, Journal of Material Processing Technology, Elsevier Science B.V., 118 (**2001**), 350–355, doi:10.1016/S0924-0136(01)00973-6

[12] F. J. Da Silva, S. D. Franco, Á. R. Machado, E. O. Ezugwu, Performance of cryogenically treated HSS tools, Wear, 261 (**2006**), 674–685, doi:10.1016/j.wear.2006.01.017

[13] Standard Test Method for Wear Testing with a Pin-on-Disk Apparatus: G99-05, Reapproved, ASTM International, 2010, USA

[14] P. Jurči, Tool steel of the ledeburutuc type, Czech Technical University Prague, 2009, 221

[15] J. Sobotová, P. Jurči, I. Dlouhý, The effect of sub-zero treatment on microstructure, fracture toughness and wear resistance of Vanadis 6 tool steel, Materials Science and Engineering A, 652 (**2016**), 192–204, doi:10.1016/j.msea.2015.11.078

[16] J. Sobotová, P. Jurči, J. Cejp, Structure and Properties of Sub-Zero Processed Vanadis 6, Metal 2011 – 20th International Conference on Metallurgy and Materials, Ostrava, 2011, 672–677

UDK 536.421.48:620.178.2:669.15-194.55:691.714
Original scientific article/Izvirni znanstveni članek

ISSN 1580-2949
MTAEC9, 51(4)591(2017)

INFLUENCE OF A CRYOGENIC TREATMENT ON THE FRACTURE TOUGHNESS OF AN AISI 420 MARTENSITIC STAINLESS STEEL

VPLIV PODHLAJEVANJA NA LOMNO ŽILAVOST MARTENZITNEGA NERJAVEČEGA JEKLA AISI 420

Germán Prieto[1,2], W. R. Tuckart[1,2], Juan Elias Perez Ipiña[2,3]

[1]National University del Sur, Tribology Group, Engineering Department, Bahía Blanca, Argentina
[2]National Scientific and Technical Research Council (CONICET), Buenos Aires, Argentina
[3]Comahue National University, Engineering Faculty, Fracture Mechanics Group, Neuquén, Argentina
german.prieto@uns.edu.ar

Prejem rokopisa – received: 2016-06-23; sprejem za objavo – accepted for publication: 2016-11-16

doi:10.17222/mit.2016.126

Cryogenic treatments have been employed over the past three decades for both tool and high-alloy steels to improve their wear resistance, mainly through the transformation of retained austenite and the precipitation of fine carbides. However, as the enhancement of one material property is often at the expense of another, it is interesting to evaluate the effect of this type of treatments on the fracture toughness. The objective of the present work was to determine the plane-strain fracture toughness of a cryogenically treated low-carbon AISI 420 martensitic stainless steel by means of standardized fracture tests, performed in accordance with the ASTM E399 and ASTM E1820 standards. In this study, it was experimentally demonstrated that cryogenically treated specimens showed a simultaneous increase in the K_{IC} and hardness of 30 % and 5 %, respectively, compared to conventionally treated specimens.

Keywords: cryogenic treatment, carbide refinement, plane-strain fracture toughness, low-carbon martensitic stainless steel

Obdelava s podhlajevanjem v zadnjih treh desetletjih, tako za orodja kot za visokolegirana jekla, pomeni izboljšanje njihove odpornosti proti obrabi, predvsem zaradi preoblikovanja zadržanega avstenita in zgoščevanja finih delcev. Kakorkoli že, izboljšanje enega materiala je pogosto, vendar na račun drugega, zato je zanimivo oceniti učinek takega tipa obdelave na lomno žilavost. Predmet pričujočega dela je bila določitev lomne žilavosti kriogensko obdelanega nizkoogljikovega martenzitnega nerjavečega jekla AISI 420, s pomočjo standardiziranih testov zlomov, izvedenih v skladu s standardoma ASTM E399 in ASTM E1820. V študiji je bilo s poizkusi dokazano, da so kriogensko obdelani vzorci pokazali hkratno povečanje K_{CI} in trdote za 30 % in 5 %, v primerjavi s konvencionalno obdelanimi vzorci.

Ključne besede: obdelava s podhlajevanjem, prečiščenje delcev, lomna žilavost, nizkoogljočno martenzitno nerjaveče jeklo

1 INTRODUCTION

AISI 420 is a martensitic stainless steel, with carbon contents ranging between 0.15 % mass fraction and 0.40 % mass fraction, while its corrosion resistance comes from the addition of chromium (12–14 % mass fractions). Due to its balance between mechanical properties and the corrosion resistance, it is widely used in power generation, turbine blades, compressors, oil extraction, chemical, petrochemical and surgical equipment. Thus, the enhancement of its mechanical properties, in particular its wear resistance, is of technological interest.[1–4] In this sense, deep cryogenic treatments (DCT) are increasingly utilized for steels and other groups of alloys for improving their tribological performance. This kind of treatment possesses several advantages, such as its relative low cost, ease of application, low environmental impact and, especially, its volumetric effect. This means that the whole volume of a workpiece exhibits a wear-resistance enhancement in comparison to superficial techniques, such as plasma nitriding, electrodeposited coatings or case carburization.

Traditionally, the improvement of the tribological resistance of steel alloys was attributed to the transformation of retained austenite[1,5–7] and to the refinement of secondary carbides.[8–10] Recent studies have shown that the martensitic transformation of retained austenite at low temperatures involves a plastic deformation of virgin martensite.[4,11] This plastic deformation causes the capture of immobile carbon atoms by gliding dislocations, forming carbon clusters that can serve as sites for nucleation of finer carbide particles during tempering, therefore influencing the carbide distribution.[12] M. Villa et al.[13] analyzed the generation of compressive strains in austenite after the transformation of martensite at a low temperature. These strains influence the stability of austenite during the subsequent tempering. However, when this transformation occurs below –133 °C, no compressive strains build up in austenite. It should be noted that this mechanism requires the presence of significant amounts of retained austenite after the quenching and before the cryogenic cooling, which is not expected to be the case for AISI 420 due to its chemical composition and excellent hardenability.[14,15]

In our prior work[16], we tested several processing routes, and the one which yielded the best combination of properties was selected to continue studying the effect

of cryogenic treatments on tribological properties and fracture toughness in the context of a PhD thesis.[17] Regarding the wear behavior, we reported, in a preliminary article[10], that cryogenic treatments increase the wear resistance of AISI 420 by 35–90 % in comparison to conventionally treated specimens.

The published results regarding fracture properties are very broad, for example, A. Bensely et al.[18] and D. Yun et al.[19] reported a significant improvement in the impact toughness, ranging between 15–30 % in DCT specimens compared to conventionally treated (CHT) ones, while studying tool steels (M2, T1) and case-carburized steels. Other researchers, such as A. Molinari et al.[20] and F. Cajner et al.[21] concluded that these treatments did not modify the impact toughness, while D. Das et al.[22] and S. Zhirafar et al.[23] reported that cryogenic treatments have a detrimental effect on the impact toughness, accounting for reductions in the order of 15–30 %. B. Podgornik et al.[24] analyzed the effect of cryogenic treatments on two P/M tool steels and one high-speed steel, using several processing routes and reporting varied results.

The purpose of this paper is to determine the influence of a cryogenic treatment on the plane-strain fracture toughness of a martensitic stainless steel, following the well-established procedures determined by ASTM standards.[25]

2 MATERIALS AND METHODS

The material used in this study was an AISI 420 martensitic stainless steel. Its chemical composition was determined using a SPECTRO SPECTROMAXX optical emission spectrometer. The results are shown in **Table 1** along with the reference composition taken from the ASTM A176 standard.[26]

A normalized bar with a diameter of 42 mm was cut into transversal slices, from which disk-shaped compact [DC(T)] specimens were machined according to the specifications of the ASTM E399 standard[25], with a radial- circumferential (R-C) notch configuration. The characteristic dimension (W) of the specimens was 25.4 mm. Except for the notch, all the machining was performed before the heat treatment in order to avoid thermal cracking or an accumulation of residual tensions at the tip of the notch. After the completion of the heat treatment, notches ending in a chevron tip were made by electro-erosion.

Two groups of specimens were prepared, namely, a conventionally heat-treated one (CHT), whose specimens were quenched in oil from 1030 °C and afterwards tempered at 410 °C for 10 min with furnace cooling. The specimens from the other group were quenched in oil from 1030 °C and then soaked in liquid nitrogen at an equilibrium temperature of –196 °C. The specimens were lowered into a vacuum flask containing liquid nitrogen, using a low-speed motor controlled with a closed-loop system using the feedback from the thermocouple attached to each specimen. The cooling rate was set at 0.45 °C /s, while the soaking time was 2 h. Finally, the specimens were tempered at 410 °C for 10 min and slowly cooled inside the furnace. The latter group was identified as DCT. Both the austenization/quenching and the tempering were performed in an argon atmosphere to prevent decarburization.

For the microstructural characterization, a CARL ZEISS EVO 40 XVP scanning electron microscope was employed to evaluate mirror-polished samples attacked with Marble's reagent (10 g $CuSO_4$ in 50 mL HCl and 50 mL water). The Vickers hardness of the specimens was measured using a FUTURE TECH FM-300 microdurometer, with the applied normal load of 500 gf. An open-source image-analysis software (Icy version 1.3.6.0)[27] with a spot-detection plug-in was used for determining the fraction area of carbides in SEM images, as well as the mean distance between the particles, considering the average between each particle and its closest five neighbors.

X-ray diffractometry was performed using a PANALYTICAL X'PERT-MPD diffractometer (Cu-K_α radiation – λ = 0.15405 nm) at an acceleration potential of 40 kV. The diffraction angle ranged from 20–120° with a 0.02° step at a speed of 0.06°/min. The diffractometer was equipped with a graphite diffracted-beam collimator and a programmable receiving slit of 0.2 mm, a divergence slit of 0.4° and an incident and collecting slit of 1°.

2.1. Fracture tests

For obtaining the required fatigue crack, a pre-cracking machine with displacement control was used with a maximum displacement of 0.25 mm at a frequency of 50 Hz. The theoretical K_{max} applied during the pre-cracking process was 20 MPa $m^{1/2}$. In all the cases, the minimum pre-crack length was between $1{\cdot}10^5$ and $1.5{\cdot}10^6$ cycles, in accordance with the ASTM E399 recommendations. This set-up was chosen in order to avoid plastic deformation above the maximum levels allowed by the standard in the surroundings of a crack tip (Equation (3)).[3]

Plane-strain fracture tests were performed in a screw-driven AMSLER vibrophore, using a load cell of 20 kN of the maximum capacity operating under displa-

Table 1: AISI 420 chemical composition, in mass fractions (*w*/%)

	C	Cr	Mn	P	S
Bar	0.17	12.83	0.76	0.05	0.017
AISI 420 Spec.	0.15 min	12.00 14.00	1.00 max	0.04 max	0.03 max

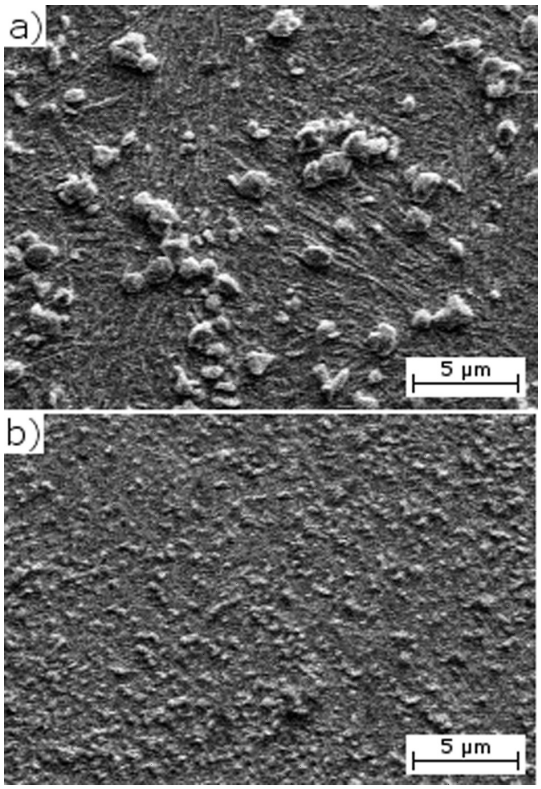

Figure 1: Secondary electron images (SEI) of: a) CHT specimen and b) DCT specimen, showing the carbide distributions

cement control, with a cross-head speed of 0.6 mm/min. The displacement of the load line was continuously recorded during the test using a linear displacement transducer (OMEGA LD600-25) sensing the movement of the machine's carriage.

After fracturing the specimens, they were scanned with a desktop flatbed scanner[28] in order to measure the average crack length. For this purpose, the size of the original crack and the final physical-crack size were measured at nine equally spaced points centered about the specimen centerline at a distance (d) of 1.38 mm, according to Equation (1) established by the ASTM E1820 standard: [29]

$$d = \frac{(B - 0.01W)}{9} \tag{1}$$

where:
B: specimen thickness, in mm,
W: specimen width, in mm.

The obtained load vs. load-line displacement (DLL) records were analyzed in order to assess the type of fracture while the conditional plane-strain fracture toughness (K_q) was calculated according to Equation (3) taken from reference.[25] If all the required conditions of linearity and small-scale plasticity were met, this K_q value was considered as K_{IC}:

$$K_q = \frac{P_q}{\sqrt{(BW)}} \times f(a/W) \tag{2}$$

where:
K_q: plane-strain fracture toughness (MPa m$^{1/2}$),
P_q: maximum load (kN),
B: specimen thickness (cm),
W: specimen width (cm),
f (a/W): crack-length polynomial factor where a is the average crack length. The terms of this polynomial for DC(T) specimens are detailed in Annex A3 of the ASTM E1820 standard.[29]

In order to evaluate the validity of the test, the K_q value and the average crack length were compared using Equation (2)[25], which guaranteed that the plastic deformation at the tip of the crack was sufficiently small to apply linear fracture mechanics. The yield stress (σ_Y) for the quenched and tempered AISI 420 was estimated as 1500 MPa.[30] The reported values correspond to the average of at least three valid tests:

$$a, B \geq 2.5\left(\frac{K_q}{\sigma_y}\right)^2 \tag{3}$$

where:
a: crack length, in mm,
B: specimen thickness, in mm,
K_q: conditional plane-strain fracture toughness, in MPa m$^{1/2}$,
σ_y: yield stress, in MPa.

Afterwards, the fracture surfaces were evaluated using a CARL ZEISS EVO 40 XVP scanning electron microscope in order to evaluate the micromechanisms involved in the fracture.

3 RESULTS

The differences in the carbide-population distribution can be seen in **Figure 1**, in which the CHT specimen

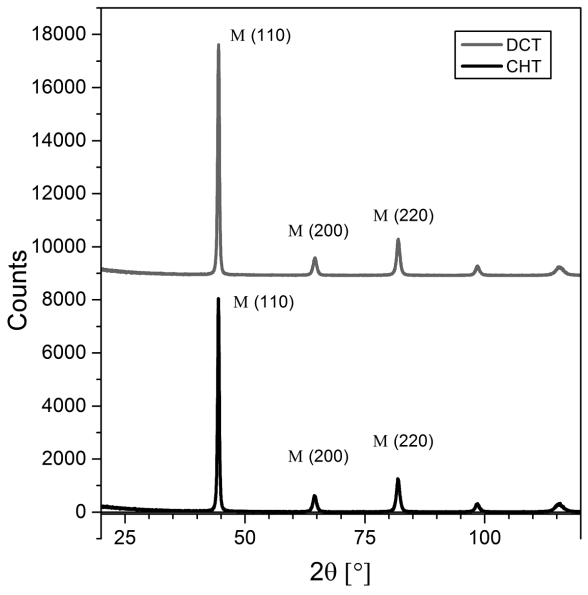

Figure 2: XRD spectra for CHT and DCT specimens

shows larger and more isolated carbides, while in the DCT sample (**Figure 1b**), the carbides are smaller and closer to each other; in addition, both the distance and the volume fraction of carbides diminished. In our previous work[16], we identified these particles as globular secondary carbides of type M_7C_3 by means of an EDS analysis. The hardness, the mean distance between the carbides and the carbide volume fraction are presented in **Table 2**. Regarding X-Ray diffractograms, it can be seen in **Figure 2** that both CHT and DCT specimens had martensitic microstructures, while austenite could not be detected; therefore, it is inferred that its volume fraction is below the detection threshold of the diffractometer (>3 % of volume fraction). The martensitic matrix shows a very fine lenticular microstructure, typical of high hardenability steels, such as AISI 420.

Table 2: Hardness and qualitative metallographic analysis

	CHT	DCT
Hardness (HV0.5)	507±7	534±9
Distance between carbides (μm)	1.73±0.72	1.37±0.46
Volume fraction of carbides (%vol)	16.9	12.2
Retained austenite (%vol)	> 3.0	> 3.0

Regarding the fracture-toughness tests, all the specimens exhibited a linear behavior before the sudden fracture; therefore, the maximum load ($P_{max} = P_q$) was taken for the calculation of K_{IC}. The propagation of a crack without a load increase is characteristic of a brittle fracture. It should also be noted that no significant pop-in events developed during the tests.

Figure 3 shows the average value of K_{IC} where it can be seen that conventionally treated specimens exhibited the average plane-strain fracture-toughness value of 49.5 MPa $m^{1/2}$, while cryogenically treated ones showed a value of 65.0 MPa $m^{1/2}$, indicating a 31 % increase in comparison to conventionally heat-treated ones.

In order to inspect the nucleation mechanism prior to the sudden fracture, SEM fractographies were taken from the middle of the specimens, at 70–80 μm, from the fatigue pre-crack front in the direction of propagation. Both groups of specimens showed a mixture of cleavage facets and dimples, but in the CHT ones the amount of dimples was higher (**Figure 4a**).

It can be appreciated that dimples are larger in the CHT specimens compared to the ones that developed in the DCT samples. Very large (~1.5 μm) dimples with carbides inside can be seen in **Figure 4a** while, in the DCT specimens, although some dimples were found, a stronger presence of ridges and cleavage facets can be seen.

4 DISCUSSION

Regarding the fracture behavior, it consisted of brittle fractures with no stable crack propagation. The SEM fractographies (**Figure 4**) showed that the microscopic failure mechanism was a confined plastic flow with a void growth responsible for crack nucleation, followed by cleavage propagation. Both groups of specimens exhibited relatively low fracture-toughness values, as expected for high-strength steels[31] tested in the lower shelf region.

From the results displayed in **Figure 3,** it can be seen that cryogenic treatments led to a simultaneous increase in both the hardness and the plain-strain fracture toughness. The hardness increment accounted for 5 %, while

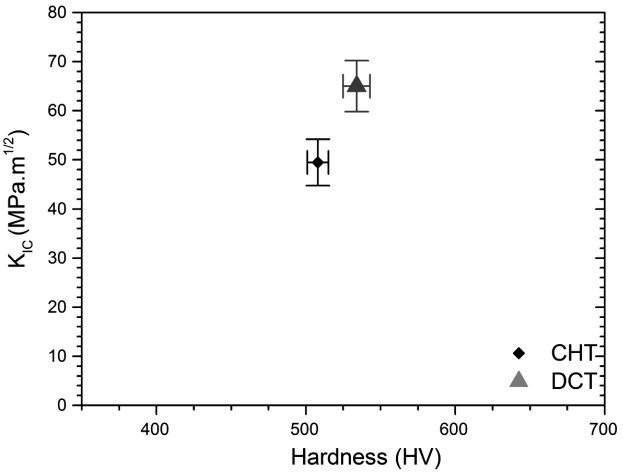

Figure 3: Plane-strain fracture toughness for conventional and cryogenically treated specimens

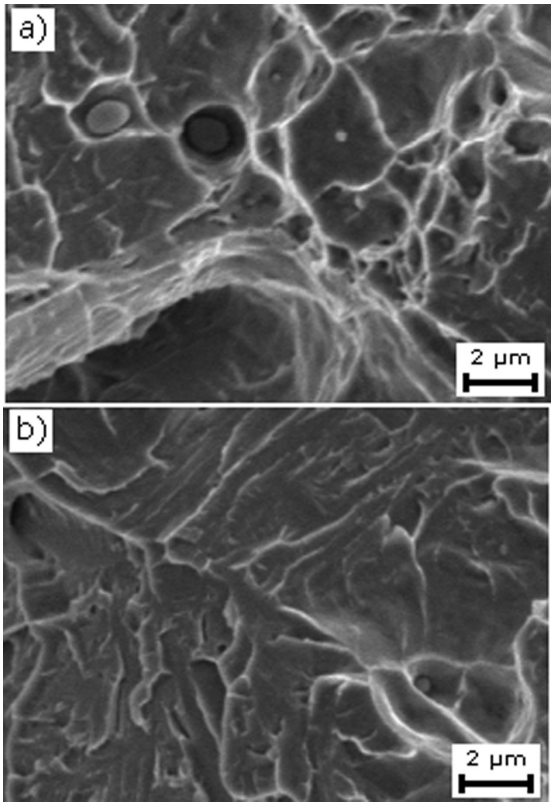

Figure 4: Secondary electron fractographies of: a) CHT and b) DCT specimens

the average K_{IC} value was 30 % higher for the cryogenically treated specimens. It should be highlighted that, in our previous work[10], we experimentally proved that this steel has a wear-resistance increase of 35–90 % when subjected to cryogenic treatments. Therefore, the present results imply that the cryogenic treatment is an effective technique to improve simultaneously the hardness, wear resistance and fracture toughness of an AISI 420 stainless steel.

When focusing on the improvement in the fracture toughness, D. Yun et al.[19] found similar results when studying cryogenically treated high-speed steels. In that case, specimens subjected to 24 h of soaking in liquid nitrogen, followed by triple tempering exhibited hardness and impact-toughness improvements of 2 % and 30 %, respectively. A. B. Prabhakaran et al.[32] reported a 14 % increase in the impact toughness combined with a 3.5 % increase in the hardness of a cryogenically treated case carburized steel, while A. Molinari et al.[20] reported that the cryogenic treatment increased the toughness – measured by means of three-point bending tests – influencing neither the hardness nor the impact toughness.

On the contrary, D. Das et al.[33] found that a deep cryogenic treatment improved the hardness of an AISI D2 die steel by ∼4.5 % at the expense of a fracture-toughness reduction of ∼7 %. It is interesting to note that in their case the dispersion of K_{IC} values was significantly higher for the DCT specimens compared to the CHT ones, whereas our results indicate that these values were very similar. In that paper, Das and his collaborators emphasized the role of the size and distribution of secondary carbides, reporting a reduction in their size and their higher volume fraction.

Regarding the influence of cryogenic treatments, B. Podgornik et al.[24] found dissimilar behaviors of the fracture properties of P/M and high-speed steels. In the case of the P/M cold-work tool steel, the improvement in the fracture toughness was associated with the formation of finer needles of martensite in combination with the plastic deformation of primary martensite, a reduced amount of dissolved carbon in the martensite and a finer distribution of carbides.

In **Figure 2**, it can be seen that AISI 420 exhibits negligible amounts of retained austenite – less than 3 % of volume fractions even when it is subjected to the conventional heat treatment. This result can be supported with the findings of Da Sun et al.[14] obtained during a study of the microstructure of a laser-cladding coating made of AISI 420, in which the volume of retained austenite was below the detection limit of the diffractometer. S. Dodds et al.[15] also reported XRD patterns of as-quenched AISI 420 samples, where no reflections corresponding to the retained austenite could be seen. The importance of these results is that they show that AISI 420 does not retain significant amounts of austenite, not even in the untempered condition. Therefore, we can infer that the mechanism of the deformation of primary martensite proposed by A. I. Tyshchenko et al.[11] can be considered marginal in the cryogenic processing of AISI 420. For this reason, we will carry out further studies to deepen the understanding of the metallurgical effects of cryogenic treatments on steel alloys.

In our case, we propose that the main mechanism responsible for the fracture-toughness increase is the refinement of carbides (**Figure 1**) as a consequence of the cryogenic cooling. Due to their different mechanical properties compared to the metallic matrix, carbides act as stress concentrators; thus, a reduction in their size leads to a decrease in the stress concentration[34], especially in the surroundings of a crack tip.

In addition, the early results reported by D. A. Curry and J. F. Knott[35] noted a detrimental influence of coarse carbides on the fracture toughness, while P. Bowen et al.[36] showed that carbides with diameters of above 0.3 μm were critical in the controlling of the fracture toughness. Similarly, X. Z. Zhang and J. F. Knott[37] concluded that carbides act as critical microcrack nuclei and highlighted the importance of having finely dispersed microstructural features in order to increase the K_{IC} values. In this sense, the coarser carbides in the CHT samples shown in **Figure 1a** promote the formation of larger dimples (**Figure 4a**) that coalesce at lower stresses forming larger cavities in the material. It should be noted that there was no evidence of carbide fracturing; therefore, the main fracture micromechanism was the aforementioned void coalescence phenomenon followed by cleavage. This way, the refinement of the carbide size and distribution due to the cryogenic treatment (**Figure 2b**) can be associated with the subsequent increase in the fracture toughness shown in **Figure 3.**

5 CONCLUSIONS

On the basis of the results obtained from the study of the fracture toughness of a cryogenically treated martensitic AISI 420 stainless steel, we conclude that there is a synergistic relationship between the carbide-size diminution generated by cryogenic cooling, which lowers the stress-concentration effect on the surroundings and, therefore, the void formation and coalescence, and the reduction in the volume fraction that lowers the probability of cleavage-fracture occurrence. This way, we can link the microstructural modifications induced by the cryogenic treatments with the simultaneous increase in both the hardness and fracture toughness.

Acknowledgments

The authors would like to thank Dr. Héctor G. Kotik and Mr. Eduardo G. Benotti from Universidad Nacional del Comahue for their assistance in performing the fracture tests. Funding was provided by Agencia Nacional de Promoción Científica y Tecnológica by means of the grant PICT 2013-0616.

6 REFERENCES

[1] R. F. Barron, Cryogenic treatment of metals to improve wear resistance, Cryogenics, 22 (**1982**), 409–413

[2] D. Das, A. K. Dutta, K. K. Ray, Correlation of microstructure with wear behaviour of deep cryogenically treated AISI D2 steel, Wear, 267 (**2009**), 1371–1380, doi:10.1016/j.wear.2008.12.051

[3] V. Leskovšek, M. Kalin, J. Vižintin, Influence of deep-cryogenic treatment on wear resistance of vacuum heat-treated HSS, Vacuum, 80 (**2006**) 507–518, doi:10.1016/j.vacuum.2005.08.023

[4] V. G. Gavriljuk, W. Theisen, V. V. Sirosh, E. V. Polshin, A. Kortmann, G. S. Mogilny, Low-temperature martensitic transformation in tool steels in relation to their deep cryogenic treatment, Acta Mater., 61 (**2013**), 1705–1715, doi:10.1016/j.actamat.2012.11.045

[5] A. Bensely, A. Prabhakaran, G. Nagarajan, Effect of cryogenic treatment on distribution of residual stress in case carburized En 353 steel, Mater. Sci. Eng. A, 479 (**2008**), 229–235

[6] D. Das, A. K. Dutta, K. K. Ray, Sub-zero treatments of AISI D2 steel: Part II. Wear behavior, Mater. Sci. Eng. A, 527 (**2010**), 2194–2206, doi:10.1016/j.msea.2009.10.071

[7] D. Das, A. K. Dutta, Optimization of the duration of cryogenic processing to maximize wear resistance of AISI D2 steel, Cryogenics, 49 (**2009**), 176–184

[8] F. Meng, K. Tagashira, H. Sohma, Wear resistance and microstructure of cryogenically treated Fe-1.4Cr-1C bearing steel, Scr. Metall. Mater., 31 (**1994**), 865–868

[9] F. Meng, T. Kohsuke, R. Azuma, H. Sohma, Role of eta-carbide precipitations in the wear resistance improvements of Fe-12Cr-Mo-V-1.4C tool steel by cryogenic treatment, ISIJ Int., 34 (**1994**), 205–210

[10] G. Prieto, W. R. Tuckart, Wear behavior of cryogenically treated AISI 420 martensitic stainless steel, Proc. of VIII Iber. Conf. Tribol., Cartagena, Spain, 2015, 68–75

[11] A. I. Tyshchenko, W. Theisen, A. Oppenkowski, S. Siebert, O. N. Razumov, A. P. Skoblik, Low-temperature martensitic transformation and deep cryogenic treatment of a tool steel, Mater. Sci. Eng. A, 527 (**2010**), 7027–7039, doi:10.1016/j.msea.2010.07.056

[12] V. G. Gavriljuk, V. A Sirosh, Y. N. Petrov, A. I. Tyshchenko, W. Theisen, A. Kortmann, Carbide Precipitation During Tempering of a Tool Steel Subjected to Deep Cryogenic Treatment, Metall. Mater. Trans. A, 45 (**2014**), 2453–2465, doi:10.1007/s11661-014-2202-8

[13] M. Villa, K. Pantleon, M. A. J. Somers, Evolution of compressive strains in retained austenite during sub-zero Celsius martensite formation and tempering, Acta Mater., 65 (**2014**), 383–392, doi:10.1016/j.actamat.2013.11.007

[14] S. Da Sun, D. Fabijanic, A. Ghaderi, M. Leary, J. Toton, S. Sun, Microstructure and hardness characterisation of laser coatings produced with a mixture of AISI 420 stainless steel and Fe-C-Cr-Nb-B-Mo steel alloy powders, Surf. Coatings Technol., 296 (**2016**), 76–87, doi:10.1016/j.surfcoat.2016.03.061

[15] S. Dodds, A. H. Jones, S. Cater, Tribological enhancement of AISI 420 martensitic stainless steel through friction-stir processing, Wear, 302 (**2013**), 863–877, doi:10.1016/j.wear.2013.01.007

[16] G. Prieto, J. E. Perez Ipiña, W. R. Tuckart, Cryogenic treatments on AISI 420 stainless steel: Microstructure and mechanical properties, Mater. Sci. Eng. A, 605 (**2014**), 236–243, doi:10.1016/j.msea.2014.03.059

[17] G. Prieto, Estudio del efecto de tratamientos térmicos de criogenia sobre el comportamiento tribológico y la tenacidad a la fractura del acero AISI 420, Universidad Nacional del Sur, 2016.

[18] A. Bensely, A. Prabhakaran, D. Mohan Lal, G. Nagarajan, Enhancing the wear resistance of case carburized steel (En 353) by cryogenic treatment, Cryogenics, 45 (**2005**), 747–754, doi:10.1016/j.cryogenics.2005.10.004

[19] D. Yun, L. Xiaoping, X. Hongshen, Deep Cryogenic Treatment of High-Speed Steel and its Mechanism, Heat Treat. Met., 3(**1998**), 55–59

[20] A. Molinari, M. Pellizzari, S. Gialanella, G. Straffelini, K. H. Stiasny, Effect of deep cryogenic treatment on the mechanical properties of tool steels, J. Mater. Process. Technol., 118 (**2001**), 350–355, doi:10.1016/S0924-0136(01)00973-6

[21] F. Cajner, V. Leskovšek, D. Landek, H. Cajner, Effect of deep-cryogenic treatment on high speed steel properties, Mater. Manuf. Process., 24 (**2009**), 743–746

[22] D. Das, K. K. Ray, Structure-property correlation of sub-zero treated AISI D2 steel, Mater. Sci. Eng. A, 541 (**2012**), 45–60, doi:10.1016/j.msea.2012.01.130

[23] S. Zhirafar, A. Rezaeian, M. Pugh, Effect of cryogenic treatment on the mechanical properties of 4340 steel, J. Mater. Process. Technol., 186 (**2007**), 298–303, doi:10.1016/j.jmatprotec.2006.12.046

[24] B. Podgornik, I. Paulin, B. Zajec, S. Jacobson, V. Leskovšek, Deep cryogenic treatment of tool steels, J. Mater. Process. Technol., 229 (**2016**), 398–406, doi:10.1016/j.jmatprotec.2015.09.045

[25] ASTM E399-12e3, Standard Test Method for Linear-Elastic Plane-Strain Fracture Toughness KIc of Metallic Materials, ASTM International, West Conshohocken, PA, 2012, doi:10.1520/E0399

[26] ASTM A176-99(2009), Standard Specification for Stainless and Heat-Resisting Chromium Steel Plate, Sheet, and Strip (withdrawn 2015), ASTM International, West Conshohocken, PA, 2009, doi:10.1520/A0176-99R09

[27] F. de Chaumont et al., Icy: an open bioimage informatics platform for extended reproducible research, Nat. Methods, 9 (**2012**), 690–696

[28] I. Korin, C. Larrainzar, J. E. Perez Ipiña, Crack length and stable crack extension measurements from images acquired by means of a conventional flatbed scanner, Fatigue Fract. Eng. Mater. Struct., 31 (**2008**), 876–884

[29] ASTM E1820-13e1, Standard Test Method for Measurement of Fracture Toughness, ASTM International, West Conshohocken, PA, 2013, doi:10.1520/E1820-13E01

[30] ASM Handbook, Vol. 19, Materials Park, OH, ASM International, 1996

[31] JSMS, Data book on fracture toughness for metallic materials, Kyoto, 1995

[32] A. B. Prabhakaran, G. Nagarajan, D. M. Lal, Effect of cryogenic treatment on impact strength of case carburized steel En 353, Proc. IMEC2004 Int. Mech. Eng. Conf., Kuwait, 2004

[33] D. Das, R. Sarkar, A. K. Dutta, K. K. Ray, Mater. Sci. Eng. A, 528 (**2010**), 589–603, doi:10.1016/j.msea.2010.09.057

[34] A. S. Pandkar, N. Arakere, G. Subhash, Microstructure-sensitive accumulation of plastic strain due to ratcheting in bearing steels subject to rolling contact fatigue, Int. J. Fatigue, 63 (**2014**), 191–202, doi:10.1016/j.ijfatigue.2014.01.029

[35] D. A. Curry, J. F. Knott, Effect of microstructure on cleavage fracture toughness of quenched and tempered steels, Met. Sci., 13 (**1979**), 341–345

[36] P. Bowen, S. G. Druce, J. F. Knott, Effects of microstructure on cleavage fracture in pressure vessel steel, Acta Metall., 34 (**1986**), 1121–1131

[37] X. Z. Zhang, J. F. Knott, Cleavage fracture in bainitic and martensitic microstructures, Acta Metall., 47 (**1999**), 3483–3495

UDK 678.027.74:62:66.011
Original scientific article/Izvirni znanstveni članek

ISSN 1580-2949
MTAEC9, 51(4)597(2017)

PREDICTIVE MODEL AND OPTIMIZATION OF PROCESSING PARAMETERS FOR PLASTIC INJECTION MOULDING

MODEL ZA NAPOVEDOVANJE IN OPTIMIZACIJO PROCESNIH PARAMETROV PRI BRIZGANJU PLASTIKE

Davorin Kramar[1], Djordje Cica[2]

[1]University of Ljubljana, Faculty of Mechanical Engineering, Ljubljana, Slovenia
[2]University of Banja Luka, Faculty of Mechanical Engineering, Banja Luka, Bosnia and Herzegovina
davorin.kramar@fs.uni-lj.si

Prejem rokopisa – received: 2016-06-25; sprejem za objavo – accepted for publication: 2017-01-16

doi:10.17222/mit.2016.129

Injection molding is one of the most widely used processes for producing engineered parts in the plastics industry. The objective of this study is to propose a fuzzy expert system for the prediction of mechanical properties of injection-molded parts where the fuzzy system is optimized using particle-swarm optimization. The input process parameters were the mold temperature, melt temperature, injection velocity, packing pressure, cooling time and packing time. The predicted values were in good agreement with the experimental ones, which indicates that the developed particle-swarm-optimization-based fuzzy expert system can be effectively used to predict the mechanical properties of molded parts. In addition, optimization based on a particle-swarm-optimization algorithm was carried out to obtain the optimum process parameters based on the objective to maximize the tensile strength of the molded product.

Keywords: plastics, injection molding, particle-swarm optimization, tensile strength

Brizganje je eden izmed najpogosteje uporabljenih postopkov za izdelavo inženirskih delov v industriji plastike. Cilj te raziskave je predlagati enostavni ekspertni sistem za napovedovanje mehanskih lastnosti delov brizganih kosov, kjer je enostavni sistem optimiziran z uporabo optimizacije z rojem delcev. Vhodni parametri procesa so temperature orodja, temperatura taline, hitrost brizganja, zapiralni pritisk, čas hlajenja in zapiralni čas. Napovedane vrednosti se dobro ujemajo z eksperimentalnimi, kar kaže, da se razvit enostavni ekspertni sistem na osnovi optimizacije z rojem delcev lahko učinkovito uporablja za napovedovanje mehanskih lastnosti brizganih delov. Algoritem optimizacije z rojem delcev je podal tudi optimalne procesne parametre za doseganje čim višje natezne trdnosti brizganega izdelka.

Ključne besede: plastika, injekcijsko brizganje, optimizacija z roji delcev, natezna trdnost

1 INTRODUCTION

Plastic injection molding is the most widely used manufacturing process for the high-volume production of relatively complex thermoplastic parts by injecting a material into a mold. Within this process, a high-pressure fluid polymer is injected to the cavity with a desired form. In the next step, under high pressure, while cooling, the fluid solidifies. However, plastic injection molding is a very complex manufacturing process due to the strong nonlinearities and a large number of interrelated parameters. Over the last few decades, artificial-intelligence (AI) methods have become the preferred trend, applied by most researchers for the optimization and prediction of various parameters of the injection-molding process.

S. Kenig et al.[1] used a feed-forward artificial neural network (ANN) with an error back-propagation algorithm for the adequate control of product properties in injection-molded plastics. W. C. Chen et al.[2] developed a self-organizing map and a back-propagation neural-network model to generate a dynamic quality predictor for the plastic-injection-molding process. C. Ozek and Y. H. Celik[3] developed software to predict the quality of the injected parts through an ANN model. H. M. Sadeghi[4] studied the possibility of predicting the quality or soundness of the injected parts through an ANN model and based on computer-aided engineering software simulations. C. F. Juang et al.[5] developed a Takagi-Sugeno-Kang-type recurrent fuzzy neural networks for the control of the mold temperature. C. Karatas et al.[6] developed an ANN model to determine the yield length in the plastic molding of commercial plastics. M. Altan[7] studied the optimum injection-molding conditions for the minimum shrinkage based on Taguchi methods, ANOVA and ANN. H. Shi et al.[8] proposed an adaptive optimization method based on an ANN model for the minimization of the warpage of injection-molded parts. A. Krimpenis et al.[9] proposed ANN meta-models in order to generalize from the examples connecting input-process variables to output variables. A neural model is employed in the fitness function of the genetic algorithm (GA) for optimization of the injection-molding process. C. Shen et al.[10] proposed a method based on a combination of the ANN and GA for optimization of the injection-molding process in order to improve the quality index of the volumetric-shrinkage variation in the part.

B. Ozcelik and T. Erzurumlu[11] determined the most important process parameters influencing warpage using finite-element-analysis results based on ANOVA, while an ANN was interfaced with an effective GA to find the minimum warpage value. Chen et al.[12] presented an effective approach in a soft-computing paradigm for the process-parameter optimization of the plastic-injection-molding process. The proposed approach integrates Taguchi's parameter-design method, ANN, GA and engineering-optimization concepts. Li et al.[13] presented a genetic neural fuzzy system to construct a quality-prediction model for the injection process from the input and output data. Mathivanan and Parthasarathy[14] investigate sink depths in injection-molded thermoplastic components by integrating the finite-element-flow analysis with the central composite design of experiments and GA. Deng et al.[15] proposed a hybrid of the mode-pursuing sampling method and the GA for the minimization of injection-molding warpage. Park and Nguyen[16] presented an injection-molding-process optimization of a plastic car fender related to the energy consumption and product quality. J. Cheng et al.[17] proposed a multi-objective optimization model including both mold and process parameters as design variables in order to achieve the optimum parameter schemes in accordance with practical requirements of injection molding. J. Cheng et al.[18] developed a fuzzy moldability-evaluation approach for the optimization of injection-mold schemes based on the variable weight-profit vector. K. T. Chiang and F. P. Chang[19] and K. T. Chiang[20] proposed an approach for optimizing process parameters of an injection-molded part with a thin shell feature based on the orthogonal array with the grey relational analysis and fuzzy logical analysis.

Despite the fact that there are numerous applications of the AI in modeling the injection-molding process reported in the literature, a review of the literature shows that only few research works are based on the fuzzy theory. Furthermore, previous approaches were based on the usual approach to designing a fuzzy system by encoding expert knowledge in a direct way using rules with linguistic labels. However, knowledge acquisition is not a trivial task so, in the present paper, an attempt was made to design an optimized fuzzy expert system (FES) using a particle-swarm-optimization algorithm for predicting the mechanical properties of the molded parts. Furthermore, the particle-swarm-optimization (PSO) algorithm is used in the process optimization in order to improve the mechanical properties of the injection-molded parts.

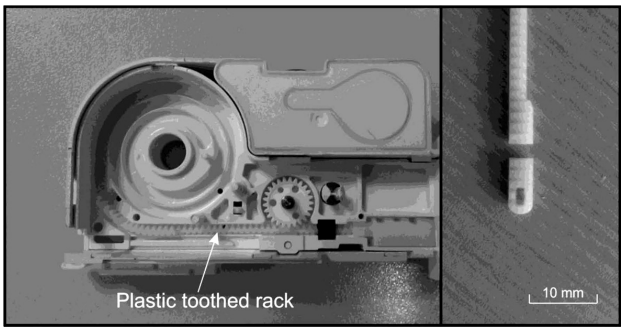

Figure 1: Plastic-toothed rack within a driving gear (left) and the usual cause of breakage (right)

2 EXPERIMENTAL PART

According to the experience with polyoxymethilene (POM) materials, the following control factors, i.e., injection-molding-process parameters influencing product mechanical properties, were selected: the mold temperature (T_M), the melting temperature (T_m), the injection velocity (v_i), the packing pressure (p_h), the packing time (t_h), and the cooling time (t_c). The levels of process parameters are shown in **Table 1**, being selected according to material-producer specifications. All the experiments were carried out on an Engel Victory 200/50 injection-molding machine with a clamping force of 500 kN and a cylinder diameter of 18 mm. The main characteristic of the investigated POM material is a high melt-flow rate of 52 g/10 min.

Table 1: Design of experiments and comparison between experimental results and the predicted breaking force of the injection-molded toothed rack

Process parameters						Experiment	FES		PSOFES	
T_M (°C)	T_m (°C)	V_i (mm/s)	p_h (bar)	t_c (s)	t_h (s)	F (N)	F (N)	Error (%)	F (N)	Error (%)
70	185	20	1000	6	2	64.6	62.3	3.6	64.6	0
70	195	40	1150	8	4	69.1	67.5	2.3	66.9	3.2
70	205	60	1300	10	6	72.7	72.8	0.1	72.9	0.3
85	185	20	1150	8	6	64.9	67.5	4	66.7	2.8
85	195	40	1300	10	2	71.8	72.8	1.4	71.9	0.1
85	205	60	1000	6	4	71.9	72.8	1.3	71.8	0.1
100	185	40	1000	10	4	59.6	62.3	4.5	60.5	1.5
100	195	60	1150	6	6	62.1	62.3	0.3	60.7	2.3
100	205	20	1300	8	2	77.3	76.3	1.3	77.1	0.3
70	185	60	1300	8	4	60.7	62.3	2.6	60.7	0
70	195	20	1000	10	6	66.9	67.5	0.9	66.9	0
70	205	40	1150	6	2	70.5	72.8	3.3	70.7	0.3
85	185	40	1300	6	6	59.8	62.3	4.2	60.7	1.5
85	195	60	1000	8	2	62.2	62.3	0.2	62.2	0
85	205	20	1150	10	4	70.2	72.8	3.7	69.6	0.9
100	185	60	1150	10	2	57.7	58.9	2.1	57.8	0.2
100	195	20	1300	6	4	74.2	72.8	1.9	73.8	0.5
100	205	40	1000	8	6	73.7	72.8	1.2	73.7	0

In this study, POM thermoplastic with commercial designation Kepital F40-03 was utilized. The material is characterized by high strength, hardness and rigidity, thermal stability and, especially, a high melt-flow rate. As such, this material can be used as an extremely easy-flowing grade for the injection molding of thin-walled precision parts. The precision of a part and mechanical properties of a product are even more important when parts for medical devices are produced. In this paper, the

injection-molding process of a plastic toothed rack used as the driving gear of a breast-biopsy system is investigated. Beside high tolerances, dimensional stability and low friction needed for a sufficient operation, the plastic rack should fulfil high stiffness and tensile-strength requirements. The rack should not break when biopsy is executed (**Figure 1**).

Orthogonal array L18 was applied to run the experiments (**Table 1**). All the experiments were repeated 10 times, and molded samples were collected. The samples were then carefully cut to remove sprue and runner from the final product: a toothed rack. The breaking point of each rack was measured with a specially designed tension test. The average value of the breaking force for 10 rack samples was then calculated. The results of experiments are shown in **Table 1**.

3 PSO-BASED FUZZY EXPERT SYSTEM

Fuzzy logic is one of the most successful technologies for developing rule-based expert systems. According to the inventor of fuzzy logic L. A. Zadeh[21], fuzzy logic attempts to formalize two human abilities: to reason in the presence of imperfect information and to carry out different mental and physical tasks without any numerical measurements or computations. A fuzzy inference system (FIS) combines the fuzzy set theory, fuzzy rules and fuzzy reasoning. According to [22], a FIS is composed of three parts: a rule base, which contains the collection of fuzzy rules, a database (or dictionary) which specifies the membership functions (MFs) used in the fuzzy rules, and a reasoning mechanism, which infers the output based on the rule base, database and the given input.

In this study, the authors designed the rule base and database of the FES, based on their knowledge of the injection-molding process. In this FES, the input variables are: the mold temperature, the melt temperature, the injection velocity, the packing pressure, the cooling time and the packing time, while the output variable is the breaking force. The input variables have three MFs labeled as low, medium and high, while the output variable, that is, the breaking force, has five MFs labeled as very fine, fine, medium, coarse and very coarse. In order to describe the fuzzy sets for the input and output variables, a triangular shape of the MFs is employed. In this study, a Mamdani-type fuzzy inference system is used, due to its relatively simple structure and intuitive nature of the rule base, for correlating the injection-molding parameters with the breaking force. However, this usual approach for the FES design is characterized by disadvantages such as dependence of the system performance on the knowledge of the human expert, adequate fuzzy rules, MFs and their boundaries. In order to overcome these shortcomings, a significant amount of research was carried out on automatic tuning of a FES using bio-inspired algorithms, such as PSO.

Particle-swarm optimization was first introduced by J. Kennedy and R. Eberhart[23] who defined a swarm as a population of interactive elements or agents, able to optimize some global objective through a collaborative search in space. PSO is a population-based method where the population is referred to as a swarm. The swarm consists of a number of individuals called the particles, which are initialized with random solutions. These particles fly in a d-dimensional space through many iterations to search a better solution for the problem. Every particle in the swarm is represented by a specific position, initialized by the initial position and by velocity, where each particle moves in the space according to a specific velocity. Furthermore, each particle holds the information about the best position, the one associated with the best fitness value the particle has achieved so far, and the global best position, the one associated with the best fitness value found among all of the particles. In this way, the trajectory of each particle is influenced by the trajectories of the neighborhood particles as well as the flight experience of the particle itself. During the iteration time, each particle updates this information and adjusts its own trajectory in order to move towards its best position and global best position.

The PSO method has many advantages, such are its effectiveness, robustness, simplicity and extreme ease of implementation without the need for cumbersome derivative calculations. The focus of this study is to employ a PSO for optimizing an already existing fuzzy-rule-based system. The main idea is the adaptation of the parameters of the input and output MFs by the PSO according to a fitness function that specifies the design criteria in a quantitative manner. In this paper, the triangular shape of MFs is employed to describe the fuzzy sets for the input and output variables, so the optimization of MF distributions is reduced to the changes of the base widths. Furthermore, fuzzy rule weights are also optimized by the PSO.

A parametric study was carried out to find the optimum values of PSO parameters in order to achieve a good result. The fitness value of a PSO solution is estimated based on the mean absolute percentage error of each training-data sample. The error of each set of the training data is the deviation of the result (the breaking force) of the PSO-based FES from that of the desired one. The optimum values of the PSO parameters for cognitive acceleration, social acceleration, number of generations and population size were 0.3, 1.3, 880 and 370, respectively. **Figure 2** shows the optimized MF distributions of the input-output MFs obtained after fine-tuning using the PSO.

To verify the performances of the proposed FES, the results of these systems were compared with that obtained using the experimental tests as shown in **Table 1**. For the author-defined Mamdani FES, Pearson's linear-correlation coefficient was 0.9644, and the mean absolute percentage error was 2.2 %, while the maximum

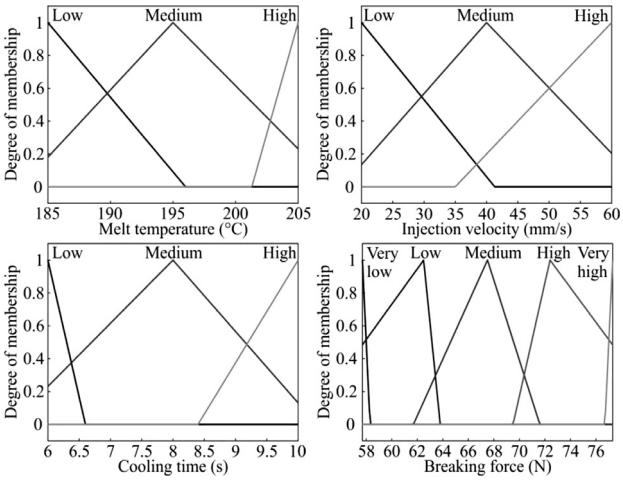

Figure 2: Optimized membership-function distributions for melt temperature, injection velocity, cooling time and breaking force of the PSO fuzzy expert system

absolute percentage error was 4.2 %. Pearson's linear-correlation coefficient of the PSO-based FES was 0.9899. The mean absolute percentage error and the maximum absolute percentage error of the PSO-based FES were 0.8 % and 3.2 %, respectively. Figure 3 shows a comparison of the predictions of the breaking force of the injection-molded toothed rack obtained using the fuzzy-rule-based expert system and the PSO-based fuzzy expert systems in terms of % error. It is obvious that there is a very good agreement between the estimated and experimental values of the breaking force for both models. On this basis, it can be concluded that the fuzzy-logic technique is a good alternative for predicting the breaking force of the injection-molded part within the range of the input parameters under consideration. However, in almost all the cases, the prediction results using a fuzzy system optimized with a PSO algorithm are more accurate than the conventional fuzzy-rule-based expert system.

4 INJECTION-PROCESS-PARAMETER OPTIMIZATION USING A PSO ALGORITHM

In addition to modeling, optimization of process parameters is one of the most important elements of injection molding. The selection of optimum process parameters enables the control of the manufacturing process to achieve better quality products at a low cost and high productivity levels. Therefore, the second goal of our research was to determine the process conditions to improve the mechanical performance of the part using the PSO technique as the optimization tool.

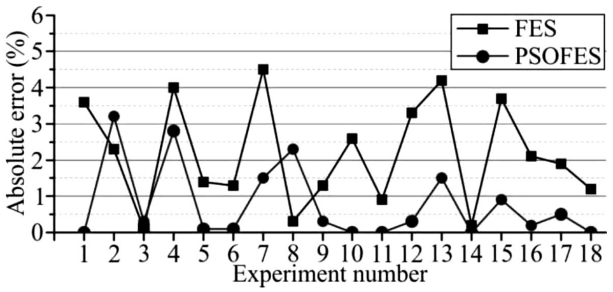

Figure 3: Error profile of the predicted breaking-force values obtained using the author-defined FES and PSO-based FES

Prior to the optimization process, it is necessary to establish the relationships between the process parameters and objective functions. For this purpose, in this paper, a systematic methodology based on the response-surface methodology was applied. A response-surface model correlating the breaking force and the considered injection-molding parameters was developed using an ANOVA[24] of the experimental results in the form of a reduced quadratic model. The determination of the significant model degree and parameter effects was based on the *F* and *P* values (**Table 2**). Model *F*-value is a test for comparing the model variance with the residual (error) variance. If the variances are close to the same, the ratio will be close to one and it is less likely that any of the factors have a significant effect on the response. Model *F*-value is calculated using the model mean square divided by the residual mean square.

The model *F*-value of 15.88 implies the model is significant. There is only a 0.02 % chance that a "model *F*-value" this large could occur due to noise. *P*-values smaller than 0.05 indicate model terms that are significant. In our case, parameters T_m and v_i, and products $T_M \cdot v_i$, and $p_h \cdot t_c$ are significant model terms. However, for statistical reasons, models contain subsets of all the possible effects that preserve the hierarchy. A model is hierarchal if the presence of quadratic terms and interactions requires the inclusion of all the linear terms contained within those of the higher order, even if they do not appear to be significant on their own. The signal-to-noise ratio of 14.28 and *R*-squared coefficient of 0.93 indicate that the model can be used for the breaking-force prediction. The following mathematical relationship is obtained with Equation (1):

$$\begin{aligned} F = &-759.2212 + 0.40865 \cdot T_{\mathrm{M}} + 8.5927 \cdot T_{\mathrm{m}} + \\ &+ 0.61292 \cdot v_i - 0.0694246 \cdot p_{\mathrm{h}} - 10.2512 \cdot t_{\mathrm{c}} - \\ &- 0.00910714 \cdot T_{\mathrm{M}} v_i + 0.00876190 \cdot p_{\mathrm{h}} t_{\mathrm{c}} - \\ &- 0.0209018 \cdot T_{\mathrm{m}}^2 \end{aligned} \quad (1)$$

Table 2: ANOVA of the experimental results from **Table 1**

Source	Model	T_{M}	T_{m}	v_i	p_{h}	t_{c}	$T_{\mathrm{M}} \cdot v_i$	$p_{\mathrm{h}} \cdot t_{\mathrm{c}}$	T_{m}^2
F-value	15.88	1.06	37.60	24.81	0.015	0.33	6.48	8.25	3.49
P-value	0.0002	0.3307	0.0002	0.0008	0.9038	0.5774	0.0314	0.0184	0.0944

The mechanical properties of injection-molded parts are influenced by many process variables, and five key-process parameters were selected as the design variables of the mathematical model: the mold temperature, melt temperature, injection velocity, packing pressure and cooling time. The mathematical model of the injection-molding optimization problem can be formulated as follows:

Find $X = [T_M, T_m, v_i, p_h, t_c]$

Maximize $F(X)$

Subject to: $70 = T_M = 100$, $185 = T_m = 205$, $20 = v_i = 60$, $1000 = p_h = 1300$, $6 = t_c = 10$.

The optimum values of the injection-molding-process parameters were efficiently obtained with the PSO algorithm. In the PSO optimization process, the commonly used PSO operation parameters were adopted; namely, the population size, the generation size, the cognitive acceleration and the social attraction were set as 340, 1240, 0.5 and 1.25, respectively. The optimized results are listed in **Table 3**. Compared with the recommended process parameters, the optimized process parameters have higher values of the breaking force. The increasing percentage is approximately 19 % of the average value of the breaking force (67.2 N).

Table 3: Optimized parameters of the injection-molding process

Optimized parameters					Predicted value
T_M (°C)	T_m (°C)	v_i (mm/s)	p_h (bar)	t_c (s)	F (N)
100	205	20	1000	6	80.4

4.1 Verification of the optimization results

A confirmation test is needed to verify the results of optimization. A set of 10 experimental repetitions with the optimum process-parameter settings were conducted. The results are shown in **Table 4**. The mean value of 10 repetitions is approximately 80 N, which is in good agreement with the predicted value.

Table 4: Results of the confirmation test

Repetition	1	2	3	4	5	6	7	8	9	10	Mean
Breaking force (N)	79	78	79	79	84	81	79	79	81	79	79.8

5 CONCLUSIONS

The present work aims at estimating the mechanical properties of injection-molded parts using two fuzzy expert systems as the tools for the prediction. First, the authors designed a conventional fuzzy expert system, based on their knowledge of the injection-molding process and the predicted results for the breaking forces achieved via this system were compared to the experimental values. The results obtained indicated that the proposed fuzzy expert system has a prediction accuracy of 97.8 %. However, the performances of the author-defined fuzzy expert system are highly dependent on the expert knowledge, adequate fuzzy rules, membership functions and their boundaries. In order to overcome these problems and significantly improve the performance of the fuzzy expert system, a particle-swarm-optimization algorithm was interfaced with the fuzzy system. The results of the developed particle-swarm-optimization-based fuzzy expert system were compared, in terms of accuracy prediction, with the real experimental data and it was shown that the hybridization between fuzzy systems and particle-swarm optimization provides a more accurate result compared to an author-defined fuzzy expert system. The accuracy of 99.2 % indicates that the particle-swarm-optimization-based fuzzy expert system can be used effectively to predict the mechanical properties for an injection-molding process.

The second objective of this work was to find the optimum process parameters to improve the mechanical properties of injection-molded parts using a particle-swarm-optimization algorithm as the optimization technique. In the first stage, the response-surface methodology was deployed to establish the relationship between the process parameters and the performance of the objective functions. In the second stage, the particle-swarm-optimization algorithm was interfaced with this nonlinear model of the injection-molding system to find the optimum values of the process parameters. The same design variables as for the fuzzy expert system were considered, while the optimum values of these process parameters were obtained for the maximization of the breaking force subject to some constraints. The research results indicate that the proposed optimization method can effectively help manufacturers to determine the optimum injection-molding-process parameters and, thereby, significantly improve the mechanical performance of injection-molded parts.

6 REFERENCES

[1] S. Kenig, A. Ben-David, M. Omer, A. Sadeh, Control of properties in injection molding by neural network, Eng. Appl. Artif. Intel., 14 (**2001**) 6, 819–823, doi:10.1016/S0952-1976(02)00006-4

[2] W. C. Chen, P. H. Tai, M. W. Wang, W. J. Deng, C. T. Chen, A neural network-based approach for dynamic quality prediction in a plastic injection molding process, Expert. Syst. Appl., 35 (**2008**) 3, 843–849, doi:10.1016/j.eswa.2007.07.037

[3] C. Ozek, Y. H. Celik, Calculating Molding Parameters in Plastic Injection Molds with ANN and Developing Software, Mater. Manuf. Process, 27 (**2012**) 2, 160–168, doi:10.1080/10426914.2011.560224

[4] B. H. M. Sadeghi, A BP-neural network predictor model for plastic injection molding process, J. Mater. Process Tech., 103 (**2000**) 3, 411–416, doi:10.1016/S0924-0136(00)00498-2

[5] C. F. Juang, S. T. Huang, F. B. Duh, Mold temperature control of a rubber injection-molding machine by TSK-type recurrent neural fuzzy network, Neurocomputing, 70 (**2006**) 1–3, 559–567, doi:10.1016/j.neucom.2005.11.003

[6] C. Karatas, A. Sözen, E. Arcaklioglu, S. Ergüney, Modelling of yield length in the mould of commercial plastics using artificial neural networks, Mater. Design, 28 (**2007**) 1, 278–286, doi:10.1016/j.matdes.2005.06.016

[7] M. Altan, Reducing shrinkage in injection molding via the Taguchi, ANOVA and neural network methods, Mater. Design, 31 (**2010**) 1, 599–604, doi:10.1016/j.matdes.2009.06.049

[8] H. Shi, Y. Gao, X. Wang, Optimization of injection molding process parameters using integrated artificial neural network model and expected improvement function method, Int. J. Adv. Manuf. Tech, 48 (**2010**) 9, 955–962, doi:10.1007/s00170-009-2346-7

[9] A. Krimpenis, P. G. Benardos, G. C. Vosniakos, A. Koukouvitaki, Simulation-based selection of optimum pressure die-casting process parameters using neural nets and genetic algorithms, Int. J. Adv. Manuf. Tech., 27 (**2006**) 5, 509–517, doi:10.1007/s00170-004-2218-0

[10] C. Shen, L. Wang, Q. Li, Optimization of injection molding process parameters using combination of artificial neural network and genetic algorithm method, J. Mater. Process Tech., 183 (**2007**) 2–3, 412–418, doi:10.1016/j.jmatprotec.2006.10.036

[11] B. Ozcelik, T. Erzurumlu, Comparison of the warpage optimization in the plastic injection molding using ANOVA, neural network model and genetic algorithm, J. Mater. Process Tech., 171 (**2006**) 3, 437–445, doi:10.1016/j.jmatprotec.2005.04.120

[12] W. C. Chen, G. L. Fu, P. H. Tai, W. J. Deng, Process parameter optimization for MIMO plastic injection molding via soft computing, Expert Syst. Appl., 36 (**2009**) 2, 1114–1122, doi:10.1016/j.eswa.2007.10.020

[13] E. Li, L. Jia, J. Yu, A genetic neural fuzzy system-based quality prediction model for injection process, Comput. Chem. Eng., 26 (**2002**) 9, 1253–1263, doi:10.1016/S0098-1354(02)00092-3

[14] D. Mathivanan, N. S. Parthasarathy, Sink-mark minimization in injection molding through response surface regression modeling and genetic algorithm, Int. J. Adv. Manuf. Tech., 45 (**2009**) 9–10, 867–874, doi:10.1007/s00170-009-2021-z

[15] Y. M. Deng, Y. Zhang, Y. C. Lam, A hybrid of mode-pursuing sampling method and genetic algorithm for minimization of injection molding warpage, Mater. Design, 31 (**2010**) 4, 2118–2123, doi:10.1016/j.matdes.2009.10.026

[16] H. S. Park, T. T. Nguyen, Optimization of injection molding process for car fender in consideration of energy efficiency and product quality, J. Comput. Design. Eng., 1 (**2014**) 4, 256–265, doi:10.7315/JCDE.2014.025

[17] J. Cheng, Z. Liu, J. Tan, Multiobjective optimization of injection molding parameters based on soft computing and variable complexity method, Int. J. Adv. Manuf. Tech., 66 (**2012**) 5, 907–916, doi:10.1007/s00170-012-4376-9

[18] J. Cheng, Y. Feng, J. Tan, W. Wei, Optimization of injection mold based on fuzzy moldability evaluation, J. Mater. Process Tech., 208 (**2008**) 1–3, 222–228, doi:10.1016/j.jmatprotec.2007.12.114

[19] K. T. Chiang, F. P. Chang, Application of grey-fuzzy logic on the optimal process design of an injection-molded part with a thin shell feature, Int. Commun. Heat Mass, 33 (**2006**) 1, 94–101, doi:10.1016/j.icheatmasstransfer.2005.08.006

[20] K. T. Chiang, The optimal process conditions of an injection-molded thermoplastic part with a thin shell feature using grey-fuzzy logic: A case study on machining the PC/ABS cell phone shell, Mater. Design, 28 (**2007**) 6, 1851–1860, doi:10.1016/j.matdes.2006.04.008

[21] L. A. Zadeh, Fuzzy logic = computing with words, IEEE T. Fuzzy Syst., 4 (**1996**) 2, 103–111, doi:10.1109/91.493904

[22] J. S. R. Jang, C. T. Sun, E. Mizutanim, Neuro-Fuzzy and Soft Computing: A Computational Approach to Learning and Machine Intelligence, Prentice Hall, New Jersey, 1997

[23] J. Kennedy, R. Eberhart, Particle swarm optimization, Proc. of 4th IEEE Int. Conf. on Neural Networks, Perth, 1995, 1942–1948

[24] D. C. Montgomery, Design and Analysis of Experiments, 5th ed., New York, Wiley, 2001

UDK 621.793.7:669.26:620.178.6
Original scientific article/Izvirni znanstveni članek

ISSN 1580-2949
MTAEC9, 51(4)603(2017)

CHROMIUM-BASED OXIDATION-RESISTANT COATINGS FOR THE PROTECTION OF ENGINE VALVES IN AUTOMOTIVE VEHICLES

PREVLEKE NA OSNOVI KROMA, ODPORNE PROTI OKSIDACIJI, KOT ZAŠČITA VENTILOV MOTORJA PRI AVTOMOBILIH

Monika Drożdż, Karol Kyzioł, Zbigniew Grzesik

AGH University of Science and Technology, Faculty of Materials Science and Technology, Department of Physical Chemistry and Modelling, Al. A. Mickiewicza 30, 30-059 Krakow, Poland
grzesik@agh.edu.pl

Prejem rokopisa – received: 2016-07-12; sprejem za objavo – accepted for publication: 2016-10-07

doi:10.17222/mit.2016.151

The influence of a thin chromium layer (1 μm) sputter-deposited on the surfaces of four valve steels (X33CrNiMn23-8, X50CrMnNiNbN21-9, X53CrMnNiN20-8 and X55CrMnNiN20-8) was studied at 900 °C under isothermal and thermal-shock conditions. It was determined that the oxidation resistance of coated steels is much better than that of uncoated ones. This situation is a result of the formation of highly protective Cr_2O_3 scales on the surfaces of coated materials. It was also demonstrated that a positive effect of a chromium addition on the oxidation resistance of the investigated steels is observed during a much longer period than the lifetime of a chromium coating.

Keywords: valve steels, chromium layer, oxidation, isothermal conditions, thermal shocks

Preučevan je bil vpliv tanke plasti kroma (1 μm), ki se je med pršenjem odlagal na površini štirih ventilov iz jekel: X33CrNiMn23-8, X50CrMnNiNbN21-9, X53CrMnNiN20-8 in X55CrMnNiN20-8, in sicer pri 900 °C, v izotermičnih pogojih in s toplotnimi šoki. Ugotovljeno je bilo, da je odpornost na oksidacijo pri premazanih jeklih veliko boljša kot pri jeklih brez prevlek. To stanje je posledica tvorbe visokozaščitnih Cr_2O_3 lestvic na površinah prevlečenih materialov. Dokazano je bilo tudi, da je pozitiven učinek proti oksidaciji, zaradi dodatka kroma, mogoče opaziti v mnogo daljšem časovnem obdobju, kot v celotni življenjski dobi preiskovanih jekel.

Ključne besede: jekleni ventili, plast kroma, oksidacija, izotermični pogoji, termični šoki

1 INTRODUCTION

Engine valves in automotive vehicles work in very severe conditions due to rather high temperatures (of up to about 900 °C), aggressive atmosphere of combustion gases and, in particular, rapid temperature changes, described in literature as thermal shocks.[1] Under thermal-shock conditions, high thermal stresses are generated at the interface between a valve and the oxidation-product layer, called the scale, due to different thermal-expansion coefficients of both materials.[2,3] Consequently, during the heating and cooling of an automobile engine, cracking and spalling of the scale are observed, which considerably lower the corrosion resistance of the valves. Thus, in addition to the protective properties of the scale, its adherence to the substrate constitutes the most important factor for determining the corrosion resistance of an oxidized material under thermal-shock conditions.[3–6] Recently, problems with corrosion degradation of engine valves in automobiles have become more and more important as a result of an increase in the working temperature in modern car engines and the application of alternative fuels like biofuels, liquid petroleum gas (LPG), compressed natural gas (CNG), etc. – the combustion products that are very aggressive.[7–13] As a consequence, protection of engine valves against high-temperature corrosion is urgently needed.

Among several protection methods for engine valves, the most promising one seems to be the application of protective coatings.[14–16] In this case, the main idea is the creation of such conditions, under which selective oxidation of chromium or aluminum takes place because oxides of both these metals (Cr_2O_3 and Al_2O_3) show excellent corrosion protection. The most frequently utilized protective coatings against high-temperature oxidation are thermal-barrier coatings (TBC).[15] The high efficiency of such coatings in protecting valve steels was proved experimentally by us many years ago.[17] Unfortunately, TBC coatings were never used in the mass production in the automobile industry due to economic reasons, i.e., relatively high costs of their production. Consequently, we designed a new generation of inexpensive coatings, which can be potentially used for the protection of engine valves. It was shown that such coatings, in contrast to the rather thick and, thereby, expensive TBC corrosion-resistant coatings, contain a very small amount of chromium, which is, however, high enough to form a continuous layer of highly-protective Cr_2O_3 oxide during the initial stage of oxidation.[18]

The stability and further growth of this chromium oxide layer is a result of outward chromium diffusion from the protected material. Thus, the proposed novel coatings only play the role of the initiator for the formation of the Cr_2O_3 layer, after which they disappear relatively fast. In spite of this fact, a better oxidation resistance of valve steels covered with thin novel coatings is observed during a much longer period than the lifetime of these coatings under isothermal conditions. Consequently, the obtained preliminary results strongly support the idea of tailoring a new generation of inexpensive coatings for mass application in protecting engine valves against high-temperature corrosion. It should be noted, however, that the beneficial influence of the discussed novel coatings on the oxidation behavior of valve steels has been investigated up to now only for two steels (X33CrNiMn23-8 and X50CrMnNiNbN21-9) under isothermal conditions.[18]

Thus, the aim of this work was to study the oxidation behavior under both isothermal and thermal-shock conditions of four valve steels, X33CrNiMn23-8 (X33), X50CrMnNiNbN21-9 (X50), X53CrMnNiN20-8 (X53) and X55CrMnNiN20-8 (X55), covered with novel coatings, utilized at present for the production of engine valves; the obtained results are reported in the present paper.

2 EXPERIMENTAL PART

Four chromium-nickel steels (X33, X50, X53 and X55), utilized for the engine-valve production, were used for the investigations of this work. The chemical compositions of these steels are presented in **Table 1**.

The samples for oxidation studies were obtained from the rods of the four above-mentioned steels with diameters of about 20 mm. These rods were cut into discs with thicknesses of approximately 1 mm. Next, disc-shaped samples were grinded with emery papers (up to 800 gradation SiC paper) and finally polished using 0.25 μm diamond pastes to obtain mirror-like surfaces. Some of these samples were covered with a chromium layer with a 1-μm thickness. Chromium coatings were deposited via magnetron sputtering in an argon atmosphere. A vacuum apparatus of the Elettorava S.p.A. company that operates at a constant current (2 kW), power supplier of the Dora company, was used in this procedure.

The substrates were mounted onto a two-fold rotary holder using a nickel-chromium wire. The chromium target was a cathode with a 25.4-mm diameter, 2-mm thickness and 99.95 % purity. After the air was evacuated to a pressure of below 10^{-3} Pa, argon-ion cleaning was conducted with the help of three ion guns. The energy of the argon ions was about 4 keV, the sample bias was changed from 0 kV to 2 kV and the cleaning time was 30 min. Magnetron sputtering of the pure chromium target was started immediately after the argon-ion cleaning. The argon pressure during the deposition was 0.39 Pa. The magnetron-sputtering process was carried out under 640 V and 1 A. The sample bias of the modulated DC current during the deposition was 50 V/0.03 A. The sputtering time was 40 min.

The oxidation kinetics of the coated and uncoated specimens was carried out in air at 900 °C in a microthermogravimetric apparatus. This apparatus is equipped with an electronic microbalance enabling the determination of weight gains of the oxidizing steel samples with an accuracy of the order of 10^{-6} g.[17] On the other hand, the corrosion tests under the thermal-shock conditions were carried out in the experimental set, described elsewhere.[19] These experiments consisted of determining the mass changes of corroded samples as a function of the number of thermal shocks. Thus, a given sample was rapidly heated from room temperature up to 900 °C and after the heat treatment at this temperature for two hours, it was cooled down rapidly (quenching) to room temperature. The duration of the heating time was approximately one min. The cooling time, in turn (quenching), took place in combustion gases passing through the reaction chamber for about two min. The temperature in both types of tests, equal to 900 °C, represents the highest possible temperature occurring in modern automobile engines.

The phase composition of the oxidation products (scales) was studied with X-ray diffraction (XRD), while the morphology and chemical composition of the reaction products were investigated using scanning electron microscopy (SEM) combined with energy-dispersive X-ray analysis (EDX).

3 RESULTS AND DISCUSSION

The results obtained during the oxidation studies under isothermal conditions of the coated and uncoated specimens are presented in **Figure 1**. From this figure, it follows that the oxidation rate of all the valve steels coated with a chromium thin layer is lower than the rate observed in the case of the uncoated materials. The best

Table 1: Chemical compositions (in mass fractions, *w*/%) of X33, X50, X53 and X55 valve steels

Type of steel	C	Mn	Si	Cr	Ni	N	W	Nb	S	P	Mo	Fe
X33CrNiMn23-8	0.35	3.30	0.63	23.40	7.80	0.28	0.02	-	<0.005	0.014	0.11	bal.
X50CrMnNiNbN21-9	0.54	7.61	0.30	19.88	3.64	0.44	0.86	2.05	0.001	0.031	-	bal.
X53CrMnNiN20-8	0.53	10.30	0.30	20.50	4.10	0.41	-	-	<0.005	0.040	0.12	bal.
X55CrMnNiN20-8	0.55	8.18	0.17	20.00	2.30	0.38	-	-	<0.005	0.030	0.11	bal.

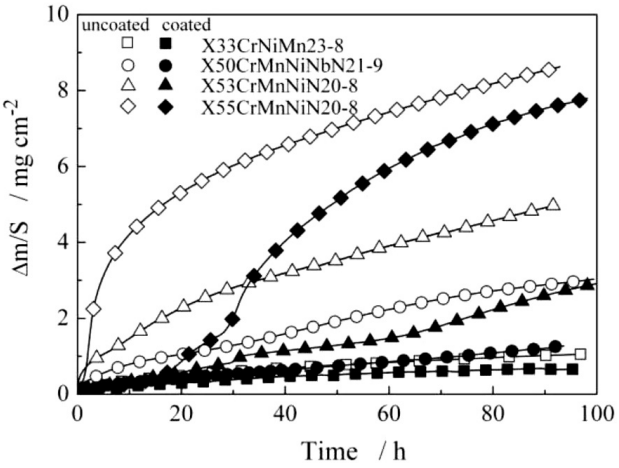

Figure 1: Comparison of the oxidation kinetics of four coated (black points) and uncoated (white points) valve steels at T = 900 °C in air, presented with a linear plot of coordinates (Δm/S – weight changes of an oxidized sample per unit surface area)

oxidation resistance was observed in the case of the coated X33 steel. However, the beneficial effect of chromium is relatively small because the oxidation rate of this steel is very low compared to the other steels under discussion. This situation is a result of the fact that the X33 steel has the highest chromium content (**Table 1**), which, after selective oxidation, can form a highly protective, continuous Cr_2O_3 chromium-oxide layer.[7,8] Thus, the high resistance of the X33 steel can be further increased to a relatively low degree by applying a thin chromium layer.

In the case of all the other steels with lower chromium contents, the deposition of a thin chromium layer considerably increases their oxidation resistance. It should be noted, however, that this effect is visible for the X55 steel only in the initial stages of the reaction, which denotes that the applied chromium layer does not exhibit sufficient thickness to ensure a full protection under the applied experimental conditions. It is very interesting that the positive effect of chromium on the oxidation resistance of the investigated steels is observed during a much longer period than the lifetime of the chromium coating. In the case of all the coated steels, the chromium layer can be observed for up to about 15 h, after which it disappears. However, in spite of the lack of the metallic chromium layer on the surface of the investigated steels, the oxidation resistances of the studied steels remained at the same level because the character of kinetic curves virtually remained unchanged.

The results of the thermal-shock experiments, obtained for all the investigated steels covered with a thin chromium layer, compared with the analogous results reported for the uncovered materials are presented in **Figure 2**. The interpretation of these results is as follows. If a given specimen gradually loses its mass with consecutive thermal shocks, it denotes that the scale cracks and spalls off from the surface of the investigated material due to thermal stresses. It means that the higher the mass losses of a given sample as a function of time, the poorer are the protective properties of the growing scale. On the other hand, if the mass of a sample virtually remains unchanged with a number of shocks (or increases only very slightly), it means that, in spite of the thermal stresses, the scale does not crack and spall off from the surface of the specimen and, consequently, satisfactorily protects the material against high-temperature corrosion.

From the comparison presented in **Figure 2**, it follows that the adherence of the scale growing on the surface of the X33 steel is very good because the mass changes of the investigated sample with a number of thermal shocks are virtually not observed. The thin chromium layer deposited on this steel has, in practice, no influence on its oxidation resistance under the thermal-shock conditions. On the other hand, the beneficial effect of the chromium deposition on the X50 and X53 steels is clearly visible. The masses of both of these uncoated steels gradually decrease during the oxidation, from the beginning of the reaction to the completion of 120 thermal shocks, and the total mass losses of the oxidized samples are about 100 mg/cm^2. On the other hand, the chromium-coated X50 steel starts to lose its mass after about 100 shocks and the total mass change after the completion of the experiment (250 shocks) is 40 mg/cm^2. This means that the cracking and spalling of the scale are only fragmentary and, consequently, this coated steel is rather well protected by the oxidation product. In other words, these results indicate that the adherence of the scale to the steel surface is rather high. Therefore, the scale protects the material, to some extent, against high-temperature corrosion under severe thermal-shock conditions.

The coated X53 steel behaves much better than the uncoated one. However, their resistance against oxidation under thermal-shock conditions is poorer than that observed for the coated X50 steel. The coated X53 steel starts to lose its mass after 40 thermal shocks and the

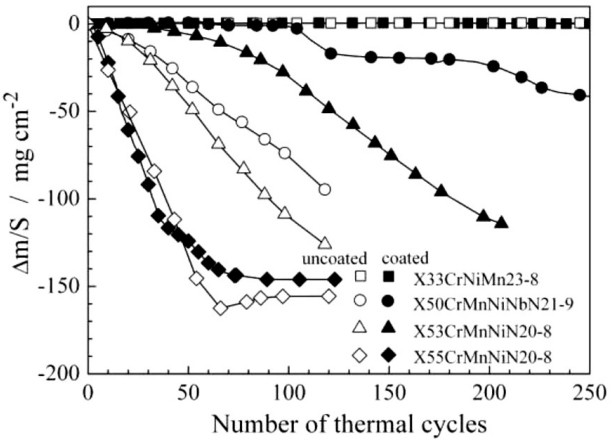

Figure 2: Results of thermal shocks for four valve steels with and without a chromium coating

total mass loss after 200 shocks is comparable to that observed for the uncoated steel after 100 shocks (110 mg/cm^2). These results may then be considered as an important proof of a good protective effect of the applied thin chromium coating in the case of both steels.

The poorest effects were obtained in the case of the X55 steel. As can be seen in **Figure 2**, no influence of the thin chromium layer on the oxidation resistance of the X55 steel under the thermal-shock conditions was observed. The chromium content in this steel (**Table 1**) is not high enough to form a highly protective chromium-oxide layer during the oxidation. As a consequence, the X55 steel corrodes very fast in all the experimental conditions that have been applied up to now.[7,8] The obtained results indicate that the relatively thin chromium coating deposited on the surface of the X55 steel does not create conditions sufficient to enable the growth of a compact and protective layer of chromium oxide. In the case of this steel, a thicker chromium layer should probably be applied.

The results of the oxidation studies of the four valve steels covered with a thin chromium layer, carried out under isothermal and thermal-shock conditions, generally confirm the beneficial influence of a chromium addition on the oxidation resistance of the investigated materials (with the exception of the X55 steel to some extent). The positive effect of chromium, deposited on the surfaces of the tested steels, is connected with the formation of Cr_2O_3 or chromium-containing spinel-oxide phases during the oxidation, instead of iron oxides (Fe_3O_4 or Fe_2O_3), the protective properties of which are much poorer than those of chromium-containing oxides. The influence of a thin chromium layer on the phase composition of the scale is shown in **Figure 3**, which presents the results of X-ray diffraction of the uncoated and coated X50 steel after the oxidation at 900 °C for 100 hours.

It should be mentioned that the kinetic results as well as the XRD analysis are in agreement with the morphological observations of the scale grown on the studied materials (**Figure 4**). It was determined, namely, that the scales formed on the coated and uncoated X33 steel samples are virtually identical (**Figures 4a, b**) because in both cases, the same fine-grained chromium oxide is present in the scale. This situation results from the fact

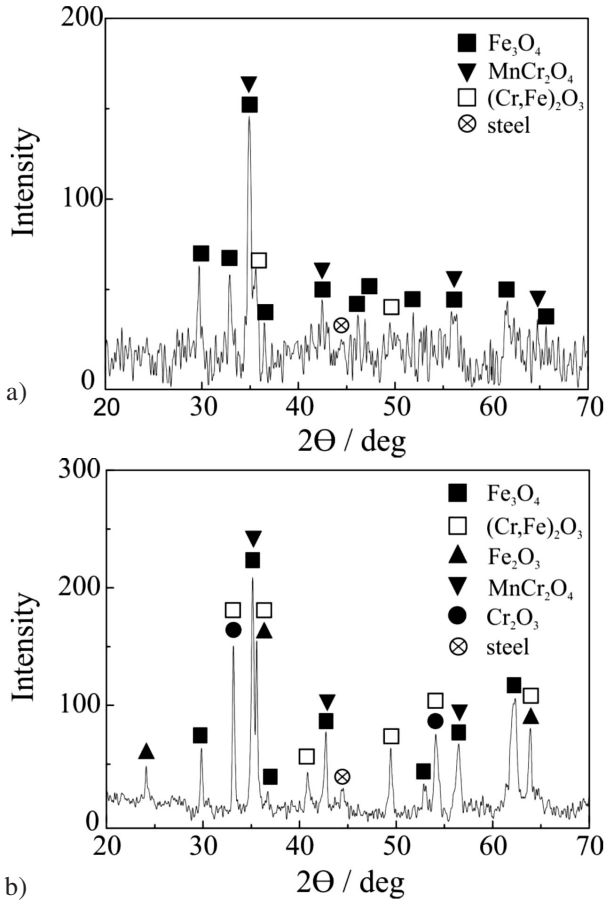

Figure 3: X-ray diffraction patterns for the X50 steel oxidized at 900 °C in air for 100 h: a) uncoated steel, b) coated steel

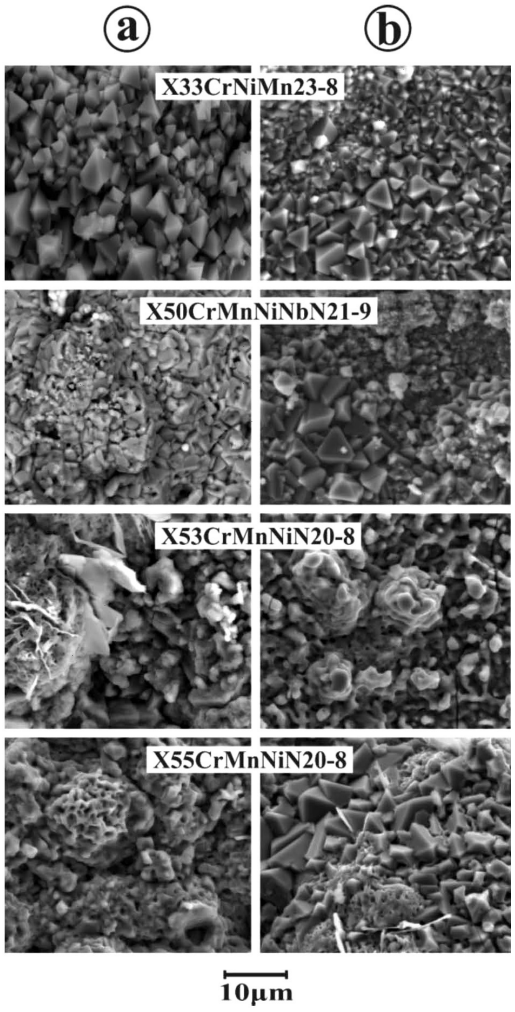

Figure 4: SEM images of the studied steels after the oxidation: a) uncoated X33 steel, b) coated X33 steel, c) uncoated X50 steel, d) coated X50 steel, e) uncoated X53 steel, f) coated X53 steel, g) uncoated X55 steel and h) coated X55 steel

that the uncoated X33 steel contains enough chromium (**Table 1**) to form a continuous layer of highly protective chromium oxide. On the other hand, in the case of all the other uncoated steels, unprotective scales are formed, which crack and spall off relatively fast. The adherence of the scales grown on the steels covered with a chromium layer is better. However, the effect of spallation can still be easily observed.

Thus, the obtained results strongly support the main thesis of this work, leading to the statement that it is possible to develop a new generation of high-temperature inexpensive thin chromium coatings for the protection of valve steels against high-temperature oxidation.

4 CONCLUSIONS

Thin layers of chromium deposited on the surfaces of the studied valve steels increase the resistance against high-temperature oxidation under isothermal conditions. In the case of the oxidation tests carried out under thermal-shock conditions, an analogous effect was observed, with the exception of the X55 steel, the oxidation resistance of which was not improved. The positive effect of chromium, deposited on the surfaces of the tested steels, is related to the formation of Cr_2O_3 or chromium-containing spinel-oxide phases during the oxidation, instead of Fe_3O_4 and Fe_2O_3. As the protective properties of chromium-rich oxides are much more effective than those of iron oxides, the chromium-coated valve steels underwent a lower degree of degradation than the uncoated materials. It should be noted that the improved oxidation resistance of coated steels is observed during a much longer period than the lifetime of chromium layers, which strongly supports the idea of tailoring a new generation of high-temperature inexpensive coatings for the protection of engine valves.

Acknowledgement

The investigations presented in this paper were supported by The Ministry of Science and Higher Education through a donation for Young Scientist made with decision no. 15.11.160.018.

5 REFERENCES

[1] C. G. Scott, A.T. Riga, H. Hong, The erosion-corrosion of nickel-base diesel engine exhaust valves, Wear, 181–183 (**1995**), 485–494, doi: 10.1016/0043-1648(95)90162-0

[2] S. Mrowec, T. Weber, Scaling-resistant iron-base alloys in Modern Scaling-Resistant Materials, National Bureau of Standards and National Science Foundation, Washington D.C., 1982, 277

[3] P. Kofstad, Development of stresses and strains, non-protective scales, phase boundary reactions in High Temperature Corrosion, Elsevier Applied Science, London and New York 1988, 278

[4] D. Naumenko, L. Singheiser, W. J. Quadakkers, Oxidation limited life of FeCrAl based alloys during thermal cycling, Proc. EFC Workshop, Frankfurt 1999, 287–306

[5] M. Beukenberg, Thermal Fatigue Evaluation of EB-PVD TBCs with Different Bond Coats, Proc. Turbine Forum, Nice 2006, 26–28

[6] Z. Grzesik, S. Mrowec, Z. Jurasz, K. Adamaszek, The behavior of valve materials utilized in Diesel engines under thermal shock conditions, High Temp. Mater. Proc., 29 (**2010**), 35–45, doi:10.1515/HTMP.2010.29.1-2.35

[7] Z. Grzesik, G. Smola, K. Adamaszek, Z. Jurasz, S. Mrowec, High temperature corrosion of valve steels in combustion gases of petrol containing ethanol addition, Corros. Sci., 77 (**2013**), 369–374, doi:10.1016/j.corsci.2013.08.030

[8] Z. Grzesik, G. Smola, K. Adamaszek, Z. Jurasz, S. Mrowec, Thermal shock corrosion of valve steels utilized in automobile industry, Oxid. Met., 80 (**2013**), 147–159, doi:10.1007/s11085-013-9363-5

[9] R. Gilbert, A. Perl, Energy and transport futures, A report prepared for national round table on the environment and the economy, Univ. Calgary, 2005, 1–96

[10] D. G. Kessel, Global warming – facts, assessment, countermeasures, J. Pet. Sci. Eng., 26 (**2000**), 157–168

[11] C. N. Hamelinck, A. P. C. Faaij, Outlook for advanced biofuels, Energy Policy, 34 (**2006**), 3268–3283, doi:10.1016/j.enpol.2005.06.012

[12] A. S. M. A. Haseeb, M. A. Fazal, M. I. Jahirul, H. H. Masjuki, Compatibility of automotive materials in biodiesel: a review, Fuel, 90 (**2011**), 922–931, doi:10.1016/j.fuel.2010.10.042

[13] Z. W. Yu, X. L. Xu, Failure analysis and metallurgical investigation of diesel engine exhaust valves, Eng. Fail. Anal., 13 (**2006**), 673–682, doi:10.1016/j.engfailanal.2004.10.018

[14] B. Gleeson, High-Temperature Corrosion of Metallic Alloys and Coatings, Materials Science and Technology, Wiley-VCH, Weinheim-New York-Chichester-Brisbane-Singapore-Toronto 2000, 174–228

[15] H. Xu, H. Guo, S. Gong, Thermal barrier coatings in Developments in High-Temperature Corrosion and Protection of Materials, Woodhead Publishing in Materials, Cambridge 2008, 476-491

[16] H. E. Evans, High Temperature Coatings: Protection and Breakdown in Shreir's Corrosion, 4th ed., Elsevier Ltd., Amsterdam 2010, 691–724

[17] K. Adamaszek, Z. Jurasz, L. Swadzba, Z. Grzesik, S. Mrowec, The influence of hybrid coatings on scaling-resistant properties of X33CrNiMn23-8 steel, High Temp. Mater. Proc., 26 (**2007**), 115–122, doi:10.1515/HTMP.2007.26.2.115

[18] D. Dulińska, W. Pawlak, Z. Grzesik, The prospects in designing new generation of high temperature coatings in automobile engines, Arch. Metall. Mater., 60 (**2015**), 903–907, doi:10.1515/amm-2015-0227

[19] Z. Grzesik, M. Migdalska, S. Mrowec, The influence of yttrium on high temperature oxidation of valve steels, High Temp. Mater. Proc., 34 (**2015**), 115–121, doi:10.1515/htmp-2014-0023

UDK 620.1:546.261:62-712
Original scientific article/Izvirni znanstveni članek

ISSN 1580-2949
MTAEC9, 51(4)609(2017)

CARBIDE DISTRIBUTION BASED ON AUTOMATIC IMAGE ANALYSIS FOR CRYOGENICALLY TREATED TOOL STEELS

PRIKAZ PORAZDELITVE KARBIDNIH DELCEV V ORODNIH JEKLIH, OBDELANIH S PODHLAJEVANJEM S POMOČJO AVTOMATSKE ANALIZE SLIK

Pello Jimbert, Maider Iturrondobeitia, Julen Ibarretxe, Roberto Fernandez-Martinez

University of the Basque Country (UPV/EHU), Faculty of Engineering, Paseo Rafael Moreno Pitxitxi, 348013, Bilbao, Spain
pello.jimbert@ehu.eus

Prejem rokopisa – received: 2016-07-14; sprejem za objavo – accepted for publication: 2016-09-29

doi:10.17222/mit.2016.165

Particle distribution in steels has been widely reported in the scientific literature in terms of quantity and size of these particles. However, in these studies there is barely any information about the homogeneity or heterogeneity of the particle distribution. A cryogenically treated AISI A8 tool steel was compared against a conventionally treated one, not only in terms of the number and size of precipitated carbides, but also their distribution. Scanning-electron-microscopy images were automatically analyzed for this quantification. The results revealed an increase of 100 % in the number of carbides and a reduction of 35 % in the mean size of the precipitates for the cryogenically treated sample. The distribution of the particles – which turned out to be more homogeneous for the cryogenically treated sample – was characterized using the methodology described here, which applies automatic image analysis. These results may lead to an improvement in the wear resistance of a cryogenically treated AISI A8 alloy.

Keywords: particle distribution, automatic image analysis, tool steel, cryogenic treatment

Porazdelitev karbidnih delcev v jeklih glede na količino in velikost je obširno predstavljena v znanstveni literaturi. Toda te študije praktično ne podajajo informacije o homogenosti oz. heterogenosti porazdelitve teh delcev. Število, velikost in porazdelitev karbidnih delcev v podhlajenem orodnem jeklu AISI A8 smo primerjali z vzorci konvencionalno pridobljenega jekla. Slike, posnete z vrstičnim elektronskim mikroskopom, smo za potrebe kvantifikacije avtomatsko analizirali. Rezultati kažejo 100 % povečanje števila karbidnih delcev in zmanjšanje povprečne velikosti karbidnih precipitatov za 35 % v podhlajenih vzorcih. Avtomatska analiza slik, razvita za potrebe te študije, podaja informacijo z izračunom porazdelitve delcev. Predstavljena študija nakazuje na bolj homogeno porazdelitev karbidnih delcev v podhlajenih vzorcih. Naši rezultati bi lahko pripomogli k izboljšanju obrabne odpornosti podhlajenih AISI A8 zlitin.

Ključne besede: porazdelitev delcev, avtomatska analiza slik, orodno jeklo, obdelava s podhlajevanjem

1 INTRODUCTION

There have been reports of carbide[1] or oxide[2,3] precipitate quantity and size distribution in steels using image-processing software, even for particle sizes at the nanoscale[4] but not so many about the homogeneity of the distribution of these particles in the microstructure. Some studies show the distribution of these particles qualitatively using different techniques without a clear explanation of the methodology they followed.[5] One of the shortcomings of this kind of particle-distribution calculation is the large amount of particles (and therefore images as well) needed to have a statistically representative quantification. In this work, an automatic methodology was developed to quantitatively analyze the microstructure of AISI A8 tool steels, by analyzing a statistically representative number of images of the bulk material.

2 MATERIALS AND METHODOLOGY

The methodology for characterizing the carbide distribution presented in this work was developed for the AISI A8 tool steel. It is a widely used tool-steel alloy that exhibits a high hardenability, good wear resistance, resistance to dynamic loading and toughness. Some of its applications include cold forming, blanking and bending dies, knurling tools, forming rolls, master dies and gages. Its chemical composition can be seen in **Table 1**.

Two samples of the AISI A8 were analyzed. Sample 1 underwent a conventional heat-treatment process of austenization at 1050 °C for 40 min, air quenching and

Table 1: Chemical composition of the AISI A8 steel

Material	C	Mn	Si	Cr	Ni	Mo	W
AISI A8	0.5-0.6	0.5	0.75-1.1	4.75-5.5	0.3	1.15-1.65	1-1.5

two tempering processes of 90 min at 500 °C. Sample 2 underwent an additional final-cyclic cryogenic treatment of 6 cycles from –73 °C to –172 °C taking 15 h after the conventional heat treatment. The cryogenic treatment is applied to different tool steels for the improvement of the wear resistance and this improvement is related to the precipitation of carbides.[6] The influence of the cryogenic treatment on the precipitation of carbides of the AISI A8 medium-alloy tool steel was investigated for the first time in this work.

Scanning electron microscope (SEM) images were used to calculate the carbide distribution and microstructural parameters such as the number of particles, their mean sizes and the total area. The images were acquired with a JEOL JSM-6400F SEM model at 10 KV and a 500× magnification. The pixel size was 9.2 pixel/μm. Ten images of 200 μm × 200 μm, acquired in different areas, were analyzed for each sample. Considering the resulting average sizes and their corresponding deviations (**Figure 1**), the number of analyzed particles (900 for sample 1 and 1800 for sample 2) is sufficient to statistically ensure that the average values are accurate within ± 0.1 μm at a 95 % confidence.

The automatic image analysis was carried out using Fiji.[7] First of all, the images were binarized using the Auto Local Threshold plug-in with different algorithms (Bernsen, Mean, MidGrey, Niblack and Sauvola). The Sauvola algorithm was chosen since it gave the most suitable binarization of the carbides over the martensitic matrix, based on our experience in this field as can be seen in **Figure 1**. The SEM images were then automatically analyzed using the Sauvola algorithm and the following information for the carbides was obtained: centroid positions, the number of particles and sizes. To calculate the distribution of the carbides, their centroids were used, computing the distances to the four closest neighbors and their averages using an in-house made script in Matlab.[8]

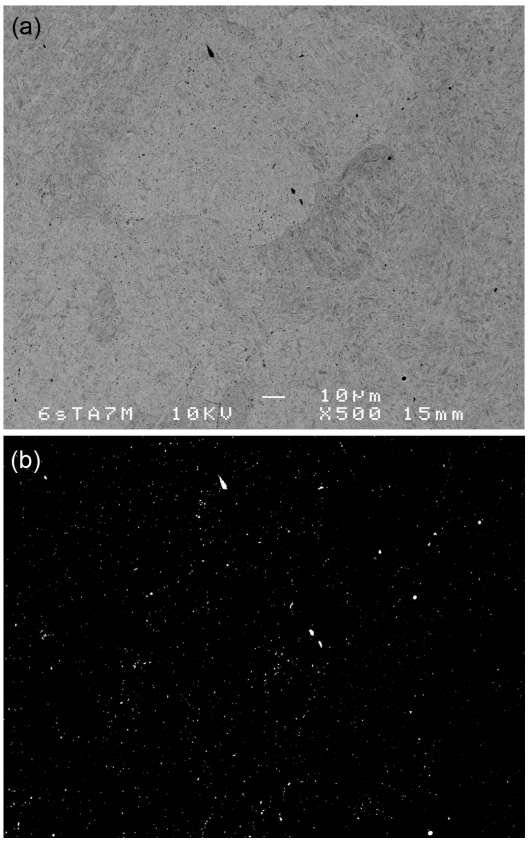

Figure 1: a) Original SEM image and b) binarized image

3 RESULTS AND DISCUSSION

The density of carbide particles increases for the cryogenically treated sample (sample 2) from 0.026 particles/μm^2 to 0.054 particles/μm^2. This indicates an increase of around 100 % in the number of particles. This result is in good agreement with the results obtained for different tool steels, which show an increase in the number of carbides when they are cryogenically treated.[9] This increase in the number of carbides is related, in the literature, with an increase in the wear resistance.[10] The observed effect is very promising regarding the possibility to include the cryogenic treatment of the AISI A8 tool steel when used for severe friction applications.

Also, the mean particle length decreases from 6.2±1.3 to 4.1±1.5 μm. This result is in concordance with those reported for other tool steels after being cryogenically treated.[10] D. Das et al.[11] concluded that the cryogenic treatment creates new carbide segregates during the cooling and this segregates grow during the heating from the cryogenic temperature to the ambient temperature creating small secondary carbides. The small size of these new carbides reduces the mean size of the precipitates present in the material.

Regarding the distribution of the particles (**Figure 2**), the distribution of the newly precipitated carbides is more homogeneous for sample 2. The percentage of the area occupied by the carbides increases from 0.4 % for the conventionally treated sample to 0.6 % for the cryogenically treated sample. The final microstructure of the

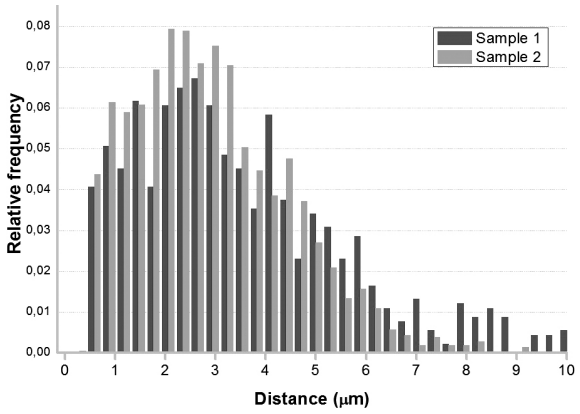

Figure 2: Carbide distribution for the conventionally treated (sample 1) and for the cryogenically treated (sample 2) samples

cryogenically treated sample has more carbides, they cover a bigger area and they are more homogeneously distributed than in the conventionally treated one.

4 CONCLUSION

The microstructure is quantitatively measured using a methodology based on automatic image analysis. The methodology used for the carbide-distribution calculation developed in this study was satisfactorily applied to tool steels and the obtained results support the suitability of this methodology.

The distribution of the carbides precipitated during the cryogenic treatment of the AISI A8 steel is more homogenous, indicating a more homogeneous final microstructure.

The AISI A8 tool steel showed a potential to be cryogenically treated since there is an increase in the number of precipitated carbides, reducing their mean sizes and covering a 43 % larger area, which may lead to an increase in the wear resistance.

Acknowledgements

This work was supported by the Department of Industry, Innovation, Trade and Tourism of the Basque Country Government through the S-PE12UN080 SAIOTEK project. The authors thank for the technical and human support provided by SGIker of UPV/EHU and European funding (ERDF and ESF).

5 REFERENCES

[1] C. Revilla, B. López, J. M. Rodriguez Ibabe, Carbide size refinement by controlling the heating rate during induction tempering in a low alloy steel, Materials and Design, 62 (**2014**), 296–304, doi:10.1016/j.matdes.2014.05.053

[2] S. F. Li , Z. J. Zhou, P. H. Wang, H.Y. Sun, M. Wang, G. M. Zhang, Long-term thermal-aging stability of a 16Cr-oxide dispersion strengthened ferritic steel at 973 K, Materials and Design, 90 (**2016**), 318–329, doi:10.1016/j.matdes.2015.10.138

[3] M. Nagini, R. Vijay, M. Ramakrishna, A.V. Reddy, G. Sundararajan, Influence of the duration of high energy ball milling on the microstructure and mechanical properties of a 9Cr oxide dispersion strengthened ferritic–martensitic steel, Materials Science & Engineering A, 620 (**2015**), 490–499, doi:10.1016/j.msea.2014.10.050

[4] C. Solenthaler, M. Ramesh, P. J. Uggowitzer, R. Spolenak, Precipitation strengthening of Nb-stabilized TP 347 austenitic steel by a dispersion of secondary Nb (C,N) formed upon a short-term hardening heat treatment, Materials Science & Engineering A, 647 (**2015**), 294–302, doi:10.1016/j.msea.2015.09.028

[5] S. Amirkhanlou, B. Niroumand, Effects of reinforcement distribution on low and high temperature tensile properties of Al356/SiCp cast composites produced by a novel reinforcement dispersion technique, Materials Science and Engineering A, 528 (**2011**), 7186–7195, doi:10.1016/j.msea.2011.06.013

[6] P. Baldissera, C. Delprete, Deep cryogenic treatment: a bibliographic review, The Open Mechanical Engineering Journal, 2 (**2008**), 1–11, doi:10.2174/1874155X00802010001

[7] J. Schindelin, I. Arganda-Carreras, E. Frise, V. Kaynig, M. Longair, T. Pietzsch, S. Preibisch, C. Rueden, S. Saalfeld, B. Schmid, J.-Y. Tinevez, D. J. White, V. Hartenstein, K. Eliceiri, P. Tomancak, A. Cardona, Fiji: an open-source platform for biological-image analysis, Nat. Methods, 9 (**2012**) 7, 676–82, doi:10.1038/nmeth.2019

[8] MATLAB Release 2014b, The MathWorks, Inc., Natick, Massachusetts, USA

[9] J. Y. Huang, Y. T. Zhu, X. Z. Liao, I. J. Beyerlein, M. A. Bourke, T. E. Mitchell, Microstructure of cryogenically treated M2 tool steel, Materials Science and Engineering A, 339 (**2003**), 241–244, doi:10.1016/S0921-5093(02)00165-X

[10] S. Akincioğlu, H. Gökkaya, I. Uygur, A review of cryogenic treatment on cutting tools, Int. J. Adv. Manuf. Technol, 78 (**2015**), 1609–1627, doi:10.1007/s00170-014-6755-x

[11] D. Das, A. K. Dutta, K. K. Ray, Sub-zero treatments of AISI D2 steel: Part I. Microstructure and hardness, Materials Science and Engineering A, 527 (**2010**), 2182–2193, doi:10.1016/j.msea.2009.10.070

UDK 669.017.12:62.1.794.61:669.058
Original scientific article/Izvirni znanstveni članek

ISSN 1580-2949
MTAEC9, 51(4)613(2017)

EFFECTS OF AN Al_2O_3 NANO-ADDITIVE ON THE PERFORMANCE OF CERAMIC COATINGS PREPARED WITH MICRO-ARC OXIDATION ON A TITANIUM ALLOY

UČINKI Al_2O_3 NANODODATKA NA TITANOVO ZLITINO PRI IZVEDBI KERAMIČNIH PREVLEK, PRIPRAVLJENO Z MIKROOBLOČNO OKSIDACIJO

Çağatay Demirbaş, Aysun Ayday

Sakarya University, Faculty of Engineering, Department of Metallurgical and Materials Engineering, Sakarya, 54187, Turkey
aayday@sakarya.edu.tr

Prejem rokopisa – received: 2016-07-15; sprejem za objavo – accepted for publication: 2016-11-08

doi:10.17222/mit.2016.194

In this research, nano-sized Al_2O_3 particles were added to silicate-based coatings and the effect of these particles on the microstructure, composition and properties of the coatings was investigated. The effects of the nano-additive on the structure, phase composition and hardness of the micro-arc oxidation (MAO) coatings were analysed using scanning electron microscopy (SEM), X-ray diffraction and micro-hardness testing. The SEM showed that the coatings with a nano-additive have lower porosities than those without a nano-additive. XRD results showed that the coatings with nano-additives contain more oxide when compared to those without nano-additives. The results showed that the nanoparticle additions improve the hardness of the MAO coatings.

Keywords: micro-arc oxidation (MAO), nano-additive, alumina, Ti6Al4V

V raziskavi so Al_2O_3 nanodelci dodani osnovi s silikatnimi prevlekami. Raziskan je bil učinek teh delcev na mikrostrukturo, sestavo in lastnosti prevlek. Analizirani so bili učinki nanodelcev na strukturo, fazno sestavo in trdoto mikroobločne oksidacije (angl. MAO) pri premazih, in sicer z vrstično elektronsko mikroskopijo (SEM), z rentgensko difrakcijo in z mikrotrdoto. SEM-analiza je pokazala, da imajo prevleke z nanododatkom nižjo poroznost od tistih, katerih prevleke ne vsebujejo nanododatkov. Rezultati XRD kažejo, da prevleke z nanododatki vsebujejo več oksidov v primerjavi s tistimi brez nanododatkov. Rezultati še kažejo, da dodatki nanodelcev izboljšajo trdoto MAO-prevlek.

Ključne besede: mikroobločna oksidacija, nanododatki, glinica, Ti6Al4V

1 INTRODUCTION

Titanium and its alloys are widely used in aerospace, automation, chemical industry and biomedicine because of their high strength, low density and good biocompatibility. However, their surface hardness and corrosion resistance limit their applications. Many studies aim to improve their hardness and corrosion resistance.[1–3]

MAO is a plasma-assisted surface treatment technique used to convert the surfaces of suitable metals to thick and hard ceramic-oxide layers.[4,5] However, ceramic coatings generally possess a foam-like structure with a high bulk porosity and relatively poor mechanical properties, which restrict them from even wider technical applications.[5] Researches mainly focused on the effects of the processing parameters, such as current density, voltage and electrolytic solution for improving the mechanical properties; nowadays, nano-additive doping of the electrolyte is also studied to improve the properties of the ceramic coatings.[4,6,7] In this research, the effect of a nano-Al_2O_3 additive to the electrolyte on the Ti6Al4V microstructure, phase composition and microhardness of MAO coatings on a titanium alloy were analysed.

2 EXPERIMENTAL PART

The Ti6Al4V substrate material used for the investigation had a chemical composition in mass fractions (*w*/%) of 6.3 Al, 4.2 V, 0.15 O, 0.11 Fe, 0.03 C, 0.02 N, 0.001 H and Ti balance. The samples with a size of Φ5 × 70 mm were ground with 1000-grit silicon-carbide papers, cleaned with alcohol and then dried in hot air. The electrolytes were prepared from solutions of 8.75 % Na_2SiO_3 g/L – 1.25 % NaOH g/L – 0.6 % $Na_2B_4O_7$ g/L (MAO-Ti) and 8.75 % Na_2SiO_3 g/L – 1.25 % NaOH g/L – 0.6 % $Na_2B_4O_7$ g/L – 3.75 % Al_2O_3 g/L (MAO (nano)-Ti) in distilled water (**Table 1**). During the MAO treatment, the applied voltage, treatment time and cooling system (electrolyte) were fixed at 400 V, 15 min and 30±5 °C, respectively. The microstructural characteristics of the coating and phase composition were investigated with scanning electron microscopy (SEM, JOEL) and X-ray diffraction (XRD, Shimadzu XRD-6000). **Table 1** shows the components, pH and conductivity of the electrolytes of the samples. The hardness values of the uncoated Ti6Al4V and coated samples were measured using a FUTURE TECH-CORP.FM-700 microhardness tester at a load of 100 g for a loading time

Table 1: Coated samples and characteristics of their coating electrolytes

Sample codes	Electrolyte components (g/L)	Nano-Al_2O_3 (g/L)	Electrolyte pH	Electrolyte conductivity (ms/cm)
MAO-Ti	(8.75%) Na_2SiO_3 / (1.25%) NaOH / (0.6%) $Na_2B_4O_7$	-	12	11.5
MAO(Nano)-Ti	(8.75%) Na_2SiO_3 / (1.25%) NaOH / (0.6%) $Na_2B_4O_7$	(3.75%)	12.3	14

of 10 s. The average of three repeated measurements was reported.

3 RESULTS AND DISCUSSION

Figure 1 shows the surface morphologies of the coated samples. A highly non-uniform porous layer, with an average pore size ranging from 5–10 μm was observed on the surface of the MAO-Ti coating (**Figure 1a** to **1b**). With an addition of nano-Al_2O_3, the coating surface became denser and smoother and the number of pores decreased (**Figure 1c** to **1d**). It can be concluded that the addition of a nanopowder plays an essential role in fabricating ceramic coatings with a lower porosity.

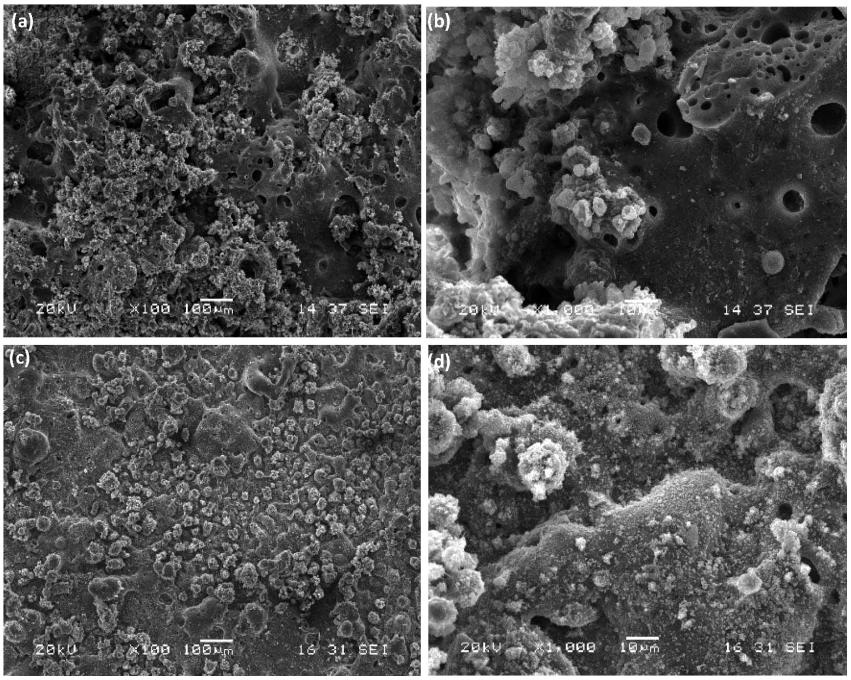

Figure 1: Surface morphologies of the MAO-treated Ti: a) to b) MAO-Ti and an addition of nano-Al_2O_3, c) to d) MAO (Nano)-Ti

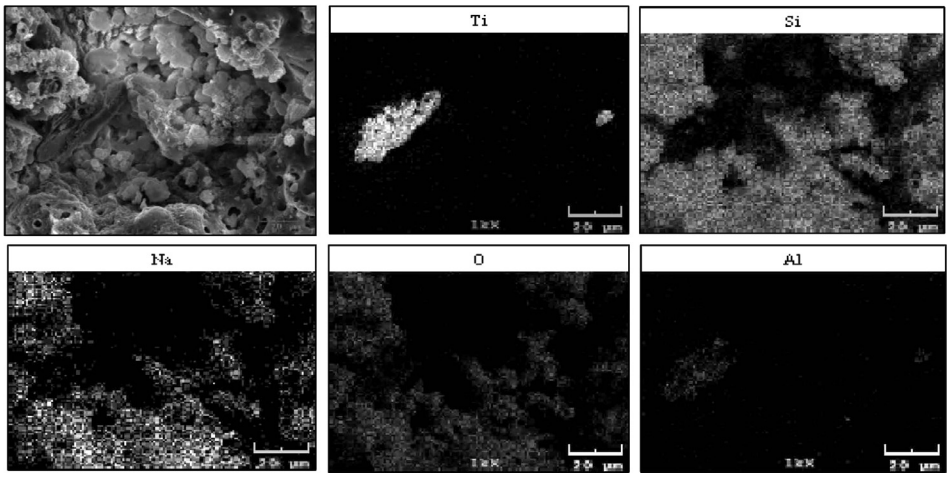

Figure 2: EDS map analysis of MAO-Ti (without a nano-additive)

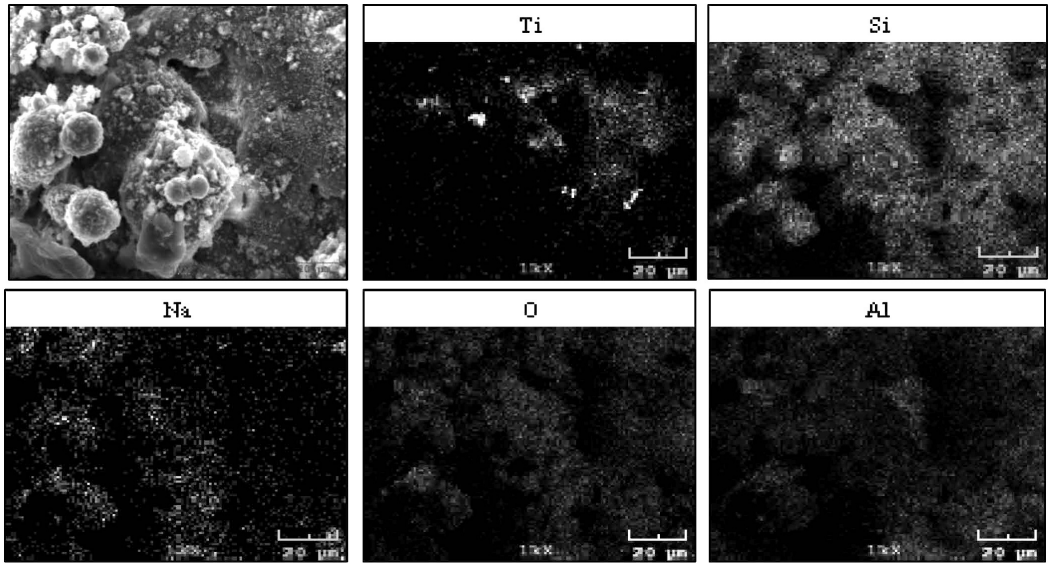

Figure 3: EDS map analysis of MAO (nano)-Ti (with a nano-additive)

Some of the Al_2O_3 nanoparticles were drawn into the discharge channel during the micro-arc discharge because of the force of the conductivity of the electrolytes. The addition of Al_2O_3 nanoparticles to the electrolyte improved its conductivity and the sparks generated in the anode reaction intensified. This led to a significant increase in the number of micro-arcs per unit time, resulting in an increase in the number of micro-arc pores and a reduction in the size of the pores formed on the sample surface. Smaller pores increase the compactness of the coating microstructure.[8]

The EDS map analysis of the MAO coatings without a nano-additive is shown in **Figure 2**. The main elements were Ti and O, which were found in all the coatings and came from the substrate. Na and Si were detected on nearly all the surfaces and these elements came from the electrolyte solution. Furthermore, the Al element was found in small parts that were not well coated and came from the substrate. **Figure 3** represents the EDS map analysis of the MAO coating with an addition of nano-Al_2O_3. It can be seen that the prepared coating mainly consists of Ti, O, Si and Na, which came from the substrate and electrolytic solution. From **Figure 3**, it can be seen that the contents of all the elements increased, the rates of O and Al changed a lot, and Al increased with the nano-Al_2O_3 additive. It might be inferred that the Al_2O_3 particles were mixed into the ceramic coating, with some regions partly rich in the Al_2O_3 particles. We thought that more and more dispersed nanoparticles entered the pores, increasing the nano-additive concentrations, so the coating surface became denser and smoother.

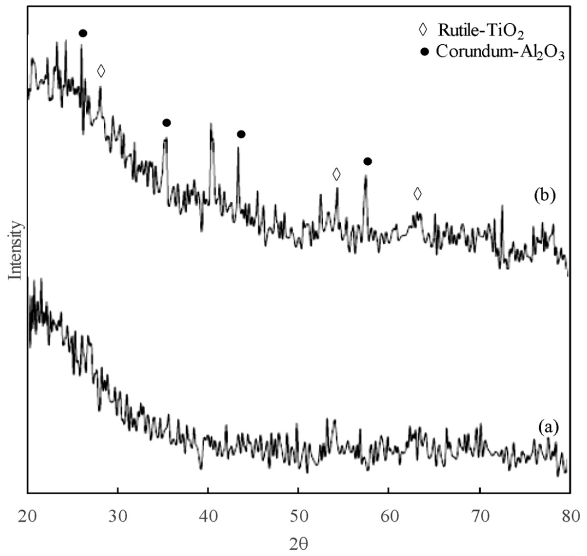

Figure 4: XRD patterns of MAO-coated Ti6Al4V with and without a nano-additive: a) MAO-Ti, b) MAO (nano)-Ti

XRD patterns of MAO coatings with and without a nano-additive are shown in **Figure 4**. For the coating prepared in the silicate solution without nano-additives, it can be seen that the prepared ceramic coatings consist of TiO_2 and the amorphous phase. The coatings prepared in the silicate solution with the Al_2O_3 nano-additive are similar; however, the peak intensity of TiO_2 increased and Al_2O_3 is observed, which indicates that nanoparticles entered the prepared ceramic coatings. As mentioned in the literature, the samples with the electrolyte containing a nano-Al_2O_3 additive exhibit high voltage. This phenomenon indicates that the Al_2O_3 nano-additive has a significant influence on the voltage and thus the formation of a MAO coating.[9,10]

The average Vickers microhardness of the uncoated alloy was 401±10 $HV_{0,1}$, 980±10 $HV_{0,1}$ and 1150±10 $HV_{0,1}$ for the MAO-Ti and MAO (nano)-Ti-coated alloys, respectively. Thus, the MAO process increased the hardness of the alloy surface significantly. This surface hardness is 2–3 times higher when compared with the uncoated sample.

4 CONCLUSIONS

Ceramic coatings were generated on Ti6Al4V substrates in a silicate electrolyte with and without an Al_2O_3 nano-additive using the MAO technique. The coated layers without a nano-additive generally consisted of rutile (TiO_2). An Al_2O_3 nano-additive was successfully incorporated into the TiO_2 layer, which was confirmed with XRD and EDS analyses. The added Al_2O_3 nanoparticles become incorporated into the coatings, increasing the density of the coating microstructures and the hardness. The surface hardness of the coatings was increased to 1150±10 $HV_{0,1}$ with the MAO(nano)-Ti. The surface hardness increased 2–3 times when compared with the uncoated sample.

Acknowledgments

The authors are very grateful to the Sakarya University of Turkey (Project No: 2016-01-08-018) for its support.

5 REFERENCES

[1] S. Liu, B. Li, C. Liang, H. Wang, Z. Qiao, Formation mechanism and adhesive strength of a hydroxyapatite/TiO2 composite coating on a titanium surface prepared by micro-arc oxidation, Applied Surface Science, 362 (**2016**), 109–114, doi:10.1016/j.apsusc.2015.11.086

[2] B. Attard, A. Matthews, A. Leyland, G. Cassar, Enhanced surface performance of Ti-6Al-4V alloy using a novel duplex process combining PVD-Al coating and triode plasma oxidation, Surface and Coatings Technology, 257 (**2014**), 154–164, doi:10.1016/j.surfcoat.2014.07.083

[3] Y. Cheng, X.-Q. Wu, Z. Xue, E. Matykina, P. Skeldon, G. E. Thompson, Microstructure, corrosion and wear performance of plasma electrolytic oxidation coatings formed on Ti–6Al–4V alloy in silicate-hexametaphosphate electrolyte, Surface and Coatings Technology, 217 (**2013**), 129–139, doi:10.1016/j.surfcoat.2012.12.003

[4] N. Xiang, R. Song, J. Zhao, H. Li, C. Wang, Z. Wang, Microstructure and mechanical properties of ceramic coatings formed on 6063 aluminium alloy by micro-arc oxidation, Transactions of Nonferrous Metals of China, (**2015**) 25, 3323–3328, doi:10.1016/S1003-6326(15)63988-7

[5] K. Korkmaz, The effect of micro-arc oxidation treatment on the microstructure and properties of open cell Ti6Al4V alloy foams, Surface and Coatings Technology, (**2015**) 272, 72–78, doi:10.1016/j.surfcoat.2015.04.022

[6] H. Ma, D. Li, C. Liu, Z. Huang, D. He, Q. Yan, P. Liu, P. Nash, D. Shen, An investigation of (NaPO3)6 effects and mechanisms during micro-arc oxidation of AZ31 magnesium alloy, Surface and Coatings Technology, (**2015**) 266, 151–159, doi:10.1016/j.surfcoat.2015.02.033

[7] Y. Wang, D. Wei, J. Yu, S. Di, Effects of Al2O3 Nano-Additive on Performance of Micro-Arc Oxidation Coatings Formed on AZ91D Mg Alloy, Journal of Material Science Technology, 30 (**2014**) 10, 984–990, doi:10.1016/j.jmst.2014.03.006

[8] Y. Hua, Z. Zhang, W. Li, Microstructure and degradation properties of C-containing composite coatings on magnesium alloy wires treated with micro-arc oxidation, Surface and Coatings Technology, 291 (**2016**), 70–78, doi:10.1016/j.surfcoat.2016.02.018

[9] H. Li, R. Song, Z. Ji, Effects of nano-additive TiO2 on performance of micro-arc oxidation coatings formed on 6063 aluminum alloy, Transactions of Nonferrous Metals of China, 23 (**2013**), 406–41, doi:10.1016/S1003-6326(13)62477-2

[10] M. Shokouhfar, S. R. Allahkaram, Formation mechanism and surface characterization of ceramic composite coatings on pure titanium prepared by micro-arc oxidation in electrolytes containing nanoparticles, Surface and Coatings Technology, 291 (**2016**), 396–405, doi:10.1016/j.surfcoat.2016.03.013

UDK 669.017.1:67.017:543.428.3
Original scientific article/Izvirni znanstveni članek

ISSN 1580-2949
MTAEC9, 51(4)617(2017)

OXIDATION OF MOLYBDENUM BY LOW-ENERGY OXYGEN-ION BOMBARDMENT

OKSIDACIJA MOLIBDENA Z NIZKOENERGETSKIM KISIKOVIM IONSKIM OBSTRELJEVANJEM

Ivana Jelovica Badovinac, Ivna Kavre Piltaver, Iva Šarić, Robert Peter, Mladen Petravić

University of Rijeka, Department of Physics and Center for Micro- and Nanosciences and Technologies, 51000 Rijeka, Croatia
ijelov@phy.uniri.hr

Prejem rokopisa – received: 2016-07-15; sprejem za objavo – accepted for publication: 2016-11-17

doi:10.17222/mit.2016.199

We have studied the oxidation of pure molybdenum metal at room temperature (RT) by low-energy oxygen-ion bombardment within an analytical, ultrahigh vacuum chamber, using x-ray photoemission spectroscopy (XPS) around the Mo 3d core level. We provide a detailed characterization of the oxidation states of pure Mo and a comparison with the Mo oxidation in the CoCrMo alloy. After the thermal oxidation of pure metal at RT up to 5000 L of oxygen, the Mo 3d photoelectron remained almost unchanged. On the other hand, Mo oxidizes quite easily within the CoCrMo alloy by thermal oxidation at RT. The XPS spectra recorded after the ion bombardment showed a complex structure consisting of Mo^{4+}, Mo^{5+} and Mo^{6+} oxidation states. Our study shows that pure Mo metal oxidizes more efficiently under oxygen-ion bombardment or when incorporated into the CoCrMo alloy. We explain our results in terms of the implantation dynamics of oxygen ions and the enhanced mobility and reactivity of oxygen atoms in the alloy, compared to the pure Mo metal.

Keywords: molybdenum, CoCrMo alloy, ion-beam oxidation, thermal oxidation, x-ray photoelectron spectroscopy

Z rentgensko fotoemisijsko spektroskopijo (angl. XPS) smo preučevali oksidacijo čiste kovine molibdena (Mo) pri sobni temperaturi (angl. RT) z obstreljevanjem z nizkoenergetskim ionskim žarkom kisika znotraj komore z ultravisokim vakuumom. V študiji smo predstavili podrobno karakterizacijo oksidacije čiste kovine Mo in jo primerjali z oksidacijo Mo v CoCrMo zlitini. Po termični oksidaciji Mo v čisti kovini pri sobni temperaturi z odmerki kisika do 5000 L, fotoemisijski spekter Mo 3d lupinskega nivoja ostane skoraj nespremenjen. Nasprotno temu, Mo oksidira z lahkoto v CoCrMo zlitini s postopkom termične oksidacije pri sobni temperaturi. Po drugi strani pa so XPS-spektri, posneti po ionskem obstreljevanju, pokazali kompleksno strukturo, ki jo sestavljajo oksidacijska stanja Mo^{4+}, Mo^{5+} ter Mo^{6+}. Naša študija kaže, da čisti Mo oksidira bolj učinkovito, če je obstreljevan z ioni kisika ali če je vključen v CoCrMo zlitino. Naše rezultate lahko interpretiramo v smislu implementacijske dinamike kisikovih ionov ter večje mobilnosti in reaktivnosti kisikovih atomov v zlitini, v primerjavi s čisto kovino Mo.

Ključne besede: molibden, CoCrMo zlitina, oksidacija z ionskim žarkom, termična oksidacija, rentgenska fotoemisijska spektroskopija

1 INTRODUCTION

The CoCrMo alloy is currently one of the most important materials for biomedical applications due to its superior wear resistance, hardness and high corrosion resistance. It is frequently used for metal-on-metal hip resurfacing joints.[1] The possible release of metal ions due to corrosion is thought to have adverse effects on the surrounding body tissue and ultimately leads to the failure of the implant. The release of the metallic ions into the body tissue can be prevented by the formation of a thin oxide layer on the surface of the implant.[2] Thus, it is important to fully understand the oxidation mechanism of the CoCrMo alloy, which seems to be quite complex[3] and requires a knowledge of the oxidation mechanisms of each metallic component. In the present paper we focus on the oxidation behaviour of molybdenum.

An additional motivation to study the oxidation of molybdenum is related to the variety of applications of molybdenum oxide films, such as heterogeneous chemistry and catalysis, microelectronics and nanotechnology.[4,5] Molybdenum oxides are important catalysts or catalyst precursors exhibiting catalytic properties in both selective oxidation and selective hydrogenation reactions.[6] Also, both pure molybdenum oxides or mixtures with tungsten oxide are promising display materials due to changes of their colour reversibly upon light irradiation.[7] Although molybdenum oxides are used in a variety of applications, the nature and catalytic properties of these materials are not yet fully understood. Since molybdenum has several oxidation states, ranging from +2 to +6, a variety of its oxide compounds may co-exist on the same surface. Therefore, any application of molybdenum oxides requires a detailed knowledge of the molybdenum oxidation states within the sample. Molybdenum oxide surfaces of varying chemical composition, complexity, crystallinity and intercalation have been extensively analyzed, especially with XPS.[8–12] However, the interpretation of the results has not been consistent in the literature due to the complexity of the XPS spectra, particularly when samples include different oxidation states.[13]

It has been shown previously that the Mo surface is quite resistant to the thermal oxidation at temperatures below 300 °C.[8] On the other hand, the ion-bombardment represents an efficient method for the oxidation of different metallic and semiconductor surfaces with controlled amount of oxidation and oxide thickness, even at room temperature.[7–10] In our previous studies, we have shown that oxygen bombardment is more efficient in creating the oxide films on Ni and Co surfaces than oxidation by electrochemical methods or thermal oxidation.[14,15]

In this paper we provide a detailed characterization of the RT oxidation of pure Mo metal by low-energy oxygen-ion bombardment or thermal oxidation in an oxygen atmosphere using X-ray photoelectron spectroscopy (XPS) and compare these results with the oxidation of Mo in the CoCrMo alloy.

2 EXPERIMENTAL PART

The Mo metal foil (M. Woite GmbH, 99.95 % of mass fractions of Mo) and CoCrMo alloy (58 % Co, 32 % Cr, 6 % Mo, 1.3 % Si) samples were first polished with SiC papers of 800–2500 grit and then washed with ethanol and redistilled water. Before any oxidation step, the Mo and CoCrMo surfaces were additionally cleaned within the analytical ultrahigh vacuum (UHV) chamber by cycles of low energy Ar^+ bombardment at room temperature (these samples are referred to as cleaned samples). All the oxidation was conducted in situ in the main chamber of the XPS instrument with a broad beam of 500 eV O_2^+ ions of the typical current density of 2 μA/cm^2. The thermal oxidation was performed by supplying the pure oxygen gas into the UHV chamber to a pressure of 6.5×10^{-4} Pa. In this case, the oxidation dose is expressed in units of Langmuir, defined as 1 L = 1.33×10^{-4} Pa.

Cleaned and oxidised Mo surfaces were characterized by XPS in a SPECS XPS spectrometer equipped with a Phoibos MCD 100 electron analyser and a monochromatized source of Al-K_α X-rays of 1486.74 eV. The typical pressure in the UHV chamber during the XPS analysis was in the 10^{-7} Pa range. For the electron pass energy of the hemispherical electron energy analyser of 10 eV used in the present study, the overall energy resolution was around 0.8 eV. The photoemission spectra were simulated with several sets of mixed Gaussian-Lorentzian functions with Shirley background subtraction using Unifit software.[16]

3 RESULTS AND DISCUSSION

The formation of different Mo-O bonds, related to the different oxidation states of the Mo, can be extracted from the chemical shifts in the photoemission spectra around the Mo 3d core-levels. We start with the thermal oxidation of Mo metal. In **Figure 1** we show several characteristic Mo 3d photoemission spectra taken on the cleaned surface and surfaces oxidized with two different oxygen doses at RT. The cleaned sample shows a characteristic spin-orbit splitting of 3.1 eV of the Mo 3d level to Mo $3d_{3/2}$ and Mo $3d_{5/2}$, at binding energies (BEs) of 231.2 and 228.1 eV, respectively. This doublet is assigned to the metallic state of Mo, Mo^0, in good agreement with the data from the literature.[8,9,11] After thermal oxidation at RT, shown in **Figure 1**, the Mo 3d photoemission remains almost unchanged up to the highest oxygen dose of 5000 L used in this study. This is in agreement with the previous studies of Mo oxidation, in which the thermal oxidation of Mo requires temperatures above 300 °C.[8]

On the other hand, bombardment with O_2^+ ions leads to significant changes in the photoemission spectra, with the development of several new and well-defined peaks around the Mo 3d level. As an example, we show in **Figure 2** several Mo 3d spectra taken from a cleaned Mo surface and surfaces bombarded with 500 eV O_2^+ ions for two different bombardment times of 5 min and 20 min, corresponding to the oxygen doses of 4.75×10^{15} O atoms/cm^2 and 1.5×10^{16} O atoms/cm^2, respectively. Obviously, the oxygen bombardment is more efficient for the formation of some new Mo bonds on the metal surface than the thermal oxidation.

The Mo 3d spectra of ion-bombarded surfaces show a quite complex structure. To identify the different components within that structure we fitted the experimental curves from **Figure 2** with the set of Voigt functions, as shown in **Figure 3**. We first note that the deconvolution

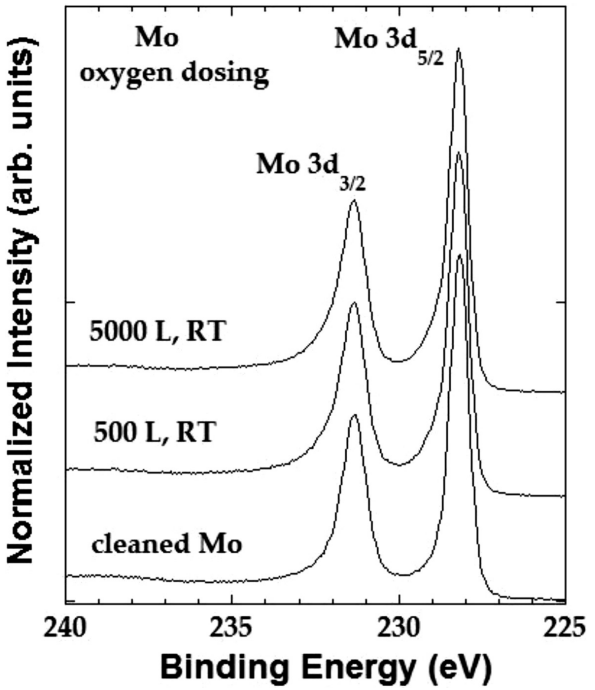

Figure 1: Mo 3d core-level photoemission spectra from a cleaned molybdenum surface and surfaces oxidized at room temperature (RT) with oxygen doses of 500 L and 5000 L

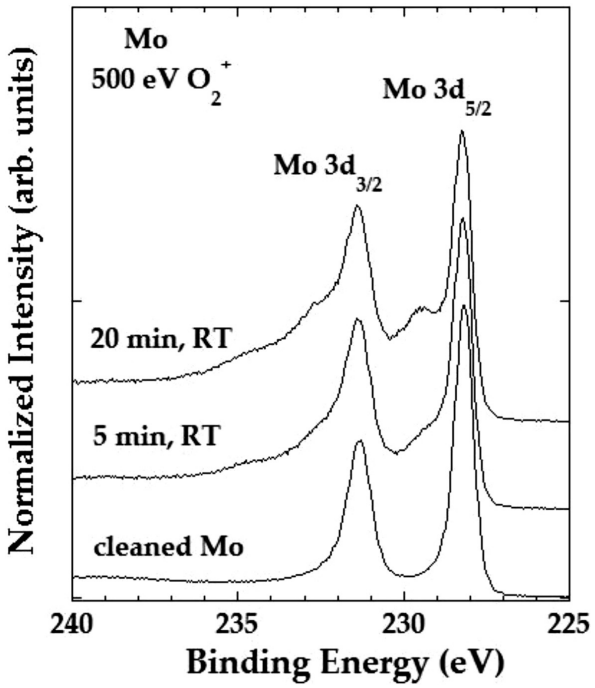

Figure 2: Mo 3d core-level photoemission spectra from a cleaned molybdenum surface and surfaces bombarded with 500 eV O_2^+ ions for 5 min and 20 min at room temperature (RT)

of the Mo 3d spectrum from the cleaned sample is dominated by the Mo $3d_{5/2}$–Mo $3d_{3/2}$ doublet assigned to the Mo^0 emission. However, a good fit of the experimental curve is obtained only by introducing two small additional doublets, with the main Mo $3d_{5/2}$ components at 229.4 eV and 230.7 eV, respectively. We assign these components to the intrinsic oxygen, most likely in the form of MoO_2 or Mo_2O_5, present in the Mo foil that has not been removed with our cleaning procedure.

Deconvolution of the spectrum from a sample bombarded to a high ion fluence of 1.5×10^{16} O atoms/cm^2 (i.e., for the 20-minute bombardment time, shown in **Figure 3**), exhibits three well-resolved doublets in addition to the Mo^0 doublet, with the dominant Mo $3d_{5/2}$ peaks at BEs of 229.4, 230.8 and 232.2 eV, respectively. We assign these additional components to the emission from MoO_2, Mo_2O_5 and MoO_3, respectively, i.e., from the Mo^{4+}, Mo^{5+} and Mo^{6+} oxidation states of Mo, respectively, in good agreement with the data from the literature.[8,9,11]

Turning now to the oxidation of the CoCrMo alloy shown in **Figure 4**, we first note that the Mo 3d XPS spectrum of the cleaned CoCrMo sample is almost identical to the spectrum from the cleaned Mo metal foil from **Figure 1**. Furthermore, the thermal oxidation of Mo at RT in the alloy is more efficient than the thermal oxidation of the pure metal at RT to the same dose of 5000 L, clearly showing the formation of MoO_2 (Mo^{4+} oxidation state), Mo_2O_5 (Mo^{5+} oxidation state) and MoO_3 (Mo^{6+} oxidation state). These oxidation states are represented in **Figure 4** by three fitting doublets, in addition to the Mo^0 doublet. Finally, the ion-bombardment of CoCrMo shows the different oxide structure of Mo, compared to the metallic molybdenum. Now the contribution from the Mo^{6+} states dominates the spectrum, as indicated in **Figure 4** for the sample bombarded with 500 eV O_2^+ ions for 20 min. At the same time, the

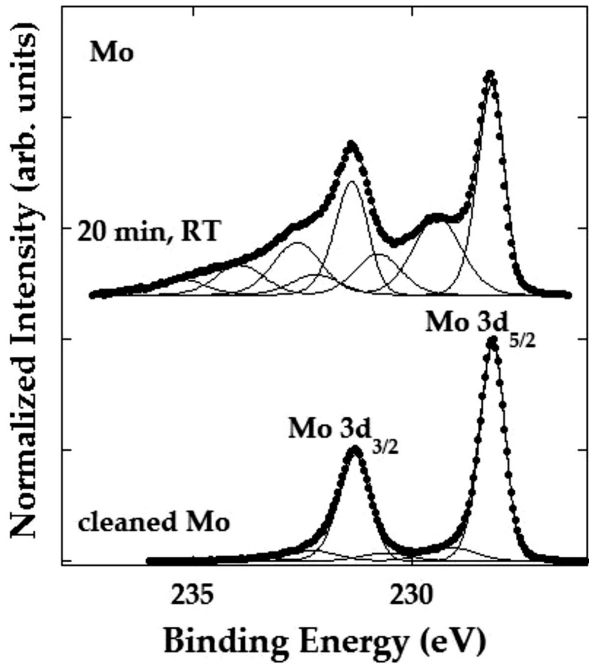

Figure 3: The deconvoluted Mo 3d spectra from a cleaned molybdenum sample and a sample exposed to 500 eV O_2^+ ions at RT for 20 min; solid lines represent product of Gaussians and Lorentzians, while closed circles represent experimental XPS spectra

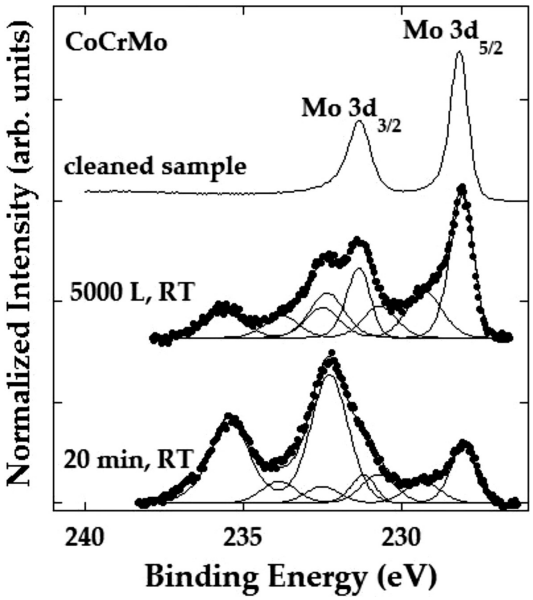

Figure 4: Comparison of Mo 3d core-level XPS spectra from a cleaned CoCrMo surface and surfaces oxidized at RT with 5000 L of oxygen or bombarded with 500 eV O_2^+ ions for 20 min (closed circles); the three fitting doublets of each spectrum (solid lines, representing product of Gaussians and Lorentzians) correspond to the emission from MoO_2, Mo_2O_5 and MoO_3

Mo^0 component in the spectrum is greatly reduced. We stress here that the Mo^0 peak is present in all ion-bombarded or thermally oxidised samples, indicating the formation of very thin oxide films on the surface. In such case, the XPS signal includes a contribution from the underlying metallic molybdenum.

The O 1s photoemission (not shown) was also recorded from all the oxidized surfaces. While the intensity of the oxygen peaks increases with the bombardment time or dose of oxygen, indicating the increase of oxygen concentration within the surface layer, the shape of O 1s peak does not show any significant changes. It is well known from the literature that the O 1s binding energies of many metal oxides fall within a very narrow range and it is not possible to separate the individual oxide contributions.[17] The main O 1s peak, observed in our spectra around 530 eV, is usually assigned to all metal oxides, while the small shoulder, observed in our spectra around 531.5 eV, is assigned to the surface hydroxide groups or oxygen defects.[18,19]

We conclude from the comparison of our results from **Figures 1** to **4** that the ion bombardment provides a more efficient oxidation process for molybdenum than the thermal oxidation, while Mo oxidizes more efficiently in the CoCrMo alloy compared to the pure Mo metal. We attribute this behaviour to the enhanced mobility and reactivity of oxygen atoms in the alloy, compared to the pure Mo metal. On the other hand, in contrast to thermal processes, the ion-induced oxidation eliminates the need for elevated temperatures and bypasses several thermally activated processes, such as absorption, dissociation, diffusion or bond breaking. The atomic collisions between the impinging oxygen and matrix atoms create different defects within the material, which are known to enhance the mobility and reactivity of oxygen anions and metal cations.[20–23] Our measurements of ion-bombarded samples show, indeed, the effects expected from the radiation-enhanced oxidation, as observed previously for some other metals and semiconductors.[15,20,21,23]

4 CONCLUSION

The thermal oxidation of Mo in pure Mo metal is not efficient at RT. However, Mo oxidises quite easily at RT within the CoCrMo alloy, showing characteristic contributions from the Mo^{4+}, Mo^{5+} and Mo^{6+} oxidation states. The presence of Co and Cr reduces the surface barrier and enables a more efficient intake of oxygen within the sample.

On the other hand, the ion-induced oxidation of Mo is quite efficient at RT in both the Mo metal and the CoCrMo alloy. It is explained by the radiation-enhanced oxidation of Mo, as observed previously for some other metals and semiconductors. Again, contributions from the Mo^{4+}, Mo^{5+} and Mo^{6+} oxidation states are present in all the oxides with the dominant contribution from the Mo^{6+} oxidation states for the high implantation doses of oxygen. Finally, the RT ion-induced oxidation of Mo is more efficient than thermal oxidation in both the CoCrMo alloy and the pure Mo metal samples.

Acknowledgements

This work was supported by the European Fund for Regional Development and the Ministry of Science, Education and Sports of the Republic of Croatia under the project Research Infrastructure for Campus-Based Laboratories at the University of Rijeka (grant number RC.2.2.06-0001); and the European Social Fund for Human Resources Development under the project SIZIF (grant number HR.3.2.01-0310).

5 REFERENCES

[1] J. Black, Biological Performance of Materials, Fundamentals of Biocompatibility, 3rd ed., New York 1999

[2] M. Metikoš-Huković, R. Babić, Some aspects in designing passive alloys with an enhanced corrosion resistance, Corrosion Science, 51 (**2009**), 70–75, doi:10.1016/j.corsci.2008.10.004

[3] I. Milošev, H.-H. Strehblow, The composition of the surface passive film formed on CoCrMo alloy in simulated physiological solution, Electrochimica Acta, 48 (**2003**), 2767–2773, doi:10.1016/S0013-4686(03)00396-7

[4] V. E. Henrich, P. A. Cox, The Surface Science of Metal Oxides, Cambridge University Press, Cambridge, 1996

[5] B. M. Weckhuysen, D. E. Keller, Chemistry, spectroscopy and the role of supported vanadium oxides in heterogeneous catalysis, Catal. Today, 78 (**2003**) 25

[6] L. E. Firment, A. Ferretti, Stoichiometric and oxygen deficient MoO_3(010) surfaces Stoichiometric and oxygen deficient MoO_3(010) surfaces Stoichiometric and oxygen deficient MoO_3(010) surfaces Stoichiometric and oxygen deficient MoO_3(010) surfaces Stoihiometric and oxygen deficient MoO_3 (010) surfaces, Surf. Sci. 129 (1983), 155, doi:10.1016/0039-6028(83)90100-0

[7] P. A. Spevack, N. S. McIntyre, A Raman and XPS Investigation of Supported Molybdenum Oxide Thin Films, 1, Calcination and Reduction Studies, J. Phys. Chem., 97 (**1993**), 11020–11030, doi:10.1021/j100144a020

[8] S. I. Castañeda, I. Montero, J. M. Ripalda, N. Diaz, L. Galán, F. Rueda, X-ray photoelectron spectroscopy study of low-temperature molybdenum oxidation process, Journal of Applied Physics, 85 (**1999**), 8415–8418, doi: 10.1063/1.370690

[9] N. V. Alov, Surface oxidation of metals by oxygen ion bombardment, Nucl. Instr. and Meth. in Phys. Res. B, 256 (**2007**), 337–340, doi:10.1016/j.nimb.2006.12.023

[10] L. D. Lopez-Carreno, G. Benitez, L. Viscido, J. M. Heras, F. Yubero, J. P. Espinos, A. R. Gonzalez-Elipe, Oxidation of Molybdenum Surfaces by Reactive Oxygen Plasma and O_2 Bombardment: an Auger and XPS Study, Surf. Interface Anal., 26 (**1998**), 235–241, doi: 10.1002/(SICI)1096-9918(199804)

[11] J. Baltrusaitis, B. Mendoza-Sanchez, V. Fernandez, R. Veenstra, N. Dukstiene, A. Roberts, N. Fairley, Generalized molybdenum oxide surface chemical state XPS determination via informed amorphous sample model, Applied Surface Science, 326 (**2014**), 151–161, doi:10.1016/j.apsusc.2014.11.077

[12] J. Światowska-Mrowiecka, S. de Diesbach, V. Maurice, S. Zanna, L. Klein, E. Briand, I. Vickridge, P. Marcus, Li-ion intercalation in thermal oxide thin films of MoO_3 as studied by XPS, RBS, and NRA, The Journal of Physical Chemistry C, 112 (**2008**), 11050–11058, doi: 10.1021/jp800147f

[13] B. Mendoza-Sánchez, T. Brousse, C. Ramirez-Castro, V. Nicolosi, P. S. Grant, An investigation of nanostructured thin film α-MoO_3 based supercapacitor electrodes in an aqueous electrolyte, Electrochimica Acta, 91 (**2013**), 253–260, doi:10.1016/j.electacta.2012.11.127

[14] M. Petravic, M. Varasanec, R. Peter, I. Kavre, M. Metikos-Hukovic, Y.-W. Yang, Electronic structure of nitinol surfaces oxidized by low-energy ion bombardment, J. Appl. Phys., 115 (**2014**), 243703–243708, doi:10.1063/1.4884835

[15] I. Saric, R. Peter, M. Petravic, Oxidation of Cobalt by Oxygen Bombardment at Room Temperature, J. Phys. Chem. *C*, (**2016**), 120 (39), 22421–22425, doi:10.1021/acs.jpcc.6b07139

[16] R. Hesse, T. Chassé, R. Szargan, Peak Shape Analysis of Core Level Photoelectron Spectra Using Unifit for Windows, Fresenius, J. Anal. Chem., 365 (**1999**), 48–54, doi:10.1007/s002160051443

[17] M. C. Biesinger, L. W. M. Lau, A. R. Gerson, R. St. C. Smart, Resolving surface chemical states in XPS analysis of first row transition metals, oxides and hydroxides: Sc, Ti, V, Cu and Zn, Appl. Surf. Sci., 257 (**2010**), 887–898, doi:10.1016/j.apsusc.2010.07.086

[18] M. C. Biesinger, B. P. Payne, A. P. Grosvenor, L. W. M. Lau, A. R. Gerson, R. St. C. Smart, Resolving surface chemical states in XPS analysis of first row transition metals, oxides and hydroxides: Cr, Mn, Fe, Co and Ni, Appl. Surf. Sci., 257 (**2011**), 2717–2730, doi:10.1016/j.apsusc.2010.10.051

[19] S. C. Petitto, E. M. Marsh, G. A. Carson, M. A. Langell, Cobalt oxide surface chemistry: The interaction of CoO(1 0 0), Co3O4(1 1 0), and Co3O4(1 1 1) with oxygen and water, Journal of Molecular Catalysis A, Chemical, 281 (**2008**), 49–58, doi:10.1016/j.molcata.2007.08.023

[20] J. S. Williams, M. Petravic, B. G. Svensson, M. Conway, Oxidation of Silicon by Low-Energy Oxygen Bombardment, J. Appl. Phys., 76 (**1994**), 1840–1846, doi:10.1063/1.357704

[21] J. S. Williams, J. M. Poate, Ion Implantation and Beam Processing, Academic Press, Sydney, Australia, 1984

[22] G. J. Koel, P. J. Gellings, Contribution of Different Types of Point-Defects to Diffusion in CoO and NiO during Oxidation of Metals, Oxid. Met., 5 (**1972**), 185–203, doi:10.1007/BF00609658

[23] I. Saric, R. Peter, I. Kavre, I. J. Badovinac, M. Petravic, Oxidation of Nickel Surfaces by Low Energy Ion Bombardment, Nucl. Instrum. Meth. B, 371 (**2016**), 286–289, doi:10.1016/j.nimb.2015.08.090

UDK 621.311.243:621.365.3:621.38
Original scientific article/Izvirni znanstveni članek

ISSN 1580-2949
MTAEC9, 51(4)623(2017)

A CARBON-NANOTUBES COUNTER ELECTRODE FOR FLEXIBLE DYE-SENSITIZED SOLAR CELLS

ELEKTRODA IZ OGLJIKOVIH NANOCEVK ZA TANKOPLASTNE BARVNO OBČUTLJIVE SONČNE CELICE

Aleksandra Drygała[1], Leszek Adam Dobrzański[1], Marzena Prokopiuk vel Prokopowicz[1], Marek Szindler[1], Krzysztof Lukaszkowicz[1], Marian Domański[2]

[1]Institute of Engineering Materials and Biomaterials, Silesian University of Technology, Konarskiego St. 18a, 44-100, Gliwice, Poland
[2]Centre of Polymer and Carbon Materials, Polish Academy of Sciences, M.Curie-Skłodowskiej St. 34, 41-819, Zabrze, Poland
aleksandra.drygala@polsl.pl

Prejem rokopisa – received: 2016-07-15; sprejem za objavo – accepted for publication: 2017-01-20

doi:10.17222/mit.2016.206

Dye-sensitized solar cells (DSSCs) are an attractive alternative to conventional crystalline silicon solar cells because of their low-cost, relatively high photon-to-current conversion efficiency for low energy consumption and simple fabrication process. The dye-sensitized solar cell consists of the following components: a photoanode, a dye, an electrolyte, and a counter electrode. The counter electrode is a crucial element, in which the triiodide is reduced to iodide by electrons flowing through the external circuit. Platinum is the most used material for a counter electrode in DSSCs, due to its electrocatalytic activity towards I_3^- reduction. However, the use of platinum may not be a suitable option because of its high cost. Additionally, to achieve widespread application of next-generation photovoltaics, it is important to develop flexible devices. Given this, the paper presents the influence of mechanical stress arising from the bending of a flexible substrate on the morphology, the resistance of counter electrode based on carbon nanotubes as well as the electrical properties of dye-sensitized solar cells.

Keywords: photovoltaics, dye-sensitized solar cells, flexible substrates, counter electrode, carbon nanotubes

Fleksibilne tankoslojne barvno občutljive sončne celice (angl. DSSCs) so privlačna alternativa konvencionalnim kristalnim silicijevim sončnim celicam zaradi nizke cene in relativno visoke učinkovitosti pretvorbe foton-tok, z nizko porabo energije in enostavnim postopkom procesom proizvodnje izdelave. Tankoplastna sončna celica je sestavljena iz naslednjih komponent: fotoanode, barvila, elektrolita in tokovne elektrode. Tokovna elektroda je ključni element, na kateri se trijodid reducira na jodid z elektroni, ki tečejo skozi zunanji tokokrog. V solarnih celicah je platina najpogosteje uporabljan material za tokovne elektrode zaradi svoje elektrokatalitične aktivnosti (redukcija I_3^- ionov). Zaradi visoke cene pa uporaba platine vendarle ni optimalna izbira. Torej, da bi dosegli široko uporabo naslednjih generacij fotovoltaike je pomembno razvijati fleksibilne naprave. Članek predstavlja vpliv mehanskih napetosti zaradi upogibanja fleksibilnega substrata na morfologijo in odpornost tokovne elektrode iz ogljikovih nanocevk, kot tudi električne lastnosti tankoslojne sončne celice.

Ključne besede: fotovoltaika, tankoslojne barvno občutljive sončne celice, fleksibilni substrati, tokovna elektroda iz ogljikovih nanocevk

1 INTRODUCTION

The utilisation of renewable energies is of significant importance because of the increase in fossil energy costs in combination with carbon dioxide reduction preventing global warming. The importance of solar energy can be considered as a sustainable energy that may successfully satisfy a part of the energy demand of future generations.[1,2] Photovoltaics seems to be the most promising new electric energy source. What is needed to transform solar power from a marginalised technology to a mainstream source of energy is cheaper materials. At present, the main scientific effort is made to lower the production costs of PV systems and improve their parameters. It is believed that in the not so distant future, thanks to new materials, solar cells could be ubiquitous and one of the cleanest energy sources all over the world. [2,3] There are many publications about the methods of shaping the surface and structure of materials to improve their properties.[4–12] Some materials exhibit a property known as the photovoltaic effect that causes them to absorb photons of light and excite an electron or other charge carrier to a higher-energy state. When these free electrons are captured, an electric current results that can be used as electricity. In recent years, most of the solar cells are based on a silicon substrate.[11–15] Although the cost per peak watt of crystalline silicon solar cells has significantly dropped, it is still expensive compared to the conventional grid electricity resources.[15]

Dye-sensitized solar cells (DSSCs) are an inexpensive alternative to the conventional p-n junction solar cells. The use of DSSCs is one of the most promising approaches towards the realisation of both high performance and low cost, thanks to their low material cost and ease of manufacturing.[16–18] One of the challenges of this technology is, however, expensive, the heavy and non-elastic glass substrate typically used in DSSCs. Therefore, scientists transfer the DSSC technology from glass substrates to lightweight, cost-efficient, and flexible plastic foils and metal sheets. Additionally, flexible dye-sensitized solar cells built on elastic substrates have

attracted great industrial interest because they can be roll-to-roll printed, which is well suited for scale mass production (accelerate production and reduce cost).[19–21]

In this paper we report on flexible DSSCs based on a carbon-nanotubes counter electrode. The influence of mechanical stress arising from the bending of the flexible substrate on the quality and resistance of the deposited layers was investigated.

A fundamental property of insulators is resistivity. The resistivity can be used to determine the dielectric breakdown, dissipation factor, moisture content, mechanical continuity and other important properties of the material. The volume resistivity of some materials, such as sapphire and Teflon®, can be as high as 10^{16} to 10^{18} Ω·cm. Because of such large magnitudes, measuring the resistivity of insulators can be difficult unless proper test methods and instrumentation are used. One test method often used for measuring the resistivity of materials is ASTM D-257, "DC Resistance or Conductance of Insulating Materials." Instruments called electrometers are used to make this measurement because of their ability to measure small currents. Two methods are mostly used to measure high resistance, i.e., the constant-voltage method and the constant-current method.[22–23]

In the constant-voltage method, a known voltage is sourced and a picoammeter or electrometer ammeter is used to measure the resulting current. The basic configuration of the constant-voltage method is shown in **Figure 1**. In this method, a constant-voltage source, *V*, is placed in series with the unknown resistor, *R*, and an electrometer ammeter, *A*. Since the voltage drop across an electrometer ammeter is negligible, essentially all the voltage appears across *R*. The resulting current is measured by the ammeter and the resistance is calculated using Ohm's law, R=V/I.[23–24]

In the constant-current method, a constant current is forced through the unknown resistance and the voltage drop across the resistance is measured. The basic configuration for the constant-current method is shown in **Figure 2**. Current from the constant-current source, *I*, flows through the unknown resistance, *R*, and the voltage drop is measured by the electrometer voltmeter, *V*. Using this method, resistances up to about 10^{14} Ω can be measured. Even though the basic procedure seems simple enough, some precautionary measures must be taken.[22–24]

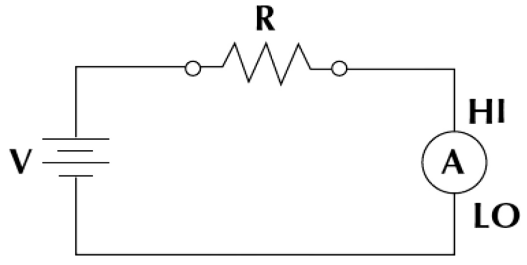

Figure 1: The constant-voltage method for measuring resistance [22–24]

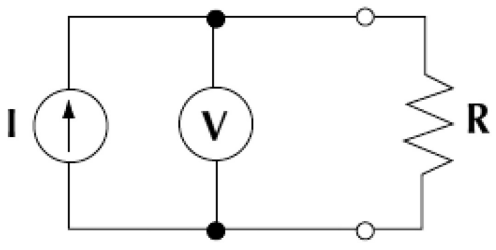

Figure 2: The constant-current method for measuring resistance [22–24]

One of the components in dye-sensitized solar cells is the counter electrode. The role of the counter electrode is to act as a catalyst for reducing the redox species, which are the mediators for regenerating the sensitizer after the electron injection, or for collecting the hole from the hole-transporting materials.[25–28] This paper presents the influence of mechanical stress arising from the bending of a flexible substrate on morphology, the resistance of the counter electrode based on carbon nanotubes with the addition of poly(3,4-ethylenedioxythiophene)-poly(styrenesulfonate) PEDOT:PSS and polyvinylpyrrolidone PVP as well as electrical properties of dye-sensitized solar cells.

2 EXPERIMENTAL PART

Multi-walled carbon nanotubes (MWCNTs) were dispersed in anhydrous ethyl alcohol using ultrasonic dispersion methods. Then the poly(3,4-ethylenedioxythiophene)-poly(styrenesulfonate) PEDOT:PSS was added. Carbon nanotubes are materials that strongly agglomerate. Therefore, they were exposed to dispersion for 45 min. To prevent the aggregation of carbon nanotubes, the mixture of 95 % of mass fractions of active material and 5 % of mass fractions of polyvinylpyrrolidone PVP was used. Using a spin coating methods, the mixture was deposited on the polymer polyethylene terephthalate (PET) with a thin layer of indium tin oxide (ITO) and dried at 60 °C for 25 min. The platinum thin film was deposited on a PET foil in a device based on the sputtering method (Physical Vapour Deposition – PVD) in an Ar atmosphere. The sputtering time was 90 s, the current was 50 mA and the voltage was 50 V.

The photoelectrode was prepared on a flexible ITO-PEN substrate by a doctor-blade technique using a commercially available TiO_2 nanocrystalline powder P 25 Degussa mixed with ethyl alcohol and distilled water. After that the films were sintered at 120 °C for 4 h. The photoelectrodes were immersed in the anhydrous ethanol solution of 0.5-mM N3 (Cis-diisothiocyanato-bis(2,2'-bipyridyl-4,4'-dicarboxylic acid) ruthenium(II), Solaronix) for 24 h at room temperature. The internal space between the photoanode and the counter electrode was controlled at 25 μm by Surlyn foil (Solaronix). The photoanode and counter electrode were sealed with a 25-μm-thick Surlyn frame at 100 °C for 15 s. After sealing the cells were filled with the electrolyte solution

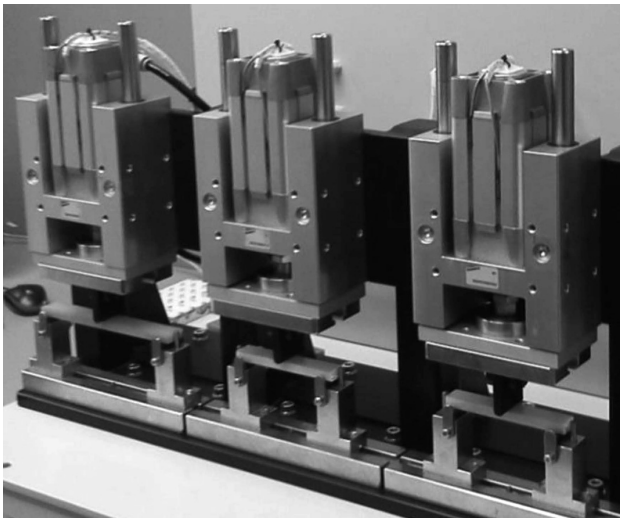

Figure 3: Tester for measuring the bending strength of polymeric materials

with redox couple I^-/I_3^- through the hole in a counter electrode.

The influence of the mechanical stress arising from the bending of the flexible substrate on the quality and resistance of counter electrode based on carbon nanotubes with the addition of PEDOT:PSS and PVP. The samples were bent with the tester for measuring the bending strength of polymeric materials (**Figure 3**).

The morphology of the counter electrodes based on platinum and carbon nanotubes deposited on a PET foil was performed using a scanning electron microscope (Zeiss Supra 35). In order to obtain images of the surface topography, the detection of secondary electrons by the detector In Lens was used.

The resistance of the prepared samples was measured using a Keithley meter. The meter was connected to a specialised adapter for testing thin films. This was in

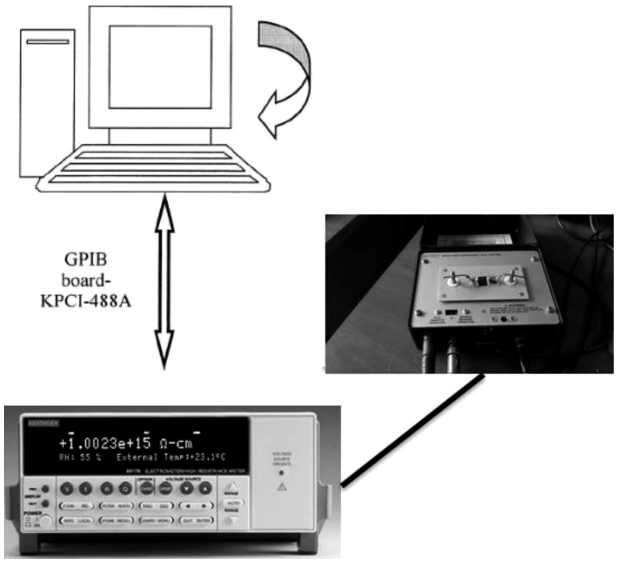

Figure 4: General measurement system set-up

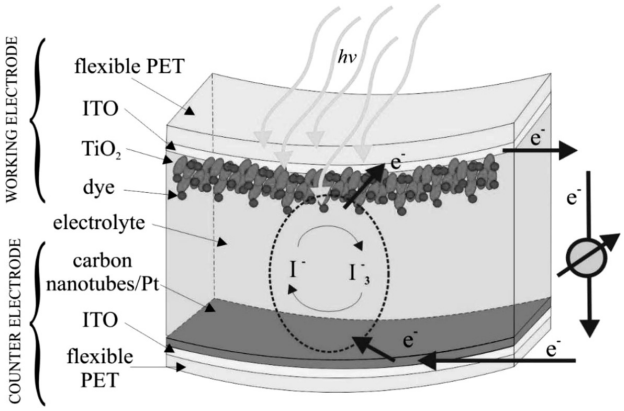

Figure 5: Construction of dye-sensitized solar cell

order to better contact and more accurately measure on the edge of the layers applied silver contacts connected to external electrodes. The measurement block diagram used for our measurements is presented in **Figure 4**.

Resistance measurements were made using a constant-voltage measurement in real time with the current running. The chosen method allows us to obtain reliable results only for layers deposited on a polymer foil. It can be assumed that the resistance of the layers is the same or similar, regardless of the substrate.

Electrical parameters of manufactured flexible dye-sensitized solar cells with ca ounter electrode based on platinum and carbon nanotubes with the addition of PEDOT:PSS and PEDOT:PSS/PVP were characterised by measurements of I-V illuminated characteristics on PV Test Solutions Tadeusz Żdanowicz Solar Cell I-V Tracer System under standard test condition (AM 1.5, 1000W/m^2). The level of irradiance was determined using the reference cells with a KG5 filter.

The construction of flexible dye-sensitized solar cells is illustrated in **Figure 5**.

The structure of produced DSSCs consists of components:

- working electrode – dye molecule (N3) coated nanocrystalline porous TiO_2 deposited on PET/ITO substrate,
- counter electrode – carbon nanotubes with the addition of PEDOT:PSS and PVP deposited on PET/ITO substrate,
- electrolyte (Iodolyte Z-150, Solaronix) containing an I^-/I_3^- redox couple.

3 RESULTS AND DISCUSSION

Figure 6 shows the morphology of the PET/ITO foil coated with the Pt film. It illustrates that the substrate is uniformly covered with the Pt film.

A detailed inspection of scanning electron microscope micrographs of PET/ITO foils coated with the Pt film after bending revealed microcracks and crevices (**Figure 7**). This indirectly indicates that platinum film

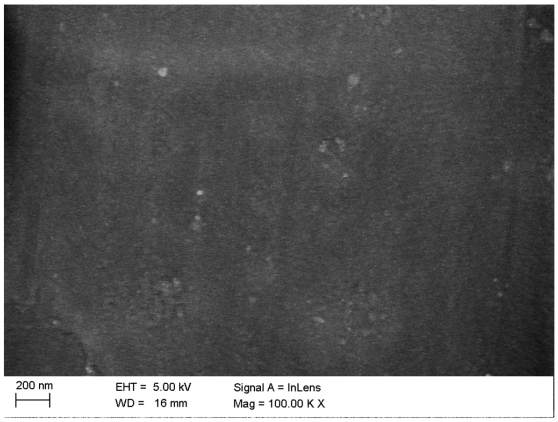

Figure 6: SEM images of platinum on PET/ITO foil

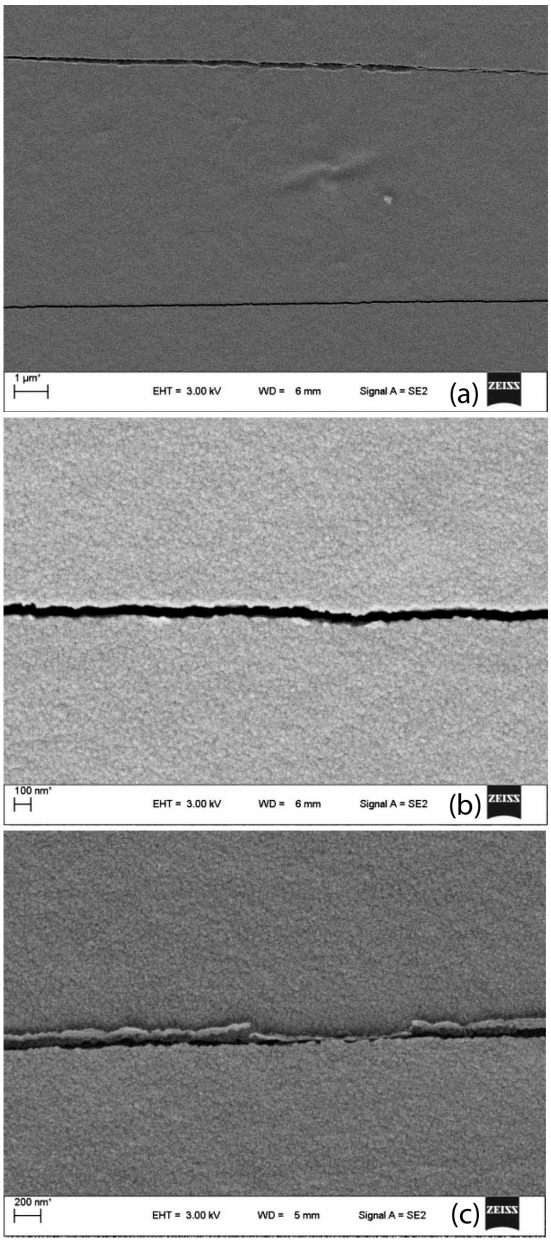

Figure 7: SEM images of platinum on PET/ITO foil after 100 bending cycles

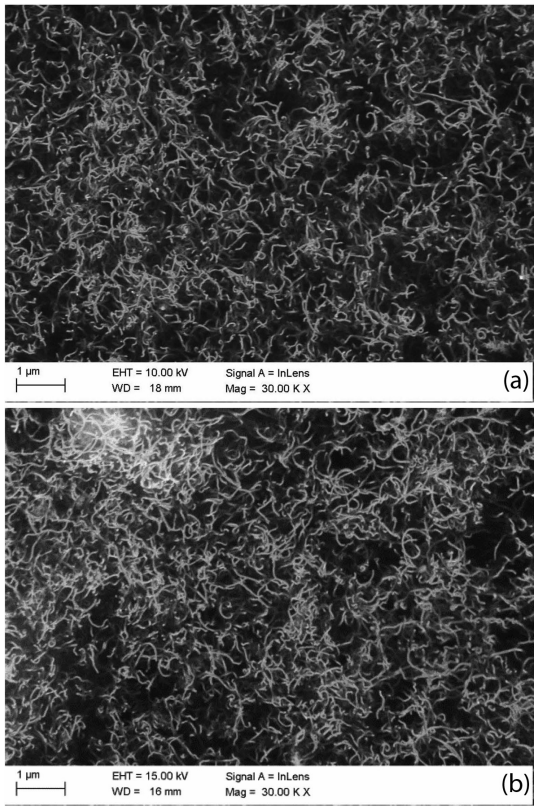

Figure 8: SEM images of counter electrode based on carbon nanotubes with addition: a) PEDOT:PSS/PVP, b) PEDOT:PSS after 100 bending cycles

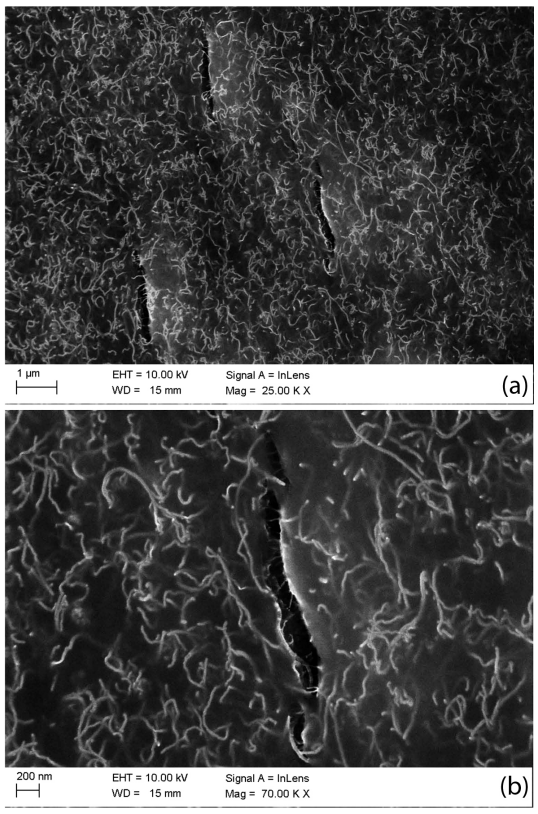

Figure 9: SEM images of counter electrode based on carbon nanotubes with addition PEDOT:PSS/PVP after 100 bending cycles

can have poor properties for catalytic activity at the counter electrode and electrical conductivity for the charge transfer. The cracks are formed mainly along the bending line. Moreover, the PET foil coated with ITO and Pt after 100 bending cycles in some places delaminates and breaks away from the elastic substrate (**Figure 7**).

Figure 8 shows the SEM images of a counter electrode based on carbon nanotubes with the addition of PEDOT:PSS and PEDOT:PSS/PVP. The addition of 5 % of mass fractions of polyvinylpyrrolidone PVP prevents the agglomeration of carbon nanotubes. It was observed that, after the same number of bending cycles, the surface of the counter electrode based on carbon nanotube with the addition of PEDOT:PSS/PVP is much more damaged than the surface of the counter electrode without PVP (**Figures 9** and **10**). However, the amount of damage and the size of the defects in the carbon-nanotubes counter electrode is much smaller than in the platinum foil. It can be seen that carbon nano-elements reduce the spread of cracks.

The resistance of the carbon-nanotubes thin films with the addition of the PEDOT:PSS polymer was about $4 \cdot 10^3$ Ω (**Figure 11**). The appearance of small cracks registered using a scanning electron microscope did not affect significantly the results of electrical measurements. Mechanical stress caused by the bending of the substrate slightly affected the resistance of the tested layer. After 50 cycles of the bending, the resistance value increased to about $5.08 \cdot 10^3$. Further bending does not result in significant changes in resistance and maintained at the similar level.

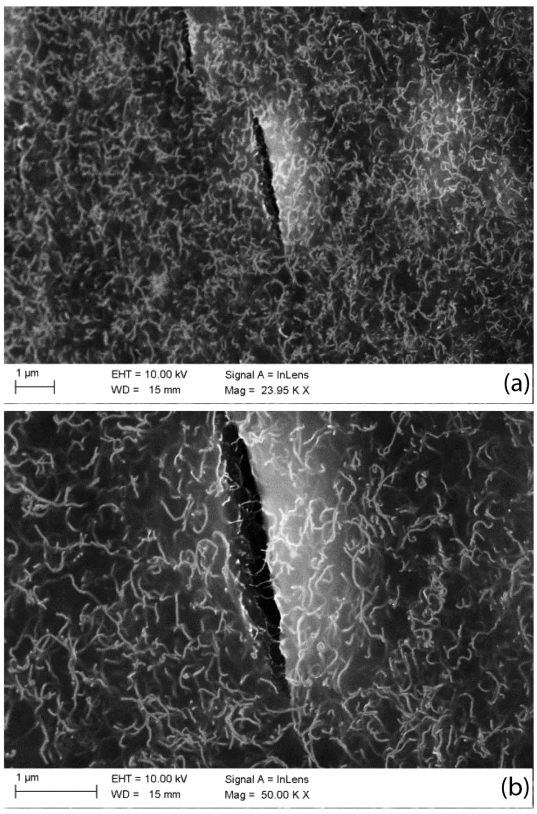

Figure 10: SEM images of counter electrode based on carbon nanotubes with addition PEDOT:PSS after 100 bending cycles

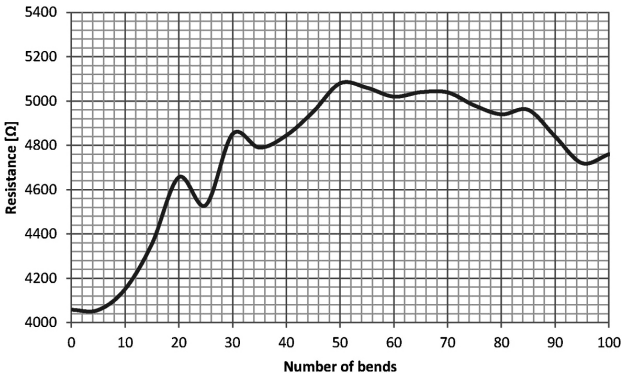

Figure 11: Influence of mechanical stress on the resistance of carbon-nanotubes thin films with the addition of PEDOT:PSS deposited on a PET foil

The addition of PVP polymer, which prevents agglomeration, caused a significant deterioration of the resistance to about $7 \cdot 10^{10}$ Ω (**Figure 12**). The results of the electrical properties measurement are correlated with the surface studies conducted on a scanning electron microscope. The impact of mechanical stress increased. The appearance of micro-cracks after 100 cycles of bending of the substrate increased the resistance to about $1.6 \cdot 10^{11}$ Ω. Therefore, registered increases the resistance by more than one order of magnitude.

Table 1: Conversion efficiency of dye-sensitized solar cells with counter electrodes based on platinum and carbon nanotubes with the addition of PEDOT:PSS and PEDOT:PSS/PVP

Number of bending cycles	Type of counter electrode		
	Platinum	Carbon nanotubes with the addition of PEDOT:PSS/PVP	Carbon nanotubes with the addition of PEDOT:PSS
0	4.02 %	3.61 %	3.42 %
100	2.42 %	2.65 %	2.96 %

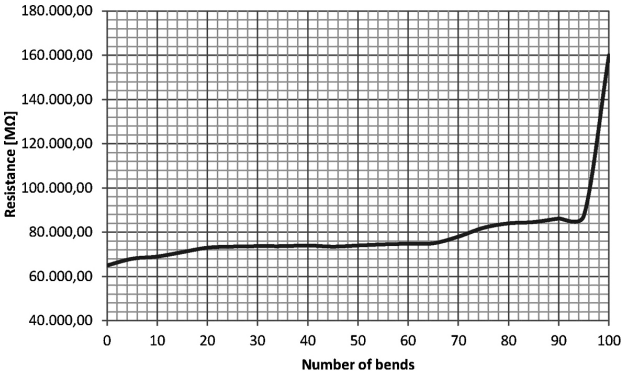

Figure 12: Influence of mechanical stress on the resistance of carbon-nanotubes thin films with the addition of PEDOT:PSS and PVP deposited on a PET foil

The efficiency of dye-sensitized solar cells with different types of counter electrodes is presented in Table 1. These results indicate that the photovoltaic properties of dye-sensitized solar cells after bending is decreased. Platinum is a preferred material for the counter electrode because of its high conductivity and catalytic activity. However, dye-sensitized solar cells based on a platinum counter electrode subjected to the impact of mechanical stress demonstrate the lowest efficiency. This is the result of damage introduced into the platinum thin film deposited by a sputtering method and its delamination from the flexible substrate (**Figure 7**). These damages have a detrimental influence on the proper working of the solar cell and reduce its properties, which could be a consequence of poorer charge transfer. It can be observed that the carbon-nanotubes counter electrode is more resistant to bending compared to the platinum counter electrode.

4 CONCLUSION

Flexible dye-sensitized solar cells built on elastic substrates have attracted great interest as they are lightweight and can be roll-to-roll printed to accelerate production and reduce costs. The study showed the possibility of replaceming the standard platinum counter electrode by carbon nanotubes deposited on the elastic substrate. In the frame of this work, we investigated the influence of mechanical stress arising from the bending of a flexible substrate on the morphology, the resistance of the counter electrode based on carbon nanotubes as well as the electrical properties of dye-sensitized solar cells.

It was found that the bending has a significant influence on the morphology of platinum layer deposited on a PET foil. It was shown that on the platinum surface after bending cracks were formed and in some places the layer was delaminated and broken away from the substrate. The addition of PVP to the counter electrode based on carbon nanomaterials with PEDOT:PSS prevents agglomeration of carbon nanotubes, but after a bending test the resistivity of the prepared layer and electrical properties of produced dye-sensitized solar cells are reduced. The amount of damage and the size of defects in the carbon nanotubes counter electrode is much smaller than in the platinum foil. Moreover, it can be seen that carbon nano-elements reduce the spread of cracks. Mechanical stress slightly effects the resistance of studied carbon nanotubes layers with the addition of PEDOT:PSS. Only the addition of the PVP polymer, which prevents agglomeration, caused a significant deterioration of the resistance as well as the increased influence of mechanical stress. These damages have a detrimental influence on the operation of solar cells and reduce their efficiency.

Acknowledgements

The project was funded by the National Science Centre on the basis of the contract No. DEC-2013/09/B/ST8/02943. This publication was co-financed by the Ministry of Science and Higher Education of Poland as the statutory financial grant of the Faculty of Mechanical Engineering SUT.

5 REFERENCES

[1] J. Jarman, E. Khalil, E. Khalaf, Energy Analyses of Thermoelectric Renewable Energy Sources. Open Journal of Energy Efficiency, 2 (**2013**), 143–153 doi:10.4236/ojee.2013.24019

[2] S. Al-Hallaj, K. Kiszynski, Renewable Energy Sources and Energy Conversion Devices, Green Energy and Technology, Springer-Verlag London, (2011) 9–29, doi:10.1007/978-1-84628-467-0_2

[3] V. V. Tyagi, Nurul A. A. Rahim, N. A. Rahim, J. A. L. Selvaraj, Progress in solar PV technology: Research and achievement, Renewable and Sustainable Energy Reviews 20 (**2013**), 443–461, doi:10.1016/j.rser.2012.09.028

[4] L. A. Dobrzański, T. Tański, A. Dobrzańska-Danikiewicz, E. Jonda, M. Bonek, A. Drygała, Structures, properties and development trends of laser-surface-treated hot-work steels, light metal alloys and polycrystalline silicon, Laser surface engineering. Processes and applications, Book Series: Woodhead Publishing Series in Electronic and Optical Materials, 65 (**2015**), 3–32, doi:10.1016/B978-1-78242-074-3.00001-5

[5] S. Lesz, R. Szewczyk, D. Szewieczek, A. Bieńkowski: The structure and magnetoelastic properties of the Fe-based amorphous alloy with Hf addition, Journal of Materials Processing Technology, 157–158 (**2004**), 743–748, doi:10.1016/j.jmatprotec.2004.07.133

[6] K. Drabczyk, G. Kulesza-Matlak, A, Drygała, M, Szindler, M. Lipiński, Electroluminescence imaging to determining the influence of metallization parameters for solar cells metallic contacts, Solar Energy, 126 (**2016**), 14–21, doi:10.1016/j.solener.2015.12.029

[7] A. Zieliński, G. Golański, M. Sroka: Influence of long-term ageing on the microstructure and mechanical properties of T24 steel, Materials Science & Engineering A, 682 (**2017**), 664–672. doi:10.1016/j.msea.2016.11.087

[8] A. Zieliński, M. Sroka, M. Miczka, A. Śliwa: Forecasting the particle diameter size distribution in P92 (X10CRWMOVNB9-2) steel after long-term ageing at 600 and 650 °C, Archives of Metallurgy and Materials, 61 2A (**2016**), 753–760, doi:10.1515/amm-2016-0128

[9] K. Drabczyk, P. Panek, Influence of screen printing parameters on the front metallic electrodes geometry of solar cells, Circuit World, 40 (**2014**) 1, 23–26, doi:10.1108/CW-10-2013-0038

[10] L. A. Dobrzański, K. Lukaszkowicz, Erosion resistant and tribological properties of coatings deposited by reactive magnetron sputtering method onto the brass substrate, Journal of Materials Processing Technology 157-158 (**2004**), 317–323, doi:10.1016/j.jmatprotec.2004.09.050

[11] A. Drygała, L. A. Dobrzański, M. Szindler, M. M. Szindler, M. Prokopiuk vel Prokopowicz, E. Jonda, Influence of laser texturization surface and atomic layer deposition on optical properties of polycrystalline silicon, International Journal of Hydrogen Energy, 41 (**2016**) 18, 7563–7567, doi:10.1016/j.ijhydene.2015.12.180

[12] L. A. Dobrzański, A. Drygała, Influence of laser processing on polycrystalline silicon surface, Materials Science Forum, 706–709 (**2012**), 829–834, doi:10.4028/www.scientific.net/MSF.706-709.829

[13] K. Drabczyk, R. Socha, P. Panek, G. Mordarski, Electrodeposition of thin metallic layer for solar cell electrodes, Soldering & Surface Mount Technology, 26(1) (**2014**), 18–21, doi:10.1108/SSMT-10-2013-0032

[14] C. Battaglia, A. Cuevas and S. De Wolf, High-efficiency crystalline silicon solar cells: status and perspectives, Energy & Enviromental Science, 9 (**2016**), 1552–1576, doi:10.1039/C5EE03380B

[15] S. Sharma, K. K. Jain, A. Sharma, Solar cells: in research and applications – a review, Materias Sciences and Applications, 6 (**2015**), 1145–1155, doi:10.4236/msa.2015.612113

[16] J. Gong, J. Liang, K. Sumathy, Review on dye-sensitized solar cells (DSSCs): Fundamental concepts and novel materials, Renewable and Sustainable Energy Reviews, 16 (**2012**), 5848–5860, doi:10.1016/j.rser.2012.04.044

[17] M. Berginc, M. Topic, U. O. Krasovec, Recovery of dye-sensitized solar cell's performance by heat treatment, Physical Chemistry Chemical Physics, 16 (**2014**), 12940–12948, doi:10.1039/C4CP01463D

[18] L. A. Dobrzański, M. M. Szindler, M. Szindler, K. Lukaszkowicz K., A. Drygała, M. Prokopiuk vel Prokopowicz, Nanocrystalline TiO_2 powder prepared by sol-gel method for dye-sensitized solar cells, Archives of Metallurgy and Materials, 61(2) (**2016**), 833–836, doi:10.1515/amm-2016-0140

[19] H. C. Weerasinghe, F Huang, Y. Cheng, Fabrication of flexible dye sensitized solar cells on plastic substrates, Nano Energy, 2 (**2013**) 2, 174–189, doi:10.1016/j.nanoen.2012.10.004

[20] G. Yue, X. Ma, W. Zhang, F. Li, J. Wu, G. Li, A highly efficient flexible dye-sensitized solar cell based on nickel sulfide/platinum/titanium counter electrode, Nanoscale Res Lett. 10 (**2015**) 1, doi:10.1186/1556-276X-10-1

[21] Y. Han, J. M. Pringle, Y. Cheng, Photovoltaic characteristics and stability of flexible dye-sensitized solar cells on ITO/PEN substrates, RSC Advances, 4 (**2014**), 1393–1400, doi:10.1039/C3RA45508D

[22] http://www-eng.lbl.gov/~shuman/NEXT/CURRENT_DESIGN/TP/MATERIALS/ASTM-D257_resistance_meas.pdf/, 30.06.2016

[23] http://www.electrotechsystems.com/manuals/2-%20PDF%20Electrostatic% 20Manuals/853%20Manual%20Rev1%209-10.pdf/, 30.06.2016

[24] https://www.ipc.org/TM/2-6-3-7.pdf/, 30.06.2016

[25] S. Thomas, T. G. Deepak, G. S. Anjusree, T. A. Arun, Shantikumar V. Nair, A. Sreekumaran Nair, A review on counter electrode materials in dye-sensitized solar cells, Journal of Materials Chemistry A, 2 (**2014**), 4474–4490, doi:10.1039/C3TA13374E

[26] A. Drygała, L. A. Dobrzański, M. Szindler, M. Prokopiuk vel Prokopowicz, M. Pawlyta, K. Lukaszkowicz, Carbon nanotubes counter electrode for dye-sensitized solar cells application, Archives of Metallurgy and Materials 61 (**2016**) 2, 803–80, doi:10.1515/amm-2016-0135

[27] L. A. Dobrzański, A. Mucha, M. Prokopiuk vel Prokopowicz, M. Szindler, A. Drygała, K. Lukaszkowicz, Characteristics of dye-sensitized solar cells with carbon nanomaterials, Mater. Tehnol., 50 (**2016**) 5, 649–654, doi:10.17222/mit.2014.134

[28] I. Y. Bu, J. Zheng, A new type of counter electrode for dye sensitized solar cells based on solution processed SnO_2 and activated carbon, Materials Science in Semiconductor Processing, 39 (**2015**), 223–228, doi:10.1016/j.mssp.2015.04.029

UDK 669.71:666.3-1:616-008.66
Original scientific article/Izvirni znanstveni članek

ISSN 1580-2949
MTAEC9, 51(4)631(2017)

POROUS HA/ALUMINA COMPOSITES INTENDED FOR BONE-TISSUE ENGINEERING

POROZNI HA/ALUMINIJEVI KOMPOZITI, NAMENJENI ZA NADOMESTNO UPORABO PRI KOSTNEM TKIVU

Eva Bartonickova, Jan Vojtisek, Jakub Tkacz, Jaromir Porizka, Jiri Masilko, Miroslava Moncekova, Ladislav Parizek

Brno University of Technology, Faculty of Chemistry, Materials Research Centre, Purkynova 464/118, 612 00 Brno, Czech Republic
bartonickova@fch.vutbr.cz

Prejem rokopisa – received: 2016-07-15; sprejem za objavo – accepted for publication: 2016-11-24

doi:10.17222/mit.2016.191

Ceramic biomaterials based on hydroxyapatite (HA) or alumina have been intensively studied due to their load-bearing applications in the bone-tissue replacement/reconstruction and dental applications. Here we present a study of the preparation and properties of HA/alumina (HA/Al) composites with a targeted porosity. The HA powder used for the composite's preparation was synthetized via a precipitation method under a variety of pH values. The resulting powders were verified with XRD, Raman and FTIR analyses. The particle size was assessed via SEM and laser diffraction. The as-prepared HA nano-powder and alumina powder (median 3 μm) were homogenously mixed having a composition of HA/Alumina = 90/10 (*w/w*). A suspension with 65 % mass fraction of the powders was properly mixed and, with the help of foaming agents, it was foamed in situ. The behavior under an increasing temperature was studied, using a heating microscope and dried foams were sintered under determined temperatures. The final sintered foams were examined in vitro in a synthetic body fluid, which predicted the behavior of bone implants in vivo. The behavior of the treated samples was studied with SEM. The newly formed HA composites were confronted with Ca^{2+} and PO_4^{3-} contents in the applied body-fluid solution.

Keywords: hydroxyapatite/Al_2O_3 composite, ceramic scaffolds, in-vitro bioactivity, SEM

Keramični biomateriali na osnovi hidroksiapatitov (HA) ali aluminijevega oksida so bili sistematsko preiskovani zaradi njihove najboljše nadomestne vloge pri nadomeščanju kostnega tkiva/rekonstrukciji in pri zobnih vsadkih. Predstavljena je študija priprave in lastnosti kompozitov HA / aluminijevega oksida (HA / Al) s ciljem preizkusa poroznosti. HA prah, ki se uporablja za pripravo kompozitov, smo sintetizirali po postopku obarjanja pri različnih pH-vrednostih. Dobljene praške smo preverili z XRD-, Raman in FTIR-analizo. Velikost delcev je bila ocenjena s pomočjo SEM in z lasersko difrakcijo. Pripravljen nanoprašek (HA) in aluminijev oksid v prahu (median 3 μm) sta bila homogeno premešana v mešanico HA/aliminij 90/10 (*w/w*). Suspenzija s 65 masnimi % praškov je bila ustrezno mešana in s pomočjo penil spenjena in situ. Raziskovali smo obnašanje v okviru naraščajoče temperature, uporabo pod ogrevanim mikroskopom in suhe pene so bile sintrane pri določenih temperaturah. Končne sintrane pene so bile pregledane in vitro kot sintetične tekočine, ki so napovedale obnašanje kostnih vsadkov in vivo. Obnašanje obdelanih vzorcev smo preučevali s SEM. Pri vstavitvi oz. stiku s telesno tekočino so bili na novo oblikovani HA v stiku z Ca^{2+} in vsebino PO_4^{3-}.

Ključne besede: hidroksiapatit/AI_2O_3 kompozit, keramična ogrodja, bioaktivnost in vitro, SEM

1 INTRODUCTION

The load-bearing system of humans, although it is very durable, can sometimes lose a vital part due to injuries, illnesses or wear. In this case, it is necessary to replace the original tissue with suitable implants. The first attempts to replace bone tissues is dated back to the early years before Christ, but the intensive development of this research area underwent a boom in the second half of the 20th century. Nowadays, the 2nd and 3rd generations of biomaterials are in progress. Hydroxyapatite belongs to biocompatible materials with osteoconductive and osteointegrating properties and exhibits chemical and physical analogies to the minerals present in human bones and teeth.[1–2] Although HA exhibits excellent bio-properties, its clinical application failed due to poor mechanical properties, a long remodeling time and a relatively slow rate of osteointegration.[3] So, the reinforcement of HA become part of the research. In recent works, HA ceramics were reinforced with metals, polymers or toughened zirconia ceramics.[4–6]

A synthesis of HA at the nanoscale has been studied very often. There are many ways of how to prepare a powder with targeted properties (i.e., at least one dimension under 100 nm). The wet procedures under the conventional or non-conventional conditions, especially precipitation, hydrothermal, sonochemical or microwave treatments, are used most commonly.[7–9] The sol-gel technique of an HA synthesis exhibits a high level of HA-powder homogeneity; nevertheless, the secondary formed calcium oxide represents extraction and biocompatibility problems.[8] The variability of the preparation of a ceramic foam is extremely wide. An in-situ foaming procedure favors scaffold-preparation procedures due to the possibility of controlling the porosity with an exact diameter, in comparison with the

widely used replica method using a polymeric sponge.[10–11]

The composite preparation was based on the same procedures. The HA matrix was reinforced with ceramic-oxide constituents such as zirconia, titania, silica, yttria, bioglass or alumina.[3,6,12–18] Alumina oxide is a cost-effective and well-accessible option for enhancing HA properties, especially the mechanical properties. The mechanical strength of a porous human bone is in a range of 2–12 MPa.[19] The reported values for pure HA are in a range of 1.2–16 MPa, depending on the foaming process.[20] A positive alumina contribution to the mechanical strength was recently reported by I. Sopyan et al.[21] and L. L. Wang et al.[17,22]

The presented paper introduces an overall scaffold preparation based on an hydroxyapatite matrix reinforced with an alumina-oxide addition. The physical properties and in-vitro behavior of the final porous scaffolds are presented.

2 EXPERIMENTAL PART

2.1 Synthesis of the hydroxyapatite powder

The hydroxyapatite powder was synthetized via a simple precipitation method from calcium nitrate ($Ca(NO_3)_2.4H_2O$; puriss; LachNer; the Czech Republic) and phosphoric acid (H_3PO_4; puriss; Penta; Czech Republic) precursors. The syntheses was carried out under laboratory conditions and via the reaction mechanism given in Equation (1):

$$10Ca(NO_3)_2 + 6H_3PO_4 + 20NH_4OH \rightarrow \rightarrow Ca_{10}(PO_4)_6(OH)_2 + 20NH_{4N}O_3 + 18H_2O \quad (1)$$

Aqueous solutions of precursors (Ca^{2+} concentration – 1.3 mol/L; PO_4^{3-} concentration – 1 mol/L) were simultaneously added dropwise into an aqueous solution with a controlled pH value. The pH value was varied from 1 to 9.6 and adjusted with an addition of ammonium hydroxide (NH_4OH; puriss; LachNer, the Czech Republic). To assess the reaction kinetics, turbidimetric measurements of the formed precipitates (2100Q Hach) combined with the reaction-yield determination were conducted. The precipitated products were centrifugally separated, washed and dried at 80 °C. The prepared powders were analyzed in the terms of phase and chemical compositions and morphology (an EMPYREAN Panalytical diffractometer in the central focusing arrangement using Co-K_α radiation, the Netherlands; a FTIR spectrometer Nicolet iS50 Thermo Fisher Scientific, U.S.A.; and an EVO CS10 ZEISS electron microscope equipped with an energy-dispersive analyzer with an Oxford X-Max 80 mm^2 detector in the back-scattering mode, respectively).

2.2 Scaffold fabrication and characterization

The synthetized HA powder and commercial alumina powder (Nabalox 325; Nabaltec AG, Germany) were properly mixed at a HA/alumina ratio of 90:10. The aqueous suspensions containing 55 % mass fraction of the HA solid loading and 65 % mass fraction of the composite solid loading were homogenously mixed to avoid the unfavorable agglomeration. The foaming agent (Schäumungsmittel Zschimmer&Scharz GmbH & Co, Germany) was added to the prepared suspensions with a concentration of 0.25 % mass fraction. The given concentrations of the solid loading and the foaming agent were previously experimentally determined. After the agent addition, the mixing rate of the magnetic stirrer was immediately accelerated to initialize the foaming process (up to 1000 min^{-1}). The foamed suspensions were cast in an open aluminium-foil mould with dimensions of (1 × 1 × 1) cm and (2 × 2 × 2) cm for apatite-forming-ability tests and determination of the mechanical properties, respectively. To avoid the formation of unfavourable cracks, the drying process was carried out in several steps – at 50 °C for 4 h; 80 °C for 10 h and, finally, 105 °C for 3 h. Dried samples were demoulded and heated to 600 °C for an organic-species removal and to 1250 °C (the temperature determined with a heating microscopy analysis (EM 201 Leitz, Germany) to carry out the foam consolidation. The porosity evaluation was examined using mercury intrusion porosimetry (Poremaster Quantachrome, U.S.A.), an image analysis (Stemi 508 ZEISS, Austria; processed via ImageJ software) and Archimedes' bulk-density determination (ISO EN 5017 2013). The mechanical properties of porous scaffolds were calculated from stress-strain curves using a universal mechanical testing machine (5985C INSTRON, U.S.).

2.3 Apatite-forming-ability testing

The behavior of the samples in the human body was simulated with a stability test. The samples were thoroughly immersed in a modified simulated body liquid (SBF) prepared via Kokubo's procedure[23] and soaked for (7, 14 and 28) d in an incubator chamber at 37 °C. The surfaces of the treated samples were observed

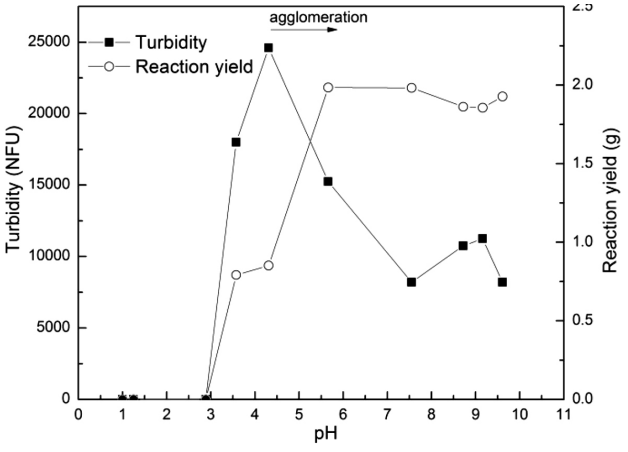

Figure 1: Turbidimetry and reaction yield as a function of pH

with SEM. The concentrations of Ca^{2+} and PO_4^{3-} in pure and treated SBFs were analyzed using ion chromatography (Metrosep C4 15/4.0 Metrohm, Switzerland) and ICP-OES (Ultima 2 Jobin Yvon Technology, France).

3 RESULTS AND DISCUSSION

3.1 Hydroxyapatite characterization and in-situ foaming

The hydroxyapatite formation was studied by means of reaction kinetics using turbidity measurements. **Figure 1** describes the yield and turbidity of the reaction product as a function of pH. An increase in pH from 1 to 6 increased the turbidity values and the product yield. The maximum turbidity was reached at a pH of 4 and corresponded to the colloidal character of the nucleated and grown HA particles. After this value, the precipitated particles started to flocculate and the suspension became unstable. Large-sized particles started to agglomerate and the sediment corresponded with lower turbidity values, whereas the yield of the reaction was unchanged.[8,24] The high level of agglomeration was confirmed with a morphology analysis and laser-diffraction measurements (**Figure 2**). The phase purity and crystallinity of the prepared powders are given in **Figure 3**. A strong dependence of the precipitation reaction on the pH is obvious (**Figure 3** and **Table 1**). A pH below 7 exhibits a heterogeneous system based on hydroxyapatite and monetite (ICCD 01-089-6438 and ICCD 01-070-0359, resp.). Similar kinetics was observed in several works where a phase-pure HA powder with nanodimensions, but agglomerated, was also synthetized.[8,25–26] Based on the results summarized above, the optimum pH of the reaction was set to 8.7. The HA powder used for the in-situ foaming was successfully and repeatedly prepared on large scale, with a 100 % phase purity and the mean agglomerate size of about 4 μm.

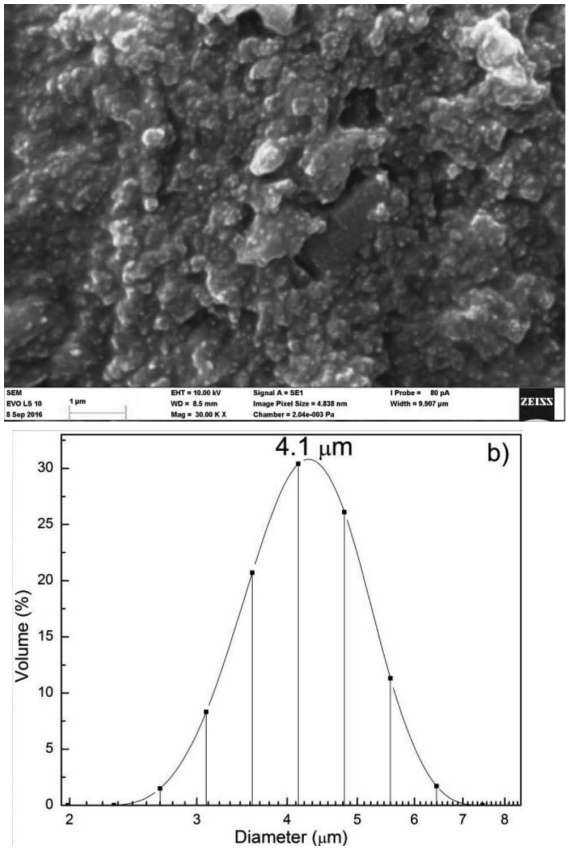

Figure 2: Synthetized hydroxyapatite powder: a) morphology, b) particle-size distribution

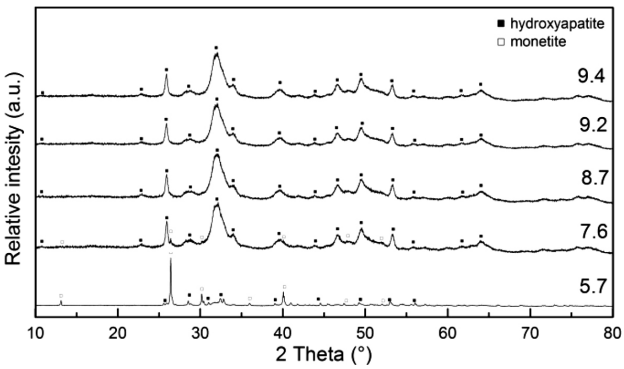

Figure 3: Dependence of the HA-product phase purity on the pH value

Table 1: Phase analysis of the synthetized HA powders under different pH values

pH	Monetite – $CaHPO_4$ (*w*/%)	Hydroxyapatite – $Ca(PO_4)_3(OH)$ (*w*/%)
4.5	100	0
5.7	87	13
6.6	18	82
8.7	0	100
9,2	0	100
9.4	0	100

A significant factor for the successful foaming of the prepared suspensions was the stability of the foam

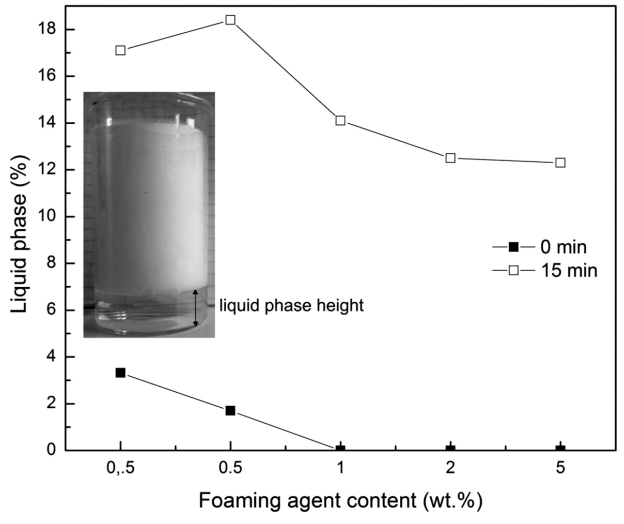

Figure 4: Foam-stability test in terms of time dependence

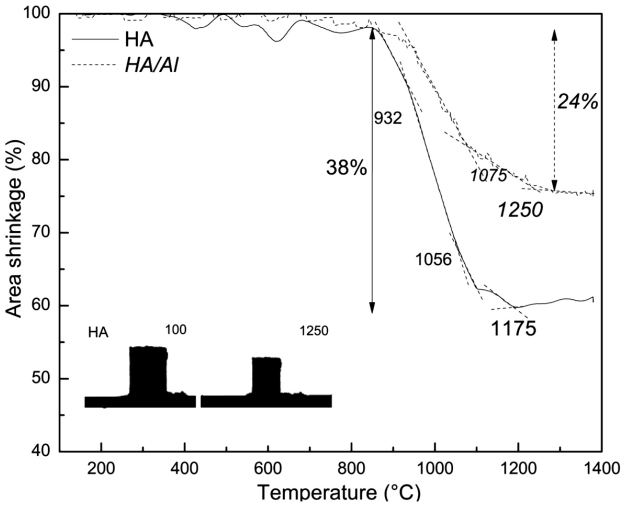

Figure 5: Sintering study provided with a heating microscope analysis

prepared without a ceramic powder. This stability was studied with respect to the content of the foaming agent (**Figure 4**) and the time to the foam structure's collapse. The 0.25 % mass-fraction content of the foaming agent was determined as the optimum value. P. Ptáček et al.[27] recently published a paper, in which an aqueous/detergent-based foam was also studied in terms of the time-stability dependence and similar experimental data was observed.

The sintering behavior of the pure powder and composite is shown in **Figure 5**. The area shrinkage was found to be 38 % for HA and 24 % for the HA/Al composite. The optimum sintering temperature for HA and HA/Al sintering was determined, according to the experimental data, to be 1250 °C. The consolidation of the closely packed particles seemed to be finished according to the sintering curve (**Figure 5**). The phase analysis of the sintered samples showed a decomposition of the HA structure to several apatite forms above the temperature of 1150 °C[18] (tricalcium phosphate, tricalcium hydrogen diphosphate, tetracalcium tetraphosphate and residual HA). In the case of the HA/Al composite sample, the formation of tricalcium phosphate and the Ca-Al phase was observed. It was reported that α- and β-tricalcium phosphates are more biodegradable apatite forms in comparison with the HA structure[28], which is closely connected with the chosen temperature of the sintering discussed above. The newly formed Ca-Al structure of the composite samples was positively identified as hibonite $CaAl_{12}O_{19}$ (ICCD 01-076-0665) with a platelet hexagonal arrangement, which is shown, in detail, in **Figure 6d**.

L.-P. Li et al.[29], M. H. Ghazanfari et al.[16] and B. Basar et al.[30] also observed the formation of the Ca-Al phase in HA/Al composites with similar particle morphologies at temperatures of 1350, 1250 and 1100 °C, respectively.

The structures of the scaffolds prepared from the pure hydroxyapatite powder and composite powder using in-situ foaming are given in **Figure 6**. The alumina contribution is clearly visible; the composite foam has a ball-shaped structure (**Figure 6b**) resulting from the foaming process, with a pore diameter of around 60 μm (obtained with the image analysis). The microstructure is apparently similar to those presented by P. Ptáček et al.[27], where the aqueous-surfactant system was also used. On the other hand, the observed microstructures of the HA foams (**Figure 6a** and **6c**) are more heterogeneous, having even smaller pores (of around 28 μm according to the image analysis) than the composite one. The presence of hibonite was also confirmed with the EDS and SEM analysis (**Figure 6d**). The HA scaffolds provided significantly higher mechanical-strength values (see the embedded image in **Figure 7**). These findings indicate a low degree of foam consolidation due to the alumina part with a higher sintering-temperature region. Similar values of the mechanical strength and the corresponding

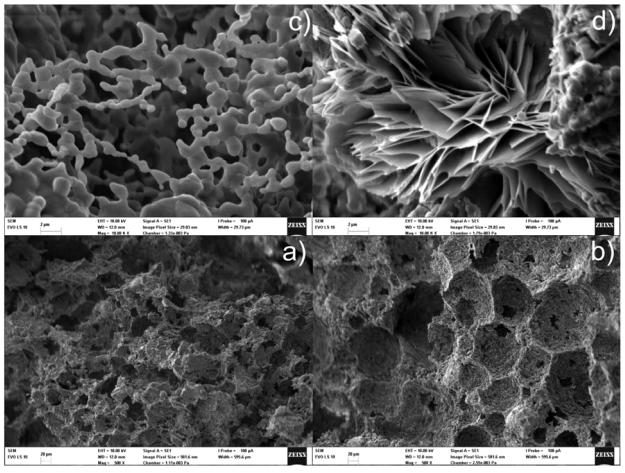

Figure 6: Microstructures of the HA and composite scaffolds: a) HA scaffold, b) HA/Alumina scaffold, c) HA scaffold – a detail, d) hibonite structure observed in the HA/Alumina scaffold

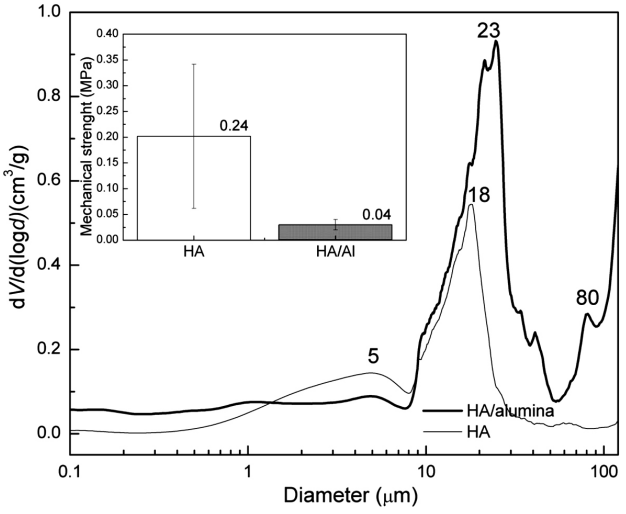

Figure 7: Porosity determination and mechanical strength (embedded) of HA and HA/Alumina scaffolds

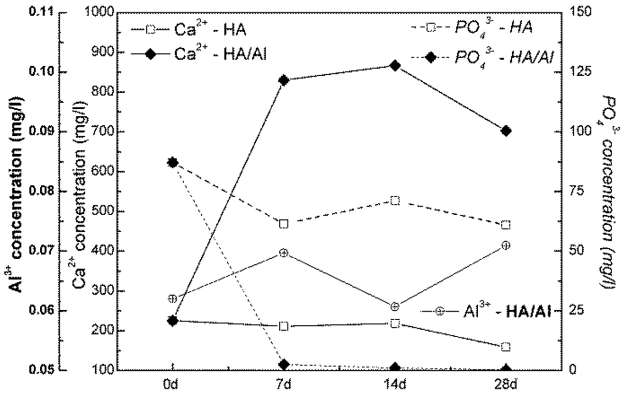

Figure 8: Cation concentration in the applied synthetic body fluid, time to release dependence

phase composition were also achieved by M. H. Ghazanfari et al.[16]

The total porosities determined with Archimedes' method were (45.9 and 63.1) % of materials theorethical density for HA and the HA/alumina composite, respectively. Pore-size distributions for both of the scaffolds are given in **Figure 7**, reflecting the effect of the alumina addition on the pore-structure evolution. The performed analysis showed a possible collapse of the HA/Al foam structure during an Hg intrusion, visible as an increasing tendency of the curve above 100 μm or the presence of significantly large pores. **Figure 7** (the embedded image) shows the mechanical properties of the prepared scaffolds. The measured values are in the equipment limits, so the relative deviation is considerable. The maximum mechanical strength reached for the pure HA structure was 0.2 MPa. The expected enhancement of the alumina addition in the mechanical properties was not confirmed. The higher strength also reflected the obtained porosity values, i.e., the HA/alumina composites showed higher total porosities with a lower sintering degree than the pure HA ones.

3.2 In-vitro behavior – the apatite-forming ability

Figures 8 and **9** summarize the in-vitro testing of the prepared scaffolds. The synthetic body fluid, prepared by T. Kokubo[23], simulated the bloody-plasma environment in the human body. In **Figure 8**, the concentrations of the most important ion species, Ca^{2+}, Al^{3+} and PO_4^{3-}, are given. The pure HA scaffolds exhibited the expected behavior; the gradual consumption of both of the ions corresponded to the formation of the new HA on the scaffold surface (**Figure 9**). The ability of a Ca-apatite formation on the surface was frequently reported in the past.[31–32] Otherwise the reactivity of the HA/Al composite in the SBF environment was slightly different. As could be seen from **Figure 8**, the PO_4^{3-} ions were totally consumed within 28 d; on the other hand, the Ca^{2+} and Al^{3+} cation concentration had an increasing tendency. The newly formed phase practically covered the composite scaffold surfaces (**Figure 9**). The performed EDS analysis could not exactly distinguish between the formations of the Ca- or Al-bonded apatite structures. The probability of the formation of both phases is almost certain. X. Chatzistavrou et al.[33] described the mechanism of the Ca-Al apatite formation on a HA/Al composite surface according to the reaction scheme in Equation (2), which is in good agreement with our data:

$$\text{Al-OH} + H_2PO_4^{2-} \rightarrow \text{Al-O-}PO_3^{-} + OH^- \qquad (2)$$

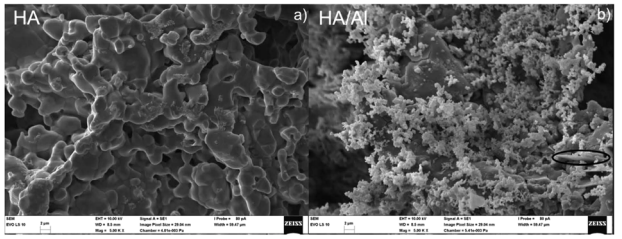

Figure 9: In-vitro evaluation of the treated HA and HA/Al scaffolds in SBF, SEM analysis after 28 d of treatment

4 CONCLUSION

In this work, a synthesis of the nanosized phase of a pure hydroxyapapatite powder was successfully performed on a large scale. Porous scaffolds based on the as-synthetized hydroxyapatite and supplied alumina powders were fabricated using the in-situ foaming process. The prepared HA scaffolds exhibited significantly better mechanical properties, with the total porosity of about 46 %, than the HA/Al scaffold with a porosity of about 64 %. In-vitro testing of both scaffolds confirmed an appropriate apatite-forming ability. The HA/Al composite was significantly more covered with the newly formed phase than the pure HA ones. A study of the nucleation and growth mechanism of Ca-Al apatite is in progress.

Acknowledgement

The paper was supported by the project Materials Research Centre at FCH BUT – Sustainability and Development, REG LO1211, with a financial support from the National Programme for Sustainability I (the Ministry of Education, Youth and Sports).

5 REFERENCES

[1] G. Tripathi, B. Basu, A porous hydroxyapatite scaffold for bone tissue engineering: Physico-mechanical and biological evaluations, Ceram. Int., 38 (**2012**) 1, 341–349, doi:10.1016/j.ceramint.2011.07.012

[2] G. Radha, S. Balakumar, B. Venkatesan, E. Vellaichamy, Evaluation of hemocompatibility and in vitro immersion on microwave-assisted hydroxyapatite-alumina nanocomposites, Mater. Sci. Eng., C 50 (**2015**), 143–150, doi:10.1016/j.msec.2015.01.054

[3] S. Khorsand, M. H. Fathi, S. Salehi, S. Amirkhanlou, Hydroxyapatite/alumina nanocrystalline composite powders synthesized by sol-gel process for biomedical applications, Int. J. Min. Met. Mater., 21 (**2014**) 10, 1033–1036, doi:10.1007/s12613-014-1005-7

[4] H. Itokawa, T. Hiraide, M. Moriya, M. Fujimoto, G. Nagashima, R. Suzuki, T. Fujimoto, A 12 month in vivo study on the response of bone to a hydroxyapatite–polymethylmethacrylate cranioplasty composite, Biomaterials, 28 (**2007**) 33, 4922–4927, doi:10.1016/j.biomaterials.2007.08.001

[5] K. R. Mohamed, H. H. Beherei, G. T. El Bassyouni, N. El Mahallawy, Fabrication and mechanical evaluation of hydroxyapatite/oxide nano-composite materials, Materials Science and Engineering, C 33 (**2013**) 7, 4126–4132, doi:10.1016/j.msec.2013.05.059

[6] W. Kantana, P. Jarupoom, K. Pengpat, S. Eitssayeam, T. Tunkasiri, G. Rujijanagul, Properties of hydroxyapatite/zirconium oxide nanocomposites, Ceram. Int. 39, Suppl. 1 (**2013**), S379–S382, doi:10.1016/j.ceramint.2012.10.098

[7] I. Mobasherpour, M. S. Heshajin, A. Kazemzadeh, M. Zakeri, Synthesis of nanocrystalline hydroxyapatite by using precipitation method, J. Alloys Compd., 430 (**2007**) 1–2, 330–333, doi:10.1016/j.jallcom.2006.05.018

[8] M. Sadat-Shojai, M.-T. Khorasani, E. Dinpanah-Khoshdargi, A. Jamshidi, Synthesis methods for nanosized hydroxyapatite with diverse structures, Acta Biomater., 9 (**2013**) 8, 7591–7621, doi:10.1016/j.actbio.2013.04.012

[9] E. K. Girija, G. S. Kumar, A. Thamizhavel, Y. Yokogawa, S. N. Kalkura, Role of material processing on the thermal stability and sinterability of nanocrystalline hydroxyapatite, Powder Technol., 225 (**2012**), 190–195, doi:10.1016/j.powtec.2012.04.007

[10] A. R. Studart, U. T. Gonzenbach, E. Tervoort, L. J. Gauckler, Processing Routes to Macroporous Ceramics: A Review, J. Am. Ceram. Soc., 89 (**2006**) 6, 1771–1789, doi:10.1111/j.1551-2916.2006.01044.x

[11] M. D. M. Innocentini, P. Sepulveda, V. R. Salvini, V. C. Pandolfelli, J. R. Coury, Permeability and Structure of Cellular Ceramics: A Comparison between Two Preparation Techniques, J. Am. Ceram. Soc., 81 (**1998**) 12, 3349–3352, doi:10.1111/j.1151-2916.1998.tb02782.x

[12] J. Y. Han, Z. T. Yu, L. Zhou, Hydroxyapatite/titania composite bioactivity coating processed by sol–gel method, Appl. Surf. Sci., 255 (**2008**) 2, 455–458, doi:10.1016/j.apsusc.2008.06.072

[13] S. M. Latifi, M. H. Fathi, M. A. Golozar, Preparation and characterisation of bioactive hydroxyapatite–silica composite nanopowders via sol–gel method for medical applications, Adv. Appl. Ceram., 110 (**2011**) 1, 8–14, doi:10.1179/174367510x12753884125325

[14] S. Salehi, M. H. Fathi, Fabrication and characterization of sol–gel derived hydroxyapatite/zirconia composite nanopowders with various yttria contents, Ceram. Int., 36 (**2010**) 5, 1659–1667, doi:10.1016/j.ceramint.2010.02.045

[15] R. Ravarian, F. Moztarzadeh, M. S. Hashjin, S. M. Rabiee, P. Khoshakhlagh, M. Tahriri, Synthesis, characterization and bioactivity investigation of bioglass/hydroxyapatite composite, Ceram. Int., 36 (**2010**) 1, 291–297, doi:10.1016/j.ceramint.2009.09.016

[16] S. M. H. Ghazanfari, A. Zamanian, Phase transformation, microstructural and mechanical properties of hydroxyapatite/alumina nanocomposite scaffolds produced by freeze casting, Ceram. Int., 39 (**2013**) 8, 9835–9844, doi:10.1016/j.ceramint.2013.05.096

[17] L.-l. Wang, X.-F. Wang, X. Ding, J.-F. Zhu, Sintering Behavior and Property of Bioglass Modified HA-Al2O3 Composite, Sci. Sinter., 44 (**2012**) 3, 265–270, doi:10.2298/sos1203265w

[18] J. Li, B. Fartash, L. Hermansson, Hydroxyapatite alumina composites and bone-bonding, Biomaterials, 16 (**1995**) 5, 417–422, doi:10.1016/0142-9612(95)98860-g

[19] L. L. Hench, J. Wilson, An Introduction to Bioceramics, World Scientific, Singapore, 1993

[20] H. Yoshikawa, A. Myoui, Bone tissue engineering with porous hydroxyapatite ceramics, Journal of Artificial Organs, 8 (**2005**) 3, 131–136, doi:10.1007/s10047-005-0292-1

[21] I. Sopyan, A. Fadli, M. Mel, Effect of hydroxyapatite and tricalcium phosphate addition on protein foaming-consolidation porous alumina, J. Porous Mater., 19 (**2012**) 5, 733–743, doi:10.1007/s10934-011-9525-2

[22] L.-L. Wang, X.-F. Wang, X. Ding, H.-T. Jiang, Preparation of HA-Bioglass-Al2O3 Biological Composite, Mater. Manuf. Processes, 28 (**2013**) 9, 980–983, doi:10.1080/10426914.2012.709339

[23] T. Kokubo, H. Takadama, How useful is SBF in predicting in vivo bone bioactivity?, Biomaterials, 27 (**2006**) 15, 2907–2915, doi:10.1016/j.biomaterials.2006.01.017

[24] H. Lange, Comparative test of methods to determine particle size and particle-size distribution in the submicron rang, Part. Part. Syst. Charact., 12 (**1995**) 3, 148–157, doi:10.1002/ppsc.19950120307

[25] S. S. A. Abidi, Q. Murtaza, Synthesis and Characterization of Nano-Hydroxyapatite Powder Using Wet Chemical Precipitation Reaction, Journal of Materials Science & Technology, 30 (**2014**) 4, 307–310, doi:10.1016/j.jmst.2013.10.011

[26] E. Kramer, J. Podurgiel, M. Wei, Control of hydroxyapatite nanoparticle morphology using wet synthesis techniques: Reactant addition rate effects, Mater. Lett., 131 (**2014**), 145–147, doi:10.1016/j.matlet.2014.05.105

[27] P. Ptáček, K. Lang, F. Šoukal, T. Opravil, L. Tvrdík, R. Novotný, Preparation and properties of nanostructured ceramic foam from kaolinite, Powder Technol., 253 (**2014**), 29–34, doi:10.1016/j.powtec.2013.10.026

[28] G. Hannink, J. J. C. Arts, Bioresorbability, porosity and mechanical strength of bone substitutes: What is optimal for bone regeneration?, Injury-International Journal of the Care of the Injured, 42 (**2011**), S22–S25, doi:10.1016/j.injury.2011.06.008

[29] L.-P. Li, Y. Yan, X.-Z. Fan, Z.-H. Hu, C.-Y. Zhao, Low-temperature synthesis of calcium–hexaluminate/magnesium–aluminum spinel composite ceramics, J. Eur. Ceram. Soc., 35 (**2015**) 10, 2923–2931, doi:10.1016/j.jeurceramsoc.2015.03.041

[30] B. Basar, A. Tezcaner, D. Keskin, Z. Evis, Synthesis, phase transitions and cellular biocompatibility of nanophase alumina-hydroxyapatite composites, Adv. Appl. Ceram., 110 (**2011**) 4, 238–243, doi:10.1179/1743676111y.0000000012

[31] S. Saber-Samandari, S. Kiyazar, J. Aghazadeh, A. Sadeghi, In vitro evaluation for apatite-forming ability of cellulose-based nanocomposite scaffolds for bone tissue engineering, Int. J. Biol. Macromol., 86 (**2016**), 434–442, doi:10.1016/j.ijbiomac.2016.01.102

[32] G. Thrivikraman, G. Madras, B. Basu, In vitro/In vivo assessment and mechanisms of toxicity of bioceramic materials and its wear particulates, RSC Advances, 4 (**2014**) 25, 12763–12781, doi:10.1039/c3ra44483j

[33] X. Chatzistavrou, N. Kantiranis, E. Kontonasaki, K. Chrissafis, L. Papadopoulou, P. Koidis, A. R. Boccaccini, K. M. Paraskevopoulos, Thermal analysis and in vitro bioactivity of bioactive glass-alumina composites, Mater. Charact., 62 (**2011**) 1, 118–129, doi:10.1016/j.matchar.2010.11.008

UDK 67.017:62-4-023.7:620.193
Original scientific article/Izvirni znanstveni članek

ISSN 1580-2949
MTAEC9, 51(4)637(2017)

COMPARISON OF THE PHYSICOCHEMICAL PROPERTIES OF Al_2O_3 LAYERS APPLIED TO THE SURFACES OF cpTi AND THE Ti6Al7Nb ALLOY USING THE ALD METHOD

PRIMERJAVA FIZIKALNO-KEMIJSKIH LASTNOSTI Al_2O_3 PLASTI, NANEŠENIH NA cpTi POVRŠINE IN ZLITINO Ti6Al7Nb Z UPORABO ALD METODE

Marcin Basiaga[1], Marcin Staszuk[2], Tomasz Tański[2], Agnieszka Hyla[1], Witold Walke[1], Cezary Krawczyk[3]

[1]Silesian University of Technology, Faculty of Biomedical Engineering, ul. Roosevelta 40, 41-800 Zabrze, Poland
[2]Silesian University of Technology, Faculty of Mechanical Engineering, ul. Konarskiego 18A, 44-100 Gliwice, Poland
[3]Zabrze Medical College, Department of Dental Technology, ul. 3 Maja 63, 41-800 Zabrze, Poland
marcin.staszuk@polsl.pl

Prejem rokopisa – received: 2016-07-22; sprejem za objavo – accepted for publication: 2016-11-08

doi:10.17222/mit.2016.220

Literature data show that atomic-layer deposition (ALD) is a very important method for depositing layers due to the mechanical and physicochemical properties of the surface. In the literature, little space is devoted to layers of Al_2O_3, which could also have a major impact on improving the physicochemical properties of metallic biomaterials. Therefore, the aim of this research was to determine the influence of the Al_2O_3 layer formed by the ALD method on the physicochemical properties of metallic biomaterials. Based on the results, a beneficial effect on the pitting and crevice-corrosion resistance of the applied Al_2O_3 layer was determined, compared to the initial state, devoid of the layer, regardless of the substrate used. On the other hand, the performed surface-wettability tests showed no influence of the ALD temperature on the obtained angle values. Proposing appropriate conditions for the surface treatment using the ALD method has some promise and will contribute to the development of a technological process with defined parameters for oxide-layer manufacture for implants used in bone surgery.

Keywords: cpTi (Grade 4), Ti6Al7Nb alloy, Al_2O_3 layer, adhesion, corrosion resistance

Podatki iz literature kažejo, da je depozicija atomskih plasti (ALD) zelo pomembna metoda za nanašanje plasti zaradi mehanskih in fizikalno-kemijskih lastnosti površine. V literaturi so plasti Al_2O_3 sicer le malo omenjene pa vendar imajo lahko velik vpliv na izboljšanje fizikalno-kemijskih lastnosti kovinskih biomaterialov. Cilj raziskave je bil zato ugotoviti vpliv Al_2O_3 sloja, tvorjenega z metodo ALD, na fizikalno-kemijske lastnosti kovinskih biomaterialov. Na osnovi rezultatov smo določili ugoden učinek uporabljene Al_2O_3 plasti pri odpornosti na luknjičasto in špranjsko korozijo, v primerjavi z začetnim stanjem, ki je bila brez sloja, ne glede na uporabljeno podlago. Po drugi strani pa so izvedeni testi površinske vpojnosti pokazali, da temperatura ALD-metode ne vpliva na dobljene kotne vrednosti. Ustrezni pogoji, predlagani za površinsko obdelavo z uporabo ALD-metode, veliko obetajo in bodo prispevali k razvoju tehnološkega procesa z določenimi parametri za izdelavo vsadkov, ki se uporabljajo v kirurški medicini in pri operacijah kosti.

Ključne besede: cpTi (Grade 4), Ti6Al7Nb zlitina, Al_2O_3 plast, oprijem, odpornost proti koroziji

1 INTRODUCTION

Material implanted into human tissues and body fluids must have a bio-electronic compatibility, and so have the appropriate electric and magnetic properties, similar to those of the surrounding living matter, which has mostly a dielectric characteristic. In addition, the selected set of mechanical properties of such a material should provide good relations in the implant-tissues-body-fluids system that are essential to the realization of biophysical cooperation and flexible load transfer. The materials' physicochemical properties chosen this way will protect the implant against the damaging process of its destruction, and consequently, general and reactive responses will be minimized and so will be the process of metalosis.[1–4]

To prevent such negative phenomena surface treatment methods, e.g., coating, are used on implants. However, until now satisfactory results have not been achieved in that manner. Therefore, a continuous search for the best solutions relating to the methodology, the chemical composition and physicochemical properties of the layers produced is being conducted by many experts in the field.[5–8] An attempt to improve the physical and chemical properties of implants used in bone surgery was taken by J. Szewczenko,[9] who carried out the process of anodic oxidation on titanium alloys. Similar studies were conducted by W. Walke,[10,11] who deposed layers of TiO_2 and SiO_2 on 316 LVM steel using the sol-gel method.

Among the many techniques for applying layers, ALD (Atomic Layer Deposition) deserves special attention because it does not change the geometrical features of the implant and allows manufacturers to control the layer thickness. The method was created in Finland in the 1970s. The method is based on the CVD technique

(Chemical Vapour Deposition). Otherwise, it can be described as layer-by-layer coating deposition. It is characterized by: chemisorption, which is the formation of strong chemical bonds between the precursors, impregnation, which is important in achieving uniformity of the layer, sequencing, which is a key feature of this method consisting of the fact that the precursors are introduced into the chambers in turns.

Literature data show that ALD is a very important method of depositing layers due to the mechanical and physicochemical properties of the surface. For this reason, numerous studies are conducted on it. A. Purniawan et al.[7] performed a study that uses a low surface roughness and the uniformity of the TiO_2 deposited by ALD in the creation of biomedical sensors used in the diagnosis of leaks during the operation of anastomosis of the colon, pancreas, etc. In this experiment, a layer of TiO_2 was used as an evanescent waveguide. After a series of tests, it was found that the layer is suitable for use as a biomedical sensor, detecting dangerous effects in humans.[3] Another example might be the use of a SiO_2 layer applied by ALD in order to improve the corrosion resistance of stainless steel. Layers were applied with different thicknesses: 300 nm, 100 nm, 30 nm, 10 nm. A measurement of the material's hardness using the Vickers method and a test of the layer's adhesion to the substrate were conducted. As a result the corrosion resistance was determined. Studies have shown that the thicker the layer the greater the delamination after the hardness test, and so the adhesion to the substrate is poorer. The layers deposited by ALD also increased the corrosion resistance of steel by reducing the corrosion current, and increasing the passive areas.[12]

In the literature, little space is devoted to layers of Al_2O_3, which could also have a major impact on improving the physicochemical properties of metallic biomaterials. Therefore, the aim of the completed research was to determine the influence of an Al_2O_3 layer formed by the ALD method on the physicochemical properties of metallic biomaterials.

2 EXPERIMENTAL PART

The study was conducted on the Al_2O_3 layer applied by ALD on the two selected metal substrates, i.e., cpTi and Ti_6Al_7Nb (**Table 1**). Samples were provided in the form of discs with a diameter of 14 mm and a thickness of 3 mm. The samples were subjected to a preliminary surface modification consisting of vibration machining using suitable ceramic grinding particles required to obtain a constant roughness $R_a < 0.4$ μm. Then, the surface of the samples was subjected to electrochemical polishing in a solution based on chromic acid (E-395 made by POLIGRAT Gmbh Company), with a current density = 10÷30 A/cm^2. The treatment made it possible to obtain a surface roughness of $R_a = 0.1$ μm. The surface was then covered with an Al_2O_3 layer using ALD (PICOSUN). The process of applying the layer was carried out under recurrent conditions for both materials. To deposit an Al_2O_3 layer using ALD, trimethylaluminum (TMA) and water vapor are sequentially pulsed through the reaction chamber.[13] The number of cycles was 830, which made obtaining a layer thickness of about 120 nm possible. Layers of this thickness are commonly used in the surface modification of metallic biomaterials in contact with bone tissue. The variable parameter was the temperature of the process. The authors proposed the execution of the process at reduced temperature of T = 150 °C and at an elevated temperature of T = 300 °C. All the samples were subjected to examinations before the sterilization treatment in an autoclave (T = 135 °C, p = 2,1 bar, t = 12 min).

2.1 Potentiodynamic test

Tests of resistance to pitting corrosion were carried out for different variants of the surface treatment using the potentiodynamic method. The study used VoltaLab® potentiostat PGP 201 by Radiometer. The reference electrode was a saturated calomel electrode (SCE), while the counter electrode was platinum wire. The anode, on the other hand, was cpTi+Al_2O_3/Ti6Al7Nb+Al_2O_3. The test was performed in Ringer solution (250ml), supplied by Baxter, at a temperature of T = 37 °C and pH = 6.8±0.2. The study was initiated by indicating the open-circuit potential E_{OCP}. Then, recording of polarization curves started from the potential $E_{start} = E_{OCP} - 100$ mV. Samples were polarized with scan rate of 0.16mV/s. Tests were carried out for five samples of each kind of substrate. Additionally, the Stern method was used to determine to the value of the polarization resistance R_p.

Table 1: Chemical composition of analyzed materials

cpTi, mass concentration, in mass fractions (*w*/%)									
Element	N	C	H	Fe	O	Ti			
ISO 5832-2	max. 0.05	max. 0.1	max. 0.0125	max. 0.5	max. 0.4	bal.			
Certificate	0.03	0.05	0.005	0.4	0.4	bal.			
Ti6Al7Nb, mass concentration, in mass fractions (*w*/%)									
Element	C	H	N	O	Ta	Fe	Al	Nb	Ti
ISO 5832-11	max. 0.08	max. 0.009	max. 0.05	max. 0.20	max. 0.50	max. 0.25	6.50–5.50	7.50–6.50	bal.
Certificate	0.008	0.003	0.03	0.08	0.37	0.22	6.24	6.84	bal.

2.2 Potentiostatic test

Evaluation of the resistance to crevice corrosion made use of the potentiostatic method, recording changes in the current density at +800mV potential for 15 min.[14] The measurement system was identical to the one used for potentiodynamic tests. The tests were carried out in the Ringer solution (250 mL), supplied by Baxter, at T = 37±1 °C and pH = 6.8 ±0.2.

2.3 Adhesion test

Adhesion of the Al_2O_3 film to the cpTi and Ti6Al7Nb was evaluated with the use of a scratch test.[15] During the test a scratch was made with the use of Rockwell diamond cone with gradual growth of the indenter's normal load. The critical force, a measure of adhesion, is the minimum normal force causing the loss of adhesion of the coat to the base. Evaluation of the critical force L_c based on the record of changes in acoustic emission, friction force and friction coefficient as well as a microscopic inspection with a light microscope, integrated with the platform. Tests were performed at the loading force, increasing from F_c = 0.03 N to 30 N and at the following working parameters: loading rate v_s = 100 N/min; table travel rate v_t = 10 mm/min, scratch length l = 3 mm.

2.4 Wettability test

Surface wettability and surface energy (SEP) were evaluated with the use of the Owens-Wendt method. The wetting-angle measurements used two liquids: distilled water (θw) (by Poch S.A.) and diiodomethane (θd) (by Merck). A measurement with a drop of the liquid and diiodomethane, placed on the outer layer of the material, was performed at the temperature T = 23 °C at the test stand incorporating a goniometer SURFTENS UNIVERSAL by OEG and a computer with Surftens 4.5 software to analyse the recorded drop image. Five drops of distilled water and diodomethane were applied onto the surface of each sample, each with capacity of 1.5 μL. The measurement began 20 s after the application of the drops. The duration of a single measurement was 60 s, with the sampling rate of 1 Hz. Next, the determined values of the contact angles θ and the surface energy were presented as mean values with a standard deviation.

3 RESULTS AND DISCUSSION

3.1 Potentiodynamic test

Polarization curves recorded for the substrates alone and samples covered with an Al_2O_3 layer deposited at a temperature of T = 150 °C and T = 300 °C for cpTi and Ti6Al7Nb are shown in **Figures 1** and **2**. Based on the received curves the characteristic values describing the resistance to pitting corrosion were determined (**Table 2**). Regardless of the type of substrate, a positive influence – improving the corrosion resistance – of the Al_2O_3 layer was established, as compared to baseline. An increase of corrosion potential E_{corr} and polarization resistance R_p was found. An increase of the application process temperature from 150 °C to 300 °C significantly reduced the corrosion resistance of the Al_2O_3 layer (**Table 2**).

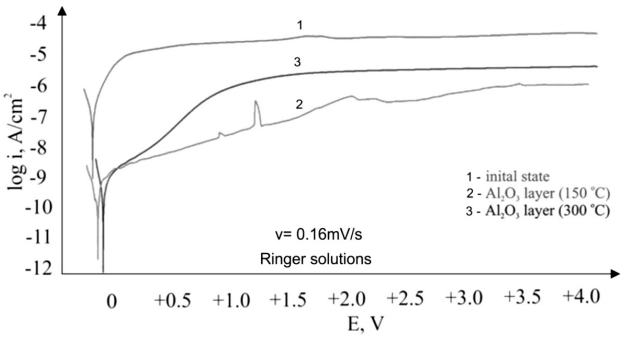

Figure 1: Polarization curves for the modified cpTi

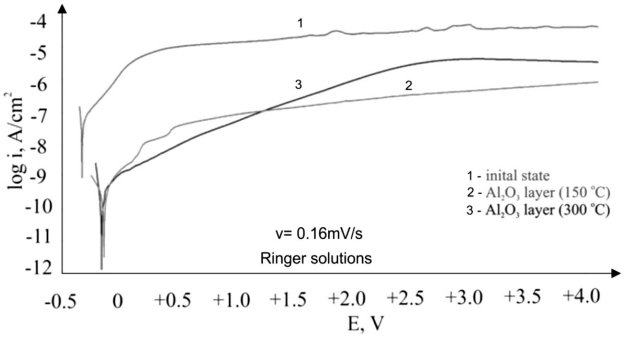

Figure 2: Polarization curves for the modified Ti6Al7Nb alloy

Table 2: The results of resistance to pitting corrosion test

Material	Temperature	E_{corr}, mV	R_p, MΩ cm²
cpTi	Initial state	-244	0.3
	150	-147	7.5
	300	-78	5.6
Ti6Al7Nb	Initial state	-309	0.1
	150	-155	5.1
	300	-126	4.0

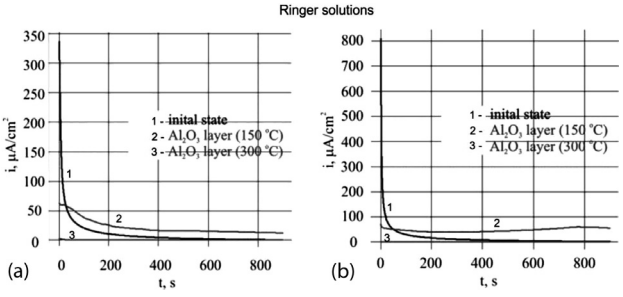

Figure 3: Examples of potentiostatic curves: a) cpTi in the initial state and with deposited Al_2O_3 layer, b) Ti6Al7Nb in the initial state and with deposited Al_2O_3 layer

3.2 Potentiostatic test

The test results of current density changes as a function of time in the test of resistance to crevice corrosion indicate that regardless of the type of the substrate (cpTi, Ti6Al7Nb), as well as the process temperature (150 °C, 300 °C) the Al_2O_3 layer is resistant to this type of corrosion (**Figures 3a** and **3b**). The results confirmed the formation of a compact Al_2O_3 oxide layer constituting a barrier separating the substrate from the corrosive environment in which the tests were performed.

3.3 Adhesion test

The results of the adhesion of the Al_2O_3 layer to the metallic substrate were shown in **Table 3** and **Figures 4** and **5**. The obtained results indicate the diverse adhesion of Al_2O_3 to the ground with both cpTi and Ti6Al7Nb. This is evidenced by the values of the individual parameters defined on the basis of the measurements. It was found that a sample with Al_2O_3 deposited on the Ti6Al7Nb surface shows better adhesion to the substrate (**Table 3**). Additionally, the influence of the process temperature on the adhesion of the analyzed layer, on both cpTi and Ti6Al7Nb, was found. Slightly better adhesion was observed in the case of the layer deposited using the ALD method at the temperature T = 300°C, regardless of the analyzed substrate material. During the test there was no acoustic emission signal, which indicates that the binding energy between the coating and the substrate was too low.

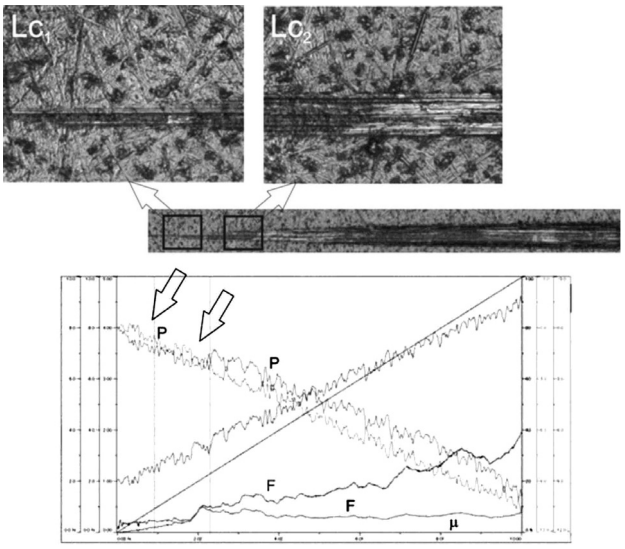

Figure 4: Examples of adhesion test results for the cpTi subjected to surface modification Al_2O_3 layer (T = 300 °C)

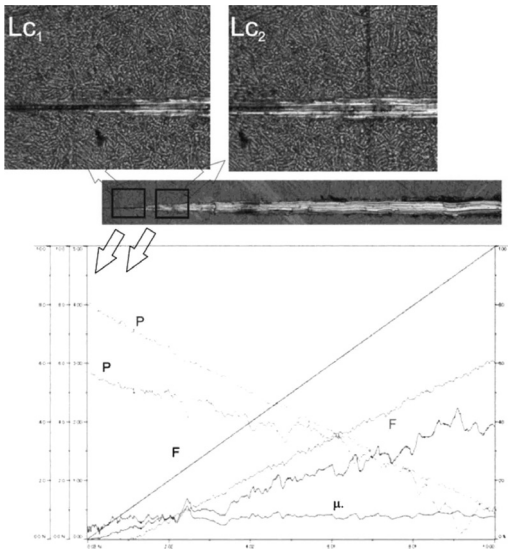

Figure 5: Examples of adhesion test results for the Ti6Al7Nb alloy subjected to surface modification Al_2O_3 layer (T = 300 °C)

Table 3: The results of scratch-test

Material	Temperature Al_2O_3 layer	Layer damages	Critical force F_n, N
cpTi	150 °C	Crack L_{c1}	0.33
		Delamination L_{c2}	1.02
	300 °C	Crack L_{c1}	0.55
		Delamination L_{c2}	1.14
Ti6Al7Nb	150 °C	Crack L_{c1}	1.32
		Delamination L_{c2}	2.42
	300 °C	Crack L_{c1}	1.20
		Delamination L_{c2}	2.89

3.4 Wettability test

The wettability test results were presented in **Table 4**. Based on the obtained results it was found that regardless of the substrate used, the Al_2O_3 layer showed hydrophobic properties. The average value of the contact angle for the Al_2O_3 layer, regardless of the temperature of the deposition process, was equal to θ_{avg} = 115°. On the other hand, the cpTi and Ti6Al7Nb substrates showed hydrophilic properties (θ_{avg} = 61°).

Table 4: Wettability test results

L_p	Ti			Ti6Al7Nb		
	Initial state (θ, °)	Al_2O_3 layer (T = 150 °C) (θ, °)	Al_2O_3 layer (T = 300 °C) (θ, °)	Initial state (θ, °)	Al_2O_3 layer (T = 150 °C) (θ, °)	Al_2O_3 layer (T = 300 °C) (θ, °)
1	56.9	118.2	116.8	68.2	117.8	112.5
2	58.1	109.7	124.3	65.3	114.0	107.2
3	57.8	111.8	121.8	66.9	119.7	117.0

4 CONCLUSIONS

In the ALD method, important parameters affecting the quality of the final layer are the number of cycles and the process temperature. Earlier works allowed the authors to specify the number of cycles for depositing layers with the best set of physicochemical properties.[11,16–17] On this basis, the application of a Al_2O_3 coating on a titanium substrate (cpTi and Ti6Al7Nb) at

temperatures of T = 150 °C and 300 °C was proposed. The number of cycles used was L_c = 830. Based on the results, a beneficial effect on pitting and crevice corrosion resistance of applied Al_2O_3 layer was determined, compared to initial state, devoid of the layer, regardless of the substrate used. The dependence was not shown during the layer's adhesion to the substrate test and the wettability test. No significant influence of the deposition process temperature on the obtained results was found. Proposing the appropriate conditions for the surface treatment using ALD method has promise and will contribute to the development of technological process with defined parameters of oxide layers manufacturing on implants used in bone surgery.

Acknowledgements

The publication was co-financed by the statutory grant of the Faculty of Mechanical Engineering of the Silesian University of Technology in 2015.

5 REFERENCES

[1] A. W. E. Hodgson, Y. Mueller, D. Forstwe, S. Virtanen, Electrochemical characterization of passive films on Ti alloys under simulated biological conditions, Electrochimica Acta, 47 (**2002**), 1913–1923

[2] B. Rahmati, A. D. Ahmed, W. Sarhan, J. Basirun, W. A. B. W. Abas, Ceramic tantalum oxide thin film coating to enhance the corrosion and wear characteristics of Ti6Al4V alloy, J. Alloys Compd., 676 (**2016**) 15, 369–376

[3] Q. Chen, G. A. Thouas, Metallic implant biomaterials, Materials Science and Engineering R87 (**2015**), 1–57, doi:10.1016/j.mser.2014.10.001

[4] G. K. Hyde, S. D. McCullen, S. Jeon, S. M. Stewart, H. Jeon, E. G. Loboa, G. N. Parsons, Atomic layer deposition and biocompatibility of titanium nitride nano-coatings on cellulose fiber substrates, Biomedical Materials, 4 (**2009**) 2, 025001, doi:10.1088/1748-6041/4/2/025001

[5] M. Basiaga, W. Walke, Z. Paszenda, A. Kajzer, The effect of EO and steam sterilization on mechanical and electrochemical properties of titanium grade 4, Mater. Tehnol., 50 (**2016**) 1, 153–158, doi:10.17222/mit.2016.241

[6] A. Kajzer,W. Kajzer, J. Dzielicki, D. Matejczyk, The study of physicochemical properties of stabilizing plates removed from the body after treatment of pectus excavatum, Acta Bioeng. Biomech., (**2015**) 2, 35–44

[7] A. Purniawana, P. J. Frencha, G. Pandraudb, P. M. Sarrob, TiO_2 ALD nanolayer as evanescent waveguide for biomedical sensor applications, Procedia Engineering 5 (**2010**), 1131–1135, doi:10.1016/j.proeng.2010.09.310

[8] M. S. Mozumder, A. H. Mourad, H. Perinpanayagam, J. Zhu, Nano-SiO_2 enriched biocompatible poweder coatings, Materials Today, (**2015**) 2, 147–152, doi:10.1016/j.matpr.2015.04.015

[9] J. Szewczenko, Formation of physical and chemical properties of surface layer on titanium alloys used for implants for traumatology and orthopedics, Wydawnictwo Politechniki Śląskiej, Gliwice, 2014

[10] W. Walke, Z. Paszenda, M. Basiaga, P. Karasiński, M. Kaczmarek, EIS study of SiO_2 oxide film on 316L stainless steel for cardiac implants, Information Technologies in Biomedicine, Advances in Intelligent Systems and Computing 284, Springer, 2014, 403–410, doi:10.1007/978-3-319-06596-0_38

[11] M. Basiaga, R. Jendruś, W. Walke, Z. Paszenda, M. Kaczmarek, M. Popczyk, Influence of surface modification on properties of stainless steel used for implants, Archives of Metallurgy and Materials, 60 (**2015**) 4, 2965–2969, doi:10.1515/amm-2015-0473

[12] E. Marin, L. Guzman, A. Lanzutti, W. Ensinger, L. Fedrizzi, Multilayer Al_2O_3/TiO_2 Atomic Layer Deposition coatings for the corrosion protection of stainless steel, Thin Solid Films, (**2012**) 522, 283–288

[13] L. Zhang, H. Jacob, G. Prosser, G. Fengb, D. Lee, Mechanical properties of atomic layer deposition-reinforced nanoparticle thin films, Nanoscale, 4 (**2012**) 20, 6543–6552, doi:10.1039/c2nr32016a

[14] ASTM F 746-04, Standard test method for pitting or crevice corrosion of metallic surgical implants materials

[15] PN-EN 1071-3:2007, Advanced technical ceramics, Methods of test for ceramic coatings, Part 3: Determination of adhesion and other mechanical failure modes in an attempt to scratch

[16] L. C. Xu, Effect of surface wettability and contact time on protein adhesion to biomaterial surfaces, Biomaterials, 28 (**2007**), 3273–3283, doi:10.1016/j.biomaterials.2007.03.032

[17] M. Basiaga, M. Staszuk, W. Walke, Z. Opilski, Mechanical properties of ALD TiO_2 layers on stainless steel substrate, Materialwissenschaft & Werkstofftechnik, 47 (**2016**) 5, 1–9

UDK 620.176.5:621.791.724:669.15
Original scientific article/Izvirni znanstveni članek

ISSN 1580-2949
MTAEC9, 51(4)643(2017)

IMPACT TOUGHNESS OF LASER-WELDED BUTT JOINTS OF THE NEW STEEL GRADE STRENX 1100MC

UDARNA ŽILAVOST LASERSKO VARJENIH ČELNIH SPOJEV PRI NOVOLEGIRANEM JEKLU STRENX 1100MC

Agnieszka Kurc-Lisiecka

University of Dąbrowa Górnicza, Rail Transport Department, Cieplaka 1C, 41-300 Dąbrowa Górnicza, Poland
a.kurc@wp.pl

Prejem rokopisa – received: 2016-07-31; sprejem za objavo – accepted for publication: 2016-11-08

doi:10.17222/mit.2016.234

The detailed influence of the energy input of autogenous laser welding by means of a modern solid-state disk laser on the structure of the weld metal, the heat-affected zone and the mechanical properties of 5.0-mm-thick butt joints of STRENX 1100MC was studied. Laser-welding trails were conducted over a wide range of energy inputs, from approximately 100 up to 400 J/mm. The studies showed no tendency for the cracking of butt joints, despite the low energy inputs of the welding. However, a significant decrease in the hardness was revealed in the heat-affected zone. The static tensile strength was found to be slightly lower (by approx. 8 %) compared to the tensile strength of the base material. There was also a strong relationship between the impact toughness of the test joints and the energy input of the laser welding. However, the impact toughness of the laser-welded joints was significantly lower than that of the base material. This article attempts to explain the drop in the toughness and the static tensile strength with respect to the structural transformations of the weld metal and the heat-affected zone, depending on the welding parameters, especially the energy input, and thus the heating conditions of the welding.

Keywords: laser welding, high-strength steel, toughness, butt joints, disk laser

Preiskovan je bil podroben vpliv dovedene energije avtogenega laserskega varjenja s pomočjo laserja na SSD-ju na strukturo varjenega jekla, na toplotno vplivano področje varjenja (angl. HAZ) in na 5.0-mm debele čelne spoje pri jeklu STRENX 1100MC. Lasersko varjene poteze so bile izvedene v širokem razponu energijskih vložkov, od približno 100 J/mm do 400 J/mm. Študije so pokazale, da čelni spoji ne pokajo kljub nizko-energijskemu dovajanju energije pri varjenju. Vendar pa se je pokazalao znatno znižanje mikrotrdote v toplotno vplivani coni. Ugotovljeno je bilo, da je statična natezna trdnost nekoliko nižja (ca. 8 %) v primerjavi z natezno trdnostjo osnovnega materiala. Ugotovljena je bila tudi močna povezava med udarno žilavostjo testnih spojev in dovedeno energijo med laserskim varjenjem. Kakorkoli, udarna žilavost lasersko varjenih spojev je bila občutno nižja kot pri osnovnem materialu. Članek poizkuša razložiti padec žilavosti in statično natezno trdnost glede na strukturne transformacije varjenega jekla in na toplotno prizadeta območja, odvisno od varilnih parametrov, zlasti dovajanja energije in s tem toplotnih pogojev varjenja.

Ključne besede: lasersko varjenje, visokotrdno jeklo, trdnost, čelni spoji, laserski disk

1 INTRODUCTION

A continuous and dynamic development in the field of steel metallurgy, plastic forming and heat treatment leads not only to an improvement of mechanical properties and overall performance of modern structural steels, but also to an implementation of completely new grades of advanced high-strength steels (AHSS) and super high-strength steels (SHSS), such as STRENX 1100MC.[1–7] This new steel grade shows the strength and yield point (1100 MPa) of quenched and tempered low-alloy steels, while being a low-carbon equivalent at a level similar to the typical thermomechanically rolled, fine-grained, microalloyed steels.[8–11] To be able to use such high strength and performance of this steel grade in practice, it is necessary to provide at least similar properties of the welded joints.[1–8,12–15] However, there is currently no method of conventional arc welding that could provide such high mechanical properties of welded joints.[16–22] Conventional welding technologies such as manual metal arc welding (MMAW), gas metal arc welding (GMAW) or submerged arc welding (SMAW) are cannot provide satisfactory properties of welded joints, especially in the case of steel grades having the yield point above the level of 900 MPa. That is why the leading steel manufacturers around the world continue to develop new steel grades, new solutions in the production process, the methods of forming properties, while paying the greatest attention to the importance of improving the weldability of modern high-strength and ultra-high-strength steels.

Therefore, the global industry's attention is focused on laser-welding technologies, which provide a much wider technological capabilities and flexibilities.[1,6,23–25] Laser-beam welding (LBW) is one of the most advanced welding technologies.[1,6,26] Its mechanisms of material heating, melting, and subsequent solidification and weld forming are significantly different, compared to conventional arc-welding processes.[6,22–28] Moreover, the intensity of laser-beam heating, the mechanism of surface melting, the penetration depth, the shaping of the fusion zone, the width/depth ratio and the volume of the weld

pool depend on laser-beam characteristics and also on processing parameters.[1,6] However, so far there has been no information about the laser welding of the new steel grade STRENX 1100MC. Therefore, the author undertook a research in the field of autogenous laser welding of the new steel grade STRENX 1100MC, recently introduced into the global industry. The aim of the work is to study the microstructure, morphology and mechanical properties of butt joints of STRENX 1100MC, 5.0 mm thick, and welded with a modern solid-state Yb:YAG disk laser.

2 EXPERIMENTAL PART

2.1 Material

The 5.0 mm thick plates of steel grade STRENX 1100MC, currently commercially available, were chosen for laser-welding tests. However, the steel plates were delivered by the WIELTON Company directly from the Swedish steelwork as experimental plates (melt).

The new grade of steel STRENX1100 MC is classified by the manufacturer as thermomechanically rolled fine-grained microalloyed steel. However, the mechanical properties of this steel go far beyond the steels specified in the standard for thermomechanically rolled steels (EN 10149-2). Additionally, details of the manufacturing process of the new steel grade are undisclosed by the manufacturer. The investigated steel with a nominal chemical composition of 0.16%C, 0.30%Si, 1.3%Mn, 0.018%Al, the sum of Nb+Ti+V with a maximum of 0.18 % in mass fractions and balance Fe has the minimum yield strength of 1100 MPa, a typical tensile strength of 1200–1460 MPa and an elongation of A5 min 6 % for a sheet thickness ≥ 3 mm. Specimens for the laser-welding test were cut from a 5.0-mm-thick steel plate into coupons with dimensions of (100.0 × 100.0) mm by means of a 2D laser cutting machine with a CO_2 generator. Surfaces to be welded were sand blasted and then cleaned with acetone.

2.2 Laser-welding procedure

The trials of welding were performed by means of a solid-state Yb:YAG disk laser emitted in the continuous-wave (cw) mode at a 1.03 μm wavelength with the maximum output power of 3.3 kW. The laser beam was focused on a diameter of 200 μm. First, the bead-on-plate welds were produced at the maximum output laser power of 3.3 kW and different welding speeds, as shown in **Table 1**. The bead-on-plate welds were produced to simulate the process of welding autogenous butt joints and to investigate the influence of the welding parameters on the penetration depth and weld shape. Based on the bead-on-plate welding trials, the optimum parameters for butt-joint welding were selected. A proper and full penetration of the 5.0-mm-thick steel plate, a proper shape of the weld with narrow face and root, and a narrow HAZ were chosen as criterions for the selection of the welding parameters for the test butt joints.

Table 1: Parameters of bead-on-plate laser welding of 5.0-mm-thick plates of STRENX 1100MC steel, using the Yb:YAG disk laser

Bead (joint)	Welding speed, m/min	Laser power (W)	Energy input (J/mm)	Remarks
1	2.0	3.3	99	LP, UF, S
2 (A)	1.5	3.3	132	HF, ERR, SP, FP
3 (B)	1.0	3.3	198	S, ERR, HF, FP
4	0.5	3.3	396	UF, S, FP, SP, HF, ERR

Other welding parameters: nominal beam-spot diameter: 200.0 μm, shielding-nozzle diameter: 8.0 mm, shielding gas: Ar (99.999%), gas feed rate on the top surface (face of a weld): 15.0 L/min, quality assessment of the welds: LP – lack of penetration, FP – full penetration, UF – undercut of the weld face, S – spatter, HF – hollow face, ERR – excessive root reinforcement, ER – excessive face reinforcement, SP – single pore

A further analysis showed that the bead-on-plate weld produced at a welding speed of 0.5 m/min (thus, the heat input was almost 400 J/mm) was extremely wide and overheated. On the other hand, the bead-on-plate weld produced at the maximum welding speed was characterized by an uneven width of the weld root at the limit of penetration. Therefore, the test butt joints used for a detailed analysis of the microstructure and for mechanical examinations were produced at the maximum laser power of 3.3 kW and welding speeds of 1.0 m/min and 1.5 m/min, respectively. Detailed parameters and technological conditions of autogenous laser welding are given in **Table 1**. The specimens to be welded were mounted to a clamping device to protect them against distortions. The weld pool was protected by an argon flow via four cylindrical nozzles with a diameter of 8.0 mm and set at an angle of 45° to the joint surface. The flow of argon was kept at 15 L/min. The laser beam with a beam spot diameter of 200.0 μm was focused on the top surfaces of the specimens to be welded.

2.3 Characterisation

When the laser-welding tests were completed, visual inspections (VT) were performed according to the procedure of quality control in welding. Next, metallographic and mechanical examinations were done. An examination of the structure was carried out by means of optical microscopes (OM) and a scanning electron microscope (SEM). The chemical composition of the base metal was determined using a glow discharge spectrometer (GDS). The mechanical tests included a technological bending test according to the PN-EN ISO 5173 standard, a static tensile test according to the PN-EN ISO 4136 standard and the Charpy V-notch test according to the PN-EN ISO 14556 standard. From each test joint, three samples were taken for the bending test, tensile test and toughness test.

Therefore, the mean values given are the results of the mechanical tests and examinations.

The Vickers microhardness was measured along the symmetry axes of the butt joints, and the microhardness profiles were determined. The microhardness values in specific regions of the surface layers were correlated with the structures.

3 RESULTS AND DISCUSSION

3.1 Macrostructure characterisation

Based on the preliminary tests of bead-on-plate laser welding, the energy input of approx. 100 J/mm (a laser power of 3.3 kW, a welding speed of 2.0 m/min) required for a full penetration of the 5.0-mm-thick plate of the STRENX 1100 MC steel was determined. The fully penetrated bead-on-plate weld was produced at the maximum output power of 3.3 kW of the applied disk laser TRUMPF TruDisk 3302 and a welding speed of 2.0 m/min. The face (top surface) width of the bead-on-plate weld produced at the minimum energy input was approx. 1.45 mm, while the root (back side) width was up to 0.25 mm. However, in some places along the weld root, the width was very small (almost zero), on the verge of a lack of penetration (**Figure 1c**).

The shape of the fusion zone (FZ) for all the bead-on-plate welds, produced with the disk laser in the investigated range of the processing parameters clearly indicates that the welds were produced in the keyhole welding mode, characteristic for a high-power-density laser beam. In the case of a bead-on-plate weld produced at the minimum energy input (100 J/mm), the FZ is columnar with almost parallel sidewalls and the depth/width ratio is 3.5. A further reduction in the speed of bead-on-plate welding at a constant value of the laser output power increased the width of the weld and the width of the heat-affected zone (HAZ) due to the increased energy input. For example, the face width of a bead-on-plate weld produced at the maximum energy input of 396 J/mm was very wide, over 6.0 mm (**Figure 1d**). It obviously indicates that the energy input was too high for the bead-on-plate laser welding of 5.0-mm-thick butt joints. Additionally, the HAZ width was very wide, over 1.5 mm (each side), indicating intensive heating and relatively slow cooling rates, which may lead to harmful structural transformations. It should also be noted that no cracks were found in the regions of the weld metal, or in the heat-affected zones. Based on the results obtained during the preliminary test of bead-on-plate laser welding, the welding speeds of 1.0 m/min and 1.5 m/min were considered as the optimum values at the laser output power of 3.3 kW, and thus energy inputs of 132 J/mm and 198 J/mm, respectively, were chosen for the laser welding of butt joints for the subsequent mechanical examinations.

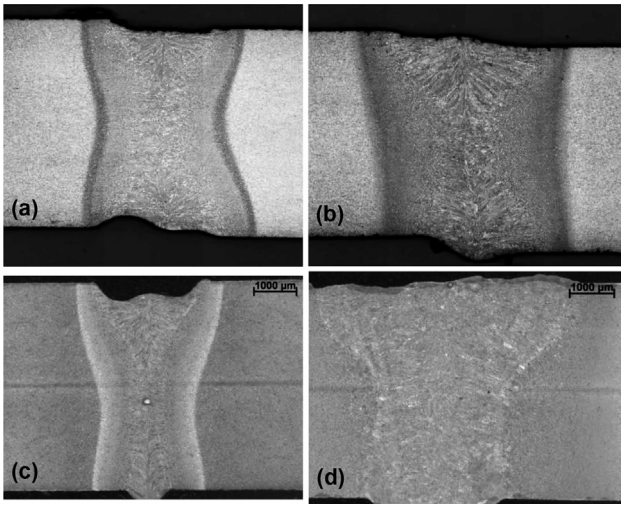

Figure 1: Optical micrographs of the 5.0-mm-thick butt joints of STRENX 1100 MC steel produced with autogenous laser welding: a) at 3.3 kW, 1.5 m/min, energy input of 132 J/mm (joint A), b) at 3.3 kW, 1.0 m/min, energy input of 198 J/mm (joint B) and bead-on-plate welds produced at: c) 3.3 kW, 2.0 m/min, energy input of 99 J/mm, d) 3.3 kW, 0.5 m/min, energy input of 396 J/mm

Direct observations, visual inspections (VT) and macrograph examinations of the test butt joints showed proper shapes of the weld face, the root and the FZ in the case of test joint B, laser welded at 1.0 mm/min and at a laser power of 3.3 kW, thus using the energy input of 198 J/mm (**Figure 1b**). The weld face and the root were very flat and even with proper reinforcements, which prove a high quality of such types of butt joints. For comparison, test joint A, welded at a slightly lower energy input of 132 J/mm (a laser power of 3.3 kW, a welding speed of 1.5 m/min), showed undercuts of the root and a slight collapse of the weld face, as can be seen in **Figure 1a**. The shapes of the FZs of both test welds were appropriate, exhibiting X configurations, the so-called hourglass configurations (**Figure 1**). Such a shape of the fusion zone during butt-joint welding with a laser beam is also typical for the keyhole-mode (deep penetration) welding. The depth/width ratio measured for test joint A was 1.9 and in the case of test joint B it was approx. 1.15. Examinations of the macrographs showed no internal imperfections of the two test butt joints.

3.2 Microhardness and mechanical examinations

The microhardness was measured on the cross-sections of the test butt joints. Based on the results, the microhardness profiles were determined (**Figure 2**). As can be seen in **Figure 2**, a sharp drop in the microhardness occurs in the HAZ region adjacent to the fusion zone, while the microhardness of the base material of the STRENX 1100 steel is in a range of 400–450 HV0.2 (**Figure 2**). The minimum value of the microhardness determined in the HAZ was a bit below 300 HV0.2, while the microhardness in the fusion zone (the weld metal) was stable and in the range 400–450 HV 0.2.

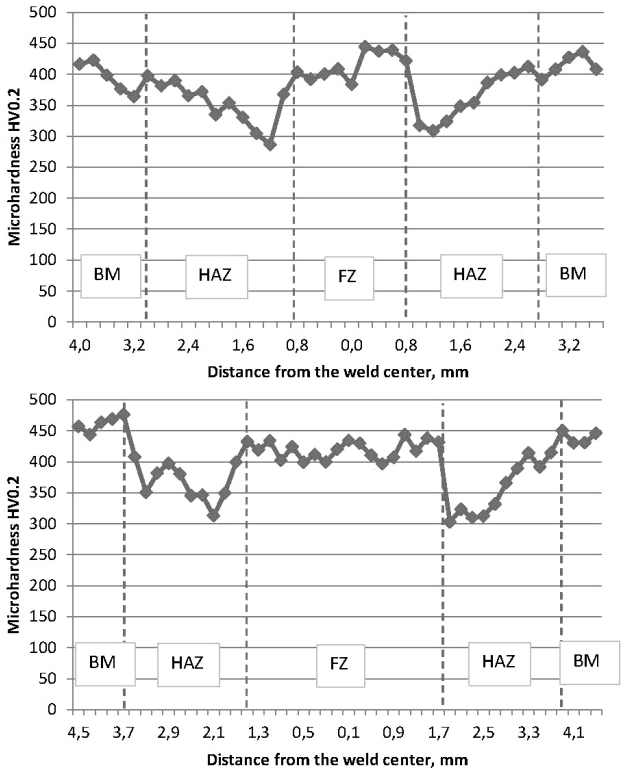

Figure 2: Microhardness profiles at the cross-sections of the 5.0-mm-thick butt joints of STRENX 1100 MC steel welded with a disk laser: a) joint A (energy input of 132 J/mm), b) joint B (energy input of 198 J/mm)

The technological bending tests exhibited a limited plasticity of the test butt joints due to a low angle of the bending, being in the range 85–90° for both test joints. On the other hand, the results of the static tensile tests showed that the tensile strength of the test joints is just slightly lower, compared to the strength of the base material (BM) of the STRENX 1100MC steel. The tensile strength for both tested joints was in a range of 1192–1295 MPa, while the tensile strength of the BM was 1324–1340 MPa. In all the tensile samples of the butt joints, fracture occurred in the weld metal. The reason for a lower tensile strength of the test joints in comparison to the BM is a decrease in the microhardness of the HAZ adjacent directly to the FZ, as shown in **Figure 2**.

The Charpy V-notch test, conducted at room temperature, showed that the impact toughness of the test butt joints is significantly lower than the impact toughness of the STRENX 1100MC steel. The experimentally determined impact toughness of the base material was in a very narrow range of 141–143 J/cm^2, while the impact toughness of test butt joint A, welded at the lower energy input of 132 J/mm (the laser power of 3.3 kW, the welding speed of 1.5 m/min) was just 57.9–78 J/cm^2, having the mean value of 70.6 J/cm^2. As can be easily calculated, the impact toughness accounts for only 50 % of that for the BM. On the other hand, the impact toughness of test joint B, welded at the higher energy input of 198 J/mm (the laser power of 3.3 kW, the welding speed of 1.0 m/min) was slightly higher, 86.13 J/cm^2, so about 60.6 % of the impact toughness of the BM.

SEM micrographs of the fracture surfaces of the test joints are presented in **Figures 3** and **4**. As can be seen, the fracture surfaces indicate a rather ductile dimple fracture mode in both cases (**Figures 3** and **4**). The impact toughness of the test joint welded at the higher energy input (joint B) is clearly higher, by about 22 %, compared to the impact toughness of the joint welded at the lower energy input (joint A). Additionally, the fracture surface of joint B exhibits a more ductile behaviour than the fracture surface of joint A (**Figures 3a** and **4a**). Thus, the results indicate that the impact toughness of the butt joints depends on the energy input of laser welding, thus on the thermal conditions, cooling rates and structure of the weld metal and the HAZ. However, high-magnification SEM micrographs of the fracture surfaces revealed discontinuities across the surfaces of both test joints, such as small pores (**Figures 3b** and **4b**). Inside the spherical discontinuities, inclusions were found.

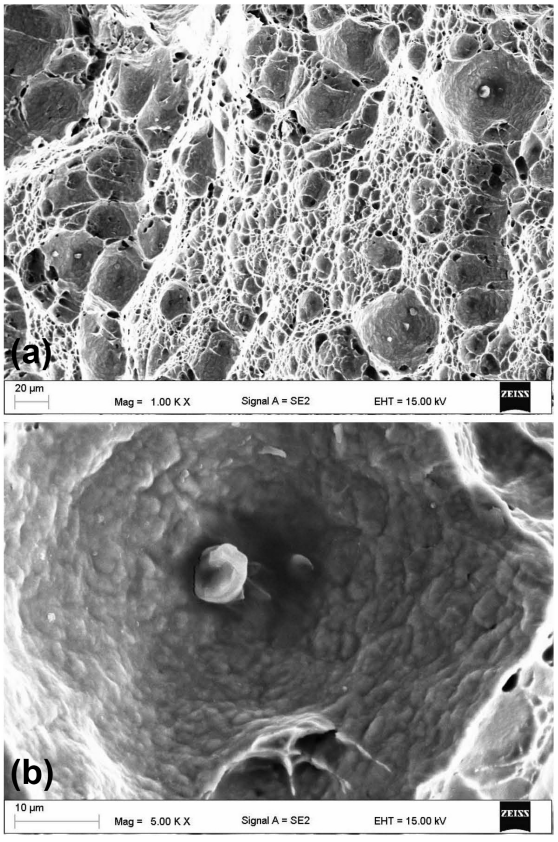

Figure 3: SEM micrographs of the fracture surface of test joint A (energy input of 132 J/mm) after the impact test of the joints: a) general view of the fracture surface, b) an inclusion placed in the material discontinuity

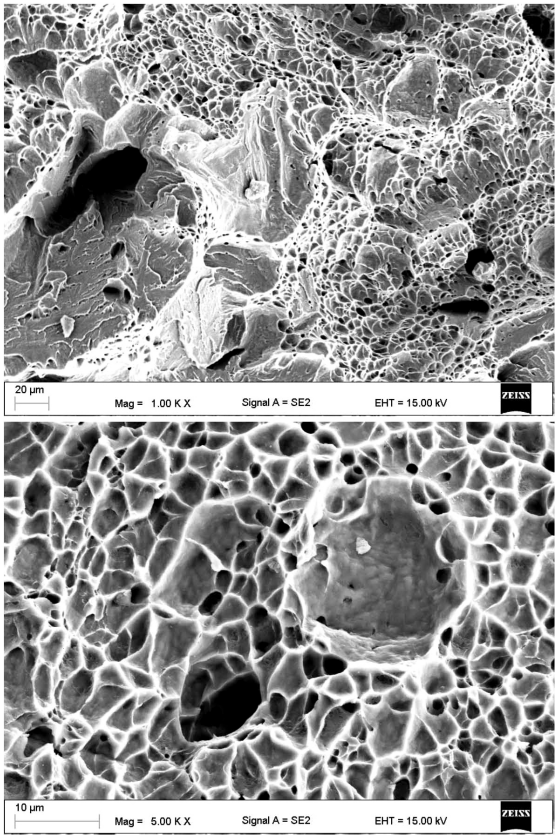

Figure 4: SEM micrographs of the fracture surface of test joint B (energy input of 198 J/mm) after the impact test of the joints: a) general view of the fracture surface, b) an inclusion placed in the material discontinuity

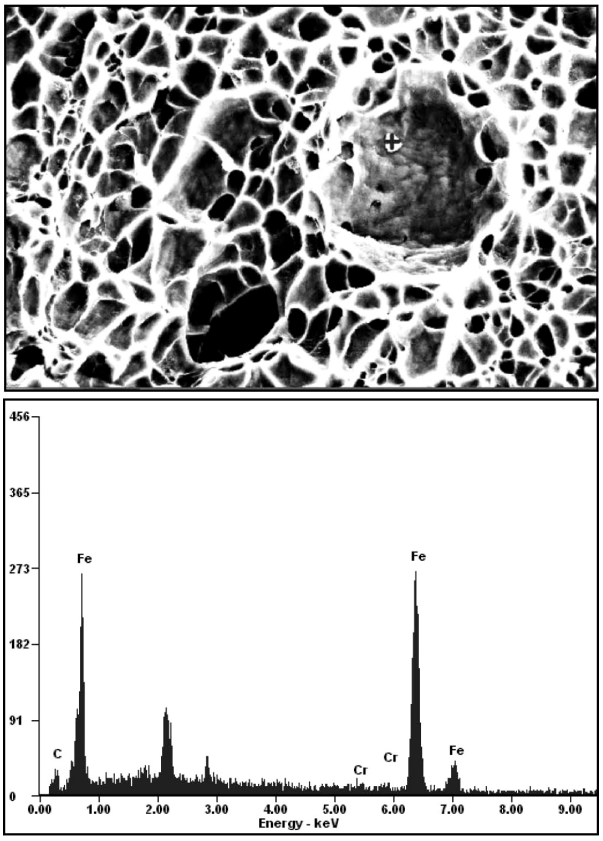

Figure 5: a) SEM micrograph of the fracture surface of test joint B (energy input of 198 J/mm) after the impact test of the joints and b) EDS spectrum of the inclusion in the spherical discontinuity

The EDS spectrum of an inclusion showed mainly iron (98.47 % Fe of mass fraction) and a small content of chromium (1.53 % Cr of mass fraction), as shown in **Figure 5b**. No traces of oxides were found. It indicates that the inclusions are rather metallic and a proper shielding-gas atmosphere was provided during the laser-welding tests. Thus, the micropores revealed during the examinations of the fracture surface are a result of the metal vapours produced during intensive heating of the liquid metal of the weld pool by the focused laser beam at a high intensity and during keyhole-mode welding, as reported by other researches.[1,17]

3.3 Microstructure examinations

In order to determine the microstructures of the weld metal and HAZ, the chemical composition of the base material was analyzed with the GDS method and the cooling times $t_{8/5}$ in a temperature range of 800–500 °C were calculated according to the procedure described in reference[17]. The cooling time $t_{8/5}$ calculated for the energy input of 198 J/mm of laser welding was below 1.3 s. The cooling time $t_{8/5}$ for the energy input of 132 J/mm was below 0.6 s. It must be noted that the cooling times are significantly shorter than the cooling times recommended for the typical quenched and tempered steel grades, which are in the range 5–15 s. Despite such short cooling times, the joints showed no tendency to cold cracking.

A detailed analysis of the chemical composition obtained with GDS showed that the investigated melt of the steel contains 0.139%C, 0.31%Si, 1.40%Mn, 0.7%Cr, 0.3%Ni, 0.06%Mo, 0.039%Al, 0.01% of both Ti and Cu, 0.006%V and 0.001%Nb.

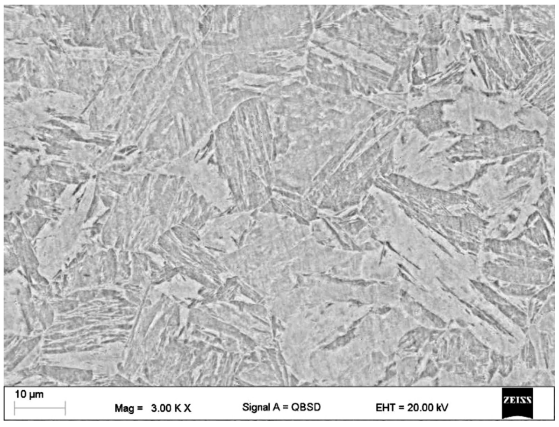

Figure 6: SEM micrograph of the base material STRENX 1100MC steel

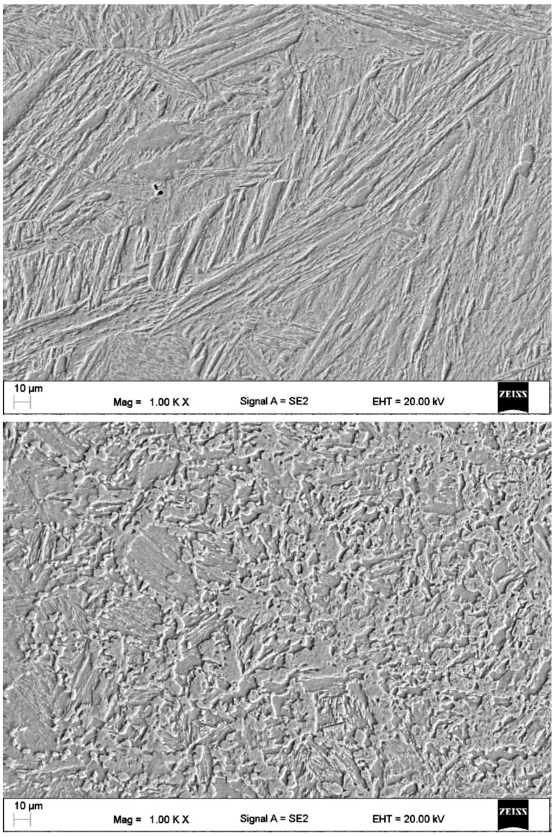

Figure 7: SEM micrographs of test butt joint A welded at the energy input of 132 J/mm (cooling time $t_{8/5}$ of 0.6 s): a) weld metal, b) HAZ region

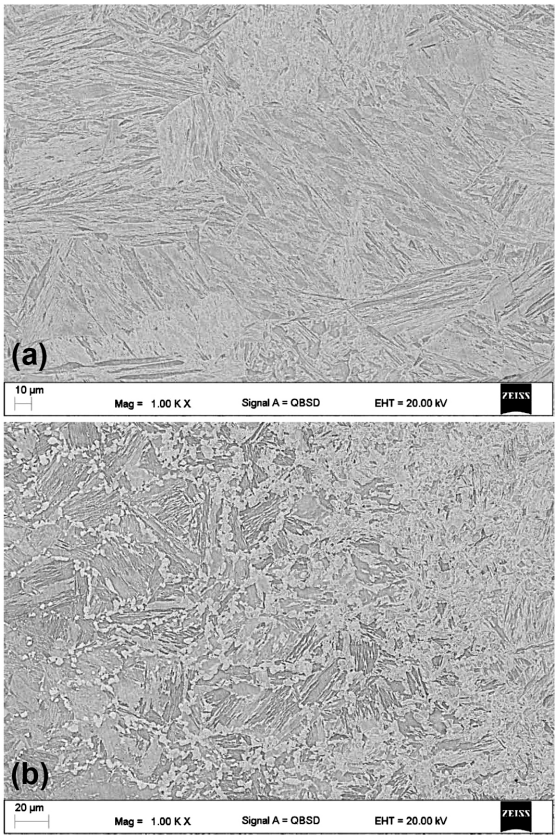

Figure 8: SEM micrographs of test butt joint B welded at the energy input of 198 J/mm (cooling time $t_{8/5}$ of 1.3 s): a) weld metal, b) HAZ region

Based on the determined chemical composition, the martensitic-transformation temperature Ms and carbon equivalent CET were calculated according to the procedure described in details in [28]. The calculated Ms temperature was 430.6 °C, while the carbon equivalent CET was just 0.328. The determined high Ms temperature and relatively low carbon equivalent, in relation to the high strength of the investigated steel, indicate that the hardenability of the steel is not very high.

SEM micrographs of the base material showed that the STRENX 1100MC steel is composed of a fine-grained bainitic-martensitic structure with a significant proportion of acicular ferrite and also traces of retained austenite (**Figure 6**). Additionally, precipitations of small carbides with a high dispersion can be identified in the structure. The structures of the weld metal and the HAZ of test butt joints are shown in **Figures 7** and **8**. It is clear that the structures and morphologies of the phase constituents in the weld metal depend on the energy input of laser welding. In general, the structure of the weld metal consists mainly of bainite, plate martensite, fine martensitic islands and also ferrite, mainly polygonal (α_{pf}) and allotriomorphic ferrite (α_{af}) (**Figures 7** and **8**).

As can be seen, the fraction (share) of plate martensite in the weld metal of test joint A, produced at the energy input of 132 J/mm (the laser power of 3.3 kW, the welding speed of 1.5 m/min) is approx. 20 % higher (calculated with planimetric measurements on the micrographs) compared to the weld metal of joint B, produced at 198 J/mm (the laser power of 3.3 kW, the welding speed of 1.0 m/min). Actually, plate martensite is the dominant structure of the weld metal of joint A, while the structure of the weld metal of joint B is more similar to the structure of the base material of STRENX 1100MC (**Figures 6, 7** and **8**). In this case, the structure is more diverse with a higher fraction of fine martensitic islands (acicular martensite). In summary, the share of the plate and acicular martensite had the greatest effect on the properties of the test joints, especially on the impact toughness. Cooling rates that are too high during the laser welding of the 5.0-mm-thick butt joints of the STRENX 1100MC steel lead to an increase in the plate martensite and thus a decrease in the toughness.

4 CONCLUSIONS

The obtained results of the laser welding of the STRENX 1100MC steel showed that it is possible to produce butt joints characterized by a proper shape, flat and even faces and roots, and free of any significant structural imperfections. The investigated high-strength

steel is characterized by a small amount of alloying elements, surprisingly low carbon equivalent CET, just 0.328, and, simultaneously, a high temperature of martensitic transformation Ms, about 430.6 °C. Despite the low carbon equivalent, the base metal has a fine-grained bainitic-martensitic structure with a high microhardness, 400–450 HV0.2. Despite a very rapid solidification of the weld metal and rapid cooling rates, no tendency to cracking of the weld metal or HAZ was found. A significant drop in the microhardness was revealed in the HAZ, resulting in the breaking of the samples during the tensile tests.

The differences in the impact toughness of the test joints are related to the share of the plate and acicular martensite in the weld metal of the tests joints. Cooling rates that are too high during the laser welding of the 5.0-mm-thick butt joints of the STRENX 1100MC steel are unfavourable because they lead to an increase in the plate martensite, which, in turn, decreases the toughness of the weld metal.

5 REFERENCES

[1] A. Lisiecki, Effect of heat input during disk laser bead-on-plate welding of thermomechanically rolled steel on penetration characteristics and porosity formation in the weld metal, Arch. Metall. Mater., 61 (**2016**) 1, 93–102, doi:10.1515/amm-2016-0019

[2] A. Kurc-Lisiecka, W. Ozgowicz, W. Ratuszek, J. Kowalska, Analysis of deformation texture in AISI 304 steel sheets, Sol. St. Phenom., 203–204 (**2013**), 105–110, doi:10.4028/www.scientific.net/SSP.203-204.105

[3] A. Lisiecki, Diode laser welding of high yield steel, Proc. SPIE 8703, Laser Technology 2012: Applications of Lasers, 87030S (January 22, 2013), doi:10.1117/12.2013429; doi:10.1117/12.2013429

[4] J. Górka, Weldability of thermomechanically treated steels having a high yield point, Arch. Metall. Mater., 60 (**2015**), 469–475

[5] A. Grajcar, M. Różański, S. Stano, A. Kowalski, Microstructure characterization of laser-welded Nb-microalloyed silicon-aluminum TRIP steel, J. Mater. Eng. Perform., 23 (**2014**), 3400–3406

[6] A. Lisiecki, Titanium matrix composite Ti/TiN produced by diode laser gas nitriding, Metals, 5 (**2015**), 54–69, doi:10.3390/met5010054

[7] R. Burdzik, Ł. Konieczny, Z. Stanik, P. Folega, A. Smalcerz, A. Lisiecki, Analysis of impact of chosen parameters on the wear of camshaft, Arch. Metall. Mater., 59 (**2014**), 957–963, doi:10.2478/amm-2014-0161

[8] J. Kusiński, S. Kac, A. Kopia, A. Radziszewska, M. Rozmus-Górnikowska, B. Major, L. Major, J. Marczak, A. Lisiecki, Laser modification of the materials surface layer – a review paper, Bull. Pol. Acad. Sci., Tech. Sci., 60 (**2012**), 711–728, doi:10.2478/v10175-012-0083-9

[9] K. Janerka, M. Pawlyta, J. Jezierski, J. Szajnar, D. Bartocha, Carburiser properties transfer into the structure of melted cast iron, J. Mat. Proc. Tech., 214 (**2014**) 4, 794–801

[10] Ł. Konieczny, R. Burdzik, B. Łazarz, Application of the vibration test in the evaluation of the technical condition of shock absorbers built into the vehicle, J. Vibroeng, 15 (**2013**) 4, 2042–2048

[11] A. Czuprynski, J. Górka, M. Adamiak, Examining properties of arc sprayed nanostructured coatings, Metalurgija, 55 (**2016**) 2, 173–176

[12] L. A. Dobrzański, W. Sitek, M. Krupiński, J. Dobrzański, Computer aided method for evaluation of failure class of materials working in creep conditions, J. Mat. Proc. Tech., 157 (**2004**), 102–106

[13] J. Bodzenta, A. Kaźmierczak, T. Kruczek, Analysis of thermograms based on FFT algorithm, J. Phys. IV, 129 (**2005**), 201–206

[14] G. Moskal, A. Grabowski, A. Lisiecki, Laser remelting of silicide coatings on Mo and TZM alloy, Sol. St. Phenom., 226 (**2015**), 121–126, doi:10.4028/www.scientific.net/SSP.226.121

[15] A. Lisiecki, Welding of thermomechanically rolled steel by Yb:Yag disk laser, Arch. Metall. Mater., 60 (**2015**), 2851–2859, doi:10.1515/amm-2015-0456

[16] A. Lisiecki, R. Burdzik, G. Siwiec, Ł. Konieczny, J. Warczek, P. Folęga, B. Oleksiak, Disk laser welding of car body zinc coated steel sheets, Arch. Metall. Mater., 60 (**2015**), 2913–2922, doi:10.1515/amm-2015-0465

[17] A. Lisiecki, Welding of thermomechanically rolled fine-grain steel by different types of lasers, Arch. Metall. Mater., 59 (**2014**), 1625–1631, doi:10.2478/amm-2014-0276

[18] R. Burdzik, T. Węgrzyn, Ł. Konieczny, A. Lisiecki, Research on influence of fatigue metal damage of the inner race of bearing on vibration in different frequencies, Arch. Metall. Mater., 59 (**2014**), 1275–1281, doi:10.2478/amm-2014-0218

[19] M. Staszuk, L. A. Dobrzański, T. Tański, W. Kwaśny, M. Musztyfaga-Staszuk, The effect of PVD and CVD coating structures on the durability of sintered cutting edges, Arch. Metall. Mater., 59 (**2014**), 269–274

[20] T. Węgrzyn, J. Piwnik, D. Hadryś, R. Wieszała, Car body welding with micro-jet cooling, J. Arch. Mater. Sci. Eng., 49 (**2011**), 90–94

[21] A. Grajcar, M. Różański, S. Stano, A. Kowalski, B. Grzegorczyk, Effect of heat input on microstructure and hardness distribution of laser welded Si-Al TRIP-type steel, Adv. Mater. Sci. Eng., 2014 (**2014**), doi:10.1155/2014/658947

[22] A. Lisiecki, Welding of titanium alloy by disk laser, Proc. SPIE 8703, Laser Technology 2012: Applications of Lasers, 87030T (January 22, 2013), doi:10.1117/12.2013431; doi:10.1117/12.2013431

[23] J. Słania, Influence of phase transformations in the temperature ranges of 1250–1000 °C and 650–350 °C on the ferrite content in austenitic welds made with T 23 12 LRM3 tubular electrode, Arch. Metall. Mater., 50 (**2005**), 757–767

[24] D. Janicki, Disk laser welding of armor steel, Arch. Metall. Mater., 59 (**2014**), 1641–1646, doi:10.2478/amm-2014-0279

[25] B. Slazak, J. Słania, T. Węgrzyn, A. P. Silva, Process stability evaluation of manual metal arc welding using digital signals, Mater. Sci. Forum, 730–732 (**2013**), 847–852

[26] W. Pakieła, T. Tański, Z. Brytan, K. Labisz, The influence of laser alloying on the structure and mechanical properties of AlMg5Si2Mn surface layers, Appl. Phys. A, 122 (**2016**), 352, doi:10.1007/s00339-016-9834-z

[27] M. Bonek, The investigation of microstructures and properties of high speed steel HS6-5-2-5 after laser alloying, Arch. Metall. Mater., 59 (**2014**), 1647–1651, doi:10.2478/amm-2014-0280

UDK 62-4-023.7:66.094.1
Original scientific article/Izvirni znanstveni članek

ISSN 1580-2949
MTAEC9, 51(4)651(2017)

FABRICATION AND OPTIMUM CONDITIONS OF A SUPERHYDROPHOBIC SURFACE USING A FACILE REDOX REACTION AND A SOLUTION-IMMERSION METHOD ON ZINC SUBSTRATES

IZDELAVA IN OPTIMALNI POGOJI ZA SUPERHIDROFOBNO POVRŠINO Z UPORABO REDOKS REAKCIJE IN Z METODO POTOPITVE V RAZTOPINO CINKOVIH SUBSTRATOV

Shichao Wei[1,2], Fumin Ma[1], Wen Li[1], Hong Li[1,2], Min Ruan[1], Zhanlong Yu[1], Wei Feng[1]

[1]Hubei Polytechnic University, Hubei Key Laboratory of Mine Environmental Pollution Control & Remediation, and School of Chemical and Materials Engineering, Huangshi 435003, China
[2]School of Physics and Electronic Science, Hubei Normal University, Huangshi 435003, China
mahongbin12345@sina.com

Prejem rokopisa – received: 2016-08-05; sprejem za objavo – accepted for publication: 2016-11-16

doi:10.17222/mit.2016.243

A superhydrophobic surface on a zinc substrate was prepared with a simple and economic redox reaction and a solution-immersion method, and the fabrication procedures and conditions were optimized. The effects of the reactant concentrations, reaction time, modifier types, modifier concentrations and modification time on the fabrication of the superhydrophobic surface were systematically studied by analyzing the water contact angle (CA) and SEM results. The results show that an excellent superhydrophobic surface was prepared when zinc plates were immersed in a 0.01-M $CuSO_4$ solution for 1 h and then modified with 5 % of mass fraction of lauric acid for 1 h. The water CA of the prepared surface was as high as 155.7°. The surface structure and composition of the superhydrophobic surfaces were characterized with SEM and FT-IR. The results show that the surface structure consists of a small number of particles and petal-like structures, and the product exhibits a long alkyl chain with a low surface energy, which contributes to the formation of the surface superhydrophobicity.

Keywords: superhydrophobic surface, cupric sulfate, redox reaction, solution immersion, optimum condition

Superhidrofobna površina na substratu iz cinka je bila pripravljena z enostavno in ekonomično redoks reakcijo in z metodo potopitve v raztopino ter z optimiziranjem postopkov in pogojev izdelave. Učinki koncentracij reagenta, reakcijski čas, modifikator učinka, njegove koncentracije in čas modifikacije pri izdelavi hidrofobne površine, so bili sistematično preučevani z analizo stika kota z vodo (CA) in s SEM- rezultati. Rezultat je pokazal, da je bila superhidrofobna površina odlično pripravljena, ko so bile cinkove plasti potopljene v 0,01-M $CuSO_4$ raztopino za 1 h in nato 1 h modificirane s 5 % lavrinske kisline. Kontaktni vodni kot pripravljene površine je 155,7°. Struktura površine in sestava superhidrofobne površine sta bili preiskovani s SEM in FT-IR analizo. Rezultati so pokazali, da je struktura površine sestavljena iz majhnega števila delcev in ima listno strukturo. Produkt ima dolgo alkilno verigo z nizko energijo površine, ki pripomore k formaciji superhidrofobnosti površine.

Ključne besede: superhidrofobna površina, bakrov sulfat, redoks reakcija, potopitev v raztopino, optimalno stanje

1 INTRODUCTION

Surface wetting is an important property, which is characterized by how a liquid makes contact with a solid surface. It depends upon the combined effects of the surface chemistry and surface morphology.[1–3] In nature, various biological surfaces, such as lotus leaves and rice leaves, exhibit surface-wetting properties, which are beneficial for their subsistence.[4–9] Superhydrophobicity and self-cleaning of lotus leaves were found to be a result of a waxy hierarchical surface structure.[10] Rice leaves exhibit anisotropic dewetting behavior due to anisotropic hierarchical structures with ordered arrangements.[11] Superhydrophobic surfaces, which exhibit self-cleaning and non-wetting properties with a water contact angle (CA) larger than 150°, have drawn much attention both in scientific research and applications based on their unique properties,[12,13] such as anti-fogging,[14] anti-icing,[15,16] and self-cleaning.[17,18] These properties are desirable for many industrial and biological applications such as anti-biofouling paints for boats, anti-sticking of snow for antennas and windows, self-cleaning wind shields for automobiles, metal refining, stain-resistant textiles, and anti-soiling architectural coatings.[17]

Inspired by nature, a large variety of methods have been developed to synthesize a superhydrophobic surface by constructing rough micro-nanostructures and modifying the surface with chemical materials with a low surface free energy, such as the sol-gel method,[19] electrohydrodynamics method,[20] plasma fluorination method,[21] laser etching,[22] chemical vapor deposition[23] and so on. Most of the methods need sophisticated and expensive equipment, so it is necessary to use a simple

method to fabricate a surperhydrophobic surface. It is well known that solution immersion is a simple method to prepare a surperhydrophobic surface. D. K. Sarkar and N. Saleema[24] prepared a leaf-like Ag micro-nanostructure on copper substrates by means of adjusting the concentration of the aqueous silver-nitrate solution and the reaction time. The water contact angle (CA) they got was about 162°. T. Ning, W. Xu and S. Lu[25] prepared a Pt micro-nanostructure on zinc substrates using solution immersion. They simply prepared a superhydrophobic surface using the replacement-deposition process. X. Hou, F. Zhou, B. Yu, W. Liu[26] prepared a superhydrophobic surface with hierarchical nanorods on zinc substrates by means of differential etching and hydrophobic modification. S. Wang, L. Feng, L. Jiang[27] fabricated a novel superhydrophobic surface merely by immersing a copper sheet into a solution of fatty acid at ambient temperature.

As a popular engineering material, zinc is widely used in industrial fields. Many ways have been used to fabricate a superhydrophobic surface on zinc substrates. H. Liu, S. Szunerits, W. Xu, R. Boukherroub[28] prepared a superhydrophobic surface on zinc substrates with a contact angle of 151° using a simple immersion technique. T. Ning, W. Xu, S. Lu[25] also introduced a simple way for constructing superhydrophobic surfaces with hierarchical flower-like micro-nanostructures using the deposition process.[25] The maximum CA value they got was about 171°. They also tested the stability of the prepared surface and proved that a pure platinum surface on a zinc substrate is stable. Nevertheless, the materials they used are not economic. It is necessary to find an economic material to fabricate a micro-nanostructure on a zinc substrate. In addition, economic surface modifiers with a lower surface energy can be used to promote the superhydrophobicity, such as lauric acid, myristic acid, palmitic acid and octadecanoic acid.

In this work, we tried to fabricate a superhydrophobic surface on a zinc substrate using a simple redox reaction and surface modification. The micro-nanostructure on the zinc substrates was created by immersing zinc plates in aqueous solutions of copper sulfate with different concentrations and for different times. The superhydrophobic surface was prepared by modifying the surface with different concentrations of the modifier and for different times. The conditions for preparing superhydrophobic surfaces were further optimized. The procedure is environmentally friendly, economic and easy to control.

2 EXPERIMENTAL PART

2.1 Materials

All the reagents used were of the analytical-reagent (AR) grade and used as received without further purification. A zinc substrate (10 × 10 × 0.2) mm with a purity of 99.9 % was obtained from Tianjin Damao Chemical Reagent Co. Ltd., China. Copper sulfate was purchased from Tianjin Kaitong Chemical Reagent Co. Ltd., China. Lauric acid was purchased from Tianjin Tailande Chemical Regent Co. Ltd., China. The other experimental chemicals of the analytical-reagent grade were purchased from Shanghai Chemical Regent Co. Ltd., China.

2.2 Preparation of a micro-nanostructure on zinc substrates

Before the experiment, the surface of zinc was polished with abrasive papers to remove the oxides and then cleaned ultrasonically in sequence with alcohol and deionized water, each time for 10 min to remove the impurities of the zinc surface. After being dried at ambient temperature, dried zinc specimens were immersed in a $CuSO_4$ solution (a series of $CuSO_4$ solutions with the Cu^{2+} concentration ranging from 0.002 to 0.05 mol/L) for a few minutes at room temperature. Then the immersed specimens were rinsed with distilled water and finally dried at 120 °C in air for 20 min. The plate with the highest CA was considered for the optimized reaction time and reactant concentration.

2.3 Modification

The plates were etched using the optimized reaction time and solution concentration and then they were modified with different modifiers for 1h, such as lauric acid, myristic acid, palmitic acid and octadecanoic acid with a concentration of 5 % mass fraction in ethanol. The plate with the highest CA was considered for the optimized modifier. Then the plates were modified with the optimized modifier at different concentrations of (1, 2, 5, 10, 15, 20, 30 and 40) % mass fractions, and then the optimized concentration could be found.

2.4 Characterizations

Both CA values were measured with a contact-angle goniometer (FTA 1000, First Ten Ångstroms Inc., USA) following the standard procedures. Water droplets were placed at four positions on one sample, and the averaged value was adopted as the contact angle. The volume of an individual water droplet used for the static CA measurements was about 5 μL. All Fourier transform infrared (FT-IR) spectra were obtained with a FT-IR spectrometer (Bruker Tensor 27, Germany). The micro-nanostructure of the superhydrophobic surfaces was observed with a scanning electron microscope (SEM, HITACHI, S-3400, Japan).

3 RESULTS AND DISCUSSION

3.1 Influence of the reactant concentration and time

The effects of the $CuSO_4$ concentration and reaction time on the surface wettability of the obtained surfaces were meticulously studied using CA measurements (**Figure 1**). The zinc plates were immersed in the solu-

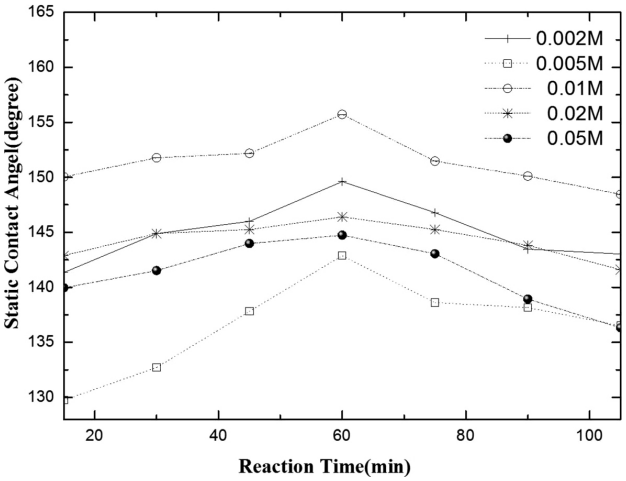

Figure 1: Curves of the water contact angle of the prepared samples as a function of the concentration of the $CuSO_4$ solution and reaction time

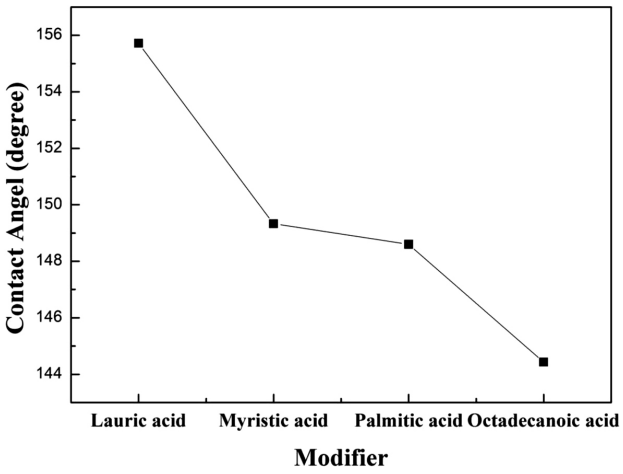

Figure 2: Curves of the contact angle versus the modifier types. The modifiers are lauric acid, myristic acid, palmitic acid and octadecanoic acid

tions with different $CuSO_4$ concentrations ranging from 0.002 to 0.05 M for different times. Then the reaction products were modified with 5 % mass fraction of lauric acid-ethanol solution for 1 h. As shown in **Figure 1**, the water CAs of the surfaces varied significantly depending upon the concentration of the $CuSO_4$ solution under the condition of a constant reaction time and the reaction time under the condition of a constant $CuSO_4$ concentration.

With an increase in the $CuSO_4$ concentration, the values of the CA increase at first. When the $CuSO_4$ concentration is 0.01 M, the CAs obtain their maximum values. As the $CuSO_4$ concentration continues to grow, the CAs decrease. In addition, the CAs reach their maximum values when the reaction time is 1 h for different concentration curves. It therefore indicates that 0.01 M is the optimum concentration and 1 h is the optimum reaction time. The change trend of the CAs may be a result of an increase of the amount of the deposition product formed on the surface and the resulting changes in the surface roughness. With an increase in the $CuSO_4$ concentration, the quantity of deposition increases under the constant reaction time. As the reaction time increases, the quantity of the product also increases under the constant $CuSO_4$ concentration. In fact, M. Miwa, A. Nakajima, A. Fujishima, K. Hashimoto, T. Watanabe[29] found that surfaces with a water contact angle of 150° could be developed by introducing a proper roughness to the materials with low surface energies. Thus, when the product quantity reaches a certain value, the value of the surface roughness is proper, resulting in the maximum CA.

3.2 Influence of the kind of modifier

Figure 2 shows the water CA for the zinc surfaces, reacted for 1 h and modified with different modifiers (lauric acid, myristic acid, palmitic acid and octadecanoic acid) for 1 h. The CA is 155.7°, 149.3°, 148.6°, and 144.4° when the surface is modified with lauric acid, myristic acid, palmitic acid and octadecanoic acid, respectively. The cause of this phenomenon is the same mass fraction because lauric acid's molecular weight is minimum, and the numbers of myristic acid's or palmitic acid's molecules in the unit volume are lower than the number of molecules of lauric acid. It can be concluded that among these modifiers, lauric acid is the most powerful for achieving the best superhydrophobicity.

3.3 Influence of modifier concentrations

Figure 3 shows the water CA for the zinc surfaces reacted for 1 h and modified with a lauric acid–ethanol solution with concentrations of (1, 2, 4, 5, 10, 15, 20 and 25) % for 1 h. The CA is 144.5°, 146.4°, 150.6°, 155.7°, 145.9°, 144.0°, 142.8° and 141.0°. The CAs of the surfaces vary significantly depending upon the concentration of the lauric acid solution under the conditions of constant reactant concentrations and reaction time

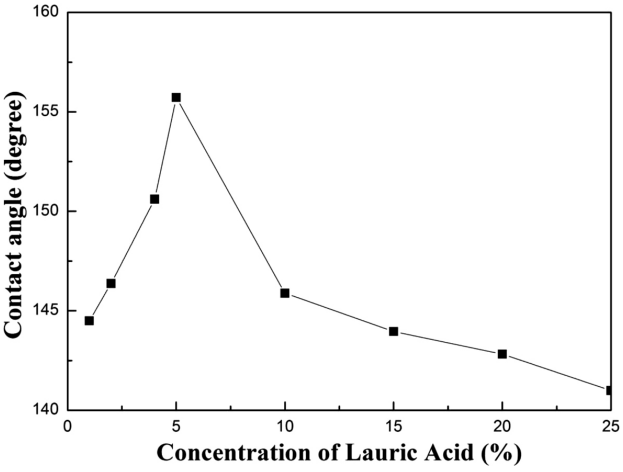

Figure 3: Curves of the contact angle versus the lauric-acid concentration

(0.01M $CuSO_4$ concentration and 1 h reaction time). When the concentration of lauric acid is 5 % mass fraction, the water CA reaches the maximum value of about 155.7°. This indicates that for the lauric-acid modifier, 5 % of mass fraction is the optimum concentration. When the concentration of lauric acid is less than 5 % of mass fraction, the CAs of the surfaces increase with the concentration of lauric acid. When the lauric-acid concentration is increased, there are more deposit products on the surface structure, which may damage the prepared micro-nanostructure on the zinc plate so that the deep-seated rough structure obtained with a redox reaction cannot play an effective role in the preparation of the final surfaces, which results in a decrease in the water CA.

3.4 Influence of the modification time

Figure 4 shows the water CAs for the zinc surfaces reacted for 1 h and modified with 5 % mass fraction of lauric acid for different modification times of (0.5, 1, 1.5, 2, 3, 4) h and 5 h. The CA is 147.3°, 155.7°, 147.7°, 145.3°, 145.2°, 145.2° and 144.6°, respectively. It is clear that 1 h is a suitable modification time. The reason for this is the fact that a chemical reaction taking 0.5 h is not completed and the surface modification is not completed either. On the other hand, if the chemical-reaction time is greater than 1 h, a layer of lauric-acid self-assembled molecular film forms on the micro-nanostructure surface, covering the original micro-nanostructure.

3.5 Surface micro-nanostructure and composition of superhydrophobic surfaces

Figure 5 shows digital images and the wetting property of water droplets on the untreated surface and the prepared superhydrophobic surface using water-contact-angle measurements, demonstrating the superhydrophobicity of the prepared surface. The water contact angle of the untreated zinc substrate is 64.1° (the inset in **Figure 5a**) while the treated zinc substrate surface exhibits a water-contact-angle value of 155.7° (the inset in **Figure 5b**). A smooth zinc surface is hydrophilic, but a rough modified zinc surface becomes superhydrophobic. It is well known that the roughness structure and the chemical composition of a surface result in the wettability of a solid surface. A successful fabrication of a superhydrophobic surface is believed to be a cooperative effect of a surface structure prepared with a redox reaction and a surface modification with low-surface-energy materials.

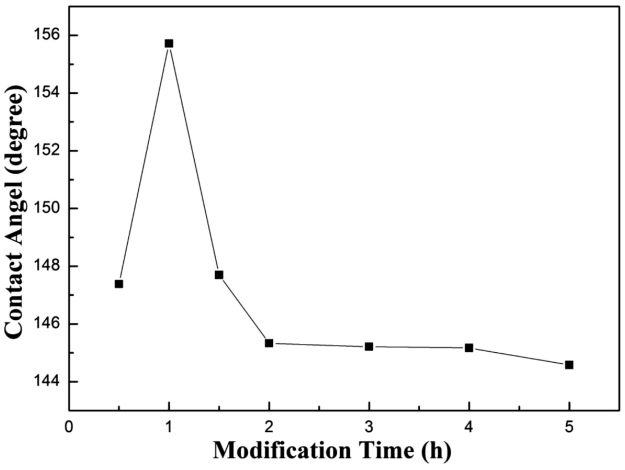

Figure 4: Water contact angles of the prepared samples for different modification times ranging from 0.5 h to 5.0 h

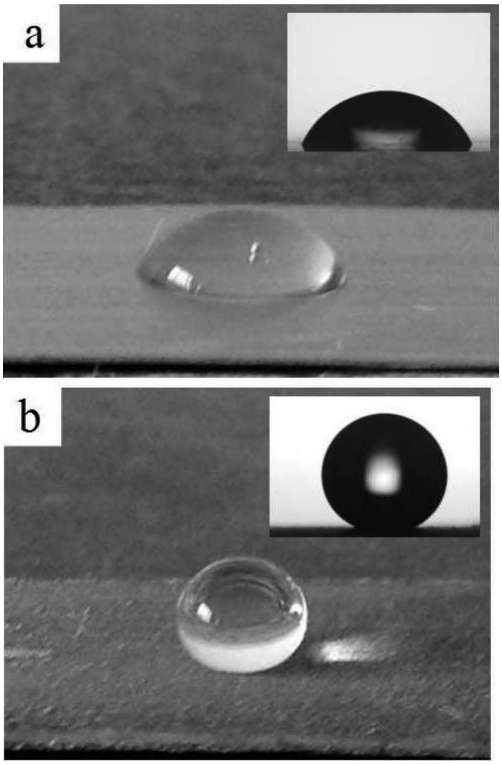

Figure 5: Photographs of a water droplet on the surfaces of: a) untreated zinc substrate and b) zinc substrate treated under the optimum condition. The insets correspond to the water contact angles

The surface micro-nanostructure was further studied with scanning electronic microscopy (SEM) as shown in **Figure 6**. There are obvious differences as the reaction time changes from 15 min to 105 min. **Figures 6a** and **6b** are SEM images of a 15-min reaction at 2000× and 6000× magnifications, respectively. The results show that a small amount of particles and petal-like structures formed on the zinc substrate. The average diameter of the particles is about 400 nm, as shown in **Figure 6b**; that is, a certain micro-nanostructure is formed, which makes the contact angle to be about 150°. **Figures 6c** and **6d** are SEM images of a 1-h reaction at 2000× and 5000× magnifications, respectively. Compared with

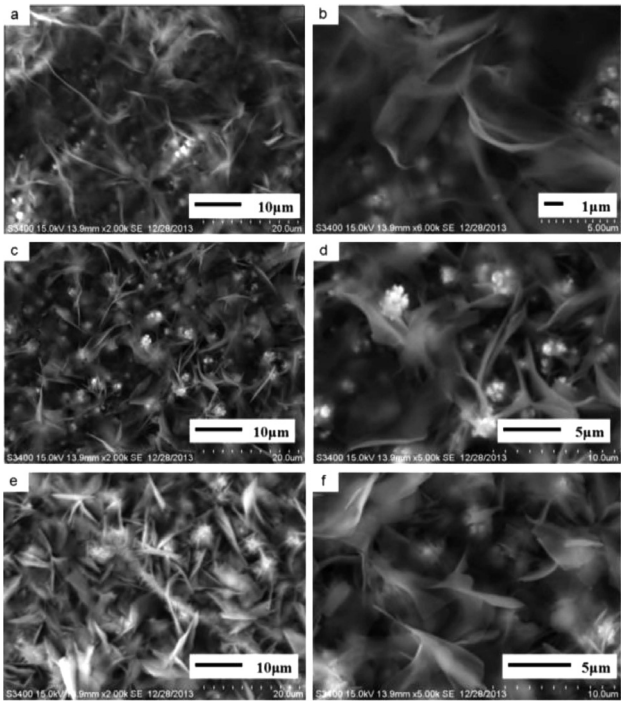

Figure 6: SEM images of the superhydrophobic surfaces on zinc substrates reacted in a 0.01 M $CuSO_4$ solution for different times and modified with 5 % of lauric acid-ethanol solution for 1 h: a) 15 min reaction, 2000×; b) magnified part of a), 6000×; c) 1 h reaction, 2000×; d) magnified part of c), 5000×; e) 105 min reaction, 2000×; f) magnified part of e), 5000×

Figures 6a and **6b**, the petal-like structures become dense and the average diameter of the particles increases to about 1 μm. A certain degree of hierarchical structure is formed when the reaction time rises to 1 h. This kind of hierarchical structure will keep the air in the interspaces when a droplet drops on the surface structure. Combined with the surface modification with a layer of low-surface-energy materials, the contact angle reaches about 155.7°. However, when extending the reaction time to 105 min, the petal-like micro-nanostructure becomes bigger as shown in **Figures 6e** and **6f**. The contact angle decreases to 148.5°.

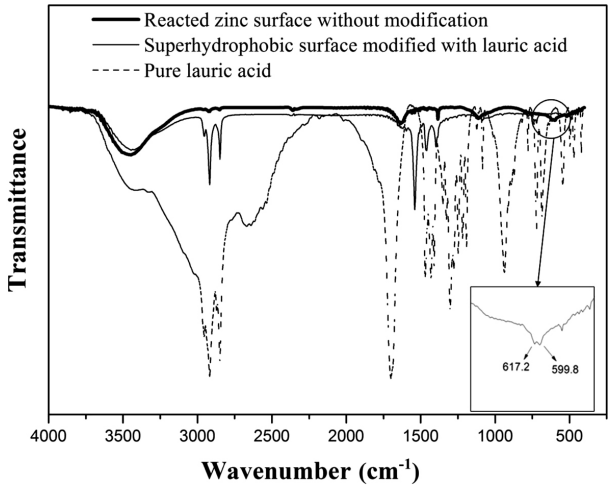

Figure 7: FT-IR spectra of lauric acid (dotted line), the zinc surface reacted for 105 min without a modification (solid line), and the surperhydrophobic surface reacted for 105 min and modified with 5 % mass fraction of lauric acid-ethanol solution for 1 h (thick line)

Figure 7 shows the change in the surface composition of the prepared superhydrophobic surfaces on the zinc substrates. The two peaks at 599.8 cm^{-1} and 617.2 cm^{-1} that appeared in the FT-IR spectra of the reacted zinc surface without a modification are the Cu-O stretching.[30,31] Compared with the reacted zinc surface without a modification, there are two new peaks at 2849 cm^{-1} and 2918 cm^{-1} in the FT-IR spectra of the superhydrophobic surface, which were identified as the symmetric and asymmetric vibrations of $-CH_2$ and $-CH_3$ groups of lauric acid, respectively. What is more, the stretching vibration of the free C=O band from lauric acid at 1701 cm^{-1} disappeared and a new band appeared at 1539 cm^{-1}. This goes to prove the C=O stretching vibration of coordinated COO^- moieties to Cu^{2+} ions. Thus, the results demonstrate that $CH_3(CH_2)_{10}COO^-$ and Cu^{2+} formed a bond of $Cu(CH_3(CH_2)_{10}COO)_2$ on the zinc surface. The combination of the product with a low surface energy and the micro-nanostructure allows the prepared surface to have superhydrophobic properties.

4 CONCLUSIONS

In summary, we have prepared surperhydrophoic surfaces on zinc substrates using a simple redox reaction and the solution-immersion method. This fabrication strategy is based upon the replacement process and modification. In addition, we also investigated the optimum conditions. The results confirmed that the surface could be prepared by immerging zinc plates in a 0.01 M $CuSO_4$ solution for 1 h, using 5 % mass fraction of lauric acid-ethanol solutions to modify the surface for 1 h. The corresponding water CA of the surface was as high as 155.7°. The present work provides a simple and economic method for preparing commendable superhydrophobic zinc surfaces, which holds bright prospects in our daily life due to its simple and economic process.

Acknowledgements

The financial assistance of the National Nature Science Foundation of China (51202082), the Natural Science Foundation of Hubei Province (2010CDA026 and 2012FFB01001), the Key Program of Hubei Provincial Department of Education (Z20104401), the Outstanding Scientific and Technological Innovation Team Project of Universities in Hubei Province (T201423) and the Talent Program of Hubei Polytechnic University (11yjz04R) is acknowledged.

5 REFERENCES

[1] S. R. Yu, J. A. Liu, W. Diao, W. Li, Preparation of a bionic microtexture on X52 pipeline steels and its superhydrophobic behavior, Journal of Alloys and Compounds, 585 (**2014**), 689–695, doi:10.1016/j.jallcom.2013.09.042

[2] C. Jin, J. Li, S. Han, J. Wang, Q. Yao, Q. Sun, Silver mirror reaction as an approach to construct a durable, robust superhydrophobic surface of bamboo timber with high conductivity, Journal of Alloys and Compounds, 635 (**2015**), 300–306, doi:10.1016/j.jallcom.2015.02.047

[3] W. Li, A. Amirfazli, Hierarchical structures for natural superhydrophobic surfaces, Soft Matter, 4 (**2008**), 462–466, doi:10.1039/b715731b

[4] G. D. Bixler, B. Bhushan, Bioinspired rice leaf and butterfly wing surface structures combining shark skin and lotus effects, Soft Matter, 8 (**2012**), 11271–11284, doi:10.1039/C2SM26655E

[5] H. Zhang, W. Li, D. Cui, Z. Hu, L. Xu, Design of lotus-simulating surfaces: Thermodynamic analysis based on a new methodology, Colloids and Surfaces A: Physicochemical and Engineering Aspects, 413 (**2012**), 314–327, doi:10.1016/j.colsurfa.2012.01.036

[6] S. H. Hsu, K. Woan, W. Sigmund, Biologically inspired hairy structures for superhydrophobicity, Materials Science and Engineering R, 72 (**2011**) 10, 189–201, doi:10.1016/j.mser.2011.05.001

[7] M. J. Hancock, K. Sekeroglu, M. C. Demirel, Bioinspired directional surfaces for adhesion, wetting, and transport, Advanced Functional Materials, 22 (**2012**) 11, 1–12, doi:10.1002/adfm.201103017

[8] K. Liu, X. Yao, L. Jiang, Recent developments in bio-inspired special wettability, Chemical Society Reviews, 39 (**2010**), 3240–3255, doi:10.1039/B917112F

[9] M. Liu, S. Wang, L. Jiang, Bioinspired multiscale surfaces with special wettability, MRS Bulletin, 38 (**2013**) 5, 375–382, doi:10.1557/mrs.2013.100

[10] A. Marmur, The lotus effect: superhydrophobicity and metastability, Langmuir, 20 (**2004**) 9, 3517–3519, doi:10.1021/la036369u

[11] L. Feng, S. Lin, Y. Li, H. Li, L. Zhang, J. Zhai, Y. Song, B. Liu, L. Jiang, D. Zhu, Super-hydrophobic surface from natural to artificial, Advanced Materials, 14 (**2002**) 24, 1857–1860, doi:10.1002/adma.200290020

[12] W. Li, A. Amirfazili, Superhydrophobic surfaces: adhesive strongly to water, Advanced Materials, 19 (**2007**), 3421–3422, doi:10.1002/adma.200601764

[13] A. Lafuma, D. Quéré, Superhydrophobic states, Nature Materials, 2 (**2003**), 457–460, doi:10.1038/nmat924

[14] J. Drelich, E. Chibowski, D. D. Meng, K. Terpilowski, Hydrophilic and superhydrophilic surfaces and materials, Soft Matter, 7 (**2011**), 9804–9828, doi:10.1039/C1SM05849E

[15] M. Ruan, W. Li, B. Wang, B. Deng, F. Ma, Z. Yu, Preparation and anti-icing behavior of superhydrophobic surfaces on aluminum alloy substrates, Langmuir, 29 (**2013**) 27, 8482–8491, doi:10.1021/la400979d

[16] J. Yang, W. Li, Preparation of superhydrophobic surfaces on Al substrates and the anti-icing behavior, Journal of Alloys and Compounds, 576 (**2013**), 215–219, doi:10.1016/j.jallcom.2013.04.060

[17] X. M. Li, D. Reinhoudt, M. Crego-Calama, What do we need for a superhydrophobic surface? A review on the recent progress in the preparation of superhydrophobic surfaces, Chemical Society Reviews, 36 (**2007**), 1350–1368, doi:10.1039/B602486F

[18] J. Hasan, H. K. Webb, V. K. Truong, G. S. Watson, J. A. Watson, M. J. Tobin, G. Gervinskas, S. Juodkazis, J. Y. Wang, R. J. Crawford, E. P. Ivanova, Spatial variations and temporal metastability of the self-cleaning and superhydrophobic properties of damselfly wings, Langmuir, 28 (**2012**) 50, 17404–17409, doi:10.1021/la303560w

[19] Y. Fan, C. Li, Z. Chen, H. Chen, Study on fabrication of the superhydrophobic sol–gel films based on copper wafer and its anti-corrosive properties, Applied Surface Science, 258 (**2012**) 17, 6531–6536, doi:10.1016/j.apsusc.2012.03.072

[20] L. Jiang, Y. Zhao, J. Zhai, A lotus-leaf-like superhydrophobic surface: a porous microsphere/nanofiber composite film prepared by electrohydrodynamics, Angewandte Chemie, 116 (**2004**), 4338–4341, doi:10.1002/ange.200460333

[21] I. Woodward, W. C. E. Schofield, V. Roucoules, J. P. S. Badyal, Super-hydrophobic surfaces produced by plasma fluorination of polybutadiene films, Langmuir, 19 (**2003**) 8, 3432–3438, doi:10.1021/la020427e

[22] F. Chen, D. Zhang, Q. Yang, B. Dao, X. Li, X. Hao, Y. Ding, J. Si, X. Hou, Anisotropic wetting on microstrips surface fabricated by femtosecond laser, Langmuir, 27 (**2011**) 1, 359–365, doi:10.1021/la103293j

[23] Y. Wu, H. Sugimura, Y. Inoue, O. Takai, Thin films with nanotextures for transparent and ultra water-repellent coatings produced from trimethylmethoxysilane by microwave plasma CVD, Chemical Vapor Deposition, 8 (**2002**) 2, 47–50, doi:10.1002/1521-3862(20020304)8:2<47::AID-CVDE47>3.0.CO;2-#

[24] D. K. Sarkar, N. Saleema, One-step fabrication process of superhydrophobic green coatings, Surface and Coatings Technology, 204 (**2010**) 15, 2483–2486, doi:10.1016/j.surfcoat.2010.01.033

[25] T. Ning, W. Xu, S. Lu, One-step controllable fabrication of superhydrophobic surfaces with special composite structure on zinc substrates, Colloid and Interface Science, 361 (**2011**) 1, 388–396, doi:10.1016/j.jcis.2011.05.060

[26] X. Hou, F. Zhou, B. Yu, W. Liu, Superhydrophobic zinc oxide surface by differential etching and hydrophobic modification, Materials Science and Engineering A, 452–453 (**2007**), 732–736, doi:10.1016/j.msea.2006.11.057

[27] S. Wang, L. Feng, L. Jiang, One-step solution-immersion process for the fabrication of stable bionic superhydrophobic surfaces, Advanced Materials, 18 (**2006**) 6, 767–770, doi:10.1002/adma.200501794

[28] H. Liu, S. Szunerits, W. Xu, R. Boukherroub, Preparation of superhydrophobic coatings on zinc as effective corrosion barriers, Applied Materials and Interfaces, 1 (**2009**) 6, 1150–1153, doi:10.1021/am900100q

[29] M. Miwa, A. Nakajima, A. Fujishima, K. Hashimoto, T. Watanabe, Effects of the surface roughness on sliding angles of water droplets on superhydrophobic surfaces, Langmuir, 16 (**2000**) 13, 5754–5760, doi:10.1021/la991660o

[30] M. A. Momin, R. Pervin, M. J. Uddin, G. M. A. Khan, M. Islam, One step synthesis and optical evaluation of copper oxide (CuO) nanoparticles, Bangladesh Electron, 10 (**2010**), 57–63

[31] E. C. Heltemes, Far-infrared properties of cuprous oxide, Physical Review, 141 (**1966**) 2, 803–805, doi:10.1103/PhysRev.141.803

UDK 620.16:666.97.035:67.017
Original scientific article/Izvirni znanstveni članek

ISSN 1580-2949
MTAEC9, 51(4)657(2017)

EXPERIMENTAL ANALYSIS OF THE INFLUENCE OF CONCRETE CURING ON THE DEVELOPMENT OF ITS ELASTIC MODULUS OVER TIME

EKSPERIMENTALNA ANALIZA VPLIVA UTRJEVANJA BETONA NA RAZVOJ MODULA ELASTIČNOSTI V DALJŠEM ČASOVNEM OBDOBJU

Dalibor Kocáb, Monika Králíková, Petr Cikrle, Petr Misák, Barbara Kucharczyková

Brno University of Technology, Faculty of Civil Engineering, Veveří 95, 602 00 Brno, Czech Republic
kralikova.m@fce.vutbr.cz

Prejem rokopisa – received: 2016-08-08; sprejem za objavo – accepted for publication: 2016-12-13

doi:10.17222/mit.2016.248

The modulus of elasticity is one of the most important properties of concrete, especially during structural analyses of buildings. It is, among others, an important parameter in the calculation of the concrete-element deflection or during the design of pre- or post-tensioned structures. The modulus of elasticity is not a specific number. It is a property with a high variability of the final values, which depend on the concrete composition (together with other factors). Some of the significant factors, which influence the final value of the elastic modulus of concrete, are also the means and quality of its curing, especially at the early stage of its setting and hardening. Apart from maintaining the temperature within the correct limits, it is important to focus on the moisture content of concrete while it is being cured. The purpose of the experiment described herein was to determine the development of the dynamic as well as static modulus of elasticity for structural concrete while using different curing methods. The experiment used four series of beam specimens with nominal dimensions of 100 × 100 × 400 mm made from air-entrained and non-air-entrained concretes of the C 30/37 strength class. A half of the specimens in each series aged in laboratory conditions and the other half was stored under water. Based on the evaluation of the experimental measurements, it can be said that the manner of storage has a significant influence on the development and final values of the static and dynamic modulus of elasticity.

Keywords: concrete, curing, modulus of elasticity, compressive strength

Ena od najpomembnejših lastnosti betona je modul elastičnosti. Njegovo poznavanje je še posebej pomembno za strukturno analizo stavb. To je, med drugim, pomemben parameter pri izračunu deformacij betonskih elementov pred ali med oblikovanjem prednapetih struktur. Modul elastičnosti ni specifična številka; je lastnost z zelo različnimi končnimi vrednostmi, ki so odvisne od sestave betona (skupaj z drugimi dejavniki). Pogoji njegovega utrjevanja so zelo pomembni. Vplivajo na končno velikost elastičnega modula betona, zlasti v zgodnji (začetni) fazi utrjevanja. Razen ohranjanja temperature v pravilnih mejah, se je pomembno osredotočiti na vsebnost vlage v betonu, medtem, ko se le-ta utrjuje. Namen opisanega preizkusa je bil določiti tako razvoj dinamičnega kot tudi statičnega modula elastičnosti konstrukcijskega betona, z uporabo različnih metod utrjevanja. V preizkusu so bile uporabljene štiri serije preizkušancev v obliki nosilcev z nazivnimi dimenzijami 100 mm × 100 mm × 400 mm, izdelanih iz zračno tretiranih in netretiranih betonov iz trdnostnega razreda C 30/37 (N/mm^2). Polovica vzorcev v vsaki seriji je bila starana v laboratorijskih pogojih, druga polovica pa je bila shranjena v vodi. Na podlagi vrednotenja eksperimentalnih meritev, lahko rečemo, da način shranjevanja pomembno vpliva na razvoj in končne vrednosti statičnega in dinamičnega modula elastičnosti.

Ključne besede: beton, utjevanje, modul elastičnosti, tlačna trdnost

1 INTRODUCTION

The recent development in civil engineering has been the cause of concrete being subject to far stricter requirements than several decades ago.[1,2] The compressive strength is no longer the single governing parameter in the design of concrete structures. Attention is paid to other properties, which affect mainly the deformation of the structural element in question and the knowledge of their real values is more frequently sought and required. Next to the very frequently discussed durability,[3,4] these properties include mainly deformation properties, among which the most important is considered to be the modulus of elasticity.[5–8] The modulus of elasticity is one of the most important physical properties, which characterise a material. This applies to concrete as well, especially when it comes to the structural calculations of the structures sensitive to deformation.[6,7,9]

The development of new kinds of concrete, such as self-compacting concrete (SCC), high-strength concrete (HSC), ultra-high performance concrete (UHPC) or freshly compressed concrete (FCC) pushes the boundaries of their material characteristics and properties and thus also their usability in civil engineering.[10–13] The compressive strength can be significantly improved with a simple addition of state-of-the-art admixtures and additives; however, an improvement in the modulus of elasticity is much harder to guarantee. This fact is visible in a very interesting comparison of the relationship between the compressive strength and the modulus of elasticity as proposed by EC2[14] and the relationships described in other sources.[2]

The concrete modulus of elasticity is not a constant[15–18]; on the contrary, it is a property with a result variability, which depends mainly on the composition of the concrete in question. The resulting value of the elastic modulus is influenced mainly by the type, fraction and amount of coarse aggregate, while a decisive factor is often the ratio of the coarse aggregate to the total volume of cement paste. The value is also affected by the type of admixtures, especially the air-entraining ones, their content or the resulting w/c ratio.[5,9,16,19] The curing of concrete, especially during the setting and early hardening, is another significant factor. Apart from maintaining the correct thermal conditions during the concrete manufacture, placement and curing, it is also necessary to pay attention to the moisture conditions after the concrete has been placed and while it ages.[20,21] Especially during placements at high ambient temperatures, it is necessary to cure the concrete carefully for the first few hours or even days in order to prevent rapid water evaporation from the concrete's surface, which can result in the formation of microcracks not only on the surface but anywhere inside it as well.

A lack of water, especially at an early age, has a critical impact on the overall advancement of hydration, which is further reflected in rapid shrinkage; this is typically the first cause of the microcracks forming inside of a concrete element's structure.[22,23] These microcracks further influence the development of physico-mechanical properties of the concrete throughout its ageing and can greatly affect the durability of the whole concrete structure. It was demonstrated that curing time (not only the curing method) also substantially influences the resulting values of the concrete's material properties.[24,25] The composition, the water content, the curing method and the time are interlinked throughout the whole duration of the concrete ageing and can be considered as influential factors, which affect the final value of its modulus of elasticity.[21]

Another aspect, which is reflected in the final value of the modulus of elasticity, is the choice of the test method for its determination. The methods commonly used in civil engineering are the dynamic ones, e.g., the ultrasonic-pulse velocity test, resonance or impact-echo method[6,26], and the static methods, such as the compressive-strength test, flexural-strength test or modified-compact-tension test (MCT).[15,27–29] The result of the dynamic tests is the initial tangent modulus of elasticity[16] and it reaches higher values than the elastic modulus obtained with the static tests. The fact of the matter is that during static tests, the loading and unloading reduce the subsequent creep, which causes a change in the steepness of the stress-strain curve. The static modulus of elasticity is thus often called the secant and its values are lower.[16] The resulting values of the modulus of elasticity obtained by means of each of the dynamic methods are not identical and this fact applies to the values obtained with the static methods as well. Apart from the choice of method, the final result is also influenced by the shape and slenderness ratio of the specimen used (beam[9] vs. cylinder[15]) or its size.[6] The issue of the modulus of elasticity of concrete is, therefore, still open and topical.

One of the key factors described above is the method of curing after concrete has been placed in a formwork. Not only the method and quality of curing have an effect, the curing time does as well. The longer and more intensively concrete is cured, the higher is the chance of improvement in its properties, including the modulus of elasticity. For this reason, the authors of this paper focused on a detailed analysis of the influences the method and time of concrete curing have on its modulus of elasticity.

2 EXPERIMENTAL PART

The purpose of the experiment described herein was to determine the development of the elastic modulus of concrete (this particular one was designed for the construction of bridges) cured under different conditions. Half of the specimens were immersed in water and the other half was stored in standard laboratory conditions with no direct contact with liquid water. The goal was to analyse the influence of the method and the time of curing on the development of the concrete's elastic modulus and its final value. Apart from the static modulus of elasticity, the concrete was tested for the dynamic modulus as well. Two non-destructive methods were used for this purpose.

2.1 Test method

The experiment used the ultrasonic-pulse velocity test and the resonance method for the determination of the dynamic modulus of elasticity. The static modulus of elasticity was determined by means of subjecting the specimens to a cyclic compressive stress.

2.1.1 Ultrasonic-pulse velocity test

The principle of the ultrasonic-pulse velocity test is the repeated releasing of ultrasonic impulses into the sample and measuring the time T required for them to travel through, which is then used for determining the velocity of ultrasonic-wave propagation v_L through the concrete. This velocity is, to some extent, a matter of consensus as the real distance the ultrasonic-pulse travels is not precisely known (i.e., the velocity is calculated with the measured time and the length of a specimen). In the end, the dynamic modulus of elasticity is calculated using Equation (1):

$$E_{cu} = D \cdot v_L^2 \cdot \frac{1}{k^2} \cdot 10^{-6} \quad (1)$$

where E_{cu} is the dynamic modulus of elasticity in MPa, D is the material's bulk density in kg/m^3, v_L is the ultrasonic-pulse velocity in m/s and k is the dimensionality coefficient.

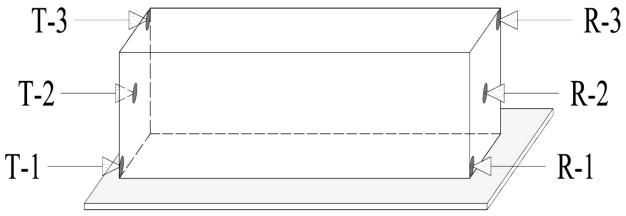

Figure 1: Diagram showing the arrangement for the test determining the time of the ultrasonic-wave passage through a specimen; the arrows indicate the positions, at which the measurement was performed; R is the receiver, T is the transmitter

The dimensionality coefficient k equals 1 for a one-dimensional environment and in the cases of two- and three-dimensional environments, it depends on the value of Poisson's ratio μ, which can be determined by means of the resonance method (as was done in the experiment described here).

The velocity of the ultrasonic-wave propagation was measured using 82 kHz transducers. The time, for which the ultrasonic pulse travelled through each specimen was measured longitudinally in three positions, as illustrated by **Figure 1**. The ultrasonic-wave velocity was calculated for each position and the average of the results was used as the velocity v_L in the calculation of the elastic modulus according to Equation (1). High-plasticity modelling clay was used to ensure a sufficient acoustic coupling between the transducers and the specimens. Prior to the measurement of each specimen, the testing instrument was calibrated using a calibration rod.

2.1.2 Resonance method

Every solid object vibrates upon a mechanical impulse, which can manifest itself in several ways. The dynamic material properties of a body with regular geometry are evaluated using the natural frequencies of longitudinal vibration f_L, flexural vibration f_f and torsional vibration f_t. Using the measured natural frequencies, the dynamic moduli of elasticity E_{crL} of the material under tension and compression (longitudinal vibration) can be calculated according to Equation (2):

$$E_{crL} = 4L^2 \cdot f_L^2 \cdot D \tag{2}$$

where E_{crL} is the dynamic compressive modulus of elasticity in MPa, L is the specimen length in m, f_L is the natural frequency of longitudinal vibration in kHz and D is the material's bulk density in kg/m^3, while E_{crf} (from flexural vibration) is obtained using Equation (3):

$$E_{crf} = 0.0789 \cdot c_1 \cdot L^4 \cdot f_f^2 \cdot D \frac{1}{i^2} \tag{3}$$

where E_{crf} is the dynamic compressive modulus of elasticity in MPa, c_1 is the correction coefficient, L is the specimen length in m, f_f is the natural frequency of flexural vibration in kHz, D is the material's bulk density in kg/m^3 and i is the cross-sectional radius of gyration of a specimen in m.

Each specimen was placed onto a soft pad and vibrated by a mechanical impulse produced by an impact hammer as seen in **Figure 2**. The natural frequencies of longitudinal f_L, flexural f_f and torsional vibration f_t were determined by means of an oscilloscope with an acoustic emission (AE) sensor.

2.1.3 Method for the static modulus of elasticity

The principle of the test for determining the static modulus of elasticity is cyclic loading of a specimen while recording its longitudinal deformation. The specimen is first stressed with 0.5 MPa, after which the load is gradually increased to one third of the expected value of the compressive strength. The relative deformation at the corresponding stress is recorded and the modulus of elasticity is calculated with Equation (4):

$$E_c = \frac{\Delta\sigma}{\Delta\varepsilon} = \frac{\sigma_a - \sigma_b}{\varepsilon_a - \varepsilon_b} \tag{4}$$

where E_c is the static compressive modulus of elasticity in MPa, σ_a is the upper loading stress in MPa, i.e., $1/3 \cdot f_c$, σ_b is the basic loading stress in MPa, i.e., 0.5 MPa, ε_a is the average deformation at the upper loading stress and ε_b is the average deformation at the basic loading stress.

In this experiment, the relative deformation was calculated from the deformations measured using mechanical strain gauges of 200 mm in length. Each specimen was always loaded with two preloading cycles and one reloading cycle, from which the value of the static modulus of elasticity was calculated using Equation (4). The expected 28- and 90-day compressive strengths of the specimens were determined from their cube compressive strength and from the measured dynamic properties. At the ages of 365 d and 730 d, the expected beam compressive strength of the concrete was determined only from the measured values of the dynamic moduli of elasticity.

After the test of the static modulus of elasticity E_c, the 28-day beam strength of one specimen was determined in order to verify the chosen upper loading stress σ_a. The remaining specimens were left for the tests of the elastic moduli carried out at later ages. The same procedure was also performed at the ages of 90 d and 365 d. Thus, the static modulus of elasticity was per-

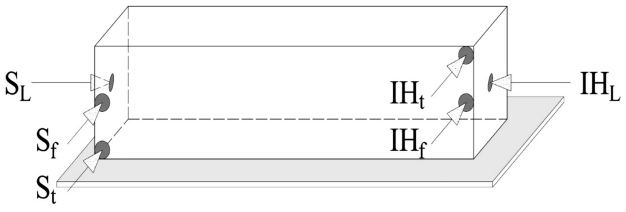

Figure 2: Diagram of the test arrangement for determining the resonance (natural) frequencies of a specimen; IH (impact hammer) indicates the place of the mechanical impulse, S is the position of the AE sensor, L is the measurement of longitudinal vibration, f is the measurement of flexural vibration and t is the measurement of torsional vibration

formed repeatedly with some of the specimens at different ages. However, it must be noted that the test beam was always loaded only up to 1/3 of its maximum compressive strength and thus E_c was only tested in terms of elastic deformations. The total maximum number of the loading cycles per specimen was 12. This is a low number and with the multiple means of loading, it does not influence the final value of the static modulus of elasticity.[16]

2.2 Material

Four series of beam- and cube-shaped specimens were made for the experiment. The dimensions of the beams were 100 × 100 × 400 mm and the cubes were 150 mm in size. All the specimens were made from a concrete of the C 30/37 strength class taken from the agitator trucks present at the construction site of the bridge on Hradecká Street in Brno (Czech Republic). **Table 1** lists the concretes used for making each series, their production dates and the parts of the bridge being built when the samples were taken.

Table 1: Specimens, type of concrete, production date

Series	Concrete formula	Concrete ID	Concrete type	Date of casting	Part of bridge
1	A	A	air-entrained	17 March 2009	abutment
2	B	B	air-entrained	1 May 2009	deck beams
3	C	C-1	not air-entrained	23 May 2009	deck slab (span 1)
4	C	C-2	not air-entrained	30 May 2009	deck slab (span 2)

Table 2: Concrete compositions

Component	kg / 1 m³ of FC		
	Concrete A	Concrete B	Concrete C
Cement CEM I 42.5 R (Mokrá)	400	400	400
Aggregate 0–4 mm (Ledce)	700	700	700
Aggregate 8–16 mm (Olbramovice)	669	669	669
Aggregate 11–22 mm (Lomnička)	284	284	284
Water	172	172	172
Air-entraining admixture (Sika Aer200)	0.60	0.30	-
Plasticiser (Sika ViscoCrete 5-800 multimix)	2.40	2.40	2.40

The first series of the specimens was made during the construction of the bridge abutment. The second series was made during the casting of deck beams, the third specimen series was made when the deck slab of the bridge's span 1 was being cast and the fourth series of the specimens was made during the casting of the deck slab of span 2. **Table 2** shows the composition of each concrete. Concrete A was taken from two agitator trucks; all the other concretes were sampled from three trucks. Fresh-concrete (FC) properties were always determined prior to the moulding of the specimens; their values are shown in **Table 3**.

Table 3: Fresh-concrete properties (the air content was not determined for concrete C as it was not air-entrained)

Concrete	Agitator truck	Slump test (mm)	Air content (%)	Bulk density (kg/m³)
A	1	130	4.5	2 240
	2	120	4.2	2 270
B	1	120	3.7	2 290
	2	120	4.1	2 280
	3	110	3.3	2 320
C-1	1	140	-	2 330
	2	140	-	2 320
	3	110	-	2 340
C-2	1	160	-	2 330
	2	150	-	2 340
	3	150	-	2 330

Table 4: Division of the test beams from individual agitator trucks (mixes) into test sets

Concrete A		Concrete B		Concrete C-1		Concrete C-2	
Specimen	Mix	Specimen	Mix	Specimen	Mix	Specimen	Mix
A/N1	1	B/N1	1	C-1/N1	1	C-2/N1	1
A/N2	1	B/N2	2	C-1/N2	2	C-2/N2	2
A/N3	2	B/N3	3	C-1/N3	3	C-2/N3	3
A/N4	1	B/N4	1	C-1/N4	1	C-2/N4	1
A/N5	1	B/N5	2	C-1/N5	2	C-2/N5	2
A/N6	2	B/N6	3	C-1/N6	3	C-2/N6	2
A/S1	1	B/S1	1	C-1/S1	1	C-2/S1	1
A/S2	1	B/S2	2	C-1/S2	2	C-2/S2	2
A/S3	2	B/S3	3	C-1/S3	3	C-2/S3	3
A/S4	1	B/S4	1	C-1/S4	1	C-2/S4	1
A/S5	1	B/S5	2	C-1/S5	2	C-2/S5	2
A/S6	2	B/S6	3	C-1/S6	3	C-2/S6	2

All the specimens from each construction day were placed onto a flat surface at the construction site, covered with moist geotextile, sprinkled with water and then covered with PE foil to prevent drying. After three days of curing, the current batch of the specimen was transported to the laboratory at the Institute of Building Testing at the BUT Faculty of Civil Engineering where they were demoulded. The beams of each series were then divided into two groups of six. The specimens from the first group were marked as N1–N6 and were immersed in water. The beam specimens from the second group were marked as S1–S6 and were stored in a normal laboratory environment with no additional water curing. The specimens with the N identification (stored in water at 20±3 °C) represented the concrete that was being cured for the entire period. The specimens bearing the S identification (stored in normal laboratory conditions, at an ambient temperature of 20±3 °C, a relative humidity of 50±10 %) represented the concrete, the curing of which

ended three days after it was cast. The assumption was that the way the specimens were stored at the construction site during the first three days was to simulate the concrete being thoroughly cured in the structure. The specimens made from the samples taken from each agitator truck were uniformly divided into individual sets (**Table 4**).

Apart from the beams, 150-mm cube specimens were also made for the purposes of determining the concretes' compressive strengths. Similarly to the beams, the cubes from each concrete were divided into two groups – N (cured under water) and S (uncured). The compressive strength was determined at the ages of 28 d and 90 d; **Table 5** shows the results.

Table 5: Cube compressive strength at the age of 28 d and 90 d in MPa; each value represents the average of three specimens

Age		28 days		90 days	
Concrete	Curing	Average value	Sample's standard deviation	Average value	Sample's standard deviation
A	N	41.0	0.57	45.6	0.25
	S	41.5	2.06	41.2	2.55
B	N	46.4	3.12	48.1	8.70
	S	50.3	1.68	52.0	4.16
C-1	N	51.7	3.44	60.5	1.56
	S	52.4	1.55	57.7	2.19
C-2	N	49.2	3.80	58.1	1.26
	S	50.5	0.55	54.2	3.59

The dynamic modulus of elasticity of the beams in every series was determined by means of the ultrasonic-pulse velocity test (E_{cu}) as well as the resonance test (E_{rcL} from the natural frequency of the longitudinal vibration and E_{rcf} from the natural frequency of the flexural vibration) at the ages of (3, 7, 28, 90, 365 and 730) d. The beams were also tested for the value of their static compressive modulus of elasticity E_c at the ages of (28, 90, 365 and 730) d.

3 RESULTS AND DISCUSSION

The dynamic modulus of elasticity of the 3-day-old concrete of all the series was tested after demoulding, i.e., before placing specimens N1–N6 in water and before placing specimens S1–S6 under laboratory conditions with no contact with liquid water. For this reason, the values of both sets (N and S) of all the series are almost identical. However, four days later, i.e., at the age of 7 d, a positive influence of curing the concrete under water is clearly visible. The dynamic modulus of elasticity for the cured sets N increased more rapidly compared to the uncured sets S. The concretes stored in laboratory conditions were not protected against drying in any way. In fact, massive water evaporation was permitted by the design. A drop in the relative humidity in the concrete pore structure influences cement hydration[30] and simultaneously affects the mechanical

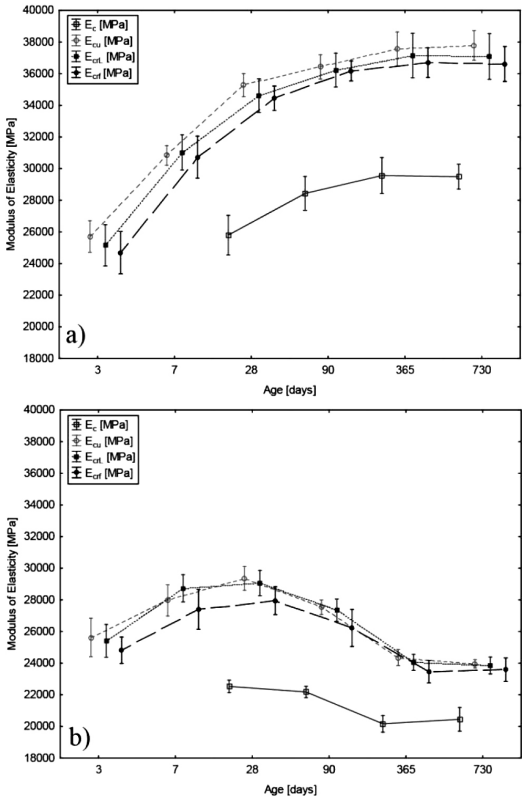

Figure 3: Diagram of the progress of the average values of elastic moduli for concrete A; the error bars indicate sample standard deviations; a) set of cured specimens N; b) set of uncured specimens S

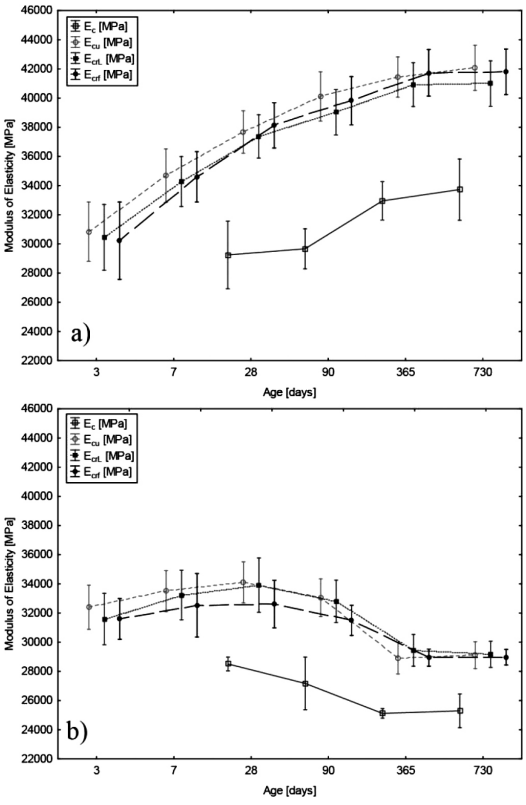

Figure 4: Diagram of the progress of the average values of elastic moduli for concrete B; the error bars indicate sample standard deviations; a) set of cured specimens N; b) set of uncured specimens S

properties of the concrete body.[20] This explains different increases in the dynamic elastic moduli of the cured and uncured concretes. The trend is clearly visible on all the concretes before the age of 28 d. The concrete stored in water saw a substantially steeper increase in the observed dynamic properties as opposed to the concrete stored in the air; **Figures 3–6**.

Apart from the dynamic moduli of elasticity E_{cu}, E_{crL} and E_{crf}, the static modulus of elasticity E_c was also determined at the age of 28 d. The cured concrete of all the series reached higher values of the static modulus of elasticity than the uncured concrete. However, the differences between the average values of 28-day elastic moduli of the individual test sets are not particularly significant. The influence of curing was of the greatest magnitude for the air-entrained concrete A, where the difference between the values of the static elastic modulus of the cured and uncured concrete was 12.8 %; **Table 6**. The data was compared and the conclusions were drawn using an analysis of variance (ANOVA) at a significance level of 0.05.

There is a very interesting difference in the behaviour of the cured and uncured concretes at the age of 28 d and 90 d. While the concrete stored under water still shows an increase in the dynamic and static modulus of elasticity, the case of the uncured concrete is different. The average 28-day values of both the static and dynamic modulus of elasticity of the uncured concrete begin to stagnate and subsequently even decrease. At the age of 90 d, the dynamic values of the uncured concrete S dropped approximately to the values of the 7-day uncured concrete of all the series. Comparing the results of the 90-day dynamic elastic moduli of uncured concrete S with the results for cured concrete N at the age of 7 d, the values of concrete S are lower for all the series (**Table 6**).

The fact that the uncured concrete S saw no continuous increase in the observed properties (in comparison with cured concrete N) can be explained with the lack of water necessary for the cement to fully hydrate.[20,30] The rapid water evaporation from the surface of the concrete specimens affects the progress and the magnitude of concrete shrinkage. The stress created as a result of volume changes in the concrete at its early age can lead to the appearance of microscopic defects in the internal structure of the concrete, which further affects the development of its mechanical properties. A similar stagnation in the material properties of the uncured concrete compared with a cured one was also published by the authors of papers[24,25], where the parameter observed was the compressive strength. Insufficient concrete curing was also reflected in the final values of the elastic modulus at the later ages of the concrete.

The dynamic moduli of elasticity of uncured concrete S at the ages of 365 d and 730 d reach lower values than those determined for the same concrete at the age 3 d

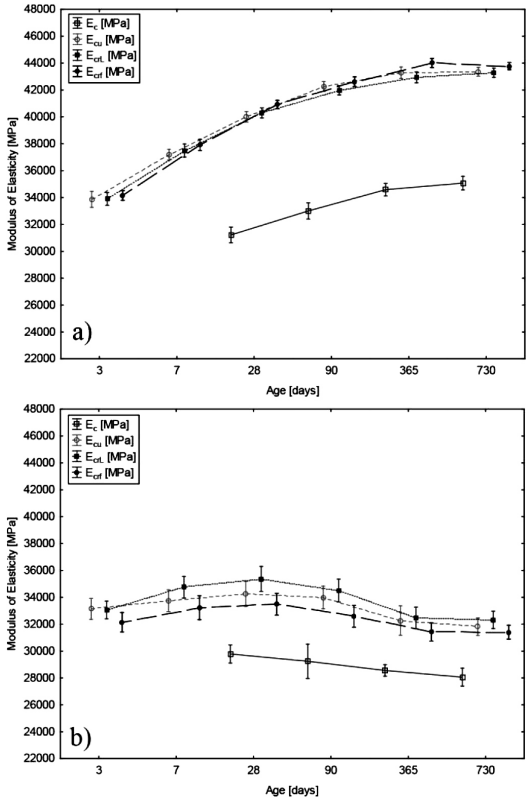

Figure 5: Diagram of the progress of the average values of elastic moduli for concrete C-1; the error bars indicate sample standard deviations; a) set of cured specimens N; b) set of uncured specimens S

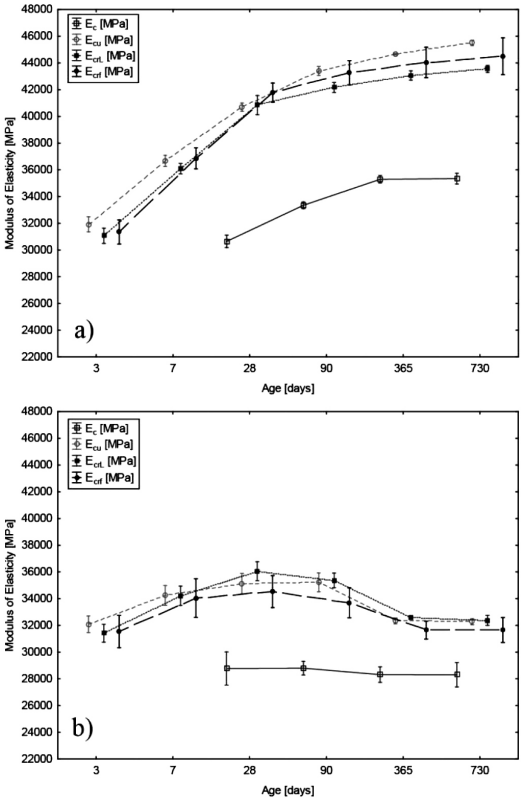

Figure 6: Diagram of the progress of the average values of elastic moduli for concrete C-2; the error bars indicate sample standard deviations; a) set of cured specimens N; b) set of uncured specimens S

Table 6: Average values of the static modulus of elasticity E_c and the dynamic modulus of elasticity E_{cu} determined by means of the ultrasonic-pulse velocity test; at the ages of 28 d and 730 d, a percentage difference between the elastic moduli of the cured and uncured concrete is calculated

Concrete	Type of elastic modulus	Set	Age (days)						Difference at the age of 28 d (%)	Difference at the age of 730 d (%)
			3	7	28	90	365	730		
A	E_c	N	-	-	25 800	28 400	29 600	29 500	12.8	30.5
		S	-	-	22 500	22 200	20 200	20 500		
	E_{cu}	N	25 700	30 800	35 300	36 400	37 600	37 800	16.7	36.5
		S	25 600	28 000	29 400	27 500	24 400	24 000		
B	E_c	N	-	-	29 200	29 700	33 000	33 700	2.4	24.9
		S	-	-	28 500	27 200	25 100	25 300		
	E_{cu}	N	30 800	34 700	37 700	40 100	41 400	42 100	9.5	30.9
		S	32 400	33 500	34 100	33 000	28 900	29 100		
C-1	E_c	N	-	-	31 200	33 000	34 600	35 100	4.5	19.9
		S	-	-	29 800	29 200	28 600	28 100		
	E_{cu}	N	33 900	37 200	40 000	42 300	43 300	43 400	14.3	26.7
		S	33 100	33 800	34 300	34 000	32 300	31 800		
C-2	E_c	N	-	-	30 600	33 300	35 300	35 300	5.9	19.8
		S	-	-	28 800	28 800	28 300	28 300		
	E_{cu}	N	31 900	36 700	40 700	43 400	44 700	45 500	13.8	29.0
		S	32 100	34 200	35 100	35 200	32 300	32 300		

(**Table 6**). The only exception is concrete C-2, for which these values are at the same level. The reason for this decrease is probably a change in the internal structure of the concrete manifesting itself as micro-defects. It was found that concrete drying causes its shrinkage, due to which microcracks and microscopic defects form in its internal structure.[31] These microcracks further change the mechanical properties of the concrete and damage its quality, modulus of elasticity and durability.[31–33]

The issue of removing concrete from direct contact with liquid water and the magnitude of shrinkage caused by doing this are documented in references[22,23,31,34]. The difference in the behaviour of the cured and uncured concrete is better and more conclusively reflected in the results of dynamic tests, which react to damage to the internal structure with a much greater sensitivity than static compressive tests. **Table 6** shows the differences between the average values of both static and dynamic moduli of elasticity; it shows the difference, in percent, between the elastic moduli of cured concrete N and uncured concrete S at the ages of 28 d and 730 d.

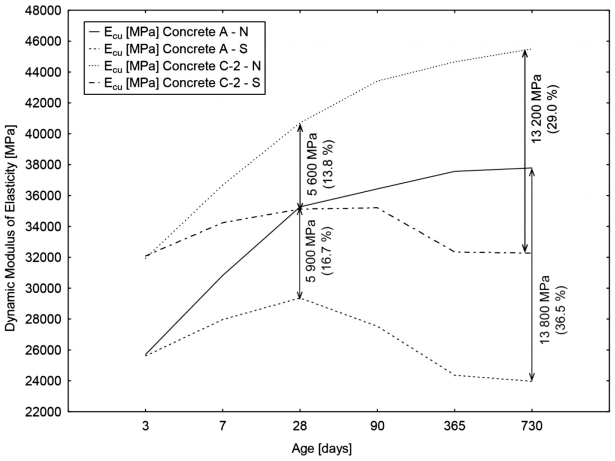

Figure 7: Diagram showing the influence of concrete curing on its dynamic modulus of elasticity E_{cu} including the difference between the resulting values

The dynamic elastic moduli determined by means of the ultrasonic-pulse velocity test (E_{cu}) showed results similar to those obtained with the resonance method (E_{crL} and E_{crf}); (**Figures 3–6**). Thus, the modulus of elasticity measured with the ultrasonic-pulse velocity test (E_{cu}) was chosen to represent the dynamic elastic moduli for the overall evaluation of the behaviour of cured and uncured concretes as shown in **Table 6**. **Figure 7** displays a diagram constructed from the data. For the sake of clarity, the diagram includes only two series of specimens – the air-entrained concrete of series 1 (concrete A) and the non-air-entrained concrete of series 4 (concrete C-2).

Concerning the air-entrained concretes A and B, the differences between the 730-day dynamic moduli of elasticity Ecu for the cured and uncured concretes are 36.5 % and 30.9 %. The differences between the static moduli of elasticity E_c are 30.5 % and 24.9 %. The non-air-entrained concrete C again shows a greater difference in the dynamic modulus of elasticity at the age of 730 d (26.7 % and 29.0 %), compared with the static modulus of elasticity (19.9 and 19.8 %). In summary, the air-entrained concretes saw a greater decrease in the observed parameters.

4 CONCLUSIONS

The experiment results show a positive influence, which the curing method has on the concrete's resulting modulus of elasticity. The concrete cured under water

sees an increase in the value of both dynamic and static modulus of elasticity over time. This trend continues at much later ages as well (an age of 90 d or more). On the other hand, the modulus of elasticity of the uncured concrete exposed to air demonstrably increases only during the first 28 d and reaches lower values than the concrete that was water cured. Between the ages of 28 d and 90 d, the dynamic modulus of elasticity of the uncured concrete stagnates and begins to decrease. It was found that the value of the static modulus of elasticity of the uncured concrete determined at the age of 730 d was lower than the value measured at the age of 28 d. In fact, the 730-day value of the dynamic modulus of elasticity of the uncured concrete was lower than the value measured at the age of 3 d. The decrease in the properties of the uncured concrete was significant. All the series of the tested concretes exhibited a similar trend in the development of the values of the elastic modulus over time for the cured as well as uncured concrete.

Acknowledgement

This paper has been worked under the project No. LO1408 "AdMaS UP - Advanced Materials, Structures and Technologies", supported by the Ministry of Education, Youth and Sports under the "National Sustainability Programme I".

5 REFERENCES

[1] H. S. Abdelgader, A. S. Elbaden, A. Diouri, N. Khachani, M. A. Talbi, Concreting method that produce high modulus of elasticity, MATEC Web of Conferences, (**2014**) 11, doi:10.1051/matecconf/20141103012

[2] C. H. Tsai, D. S. Hsu, Diagnosis of Reinforced Concrete Structural Damage Base on Displacement Time History Using the Back-Propagation Neural Network Technique, Journal of Computing in Civil Engineering, 16 (**2002**) 1, 49–58, doi:10.1061/(ASCE)0887-3801(2002)16:1(49)

[3] T. Komarkova, M. Kralikova, P. Kovacs, Application of computed tomography in comparison with the standardized methods for determining the permeability of cement-composite structures, Mater. Tehnol., 49 (**2015**) 4, 587–595, doi:10.17222/mit.2014.194

[4] L. Pazdera, L. Topolar, J. Smutny, K. Timcakova, Nondestructive Testing of Advanced Concrete Structure during Lifetime, Advances in Materials Science and Engineering, 1–5 (**2015**), doi:10.1155/2015/286469

[5] H. Yıldırım, O. Sengul, Modulus of elasticity of substandard and normal concretes, Construction and Building Materials, 25 (**2011**) 4, 1645–1652, doi:10.1016/j.conbuildmat.2010.10.009

[6] B. Lee, S. H. Kee, T. Oh, Y. Y. Kim, Effect of Cylinder Size on the Modulus of Elasticity and Compressive Strength of Concrete from Static and Dynamic Tests, Advances in Materials Science and Engineering, 1–12 (**2015**), doi:10.1155/2015/580638

[7] R. V. Silva, R. Vasco, J. De Brito, R. K. Dhir, Establishing a relationship between modulus of elasticity and compressive strength of recycled aggregate concrete, Journal of Cleaner Production, 112 (**2016**), 2171–2186, doi:10.1016/j.jclepro.2015.10.064.

[8] M. Zhang, A. P. Jivkov, Micromechanical modelling of deformation and fracture of hydrating cement paste using X-ray computed tomography characterisation, Composites Part B: Engineering, 88 (**2016**), 64–72, doi:10.1016/j.compositesb.2015.11.007

[9] Y. Zhou, J. Gao, Z. Sun, W. Qu, A fundamental study on compressive strength, static and dynamic elastic moduli of young concrete, Construction and Building Materials, 98 (**2015**), 137–145, doi:10.1016/j.conbuildmat.2015.08.110

[10] J. S. Park, Y. Kim, J. R. Cho, S. J. Jeon, Early-Age Strength of Ultra-High Performance Concrete in Various Curing Conditions, Materials, 8 (**2015**) 8, 5537–5553, doi:10.3390/ma8085261

[11] M. Dehestani, I. M. Nikbin, S. Asadollahi, Effects of specimen shape and size on the compressive strength of self-consolidating concrete (SCC), Construction and Building Materials, 66 (**2014**), 685–691, doi: 10.1016/j.conbuildmat.2014.06.008

[12] C. K. Ma, A. Awang, W. Omar, Flexural ductility design of confined high-strength concrete columns: Theoretical modelling, Measurement, 78 (**2016**), 42–48, doi:10.1016/j.measurement.2015.09.039

[13] M. Nematzadeh, M. Naghipour, Compressive strength and modulus of elasticity of freshly compressed concrete, Construction and Building Materials, 34 (**2012**), 476–485, doi:10.1016/j.conbuildmat.2012.02.055

[14] EN 1992-1-1, Eurocode 2: Design of concrete structures – Part 1-1: General rules and rules for buildings, 1 Brussels, Belgium: Comité Européen de Normalisation (CEN), 2008

[15] M. Shariq, J. Prasad, H. Abbas, Effect of GGBFS on age dependent static modulus of elasticity of concrete, Construction and Building Materials, 41 (**2013**), 411–418, doi:10.1016/j.conbuildmat.2012.12.035

[16] A. Neville, J. Brooks, Concrete technology, 2nd ed., Harlow, England, Prentice Hall, 2010

[17] J. Newman, B. S. Choo, Advanced concrete technology: Concrete properties, 1st edition, Amsterdam, Elsevier, 2003

[18] A. Neville, Properties of concrete, 5th ed., New York, Pearson, 2011

[19] N. Kockal, Validity and reliability of estimated modulus of elasticity of cementitious materials, IOP Conference Series: Materials Science and Engineering, 103 (**2015**), doi:10.1088/1757-899X/103/1/012024

[20] B. Liu, W. Lv, L. Li, P Li, Effect of moisture content on static compressive elasticity modulus of concrete, Construction and Building Materials, 69 (**2014**), 133–142, doi:10.1016/j.conbuildmat.2014.06.094

[21] S. N. Shoukry, G. W. William, B. Downie, M. Y. Riad, Effect of moisture and temperature on the mechanical properties of concrete, Construction and Building Materials, 25 (**2011**) 2, 688–696, doi:10.1016/j.conbuildmat.2010.07.020

[22] M. Maslehuddin, M. Ibrahim, M. Shameem, M. R. Ali, M. H. Al-Mehthel, Effect of curing methods on shrinkage and corrosion resistance of concrete, Construction and Building Materials, 41 (**2013**), 634–641, doi:10.1016/j.conbuildmat.2012.12.064

[23] A. S. Al-Gahtani, Effect of curing methods on the properties of plain and blended cement concretes, Construction and Building Materials, 24 (**2010**) 3, 308–314, doi:10.1016/j.conbuildmat.2009.08.036

[24] M. Uddin, M. Jameel, H. Sobuz, M. Islam, N. Hasan, Experimental study on strength gaining characteristics of concrete using Portland Composite Cement, KSCE Journal of Civil Engineering, 17 (**2013**) 4, 789-796, doi:10.1007/s12205-013-0236-x

[25] B. Ozer, M. H. Ozkul, The influence of initial water curing on the strength development of ordinary portland and pozzolanic cement concretes, Cement and Concrete Research, 34 (**2004**) 1, 13–18, doi:10.1016/S0008-8846(03)00185-6

[26] X. Lu, Q. Sun, W. Feng, J. Tian, Evaluation of dynamic modulus of elasticity of concrete using impact-echo method, Construction and Building Materials, 47 (**2013**), 231–239, doi:10.1016/j.conbuildmat.2013.04.043

[27] H. Simonova, I. Havlikova, P. Danek, The effect of a superplasticizer admixture on the mechanical fracture parameters of concrete, Mater. Tehnol., 49 (**2015**) 3, 417-421, doi:10.17222/mit.2014.114

[28] T. Holusova, S. Seitl, A. Fernández-Canteli, Numerical Simulation of Modified Compact Tension Test Depicting of Experimental Measurement by ARAMIS, Key Engineering Materials, 627 (**2014**), 277–280, doi:10.4028/www.scientific.net/KEM.627.277

[29] İ. B. Topçu, Alternative estimation of the modulus of elasticity for dam concrete, Cement and Concrete Research, 35 (**2005**) 11, 2199–2202, doi:10.1016/j.cemconres.2004.08.010

[30] J. Newman, J. B. Choo, Advanced concrete technology: Concrete properties, 1st edition, Amsterdam: Elsevier, 2003

[31] Y. Wei, W. Guo, X. Zheng, Integrated shrinkage, relative humidity, strength development, and cracking potential of internally cured concrete exposed to different drying conditions, Drying Technology, 34 (**2015**) 7, 741–752, doi:10.1080/07373937.2015.1072549

[32] G. De Schutter, Hydration and temperature development of concrete made with blast-furnace slag cement, Cement and Concrete Research, 29 (**1999**) 1, 143–149, doi:10.1016/S0008-8846(98)00229-4

[33] G. De Schutter, L. Taerwe, General hydration model for portland cement and blast furnace slag cement, Cement and Concrete Research, 25 (**1995**) 3, 593–604, doi:10.1016/0008-8846(95)00048-H

[34] S. H. Alsayed, M. A. Amjad, Effect of curing conditions on strength, porosity, absorptivity, and shrinkage of concrete in hot and dry climate, Cement and Concrete Research, 24 (**1994**) 7, 1390–1398, doi:10.1016/0008-8846(94)90124-4

UDK 620.1/.2:67.017:546.281'261
Original scientific article/Izvirni znanstveni članek

ISSN 1580-2949
MTAEC9, 51(4)667(2017)

EFFECT OF PARTICLES SIZE ON THE MECHANICAL PROPERTIES OF SiC-REINFORCED ALUMINIUM 8011 COMPOSITES

VPLIV VELIKOSTI DELCEV NA MEHANSKE LASTNOSTI S SiC OJAČANIH ALUMINIJEVIH 8011 KOMPOZITOV

Nagaraj Ashok, Palanisamy Shanmughasundaram

Karpagam Academy of Higher Education, Karpagam University, Department of Mechanical Engineering, Coimbatore 641021, India
sunramlec@rediffmail.com, ashok2488@rediffmail.com

Prejem rokopisa – received: 2016-08-11; sprejem za objavo – accepted for publication: 2016-11-14

doi:10.17222/mit.2016.252

The effects of the SiC particle size on the mechanical properties of aluminium 8011-SiC composites are reported. Three different particle sizes of SiC (63, 76, 89) μm with two different mass fractions of 2 % and 4 % reinforced with aluminium 8011 were processed using the stir-casting method. The mechanical properties, like hardness, tensile strength, yield strength, ductility, and toughness, of the composites and the unreinforced alloy were tested. It was observed that the hardness, tensile strength, yield strength, ductility, and toughness increase with a decrease in the particle size of the SiC. The increase in weight fraction of the SiC improves all the mechanical properties, except for the ductility and toughness of the composites. The results reveal that the fine 63 μm (220 mesh) SiC particles introduced superior mechanical properties compared to the intermediate 76 μm (180 mesh) SiC particles and the coarse 89 μm (150 mesh) SiC.

Keywords: composites, particle size, stir casting method, weight fractions, mechanical properties

Delo poroča o učinkih velikosti delcev SiC na mehanske lastnosti aluminijevih 8011 kompozitov. Tri različne velikosti delcev SiC (63, 76, 89) μm z dvema različnima deležema teže (2 in 4) %, ojačane z aluminijem 8011, so bile obdelane z metodo mešanja in litja. Testirane so bile mehanske lastnosti, kot so: trdota, natezna trdnost, meja tečenja, duktilnost in žilavost kompozitov in neojačane zlitine. Ugotovljeno je bilo, da se trdota, natezna trdnost, meja tečenja, duktilnost in žilavost povečajo z zmanjšanjem velikosti delcev SiC. Povečanje deleža masnega odstotka SiC izboljšuje vse mehanske lastnosti razen razteznosti in žilavosti kompozitov. Rezultati kažejo, da drobni 63 μm (220 mesh) SiC delci pokažejo nadpovprečne mehanske lastnosti v primerjavi z vmesnim 76 μm (180 mesh) SiC delci in grobimi 89 μm (150 mesh) SiC.

Ključne besede: kompoziti, velikost delcev, metoda mešanja in litja, masni deleži, mehanske lastnosti

1 INTRODUCTION

Aluminium metal-matrix composites are being used as materials for automobile and aerospace applications. Aluminium- and magnesium-based Metal-Matrix Composites (MMCs) are an important class of high-potential engineering materials.[1] Aluminium alloy reinforced with silicon carbide displays better mechanical and tribological properties than the unreinforced alloy because of their high strength-to-weight ratio. Silicon carbide is often the preferred reinforcement in the production of aluminium powder composites.[2] Stir casting can be used to fabricate the composites for a better homogenous distribution of reinforcement particles in the matrix. P. Shanmughasundaram et al.[3] investigated the effect of the addition of fly ash on the mechanical and wear behaviour of Aluminium–fly ash composites. The composites were prepared with the varying weight percentage of fly ash (5, 10, 15, 20 and 25) by a two-step stir-casting method. They concluded that hardness, tensile strength and compressive strength of the composites increases up to the addition of 15 % of mass fractions of fly ash, so it is the maximum reinforcement level to obtain the desired property. S. G. Kulkarni et al.[4] investigated the effect of fly ash and alumina on the mechanical property of aluminium 356 alloy. They have concluded that the addition of fly ash and alumina increases the mechanical properties like hardness, tensile strength and compressive strength of the composites. Sudarshan et al.[5] analysed the mechanical properties of Al356-fly ash composites prepared by stir casting and hot extrusion. They used narrow-size-range (53–106 μm) and wide-size-range (0.5–400 μm) fly ash particles as reinforcement. Their results revealed that small size particles (53–106 μm) display higher mechanical properties than the larger size particles. P. Shanmughasundaram et al.[6] applied ANOVA and Taguchi methods for the selection of optimum level of parameters to obtain the maximum mechanical properties of Al-fly ash composites. They concluded that a modified two-step stir-casting method enhances the uniform distribution of fly ash particles in the aluminium matrix and improves the mechanical properties. Baradeswaran et al.[7] investigated the mechanical and wear properties of Al 7075/Al_2O_3/graphite hybrid composites. The hybrid composites were prepared with the reinforcement of different weight percentages of alumina (2, 4, 6, and 8)

and 5 % mass fractions of graphite. They concluded that the mechanical properties increased due to the increase in solid-solution strengthening. V. Ramnath et al.[8] analysed the mechanical behaviour of aluminium-boron carbide-alumina composites produced by the stir-casting method. They concluded that the hardness and toughness of the aluminium-boron carbide (3 % of mass fractions) alumina (2 % of mass fractions) composites exhibit superior properties than the other composites and unreinforced alloy. Veereshkumar et al.[9] have studied Al6061-SiC and Al7075-Al_2O_3 composites produced by liquid metallurgy technique. R. Harichandran et al.[10] investigated the effect of micro and nanoparticle reinforcement of boron carbide on the aluminium alloy by ultrasonic cavitation-assisted stir casting. T. Thirumalai et al.[11] analysed the aluminium matrix composites reinforced with boron carbide and graphite fabricated by the stir-casting method. Different weight fractions of boron carbide (3, 6, 9, and 12 % of mass fractions) and graphite (3 % of mass fractions) were reinforced with LM25Al alloy. Their results revealed that the hardness of the composites was higher than that of the unreinforced alloy. J. Hashim et al.[12] analysed the low-cost stir-casting method for the preparation of high-quality aluminium-SiC composites. They found that by controlling the various process parameters like position of the impeller, size of the impeller, holding temperature, stirring speed and addition of weight percentage of reinforcement a wide range of mechanical properties were obtained. P. Pugalenthi et al.[13] conducted tests on the mechanical properties of 7075 aluminium alloy reinforced with 2 % of mass fractions of SiC and (3, 5, 7, 9) % of mass fractions of alumina hybrid composites. Their result revealed that the hardness and tensile strength of the composites increase with an increase in the reinforcement of SiC and alumina. S. M. L. Nai et al.[14] analysed the effect of stirring speed on the synthesis of Al/SiC based functionally gradient materials. They concluded that an increase of the stirring speed will lead to a more homogeneous distribution of SiC particulates alongside the deposition direction. N. Radhika et al.[15] analysed the mechanical properties and tribological behaviour of LM25/SiC/ Al_2O_3 composites with reinforcement of (5, 10, 15) % mass fractions of SiC and (5, 10, 15) % of mass fractions of alumina. It was found that the composites with reinforcement of 30 % (15 % SiC and 15% alumina) have higher hardness and tensile strength than the unreinforced base alloy. K. Komai et al.[16] investigated the tensile and fatigue fracture behaviour of Al7075/SiC composites. They reported that the mechanical properties of Al7075/SiC composites were superior to the unreinforced alloy. T. J. A. Doel et al.[17] analysed the tensile properties of Al-SiC composites. The three different particle size of SiC (5, 13, 60) μm, were used as reinforcement. They concluded that coarse SiC particles fracture easily at low load than the fine and intermediate SiC particles. C. Sun et al.[18] investigated the effect of SiC particle size on the mechanical properties of aluminium-SiC composites. They concluded that the tensile strength and yield strength of the composites increases due to the addition of fine SiC particles. H. C. Anilkumar et al.[19] investigated the effect of fly ash particle size (4–25, 45–50 and 75–100) μm and reinforcement weight fractions (10, 15 and 20) % on the mechanical properties of Al6061 composites reinforced with fly ash. Their result reveals that the tensile strength, compressive strength and hardness of the aluminium alloy (Al 6061) composites increased with an increase in the weight fraction of reinforced fly ash and decreased with an increase in the particle size of the fly ash. M. Kok[20] analysed the effect of particle size and the weight fraction of alumina on the mechanical properties of Al2024-alumina composites. Three different particle sizes (16, 32 and 66) μm and three different mass fractions (10, 20 and 30) % of alumina were used as the reinforcement to produce composites by the vortex method, followed by applied pressure. The results reveal that the reinforcement of fine alumina particles exhibits a higher mechanical property than the intermediate and coarse particles. M. Rahimian et al.[21] investigated the effect of particle size and weight fraction of alumina on the mechanical properties of aluminium matrix composite produced by powder metallurgy. Three different weight fractions (5, 10, 15) and three different particle sizes of alumina (3, 12, 48) μm were used as the reinforcement. Their results show that the finer particle (3 μm) has the highest yield strength, hardness, compressive strength, elongation than the intermediate (12 μm) and coarse particle (48 μm) reinforcement. M. Kok et al.[22] examined the effect of two different particle sizes of alumina on the mechanical and wear behaviour of the Al 2024 alloy. They revealed that the hardness and tensile strength of the smaller particle reinforcement were much higher than the larger particle size. S. Mahdavi et al.[23] analysed the hardness and wear behaviour of Al6061 composites with the reinforcement of three different SiC particles (19, 93, 146) μm. Their result shows that the hardness increases with a decrease in the particle size of the SiC reinforcement. From the literature it was observed that the mechanical properties of the composites depend on the size and quantity of the reinforcement particles. Earlier studies indicated that the mechanical properties of the composites can be improved with a decrease in the particle size and an increase in the reinforcement content. Hence, a systematic study has to be carried out to study the effect of particle size and weight fraction of reinforcement on the mechanical behaviour of the composites. In this present work Al8011-SiC composites with the reinforcement of three different particle sizes of SiC (63, 76 and 89) μm and two different weight fractions (2 and 6) % of SiC were fabricated using the stir-casting method and its various mechanical properties like hardness, tensile

strength, yield strength, ductility and toughness were tested.

2 EXPERIMENTAL PART

2.1 Stir-casting method

In this research work, Al 8011-SiC composites were fabricated with three different particle sizes 89 μm (coarse), 76 μm (intermediate) and 63 μm (fine) and two different weight fractions (2 and 6) % of SiC were used as reinforcement by stir the casting method. The composition of Al 8011 alloy is presented in **Table 1**.

Table 1: Composition of Al alloy 8011 alloy

Element	In mass fractions, (*w*/%)
Al	97.14
Si	0.53
Fe	0.99
Cu	0.27
Mn	0.21
Mg	0.25
Cr	0.049
Zn	0.19
Ti	0.028
Pb	0.10
Ca	0.008
Ni	0.045

Stir-casting setup that was used to fabricate the composites is shown in **Figure 1**.

To remove the moisture content from the SiC particles, they were preheated for 60 min in a separate muffle furnace. Aluminium 8011 was added to the graphite crucible and the furnace temperature was maintained at

Figure 1: Stir casting setup[3]

Figure 2: Examined hardness test samples of Al8011 and Al 8011-SiC composites

780 °C, then the Al scraps were melted completely. The melt temperature was reduced to 720 °C to obtain the semi-solid state, then the preheated SiC particles and 1.5 % of mass fractions of Mg was added to the molten slurry. Stirring was done for 5 min. Mg were added to the mixture to increase the wettability between the Al matrix and SiC particles. The stirring speed was maintained at 300 min^{-1} throughout the process. Then, finally again the temperature was raised to the liquid state and poured into the mould for solidification.

3 MECHANICAL PROPERTIES

3.1 Hardness test

The hardness tests of Al8011-SiC composites and unreinforced alloy were carried out using Rockwell hardness machine MSM model with ASTM E18:2014 standard with 1/16" inch ball indenter with a load of 980 N. The loading time for the test period was 15 s. The average of three readings was taken to eliminate the error at room temperature. The examined hardness test samples of Al8011 and Al 8011-SiC composites are shown in **Figure 2**.

3.2 Tensile test

Tensile tests were carried out using UTM testing machine M30 model as per ASTM E8:2015 standard for the Al8011 and Al8011-SiC composites. Three samples were taken and tested and the average of three test readings was taken and noted. The examined tensile test samples of Al8011 and Al 8011-SiC composites are shown in **Figure 3**.

3.3 Impact test

The toughness test was carried out by using charpy impact test machine (AIT-300-EN). The energy required to break the specimen was measured in terms of Joules. The final energy measured was the difference between the total energy supplied to break the specimen to the en-

Figure 3: Examined tensile test samples of Al8011 and Al 8011-SiC composites

ergy available after the specimen fracture. The test method used was ISO-148-1:2009. The standard specimen size for this impact test method was 10 mm × 10 mm × 55 mm. Three specimens were tested and the average of three readings was noted. Examined Charpy impact test samples of Al8011 and Al 8011-SiC composites are shown in **Figure 4**.

Mechanical properties of pure Al and Al8011-SiC Composites are presented in **Table 2**.

Table 2: Mechanical Properties of Al8011-SiC Composites

Sic (*w*/%)	Hardness (RHB)	Yield strength (MPa	Tensile strength (MPa)	Elongation %	Toughness (J)
0	90	46	67	7	10
2 % (89 μm)	92	54	73	7.5	15
2 % (76 μm)	94	58	78	7.8	16
2 % (63 μm)	96	63	84	8.4	17
6 % (89 μm)	98	76	98	7.2	12
6 % (76 μm)	102	81	105	7.4	13
6 % (63 μm)	105	87	111	7.7	14

Figure 4: Examined Charpy impact test samples of Al8011 and Al 8011-SiC composites

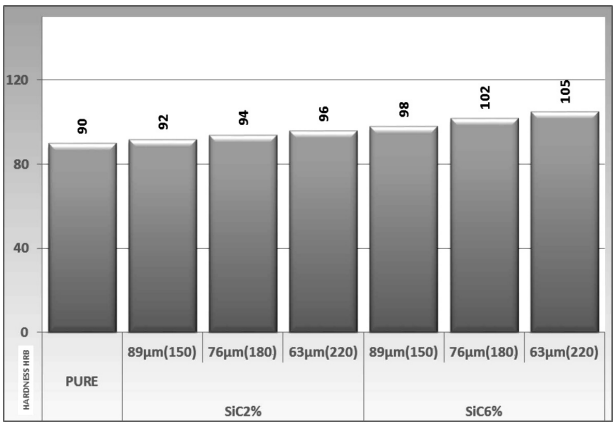

Figure 5: Effect of mesh size of SiC on the hardness of Al8011-SiC composites

4 RESULTS AND DISCUSSION

From **Figure 5** it can be observed that as the particle size decreases the hardness of the composite increases for 2 % and 6 % of mass fractions reinforcement of SiC. The hardness of Al8011-SiC-63 μm (220 mesh) for 6 % of mass fraction was observed to be 105 HRB, which was 16 % more than the unreinforced alloy (90 HRB). Hard SiC particles act as a barrier to the applied load. Hardness of the Al8011-SiC composites was greater than the unreinforced alloy because of the hard nature of the SiC particles. The addition of hard ceramic particles increased the bulk hardness of the aluminium alloy. Fine particle size 63 μm (220 mesh) reinforcement of SiC exhibit superior hardness than the intermediate SiC-76 μm (180 mesh) and coarse SiC-89 μm (150 mesh). This result was similar to the statement concluded by M. Kok.[20] M. Kok reported that the hardness of the composites increased with decreasing size and increasing weight fraction of the reinforcement particles. The increase in hardness was due to the presence of a larger interfacial area

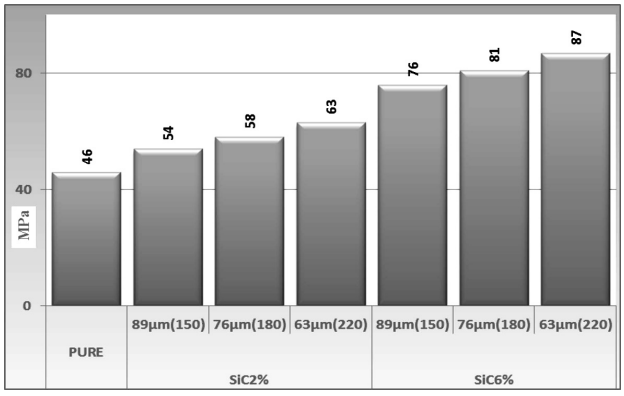

Figure 6: Effect of mesh size of SiC on the yield strength of Al8011-SiC composites

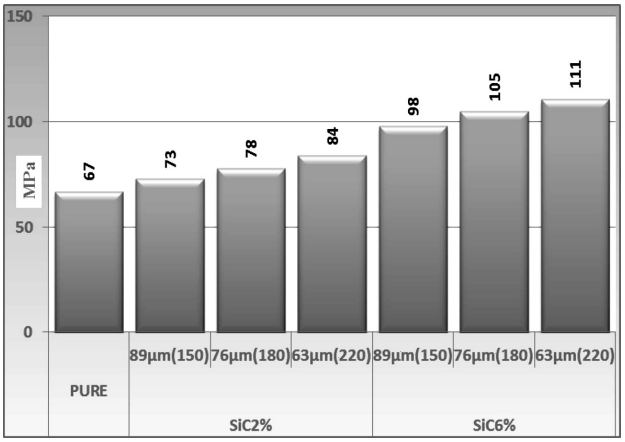

Figure 7: Effect of mesh size of SiC on the tensile strength of Al8011-SiC composites

between the soft and hard phases. Decreasing the alumina particle size increases the hardness. A similar observation was made by M. Rahimian.[21]

From **Figure 6** it is observed that yield strength increases as the weight fraction of SiC increases. The yield strength of Al8011-6 % of mass fractions of SiC-63 µm (220 mesh) was observed to be 87 MPa which was 89 % higher than the unreinforced alloy. The yield strength also increases with the decrease in particle size of SiC. It was noted that the value of yield strength was 54 MPa for Al8011-2 % of mass fractions of SiC-89 µm (150 mesh), 58 MPa for Al8011-2 % of mass fractions of SiC-76 µm (180 mesh) and 63 MPa for Al8011-2 % of mass fractions of SiC-63 µm (220 mesh), that was 16 % increase when compared to the 150 mesh size.

From **Figure 7** it is clear that the tensile strength of the composites was higher than the pure Aluminium 8011. The tensile strength of unreinforced Al8011 was 67 MPa and the value increased to 84 MPa for Al8011-2 % of mass fractions of SiC-63 µm (220 mesh). An increase of 25 % in tensile strength was observed. Similarly 111 MPa for Al 8011-6 % of mass fractions of SiC-63 µm

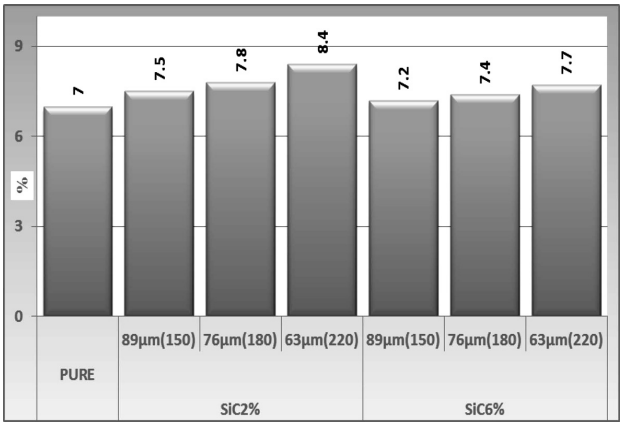

Figure 8: Effect of mesh size of SiC on the elongation of Al8011-SiC composites

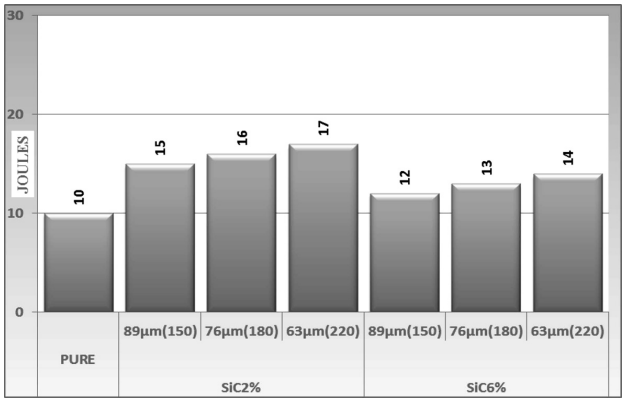

Figure 9: Effect of mesh size of SiC on the toughness of Al8011-SiC composites

(220 mesh), increase of 65 % was observed when compared to the unreinforced alloy.

From **Figure 8** it is clear that the elongation of the composites increases with the decrease in the particle size. The elongation tends to decrease when the amount of reinforcement increases. The Al 8011-2 % of mass fractions of SiC has a higher elongation than the Al8011-6 % of mass fractions of SiC composites. The elongation decreases to 7.7 % from 8.4 % drop of 9 % was observed. The increase in tensile strength and yield strength was due to the increase in dislocation density caused by the reinforcement of the hard SiC particles. As smaller reinforcement particle size reduces the distance between the reinforcement particles, the movement of dislocations tends to decrease, leading to a higher strength of the composites. The grain boundary acts as a barrier to the movement of dislocations caused by the plastic deformation. Therefore, at a higher mess size, high grain boundaries are formed, which act as a barrier against the movement of the dislocation.

From **Figure 9** it is observed that the highest toughness of 17 J was observed for Al8011-2 % SiC-63 µm (220 mesh). The value was 16 J for Al8011-2 % of mass fractions of SiC-76 µm (180 mesh) and 15 J for Al8011-2 % of mass fractions of SiC-89 µm (150 mesh). But the toughness decreases for the reinforcement of 6 % of mass fractions of SiC particles.

5 CONCLUSIONS

Al 8011-SiC composites were produced successfully by the stir-casting method and a homogenous distribution of SiC particles in the Al8011 matrix was obtained. From the tests conducted the following conclusions can be drawn:

1. Hardness increased with the decrease in SiC particle size. The highest hardness (105 HRB) was obtained for 6 % of mass fractions of SiC particle reinforced composites with 63 µm particle size.
2. The coarse particle size of SiC has a lesser yield strength and tensile strength. The highest amount of

yield strength and tensile strength were 87 MPa, 111 MPa for the sample containing 6 % of mass fractions of SiC with 63 μm particle size.

3. Elongation decreased as the weight fraction of SiC increases. The 6 % of mass fractions of SiC particle reinforced composite with 63 μm SiC particles has the elongation of 7.7 % which was 8 % less than the 2 % of mass fractions of SiC particle-63 μm (220 mesh).
4. Toughness increased with the decrease in particle size for both the 2 % and 6 % mass fractions of SiC particle reinforced composites. The highest amount of toughness was 17 J for the sample containing 2 % of mass fractions of SiC with 63μm SiC particles.

Hardness, yield strength, and tensile strength increase with the increase in weight fraction of SiC, while the toughness and ductility decrease. Fine reinforcement of SiC-63 μm (220 mesh) with Al 8011 exhibit superior mechanical properties than the coarse SiC-89 μm (150 mesh) and intermediate SiC-76 μm (180 mesh) particles.

6 REFERENCES

[1] S. Sahin, N. Yüksel, H. Durmus, S. G. Irizalp, Wear behavior of Al/SiC/Graphite and Al/FeB/Graphite hybrid composites, Mater. Tehnol., 48 (**2014**), 639–646

[2] V. M. Kevorkijan, Experimental investigation of the stability of particulate dispersoid suspensions in aluminum and magnesium melts, Mater. Tehnol., 34 (**2000**), 419–423

[3] P. Shanmughasundaram, R. Subramanian, G. Prabhu, Some studies on Aluminium – fly ash composites fabricated by two step stir casting method, European Journal of Scientific Research, 63 (**2011**), 204–218

[4] S. G. Kulkarni, J. V. Meghnani, A. Lal, Effect of fly ash hybrid reinforcement on mechanical property and density of Aluminium 356 alloy, Procedia Material Science, 5 (**2014**), 746–754, doi:10.1016/j.mspro.2014.07.324

[5] Sudarshan, M. K. Surappa, Synthesis of fly ash particle reinforced A356 Al composites and their characterization, Materials Science and Engineering A, 480 (**2008**), 117–124, doi:10.1016/j.msea.2007.06.068

[6] P. Shanmughasundaram, R. Subramanian, G. Prabhu, Synthesis of Al–fly ash composites by modified two step stir casting method, Advanced Materials Research, 488-489, (**2012**), 775–781, doi:10.4028/www.scientific.net/AMR.488-489.775

[7] A. Baradeswaran, A. Elaya Perumal, Study on mechanical and wear properties of Al 7075/Al_2O_3/graphite hybrid composites, Composites: Part B, 56 (**2014**), 464–471, doi: 10.1016/j.compositesb.2013.08.013

[8] B. Vijaya Ramnath, C. Elanchezhian, M. Jaivignesh, S. Rajesh, C. Parswajinan, A. Siddique Ahmed Ghias, Evaluation of mechanical properties of aluminium alloy–alumina–boron carbide metal matrix composites, Materials and Design, 58 (**2014**), 332–338, doi:10.1016/j.matdes.2014.01.068

[9] G. B. Veeresh Kumar, C. S. P. Rao, N. Selvaraj , M.S. Bhagyashekar, Studies on Al6061-SiC and Al7075-Al_2O_3 metal matrix composites, Journal of Minerals & Materials Characterization & Engineering, 9 (**2010**), 43–55, doi: 10.4236/jmmce.2010.91004

[10] R. Harichandran, N. Selvakumar, Effect of nano /micro B_4C particles on the mechanical properties of aluminium metal matrix composites fabricated by ultrasonic cavitation-assisted solidification process, Archives of Civil and Mechanical Engineering (**2015**), doi:10.1016/j.acme.2015.07.001

[11] T. Thirumalai, R. Subramanian, S. Kumaran, S. Dharmalingam, S.S. Ramakrishnan, Production and characterization of hybrid aluminum matrix composites reinforced with boron carbide and graphite, Journal of Scientific & Industrial Research, 73 (**2014**), 667–670

[12] J. Hashim, L. Looney, M. S. J Hashmi, Metal matrix composites: production by the stir casting method, Journal of Material Processing and Technology, 92–93 (**1999**), 1–7, doi:10.1016/S0924-0136(99)00118-1

[13] P. Pugalenthi, M. Jayaraman, A. Natarajan, Evaluation of mechanical properties of Aluminium alloy 7075 reinforced with SiC and Al_2O_3 hybrid metal matrix composites, Applied Mechanics and Materials, 766-767 (**2015**), 246–251, doi:10.4028/www.scientific.net/AMM.766-767.246

[14] S. M. L. Nai, M. Gupta, Influence of stirring speed on the synthesis of Al/SiC based functionally gradient materials, Composite Structures, 57 (**2002**), 227–233, doi: 10.1016/S0263-8223(02)00089-2

[15] N. Radhika, T. V. Balaji, S. Palaniappan, Studies on mechanical properties and tribological behaviour of LM25/SiC/AL_2O_3 composites, Journal of Engineering Science and Technology, 10 (**2015**), 134–144

[16] K. Komai, K. Minoshima, H. Ryoson, Tensile and fatigue fracture behavior and water-environment effects in a SiC-whisker/7075-aluminum composite, Compos Sci Technol, 46 (**1993**), 59–66

[17] T. J. A. Doel, P. Bowen, Tensile properties of particulate-reinforced metal matrix composites, Composites Part A, Appl S, 27 (**1996**), 655–665

[18] C. Sun, M. Song, Z. Wang, and Y. He, Effect of particle size on the microstructures and mechanical properties of SiC-reinforced pure Aluminum composites, Journal of Materials Engineering and Performance, 20 (**2011**), 1606–1612, doi: 10.1007/s11665-010-9801-3

[19] H. C. Anilkumar, H. S. Hebbar, K. S. Ravishankar, Mechanical properties of fly ash reinforced Aluminium alloy (Al6061) composites, International Journal of Mechanical and Materials Engineering, 6 (**2011**), 41–45

[20] M. Kok, Production and mechanical properties of Al_2O_3 particle-reinforced 2024 aluminium alloy composites, Journal of Materials Processing Technology, 161 (**2005**), 381–387, doi:10.1016/j.jmatprotec.2004.07.068

[21] M. Rahimian, N. Parvin, N. Ehsani, Investigation of particle size and amount of alumina on microstructure and mechanical properties of Al matrix composite made by powder metallurgy, Materials Science and Engineering A, 527 (**2010**), 1031–1038. doi:10.1016/j.msea.2009.09.034

[22] M. Kök, K. Özdin, Wear resistance of aluminium alloy and its composites reinforced by Al_2O_3 particles, Journal of Materials Processing Technology, 183 (**2007**), 301–309, doi:10.1016/j.jmatprotec.2006.10.021

[23] S. Mahdavi, F. Akhlaghi, Effect of the SiC particle size on the dry sliding wear behavior of SiC and SiC–Gr-reinforced Al6061 composites, Journal of Materials Science, 46 (**2011**), 7883–7894, doi:10.1007/s10853-011-5776-1

UDK 620.19:669.018.41:621.793.7
Original scientific article/Izvirni znanstveni članek

ISSN 1580-2949
MTAEC9, 51(4)673(2017)

INCREASING THE WEAR RESISTANCE OF Al-Mg COMPONENTS USING THERMAL-SPRAY COATINGS

POVEČEVANJE ODPORNOSTI Al-Mg KOMPONENT PROTI OBRABI Z UPORABO TOPLOTNO NAPRŠENIH PREVLEK

Raimonda Lukauskaitė[1], Olegas Černašėjus[1], Jelena Škamat[2], Svajus Asadauskas[3], Alma Ručinskienė[3], Regina Kalpokaitė-Dičkuvienė[4], Nikolaj Višniakov[1]

[1]Vilnius Gediminas Technical University, Faculty of Mechanics, 28 J. Basanavičiaus Street, 03224 Vilnius, Lithuania
[2]Vilnius Gediminas Technical University, Scientific Institute of Thermal Insulation, 28 Linkmenų Street, 08217 Vilnius, Lithuania
[3]Institute of Chemistry of Center for Physical Sciences and Technology, 3 Saulėtelio av., 10222 Vilnius, Lithuania
[4]Lithuanian Energy Institute, 3 Breslaujos Street, 44403 Kaunas, Lithuania
olegas.cernasejus@vgtu.lt

Prejem rokopisa – received: 2016-08-16; sprejem za objavo – accepted for publication: 2016-11-24

doi:10.17222/mit.2016.255

In the present work, plasma-spray technology was applied as a means to improve the durability of Al-Mg alloy parts. NiCrSiBFe coatings deposited on aluminium-magnesium alloy substrates with different thickness values were studied. Before spraying, the surfaces of aluminium-magnesium alloy were modified upon applying different surface pre-treatment methods. The phase composition, microstructure, microhardness, porosity and adhesion of the deposited coatings were characterized. Ball-on-plate wear tests of the NiCrSiBFe coatings were carried out in dry and lubricated conditions, using a scanning electron microscope to characterize the worn track and the wear mechanism. The correlation of the coating porosity and the adhesion strength with the thickness of a deposited layer was determined. The results revealed that the plasma-sprayed NiCrSiBFe coatings, compared with the uncoated Al-Mg substrate, provide both a stable friction coefficient and an improved wear resistance, which is about two times better under dry sliding and about five times better under lubricated sliding.

Keywords: aluminium-magnesium substrate, NiCrSiBFe coatings, plasma spray, sliding wear, adhesion strength

V prikazanem delu je bila za izboljšanje trajnosti delov iz Al-Mg zlitin uporabljena tehnologija pršenja s plazmo. Predmet preučevanja so bile NiCrSiBFe prevleke nanesene na podlago iz aluminij-magnezijevih zlitin. Pred nanašanjem so bile površine aluminij-magnezijevih zlitin obdelane z različnimi postopki predpriprave površin. Določene so bile fazna sestava, mikrostruktura, mikrotrdota, poroznost in oprijem napršenih prevlek. Za določitev sledi obrabe in mehanizma je bil na NiCrSiBFe prevlekah izveden preizkus s kroglico, v suhih in naoljenih pogojih, in bil karakteriziran s pomočjo vrstičnega elektronskega mikroskopa. Določena je povezava med poroznostjo in jakostjo oprijema ter debelino nanešenega sloja. Rezultati so pokazali, da plazemsko napršene NiCrSiBFe prevleke v primerjavi z Al-Mg zlitino brez prevlek, omogočajo stabilen koeficient trenja in izboljšujejo odpornost, ki je dvakrat boljša pri drsenju po suhi podlagi, in petkrat boljša pri drsenju po naoljeni podlagi.

Ključne besede: aluminij-magnezijeva podlaga, NiCrSiBFe prevleke, pršenje s plazmo, drsna obraba, trdnost oprijema

1 INTRODUCTION

Aluminium and its alloys are used in almost all the industrial fields including civil engineering, aeronautics, transport, mechanical engineering, equipment, electric engineering, electronics, etc. However, a low melting point and hardness of aluminium parts restrain their wider applications under elevated temperatures, frictional working conditions and wear of various types.[1,2] Covering aluminium items with strengthening coatings is probably one of the most hopeful ways to reduce their wear loss, minimize friction and to extend their service life.

Plasma spraying, being a very flexible process in terms of component geometry, coating materials and properties of the layer composite material achieved, look promising for aluminum parts. Due to the variety of coating materials that can be applied (including metals, ceramics and cermets), the properties of plasma-sprayed coatings may cover a wide range of applications. It was shown in a number of works[3–9] that the wear conditions of aluminium parts may be significantly improved with the use of protective coatings manufactured of cast iron, Fe-based alloys, Al-based alloys and their mixtures with hard particles (B_4C, SiC). There are also positive results reported on composite coatings containing oxides of rare metals[10,11] and duplex thermal-barrier coating.[12]

With respect to aluminium parts, the application of Ni-based coatings is of particular interest as well. It is known that nickel is tough and ductile due to the face-centred cubic lattice structure, existing up to the melting point; nickel has a good resistance to corrosion in many environments and shows an extensive solid solubility with many alloying elements, which, together with nickel, can form precipitate and dispersoid particles as well as unique intermetallic phases.[13] A change in a spraying-powder chemical composition enables variations in the final properties of Ni-based coatings in a wide range from soft (~300 HV) antifriction coatings with an excellent resistance to corrosion and oxidation to

hard (~780 HV) coatings with a good wear and erosion resistance. Therefore, the Ni-based coating is widely used for a multifunctional protection of the parts under various working conditions.[14,15] NiCrSiBFe coatings are widely applied due to their excellent wear resistance at low and moderated temperatures. Chromium forms hard phases and improves the mechanical and wear properties of a coating. [15,16] Boron reduces the melting point of an alloy and makes the deposition process easier; together with silicon, it also acts as a deoxidizer; both of these elements participate in the formation of hard precipitations.[16,17] When an alloy contains a particular amount of alloying elements (C, Cr, Si, B and others), the coating formed may reach high hardness; at the same time, it remains ductile enough to prevent the coating crumbling and the propagation of cracks. Nowadays, such coatings are widely used for the protection of steel parts from corrosion, high-temperature oxidation and wear of various kinds.[15] It is possible that such coatings may also be effective in the improvement of the frictional and wear conditions of aluminium alloys parts.

The friction and wear performance of coated parts is mainly determined by the properties of the coating. As is known, the wear loss and friction coefficient are two main indicators used to evaluate the wear conditions of the parts under a sliding contact; however, they are influenced, besides other factors, by a number of exterior elements such as lubrication, humidity, temperature, etc.[18] This makes it difficult to use numerical modelling for predicting the tribological performance of an applied system. The present study was developed in order to evaluate the efficiency of the NiCrSiBFe plasma-sprayed coatings used for the improvement of the aluminium-alloy-part performance under sliding wear conditions. For this purpose, the properties of the NiCrSiBFe coatings deposited on aluminium-magnesium alloy substrates were characterized and compared with those of the uncoated substrate.

2 EXPERIMENTAL PART

A self-fluxing Ni-based alloy powder (with a chemical composition, in mass fractions (w/%) of: ~12 % Cr, ~4 % Si, ~2.5 % B, max. 2 % Fe, ~0.5 % C, Ni – balance) was deposited on a hot-rolled AW 5754 aluminium alloy substrate (140 × 20 × 4 mm) with the plasma-spray technique. Two different pre-treatment techniques were employed to prepare the surfaces of the specimens prior to spraying: sandblasting and its combination with chemical etching (30 % H_3PO_4). The designation of the specimens according to the applied surface processing and the thickness of the deposited layer are presented in **Table 1**.

The parameters of plasma spraying were as follows: plasma power – 33.4 kW, spraying distance – 90 mm, shielding gas – argon, plasma-forming gas – nitrogen. The difference in the thickness of the coating was obtained by changing the number of spray passes. The coating thickness was evaluated from digital micrographs obtained with optical microscopy and the microhardness was obtained with cross-sectional measurements using a Vickers indenter (load – 50 g).

Table 1: Designation of the NiCrSiBFe coatings deposited on differently prepared Al-Mg substrates

	Series A			Series B		
Specimen	A1	A2	A3	B1	B2	B3
Pre-treatment of the substrate surface	Sandblasting			Sandblasting + etching 30 % H_3PO_4		
Roughness of the pre-treated surface /μm	3.91	3.91	3.91	3.83	3.83	3.83
Thickness of the deposited layer (±5) /μm	125	170	315	125	170	315

The microstructures of the deposited coatings were examined on the polished and etched transverse cross-sections using a ZEISS EVO/MA 10 scanning electron microscope (SEM) coupled with an energy dispersive spectrometer (EDS) for an X-ray micro-analysis. The last polishing step was carried out using a diamond polishing paste with a grit size of up to 1 μm. A 50 mL HCl /1.25 mL H_2O_2 solution was used for the etching. A qualitative phase analysis of the obtained coatings was performed using the data measured on a Bruker D8 Advance X-ray diffractometer with K_α(Cu) radiation in steps of $\Delta 2\theta$–0.02° and the exposure time per step of 0.058 s.

The determination of the porosity of the sprayed NiCrSiBFe coatings was performed on the polished transverse cross-sections using an optical NICON ECLIPSE MA200 microscope and image-analysing software "Scion Image". The last polishing step was carried out using a diamond polishing paste with a grit size of up to 1 μm. A 500× magnification was used. The porosity was estimated on three specimens for each set and the average was presented.

The adhesion strength was measured using a "PosiTest" pull-off tester and epoxy glue (Araldite® 2011). The abruption along the interface between the substrate and the coating was observed on all the tested samples. The average of the three individual measurements is presented in this paper.

For the evaluation of the surface wear resistance, a pin-on-disc-type tribometer (CSM Instruments) was configured into a linear reciprocal ball-on-plate regime and used under the following conditions: the total sliding distance of 40 m, a speed of 2 cm/s, a chamber temperature of 25 °C and 50 % relative humidity. A specimen tested was fixed as a plate onto the bottom and the ball, made of 100Cr6 steel (Ø = 6 mm), was applied from the top under either dry or lubricated sliding conditions. The normal load applied on the sample was 10 N and a sliding amplitude of 4 mm was employed for the reciprocal motion. Lubricated sliding was obtained by dropping

1–2 ml of Elfa oil (synthetic, 5W-30, API:SL/C). The test was performed according to the ASTM G-133 standard. The friction coefficient was recorded at a rate of 50 times per second and its average was calculated on the basis of the readings from the central 80 % segment of the reciprocal motion, excluding both edges. The wear resistance was calculated with the weight residual method. The mass loss of the specimens tested was measured after the completion of every cycle of the experiment with an electronic balance KERN with a 0.001 g accuracy. The volume loss, coating density, wear rate and resistance were calculated using the procedure described in[19]. The coefficient of friction was calculated using software package InstrumX.

3 RESULTS AND DISCUSSION

An X-ray diffraction analysis of the coating deposited on the Al-Mg alloy substrate was performed and the results are presented in **Figure 1**. According to the XRD data, the NiCrSiBFe coating with a high probability consists mainly of the nickel-chromium-iron solid solution $Ni_{0.73}Cr_{0.18}Fe_{0.09}$, iron boride Fe_3B and boron silicide $B(Fe,Si)_3$. In the region of 2Θ = 40–50, there were also reflections attributable to other phases such as nickel-silicon boride Ni_6Si_2B, chromium or iron carbide $(Cr, Fe)_{23}C_6$, carbon-iron-silicon solid solution C-Fe-Si and chromium silicide Cr_3Si. A comparison of related publications[19–21] shows that such a phase composition is typical for the NiCrSiBFe coating produced of powders with similar compositions.

The microstructure of the obtained coating and the results of the EDS analysis are provided in **Figure 2** and **Table 2,** respectively. At least three areas of different elemental compositions can be seen in the micrograph. The nickel-rich white area, denoted in **Figure 2** as A and containing ~16 % of chromium along with some amount of iron, is most likely the nickel-chromium-iron solid solution detected also with XRD ($Ni_{0.73}Cr_{0.18}Fe_{0.09}$). Darker, coloured, coarser inclusion B and dispersive precipitates in the C area indicate a presence of the elements with a lighter atomic weight, such as carbon and/or boron. Area B shows a higher chromium content. This, along with the XRD results, allows us to assume that in the B area and similar areas there may be chromium carbides and/or borides. In area C, where many fine, dark, dispersive inclusions, incorporated in the nickel-based matrix can be seen, the highest nickel content was detected. Spatial resolution of the X-ray analysis exceeds the size of individual inclusions.

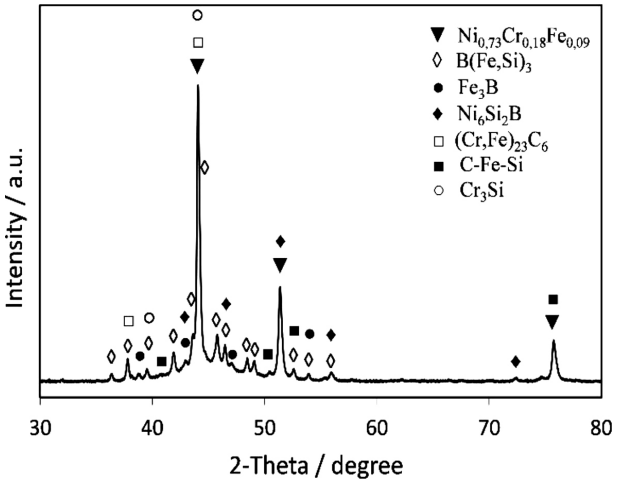

Figure 1: XRD pattern of the NiCrSiBFe coating obtained on the A1 specimen

Table 2: Chemical compositions based on EDS of the areas denoted in **Figure 2** (*w*/%)

Area	Si-*K*	Cr-*K*	Fe-*K*	Ni-*K*
A	4.09	15.54	2.61	77.77
B	2.31	46.93	2.48	48.28
C	4.69	9.05	2.30	83.95

Therefore, the chemical compositions listed in **Table 2** for the C area, are the results of two phases – the solid solution (A) and the dark dispersive inclusions (C). Taking into account the increased nickel content and based on the XRD data (**Figure 1**) along with the results reported in references,[19–21] it was assumed that in the C area there are phases of Ni borides and/or silicides (such as the one obtained with XRD – Ni_6Si_2B) dispersed in the Ni-Cr-Fe solid solution. Other phases identified in the coating with the XRD analysis (such as iron borides or chromium silicides) are most likely also in the form of dispersive precipitates, which is typical for such compounds.

The microstructural analysis of the deposited layers with various thickness values formed on differently pre-treated substrates did not show significant differences in the coating morphology. Thus, the plasma-spray technique, employed for the coating deposition in this work, formed low-porous layers, consisting of nickel-based matrix with many incorporated hard precipitations, where chromium together with carbon participates in the formation of carbide phases, boron and silicon form

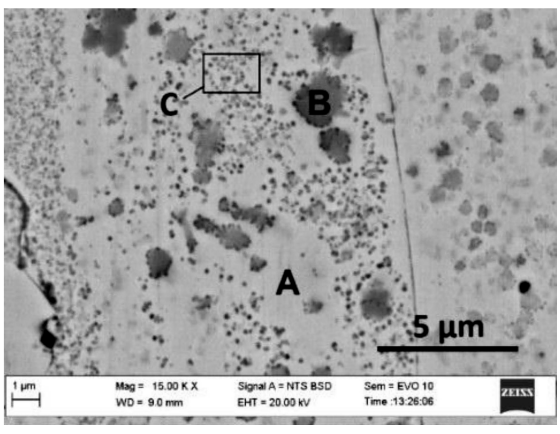

Figure 2: Microstructure of the coating

nanosized nickel borides and/or silicides and provide dispersion strengthening of the solid solution. It all results in a high coating microchardness, which, according to the Vickers measurements performed, varies between 674 and 831 HV. Such microhardness values are in good agreement with the results reported in other publications,[19,22,23] which show that the microhardness of NiCrSiBFe coatings can vary from 611 to 823 HV[19,22] when sprayed with the plasma method, and can ranged from 394 to 973 HV[23] when the plasma-transferred arc method is used.

The average values of the coating porosity, calculated as the ratio of the total pore area and the analyzed surface area, along with the values of adhesion determined, are presented in **Figure 3**. A significant increase in the porosity was observed with the increase in the coating thickness. Such a tendency is related to the gas evolution from the liquid phase during the coating crystallization and is common for thermal-spray coatings.[24] The lowest porosity, determined for the coatings with the minimum thickness (A1 and B1), is 0.8 % and 1.1 %, respectively; the highest porosity determined does not exceed 4.5 %. The influence of the substrate-surface pre-treatment on the porosity of the coating was not observed.

The bonding of the coating to the substrate may be realized through various mechanisms and their combinations where mechanical interlocking (anchoring) is usually dominant. Beside other factors, the condition of the substrate surface plays an important role. Mechanical roughening of the substrate removes contaminated oxidized surface layer and, due to formed surface irregularities, increases the real surface area and the probability of mechanical splats' interlocking. Here, a sandblasted surface having the average roughness Ra of 3.91 μm provided a 13.5 MPa adhesion strength when the thickness of the deposited layer was 120 μm.

Additional surface etching with orthophosphoric acid resulted in a slight roughness decrease (3.83 μm) due to a partial dissolving of sharp surface irregularities. The average adhesion value obtained (14.3 MPa) does not

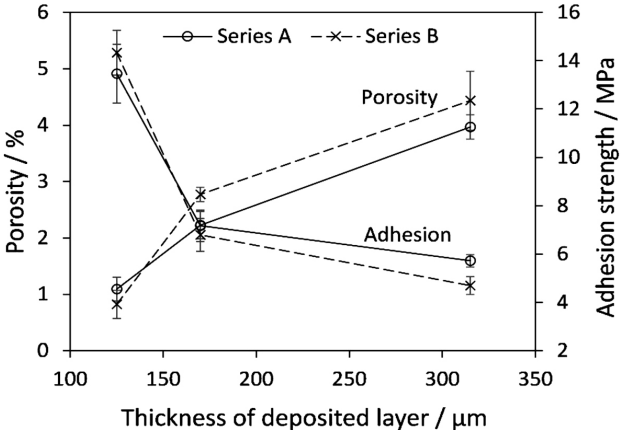

Figure 3: Porosity and adhesion of deposited coatings in dependence of their thickness

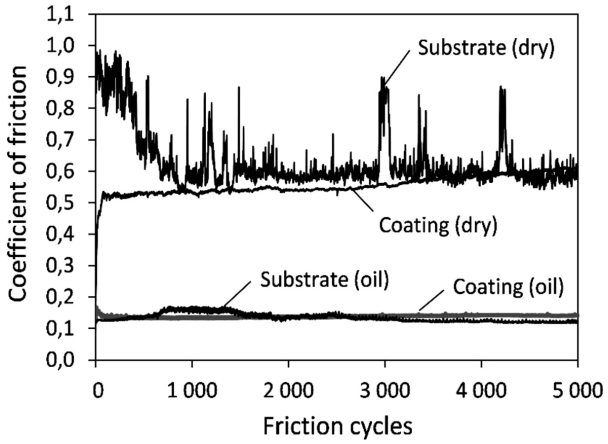

Figure 4: Friction curves

differ significantly from that of the sandblasted sample: the difference measured is in the range of the standard deviation. The adhesion bonding dramatically decreased with the increase in the coating thickness, indicating the domination of the residual-stress factor in the coating failure for thicker layers. Thus, for the sandblasted samples, the coating thickness increased by 1.36 and 2.52 times led to an adhesion decrease by 1.9 and 2.4 times, respectively. Very similar results were obtained for the samples of series B.

Tribological tests under dry and lubricated conditions were performed for all the investigated samples and the results are presented in **Table 3**, **Figures 4** and **5**. No significant difference in the friction behaviour and wear loss was observed for the coatings of different series and thickness values. Under dry conditions, the values of the friction coefficient of the A1–A3 specimen coatings

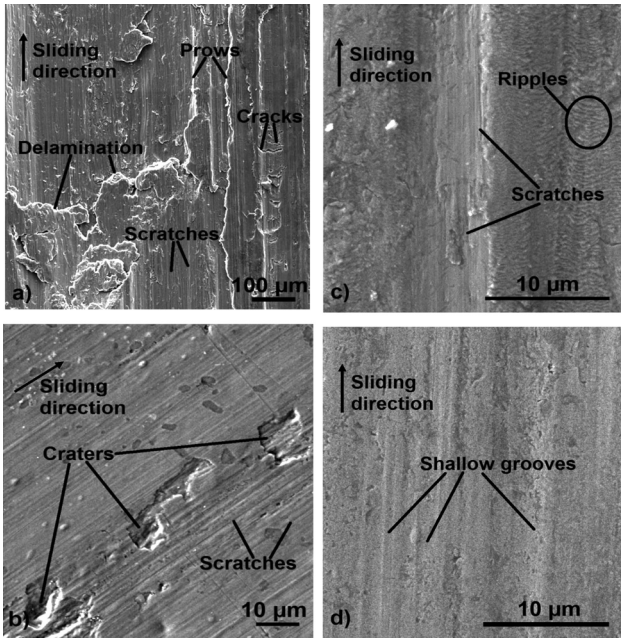

Figure 5: Wear tracks after a ball-on-plate test on the substrate: a) under dry condition, b) in oil and coating, c) under dry condition, d) in oil

ranged from 0.57 to 0.64 and for the B1–B3 specimen coatings, they ranged from 0.56 to 0.63, which are typical values for metallic contacts in the case of dry sliding conditions. For the Al-Mg substrate, the average friction coefficient of 0.60 was determined under dry sliding. As it was expected, the friction of both the substrate and the coating was reduced dramatically under lubrication. A stable friction-coefficient value of about 0.14 was estimated for the coatings, while for the substrate, the value varied between 0.12 and 0.17. As can be clearly seen from the typical friction curves presented in **Figure 4**, the plasma-sprayed NiCrSiBFe coating provides a more steady friction behaviour and a stable friction coefficient compared with the Al-Mg substrate, especially during dry sliding.

Table 3: Results of the wear test

	Volume loss / mm^3	Wear rate / mm^3/m	Wear resistance / m/mm^3
Substrate (dry)	0.4978	0.0124	80.35
Coating (dry)	0.2489	0.0062	160.71
Substrate (oil)	0.0610	0.0015	655.74
Coating (oil)	0.0124	0.0003	3225.81

The cracks and fragmentation of the surface layer and its delamination along with more or less deep scratches, observed on the worn surface of the substrate after the dry-sliding test (**Figure 5a**), testify to the prevalence of delamination and abrasive-wear mechanisms. The presence of the longitudinal prows and cracks, transverse to the sliding direction, shows that the plastic deformation along with the adhesive wear take place during dry sliding. The delamination of coarse debris mainly causes the significant mass loss and the fluctuation of friction that is clearly observed from the presented friction curve. Lubricated sliding of the Al-Mg substrate is characterized by a worn surface, containing mainly craters and scratches along the sliding direction (**Figure 5b**), indicating abrasion and delamination as the predominant wear mechanisms.

Significantly fewer damage signs were observed on the worn surfaces of the coatings. Here, typical wear traces after dry sliding (**Figure 5c**) were shallow abrasive scratches and fine transverse ripples, most likely attributable to the excessive traction due to surface heating during dry sliding. Under the lubrication, the coating surface was damaged minimally: shallow grooves were mainly observed, indicating that a slight surface abrasion due to the asperities on the counter-body may be the dominant wear mechanism (**Figure 5d**). The estimated wear parameters presented in **Table 3** show that, under dry sliding, the wear loss of the Al-Mg substrate is ~2 times bigger, compared to the much harder NiCrSiBFe coating. The lubricating oil film significantly reduces the wear loss of both the substrate (> 8 times) and the coating (~20 times) and, under the lubrication, the sliding wear resistance of a coated surface is ~5 times better, compared to the uncoated substrate.

4 CONCLUSION

The plasma-spray technique, employed in this work, allows the formation of a protective low-porous NiCrSiBFe layer on an Al-Mg substrate; hard inclusions and dispersion strengthening of the solid solution provide a high coating microhardness varying between ~670 and ~830 HV.

Both the mechanical substrate pre-treatment and its combination with chemical etching, conventionally used for the aluminium-component preparation, fail to provide a satisfactory coating adhesion, particularly, when the coating thickness is increased; this indicates that further development of the pre-treatment techniques for aluminium components is of great importance.

A plasma-sprayed NiCrSiBFe coating provides a more steady friction behaviour and a stable friction coefficient compared with the Al-Mg substrate and it significantly improves the wear conditions of the coated parts: the wear resistance of a coated surface, compared to the uncoated substrate, is ~2 times better under dry sliding and ~5 times better under lubricated sliding.

5 REFERENCES

[1] Y. Tan, L. He, X. Wang, X. Hong, W. Wang, Tribological properties and wear prediction model of TiC particles reinforced Ni-base alloy composite coatings, Transaction of Nonferrous Metals Society of China, 24 (**2014**) 8, 2566–2573, doi:10.1016/S1003-6326(14)63384-7

[2] L. He, Y. Tan, H. Tan, C. Zhou, L. Gao, Tribological properties of nanostructured Al_2O_3–40%TiO_2 multiphase ceramic particles reinforced Ni-based alloy composite coatings, Transaction of Nonferrous Metals Society of China, 23 (**2013**) 9, 2618–2627, doi:10.1016/S1003-6326(13)62776-4

[3] S. Uozato, K. Nakata, M. Ushio, Evaluation of ferrous powder thermal spray coatings on diesel engine cylinder bores, Surface and Coatings Technology, 200 (**2005**) 7, 2580–2586, doi:10.1016/j.surfcoat.2005.05.042

[4] S. Uozato, K. Nakata, M. Ushio, Corrosion and wear behaviors of ferrous powder thermal spray coatings on aluminum alloy, Surface and Coatings Technology, 169–170 (**2003**), 691–694, doi:10.1016/S0257-8972(03)00141-5

[5] W. J. Kim, S. H. Ahn, H. G. Kim, J. G. Kim, I. Ozdemir, Y. Tsunekawa, Corrosion performance of plasma-sprayed cast iron coatings on aluminum alloy for automotive components, Surface and Coatings Technology, 200 (**2005**) 1–4, 1162–1167, doi:10.1016/j.surfcoat.2005.02.220

[6] M. F. Morks, Y. Tsunekawa, N. F. Fahim, M. Okumiya, Microstructure and friction properties of plasma sprayed Al-Si alloyed cast iron coatings, Materials Chemistry and Physics, 96 (**2006**) 1, 170–175, doi:10.1016/j.matchemphys.2005.07.002

[7] K. Nakata, M. Ushio, Effect of Fe content on wear resistance of thermal-sprayed Al-17Si-XFe alloy coatings on A6063 Al alloy substrate, Surface and Coatings Technology, 169–170 (**2003**), 443–446, doi:10.1016/S0257-8972(03)00187-7

[8] O. Sarikaya, S. Anik, S. Aslanlar, S. C. Okumus, E. Celik, Al-Si/B_4C composite coatings on Al-Si substrate by plasma spray technique, Materials and Design, 28 (**2007**) 9, 2443–2449, doi:10.1016/j.matdes.2006.09.007

[9] M. Gui, S. B. Kang, Aluminum hybrid composite coatings containing SiC and graphite particles by plasma spraying, Materials Letters, 51 (**2001**) 5, 396–401, doi:10.1016/S0167-577X(01)00327-5

[10] L. He, Y. Tan, X. Wang, T. Xu, X. Hong, Microstructure and wear properties of Al_2O_3-CeO_2/Ni-base alloy composite coatings on aluminum alloys by plasma spray, Applied Surface Science, 314 (**2014**), 760–767, doi:10.1016/j.apsusc.2014.07.047

[11] L. He, Y. Tan, H. Tan, Y. Tu, Z. Zhang, Microstructure and tribological properties of WC-CeO_2/Ni-base alloy composite coatings, Rare Metal Materials and Engineering, 43 (**2014**) 4, 823–829, doi:10.1016/S1875-5372(14)60092-8

[12] L. Gu, X. Fan, Y. Zhao, B. Zou, Y. Wang, S. Zhao, X. Cao, Influence of ceramic thickness on residual stress and bonding strength for plasma sprayed duplex thermal barrier coating on aluminum alloy, Surface and Coatings Technology, 206 (**2012**) 21, 4403–4410, doi:10.1016/j.surfcoat.2012.04.070

[13] J. R. Davis, Nickel, Cobalt, and their Alloys, ASM Specialty Handbook, ASM International, Materials Park, USA 2000, 442, doi:10.1361/ncta2000p013

[14] C. Navas, R. Colaco, J. de Damborenea, R. Vilar, Abrasive wear behavior of laser clad and flame sprayed-melted NiCrBSi coatings, Surface and Coatings Technology, 200 (**2006**), 6854–6862, doi:10.1016/j.surfcoat.2005.10.032

[15] T. Gomez-del Rio, M. A. Garrido, J. E. Fernandez, M. Cadenas, J. Rodriguez, Influence of the deposition techniques on the mechanical properties and microstructure of NiCrBSi coatings, Journal of Materials Processing Technology, 204 (**2008**), 304–312, doi:10.1016/j.jmatprotec.2007.11.042

[16] H. J. Kim, S. Y. Hwang, Ch. H. Lee, P. Juvanon, Assessment of wear performance of flame sprayed and fused Ni-based coatings, Surface and Coatings Technology, 172 (**2003**), 262–269, doi:10.1016/S0257-8972(03)00348-7

[17] V. Stoica, R. Ahmed, T. Itsukaichi, Influence of heat-treatment on the sliding wear of thermal spray cermet coatings, Surface and Coatings Technology, 199 (**2005**), 7–21, doi:10.1016/j.surfcoat.2005.03.026

[18] K. G. Budinski, Friction, Wear and Erosion Atlas, CRC Press, London 2013, 277

[19] N. L. Parthasarathi, M. Duraiselvam, U. Borah, Effect of plasma spraying parameter on wear resistance of NiCrBSiFe plasma coatings on austenitic stainless steel at elevated temperatures at various loads, Materials and Design, 36 (**2012**), 141–151, doi:10.1016/j.matdes.2011.10.051

[20] C. Navas, R. Vijande, J. M. Cuetos, M. R. Fernandez, J. Damborenea, Corrosion behavior of NiCrBSi plasma-sprayed coatings partially melted with laser, Surface and Coatings Technology, 201 (**2006**) 3–4, 776–785, doi:10.1016/j.surfcoat.2005.12.032

[21] D. Felgueroso, R. Vijande, J. M. Cuetos, R. Tucho, A. Hernandez, Parallel laser melted tracks: effects on the wear behavior of plasma-sprayed Ni-based coatings, Wear, 264 (**2008**) 3–4, 257–263, doi:10.1016/j.wear.2007.03.015

[22] J. M. Miguel, J. M. Guilemany, S. Vizcaino, Tribological study of NiCrBSi coating obtained by different processes, Tribology International, 36 (**2003**), 181–187, doi:10.1016/S0301-679X(02)00144-5

[23] T. Liyanage, G. Fisher, A. P. Gerlich, Influence of alloy chemistry on microstructure and properties in NiCrBSi overlay coatings deposited by plasma transferred arc welding (PTAW), Surface and Coatings Technology, 205 (**2010**), 759–765, doi:10.1016/j.surfcoat.2010.07.095

[24] J. R. Davis, Handbook of Thermal Spray Technology, ASM International, Materials Park, OH, USA, 2004, 339

UDK 621.763:621.762.3:620.172.22
Original scientific article/Izvirni znanstveni članek

ISSN 1580-2949
MTAEC9, 51(4)679(2017)

FORMATION OF Ni-Ti INTERMETALLICS DURING REACTIVE SINTERING AT 800–900 °C

OBLIKOVANJE NiTi INTERMETALNIH ZLITIN MED REAKTIVNIM SINTRANJEM PRI 800–900 °C

Pavel Novák[1], Vladimír Vojtěch[1], Zuzana Pecenová[1], Filip Průša[1], Petr Pokorný[1], Davy Deduytsche[2], Christophe Detavernier[2], Adriana Bernatiková[1], Pavel Salvetr[1], Anna Knaislová[1], Kateřina Nová[1], Lucyna Jaworska[3]

[1]University of Chemistry and Technology, Department of Metals and Corrosion Engineering, Technická 5, 166 28 Prague 6, Czech Republic
[2]Ghent University, Department of Solid State Sciences, Krijgslaan 281, S1 9000 Gent, Belgium
[3]Institute of Advanced Manufacturing Technology, 37a Wroclawska St., 30-011 Krakow, Poland
panovak@vscht.cz

Prejem rokopisa – received: 2016-08-17; sprejem za objavo – accepted for publication: 2016-11-16

doi:10.17222/mit.2016.257

In this work the formation of intermetallics in the Ni-Ti system by reactive sintering at 800–900 °C was studied. The mechanism and kinetics of the reactions, which led to Ni-Ti phases, were determined by thermal analysis, in-situ XRD and the application of an experimental model consisting of nickel-plated titanium. It was found that the formation of Ni-Ti phases below the transformation temperature of titanium is controlled by diffusion. Above this temperature, the reactions switch to the rapid Self-propagating High-temperature Synthesis (SHS) mode.

Keywords: reactive sintering, powder metallurgy, NiTi

V delu je bil raziskan nastanek intermetalnih zlitin v sistemu NiTi pri reaktivnem sintranju na 800-900 ° C. S termično analizo, XRD-in situ analizo in uporabo eksperimentalnega modela, nikljanega s titanom, sta bila določena mehanizem in kinetika reakcij, ki sta vodila k NiTi fazam. Ugotovljeno je bilo, da je tvorba NiTI faze pod transformacijsko temperaturo titana, nadzorovana z difuzijo. Nad to temperaturo se reakcije spremenijo na hitro rastoči temperaturno -sintezni način (SHS).

Ključne besede: reaktivno sintranje, metalurgija prahov, NiTi

1 INTRODUCTION

The Ni-Ti alloy called nitinol, in approximately equimolar proportions, is the most widely known shape-memory alloy. The shape-memory effect in this alloy is connected with the transformation between high-temperature cubic austenite and low-temperature monoclinic martensite.[1,2] For the practical application of these alloys, superelasticity is very important. This phenomenon occurs when the NiTi alloy is deformed slightly above the martensite → austenite transformation temperature. Deformation induces the formation of the martensite phase, which is continuously transformed to austenite during unloading. Due to this phenomenon, this alloy behaves like an enormously elastic material.[1,2] In addition, the NiTi alloy is also a corrosion-resistant material.[3] Due to its exceptional properties, the NiTi alloy is applied in both medical (dental implants, stents, scaffolds)[4,5] and technical applications (actuators, robotics, etc.).[6–8]

The most commonly applied techniques in the industrial production of nitinol alloy are melting metallurgy processes – vacuum induction melting (VIM) and vacuum arc remelting (VAR).[9,10] In the VIM of Ti-containing alloys there is a serious danger of a strong contamination of the melt due to the high reactivity of molten titanium.[11] The VAR technique makes it possible to prepare alloys of higher purity, but there is a problem with homogeneity. To obtain a sufficiently homogenous product, the VAR process has to be repeated even more than 4 times.[10] This implies that it is costly and relatively problematic to obtain a NiTi shape-memory alloy. If a simple production technology would be developed, the NiTi alloy could be more frequently applied, not only in specific areas requiring the shape-memory effect, but also in other technical branches as a corrosion-resistant alloy. It will be beneficial for European economy, because this alloy does not contain any elements listed as critical raw materials.[12]

A promising alternative to melting metallurgy production routes is powder metallurgy (PM). A simple non-conventional PM production technology is reactive sintering. In general, the reactive sintering is a densification process, where initial components in powder form are transformed to a compact product via thermally-activated chemical reactions.[13] These reactions are mostly exothermic when intermetallics are formed. The route from powders to the compact usually contains powder blending, cold pressing and sintering.[13,14] When pure powders and an efficient protective atmosphere are

applied, a high-purity product is obtained due to the limited contact of the compressed reaction mixture with the crucible or support during the process.

The reactive sintering process of many intermetallics, including the Ni-Ti alloy, proceeds in two stages: a lower-temperature diffusional stage and a rapid high-temperature process called Self-propagating High-temperature Synthesis (SHS).[13–15]

In the case of the reactive sintering of NiTi alloy, the following mechanism is proposed in the literature. During heating to 900 °C, the slow diffusional formation of three intermetallics (Ti_2Ni, NiTi and Ni_3Ti) proceeds. In our previous paper we found that traces of the Ti_2Ni phase start to form already at 471 °C, being followed by NiTi and Ni_3Ti at 632 °C.[16] The transformation of α-Ti to β-Ti takes place as the temperature increases and after that the β-Ti rapidly saturates with nickel. When the temperature exceeds 942 °C, a liquid phase is formed from the solid solution of nickel in β-Ti by eutectic transformation and thus ignites the SHS reaction.[15] However, in our previous paper about the optimization of the conditions for the reaction synthesis of the NiTi shape memory alloy the structure corresponding to the SHS reaction was observed already after heating to 900 °C, being very similar to the material processed at 1100 °C.[17]

This paper aims to explain how it is possible to initiate the SHS reaction in NiTi alloy at 900 °C. To prove it, the mechanism and kinetics of the Ni+Ti reactions were studied by thermal analysis, in-situ XRD analysis and an experimental model.

2 MATERIALS AND METHODS

As mentioned above, the structure appearing to result from SHS reaction was observed in the NiTi alloy already at 900 °C using a heating rate of approximately 300 °C/min,[17] even though other references state that the SHS reaction is triggered by the melt formation by eutectic reaction at 942 °C. To prove the possibility to initiate the SHS reaction under these conditions and to describe the reaction mechanism, the following steps were carried out:

- Thermal analysis during heating from room temperature to approximately 1200 °C with the heating rate of approximately 300 °C/min. The heating rate was the same as in our previous paper, where the structure corresponding to the SHS reaction was observed after the process at 900 °C.[17]
- In-situ XRD analysis during heating from the laboratory temperature to 900°C with the heating rate of 60 °C/min. The heating rate was limited by the capabilities of the device.
- Description of mechanism and kinetics of the Ni-Ti phases' formation at 800 °C and 900 °C using an experimental model.
- Reactive sintering of Ni-Ti samples at 800 °C and 900 °C with the heating rate of 300 °C/min.

Experimental material for thermal analysis and in-situ XRD was prepared by blending of nickel powder (particle size < 150 μm, > 99.99 % purity, supplied by Aldrich) and titanium powder (particle size <44 μm, > 99.5 % purity, supplied by Alfa Aesar). Green bodies with a cylindrical shape of 10 mm in diameter and approximately 5 mm in height were prepared by uniaxial cold pressing of the powder blends under a pressure of 630 MPa using LabTest 5.250SP1-VM universal loading machine.

Thermal analysis was carried out during heating in the induction furnace from room temperature to 900 °C with the heating rate of approximately 300 °C/min. An optical pyrometer (Optris P20 2M) was used to record the temperature profile of the reaction.

In-situ XRD analysis (Cu-K_α radiation) was carried out during heating from laboratory temperature to 900 °C in a helium atmosphere with a heating rate of 60 °C/min.

An experimental model was established and successfully applied in our previous works in the Fe-Al, Fe-Al-Si and Ti-Al-Si systems.[18,19] In the mentioned papers, the experimental model consisted of an iron or titanium sample submerged in molten aluminium or Al-Si alloy. The aim of these experiments was to describe the kinetics of the formation of intermetallics in these particular alloys systems, because directly in reactive sintering process it is not possible. In the present work a model (Ni-Ti diffusion couple) consisting of a titanium bulk sample coated with nickel was applied. The nickel-plated titanium simulates the interaction between the compressed titanium and nickel powder particles. The galvanic nickel plating was carried out at 60 °C in a Watts's bath containing 300 g/L $NiSO_4.7H_2O$, 40 g/L $NiCl_2$ and 40 g/L H_3BO_3 using a current density of 10 A/m to the final thickness of approximately 20 μm. Before galvanic plating, titanium samples were sand-blasted with alumina for 10 min, pickled in 35 % HCl at 60 °C for 12 min and activated in 35 % HCl at 20 °C for 15 s. The coated samples were annealed for 30–180 min in evacuated and sealed silica ampoules at 800 °C. At 900 °C, the experiment was stopped after 120 min, because the whole thickness of the nickel coating reacted to form Ni-Ti phases. The heating rate during the experiments was approximately 300 °C/min. The phase composition of the obtained multilayer systems was identified by the X-ray diffraction (XRD) method using PANalytical X'Pert Pro diffractometer (Cu-K_α radiation). PANalytical X'Pert HighScore Plus software with the PDF-2 database was used to process and to evaluate the XRD patterns. The microstructure of intermetallics' layers was examined with a TESCAN VEGA 3 scanning electron microscope equipped with OXFORD Instruments X-max EDS SDD 20 mm^2 detector (SEM-EDS). Samples were mechanically ground, polished and etched using modified Kroll's reagent (10 mL HF, 40 mL HNO_3

and 50 H_2O) before the microstructure observation. Image analysis was carried out by the means of ImageJ software in order to determine the thickness of the intermetallics' layers. A process controlling the formation of intermetallics was determined by fitting the layer thickness with a parabolic growth equation. When a process is controlled by diffusion of species through a reaction product, it is generally described by the parabolic law, written as Equation (1):

$$d = \sqrt{k_p \cdot t} \tag{1}$$

where d is the layer thickness (μm) and t represents the annealing duration (s).[20]

3 RESULTS AND DISCUSSION

The temperature profile during heating of the compressed powder mixture of nickel and titanium was recorded using an optical pyrometer. During heating in an induction furnace by the rate of nearly 300 °C/min, the temperature increased almost linearly up to approximately 880 °C (**Figure 1**). After that, the increase of the slope, i.e., the heating rate, can be observed. This increase can be probably be attributed to the initiation of the strongly exothermal SHS reaction. This temperature corresponds well with the transformation of titanium from hexagonal (hcp) structure to cubic (bcc) one.[21] After achieving approximately 940 °C, the slope of the curve increases even more rapidly, probably due to the formation of a liquid phase by the eutectic transformation in the Ni-Ti system (942 °C).[21] The liquid medium supports the SHS reaction by increasing the diffusion rate of the reactants. The maximum temperature achieved by the reactions was 1137 °C. This indicates that the sample was partially molten due to eutectic reactions at 942 °C and 1118 °C, but did not exceed the melting point of the NiTi phase (1310 °C).[21] It can be expected that the temperature at the reaction front can be even higher, but the heat is quickly transferred to the rest of the sample and therefore the overall temperature of the sample is lower.

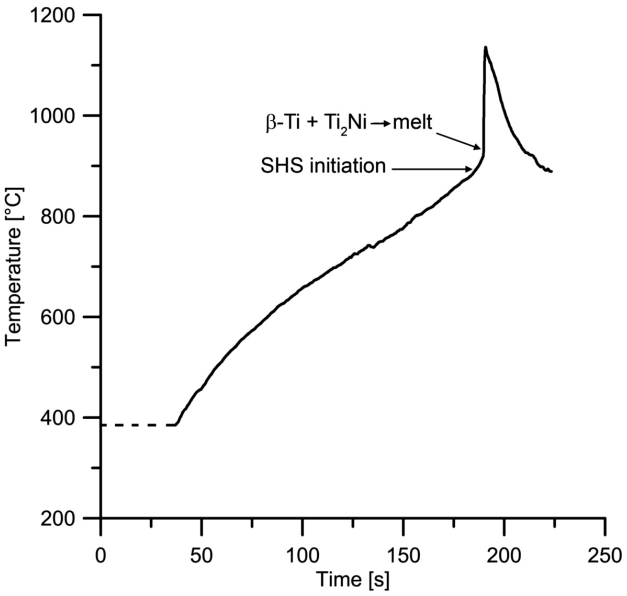

Figure 1: Heating curve of Ni-Ti compressed powder mixture (heating rate of approx. 300 °C min^{-1}, recorded by optical pyrometer)

The in-situ XRD analysis during heating of the compressed powder mixture from the room temperature to 900 °C with a rate of 60 °C/min (**Figure 2**) shows the continuous shift of the diffraction lines of nickel and titanium to lower angles with increasing temperature. This phenomenon is caused by the thermal expansion of the powders. In addition, the phase transformation of hexagonal α-Ti to cubic β-Ti can be observed around the temperature expected according to the Ni-Ti phase diagram (882 °C).[21] In addition to this phase transformation, the weak diffraction lines of the Ti_2Ni (cubic structure $Fd\bar{3}m$)[21] and NiTi (austenite, cubic structure $Pm\bar{3}m$)[21] phases start to be visible at approximately 750 °C. The intensity of the lines of the Ti_2Ni phase increase very rapidly, when a temperature of approximately 880 °C is achieved (**Figure 2**). This increase is immediately followed by the rapid formation of NiTi (austenite, cubic structure $Pm\bar{3}m$)[21] and Ni_3Ti (hexagonal $P6_3/mmc$)[21]. It implies that the SHS reaction between nickel and titanium is initiated by the transformation of titanium to its cubic allotropic modification. It forms the Ti_2Ni phase, which then reacts with nickel and/or the Ni_3Ti phase to form NiTi (austenite). The same phases' formation sequence was also observed for the diffusion stage of the reactive sintering process during long-term annealing at 500–650 °C. It implies that Ti_2Ni forms preferentially and it cannot be avoided in both low-temperature diffusion process, as well as during SHS mode.

To be able to describe the kinetics of the formation of intermetallics, the experimental model simulating the interaction between compressed nickel and titanium particles was applied. The model consisted of a bulk titanium sample covered by a nickel layer of approximately 20 μm in thickness. The model samples were

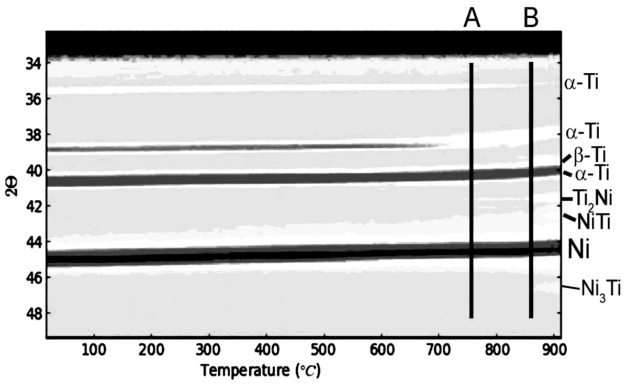

Figure 2: Variation of XRD intensities of NiTi46 (in mass fractions, (*w*/%)) compressed powder mixture during heating from room temperature to 900 °C (heating rate of 60 °C min^{-1})

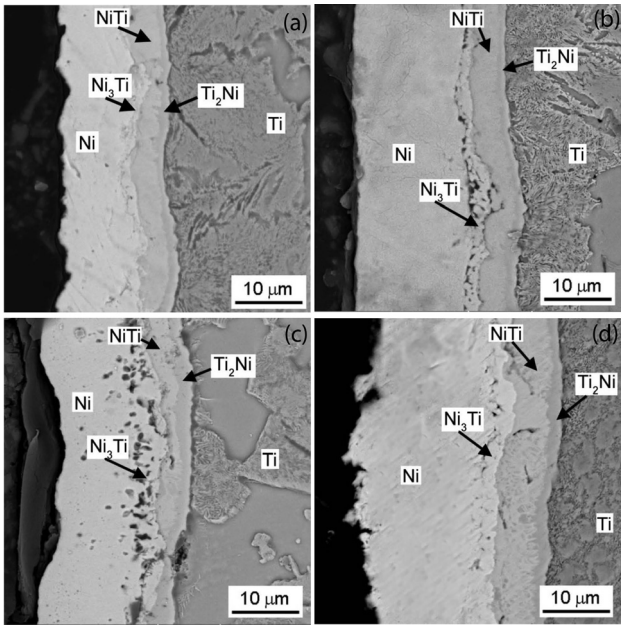

Figure 3: Microstructure of Ni-Ti model samples annealed at 800 °C for: a) 30 min, b) 60 min, c) 120 min and d) 180 min

annealed at 800 °C and 900 °C and the thickness of formed layers of intermetallics was measured to describe the difference between in the mechanism and kinetics of the Ni+Ti reactions below and above the $\alpha \rightarrow \beta$ transformation temperature in titanium. During annealing at 800 °C, the layers of Ti_2Ni, NiTi and Ni_3Ti are formed between the titanium and nickel coating (**Figure 3a** to **3d**). The presence of these phases was confirmed by the XRD (**Figure 4**) and local EDS analysis (**Table 1**). While the XRD analysis revealed all present layers on the sample, the EDS analysis was used to identify the sequence of the layers between the reacting titanium and nickel. The dependences of the thickness of the Ti_2Ni and NiTi layers on the process duration exhibit the parabolic shape (**Figure 5**). The calculated parabolic rate constants for all the samples indicate that the growth of these layers slightly slows down with the process duration (**Table 2**). The layer of Ni_3Ti (hexagonal $P6_3/mmc$)[21] phase starts to grow after 60 min of annealing and then it follows the parabolic law. The formation of the Ni_3Ti phase is probably the reason why the growth of the NiTi and Ti_2Ni layers decelerates during longer annealing. As the Ni_3Ti phase grows, NiTi and/or Ti_2Ni are consumed, as well as nickel. The results confirm that during the diffusion stage, the process starts with the formation of Ti_2Ni and NiTi layers, followed by Ni_3Ti after longer annealing duration. Almost the same shape of the kinetic curves was also observed during annealing at 650 °C in our previous paper, where the formation of Ni-Ti intermetallics was studied during long-term annealing at 500-650 °C.[16]

Table 1: Chemical composition (EDS) of layers observed after annealing of model samples at 800 °C for 120 min

Phase	Content (in amount fractions, (*a*/%))	
	Ti	Ni
Ni	4.0±0.2	96.0±0.2
Ti_2Ni	65.7±0.6	34.3±0.6
NiTi	51.4±0.4	48.6±0.4
Ni_3Ti	27.9±1.8	72.1±1.8
Ti	98.4±0.2	1.6±0.2

Annealing at 900 °C leads to the layers of Ti_2Ni and NiTi (**Table 3, Figure 4**), which grow slightly more rapidly up to 60 min (**Figure 6a**) than at 800 °C (**Figure 5**). However, the thickness of the NiTi phase layer is very non-uniform. After 60 min, the thick layer of Ni_3Ti (hexagonal $P6_3/mmc$) phase arises in the structure. The

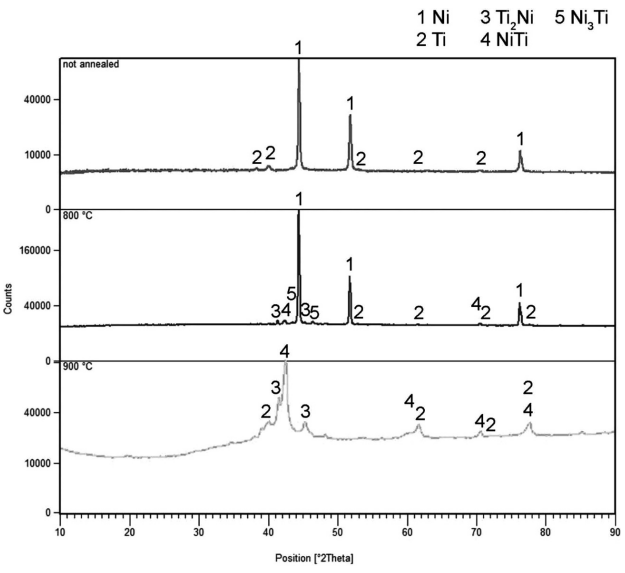

Figure 4: XRD patterns of model samples annealed at 800 °C and 900 °C

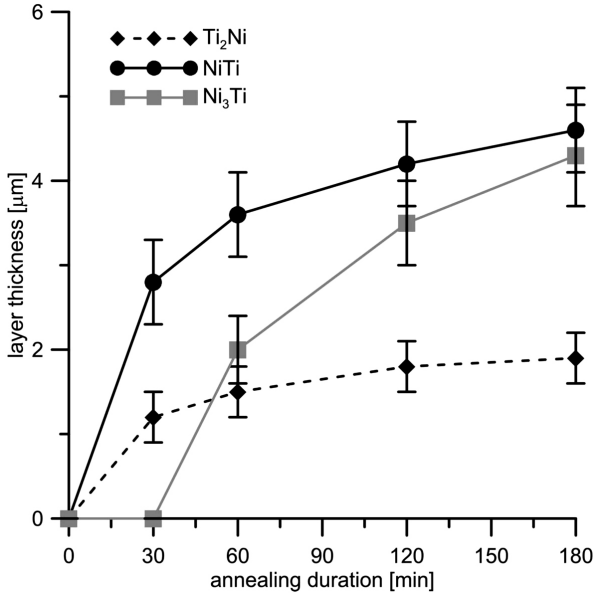

Figure 5: NiTi, Ti_2Ni and Ni_3Ti layer thickness on model samples vs. duration of annealing at 800 °C

Table 2: Parabolic rate constant of the formation of Ti_2Ni, NiTi and Ni_3Ti layer vs. annealing duration at 800 °C

Annealing duration (min)	Parabolic rate constant of the growth of layers ($\times10^{-4}$ μm s^{-1})		
	Ti_2Ni	NiTi	Ni_3Ti
30	8.0	43.6	0
60	6.3	36.0	11.1
120	4.5	24.5	17.0
180	3.3	19.6	17.1

Table 3: Chemical composition (EDS) of layers observed after annealing of model samples at 900 °C for 120 min

Phase	Content (in amount fractions, (*a*/%))	
	Ti	Ni
Ti_2Ni	66.8±0.5	33.2±0.5
NiTi	53.2±0.9	46.8±0.9
Ti	97.8±0.3	2.2±0.3

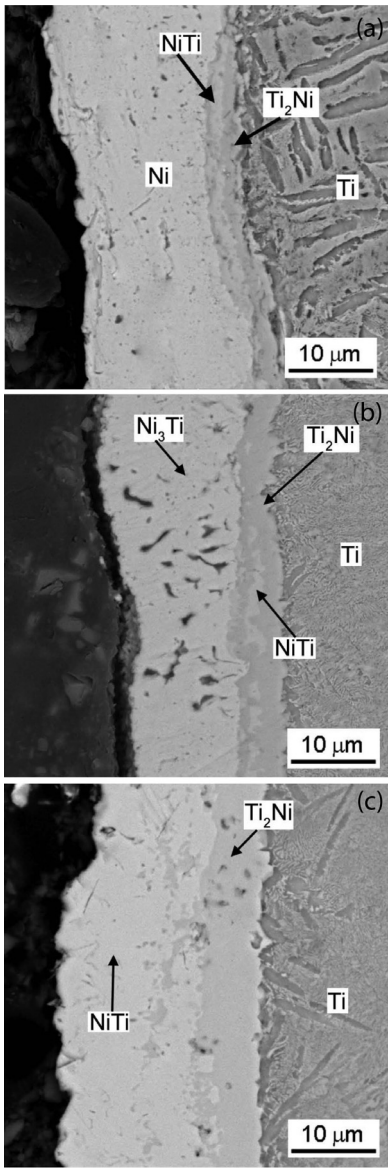

Figure 6: Microstructure of Ni-Ti model samples annealed at 900 °C for: a) 30 min, b) 60 min and c) 120 min

Ni_3Ti layer consumes almost the whole residual thickness of the nickel coating (**Figure 6b**). The Ni_3Ti layer is very porous, which confirms the previous results, where the Ni_3Ti phase was found to be a source of porosity.[16] When continuing the annealing, the Ni_3Ti phase disappears completely, since it reacts with Ti_2Ni in order to form a thick layer of NiTi phase (**Figure 6c**). The experiment was stopped after 120 min, because the whole layer was composed of NiTi and Ti_2Ni phases (**Figures 6c** and **7**). Calculated parabolic rate constants (**Table 4**) show that the formation of NiTi (austenite) and Ni_3Ti is not diffusion-controlled at 900 °C, because the constants vary strongly with the process duration. It confirms that the process runs in SHS mode.

Table 4: Parabolic rate constant of the formation of Ti_2Ni, NiTi and Ni_3Ti layer vs. annealing duration at 900 °C

Annealing duration (min)	Parabolic rate constant of the growth of layers ($\times10^{-4}$ μm s^{-1})		
	Ti_2Ni	NiTi	Ni_3Ti
30	16.1	46.7	0
60	87.1	40.1	267.0
120	50.0	325.0	0

To prove the results of the experimental model, the real compressed powder mixtures were prepared and heated at 800 °C and 900 °C with a holding time of 120 min. The same heating rate as in the experimental model (approx. 300 °C/min) was applied. The sample prepared by heating at 800 °C is composed of unreacted nickel and titanium particles covered by layers of Ti_2Ni, NiTi and Ti_3Ti of very similar thickness like in the model system (**Figure 8a**). On the other hand, the sample reactively sintered at 900 °C is comprised of Ti_2Ni particles in a NiTi matrix. The morphology of the sample changed from cylindrical shape to irregular shape due to partial melting during the process (**Figure 9**). This indicates that

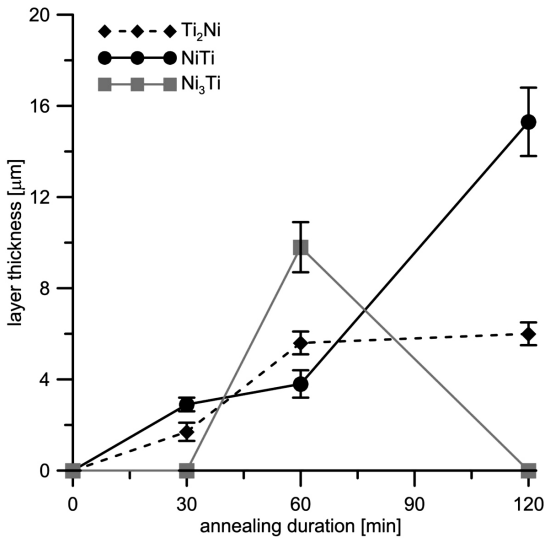

Figure 7: NiTi, Ti_2Ni and Ni_3Ti layer thickness on model samples vs. duration of annealing at 900 °C

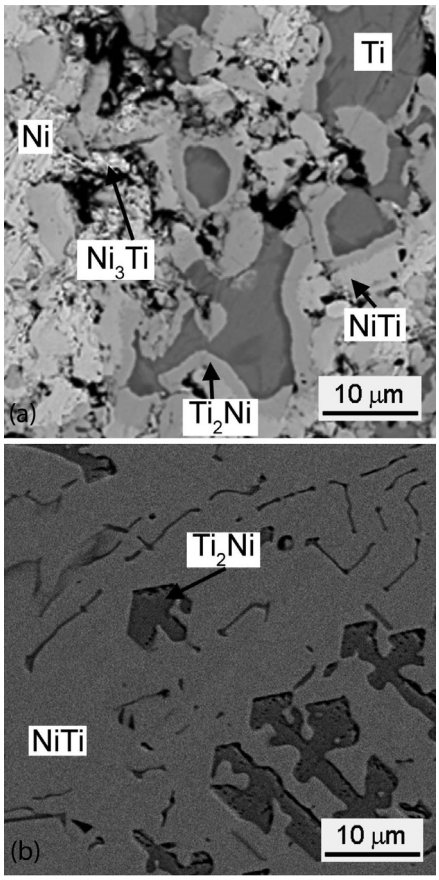

Figure 8: Microstructure of NiTi46 (in mass fractions, (*w*/%)) compressed powder mixtures reactively sintered at: a) 800 °C for 120 min and b) 900 °C for 120 min

during annealing of the powder mixture at 900 °C, enormous heat is evolved due to the SHS reaction.

The above-presented results show that the SHS reaction can be initiated immediately after exceeding the $\alpha \rightarrow \beta$ transformation temperature of titanium. It means that it is not necessary to achieve the melt formation by a eutectic reaction at 942 °C. In addition, the rapid SHS process is supported significantly when a high heating rate is applied.[17] During rapid heating, the diffusion is strongly suppressed. Therefore, the SHS can be initiated by the reaction of solid particles of nickel and titanium, having a cubic structure, producing a mixture of cubic Ti_2Ni and NiTi phases at the end of the process.

Figure 9: Morphology of NiTi46 (in mass fractions, (*w*/%)) compressed powder mixture reactively sintered 900 °C for 120 min

4 CONCLUSIONS

In this work the mechanism and kinetics for the formation of Ni-Ti phases at 800 °C and 900 °C were studied. The results revealed that the rapid SHS reaction is initiated in the solid state by the $\alpha \rightarrow \beta$ phase transformation of titanium. Below this temperature, the growth of Ni-Ti intermetallics is controlled by diffusion of the reactants. Above this temperature, the rapid SHS reaction is initiated. It was proved with an experimental model, where a significant change in the rate constant of the formation of Ni-Ti intermetallics was observed at 900 °C, compared with 800 °C. It was confirmed by the change of the slope of the heating curve in thermal analysis, as well as by the in-situ XRD analysis, where a rapid increase of the intensity of the diffraction lines of Ni-Ti intermetallics was observed after exceeding approximately 880 °C. The SHS process starts with the formation of Ni_3Ti phase, which reacts with Ti_2Ni already present from diffusion stage and forms the NiTi shape-memory phase. The temporary formation of Ni_3Ti phase results in an increase of the materials' porosity.

Acknowledgement

This research was financially supported by Czech Science Foundation, project No. 14-03044S. Partial support by COST Action CA15102 is also greatly appreciated.

5 REFERENCES

[1] C. M. Wayman, K. Shimizu, The Shape Memory (Marmem), Effect in Alloys, Materials Science and Technology, 6 (**1972**) 1, 175–183, doi:10.1179/030634572790446028

[2] M. Elahinia, M. Ahmadian, An enhanced SMA phenomenological model. Part I, The shortcomings of the existing models, Smart Materials Structures, 14 (**2005**) 6, 1297–308, doi:10.1088/0964-1726/14/6/022

[3] M. H. Elahinia, M. Hashemi, M.Tabesh, S. B. Bhaduri, Manufacturing and processing of NiTi implants: A review, Progress in Materials Science, 57 (**2012**) 5, 911–946, doi:10.1016/j.pmatsci.2011.11.001

[4] S. A. Thompson, An overview of nickel–titanium alloys used in dentistry, International Endodontic Journal, 33 (**2000**) 4, 297–310, doi:10.1046/j.1365-2591.2000.00339.x

[5] K. Kanjwal, K. R. Yeasting, C. Baptista, H. Elsamaloty, M. Sheikh, M. Elahinia, W. Anderson, J. D. Maloney, Retro-cardiac esophageal mobility and deflection to prevent thermal injury during atrial fibrillation ablation: an anatomic feasibility study, Journal of Interventional Cardiac Electrophysiology, 30 (**2011**) 1, 45–53, doi:10.1007/s10840-010-9524-2

[6] M. Elahinia, J. Koo, M. Ahmadian, C. Woolsey, Backstepping control of an SMA-actuated robotic arm, Journal of Vibration and Control, 11 (**2005**) 3, 407–429, doi:10.1177/1077546305051201

[7] E. Williams, M. Elahinia, An automotive SMA mirror actuator: modeling, design and experimental evaluation, Journal of Intelligent Material Systems and Structures, 19 (**2008**) 12, 425–1434, doi:10.1177/1045389X07087328

[8] D. Stockel, F. Tinschert, Temperature Compensation with Thermo-variable Rate Springs in Automatic Transmissions, SAE Technical Paper Series, (**1991**), doi:10.4271/910805

[9] R. Venugopalan, C. Trepanier, Assessing the corrosion behaviour of Nitinol for minimally-invasive device design, Minimally Invasive Therapy & Allied Technologies, 9 (**2000**) 2, 67–74, doi:10.3109/13645700009063052

[10] A. Foroozmehr, A. Kermanpur, F. Ashrafizadeh, Y. Kabiri, Investigating microstructural evolution during homogenization of the equiatomic NiTi shape memory alloy produced by vacuum arc remelting, Materials Science and Engineering, A528 (**2011**) 27, 7952–7955, doi:10.1016/j.msea.2011.07.024

[11] S. K. Sadrnezhaad, S. B. Raz, Interaction between Refractory Crucible Materials and the Melted NiTi Shape-Memory Alloy, Metallurgical and Materials Transactions B, 36B (**2005**) 3, 395–403, doi:10.1007/s11663-005-0068-2

[12] https://ec.europa.eu/growth/sectors/raw-materials/specific-interest/critical_cs

[13] C. B. Wang, S. Zhang, Q. Shen, L. M. Zhang, Investigation on reactive sintering process of boron carbide ceramics by XRD, Materials Science and Technology 25 (**2009**) 6, 809–812, doi:10.1179/174328408X363371

[14] P. Novák, A. Michalcová, J. Šerák, D. Vojtěch, T. Fabián, S. Randáková, F. Průša, V. Knotek, M. Novák, Preparation of Ti-Al-Si alloys by reactive sintering, Journal of Alloys and Compounds, 470 (**2009**) 1–2, 123–126, doi:10.1016/j.jallcom.2008.02.046

[15] M. Whitney, S. F. Corbin, R. B. Gorbet, Investigation of the mechanisms of reactive sintering and combustion synthesis of NiTi using differential scanning calorimetry and microstructural analysis, Acta Materialia, 56 (**2008**) 3, 559–570, doi:10.1016/j.actamat.2007.10.012

[16] P. Novák, P. Pokorný, V. Vojtěch, A. Knaislová, A. Školáková, J. Čapek, M. Karlík, J. Kopeček, Formation of Ni-Ti intermetallics during reactive sintering at 500-650 °C, Materials Chemistry and Physics, 155 (**2015**), 113–121, doi:10.1016/j.matchemphys.2015.02.007

[17] P. Novák, L. Mejzlíková, A. Michalcová, J. Čapek, P. Beran, D. Vojtěch, Effect of SHS conditions on microstructure of NiTi shape memory alloy, Intermetallics, 42 (**2013**), 85–91, doi:10.1016/j.intermet.2013.05.015

[18] P. Novák, V. Knotek, M. Voděrová, J. Kubásek, J. Šerák, A. Michalcová, D. Vojtěch, Intermediary phases formation in Fe–Al–Si alloys during reactive sintering, Journal of Alloys and Compounds, 497 (**2010**) 1–2, 90–94, doi:10.1016/j.jallcom.2010.03.028

[19] P. Novák, J. Kubásek, J. Šerák, D. Vojtěch, A. Michalcová, Mechanism and kinetics of the intermediary phase formation in Ti–Al and Ti–Al–Si systems during reactive sintering, International Journal of Materials Research, 100 (**2009**) 3, 353–355, doi:10.3139/146.110028

[20] A. T. Fromhold, Parabolic oxidation of metals, Physics Letters, A, 29 (**1969**) 3, 157–158, doi:10.1016/0375-9601(69)90088-7

[21] T. B. Massalski, Binary Alloy Phase Diagrams, 1990, ASM, Materials Park

UDK 621.791.4:621.791.47:67.017
Original scientific article/Izvirni znanstveni članek

ISSN 1580-2949
MTAEC9, 51(4)687(2017)

EFFECT OF TOOL GEOMETRY AND WELDING PARAMETERS ON THE MICROSTRUCTURE AND STATIC STRENGTH OF THE FRICTION-STIR SPOT-WELDED DP780 DUAL-PHASE STEEL SHEETS

VPLIV GEOMETRIJE ORODJA IN PARAMETROV VARJENJA NA MIKROSTRUKTURO IN STATIČNO TRDNOST TORNO VRTILNEGA TOČKOVNEGA VARJENJA DVOFAZNE JEKLENE PLOČEVINE DP780

Omid Abedini, Eslam Ranjbarnodeh, Pirooz Marashi

Amirkabir University of Technology, Department of Mining and Metallurgical Engineering, 424 Hafez Ave., Tehran, Iran
islam_ranjbar@aut.ac.ir

Prejem rokopisa – received: 2016-09-03; sprejem za objavo – accepted for publication: 2016-09-27

doi:10.17222/mit.2016.278

In this study, friction-stir spot welding is performed on DP780 dual-phase steel sheets to investigate the effect of the tool geometry and welding parameters on the static strength, the failure mode and the microstructure of the welds. First, the effects of two different parameters, the tool plunge depth and the tool holding time, were evaluated, where the tool penetration varied between 1.9–2.8 mm and the dwell time between 8–16 s. The tensile shear strength was first increased with the tool penetration and then decreased, while a longer tool holding time increased the tensile shear strength of the joints. Next, welds were made to compare the effects of two tool geometries, i.e., the conventional tapered pin and the triangular pin, on the hook shape, microstructure and static strength. The difference in the hook geometry led to differences in the tensile shear strength of the welds. The static strength of the welds made with the triangular pin was higher than that obtained using the tapered pin.

Keywords: friction-stir spot welding, tool geometry, static strength, dual-phase steel, microstructure

V študiji je izvedeno torno vrtilno točkovno varjenje na DP780 dvofazni jekleni pločevini, z namenom raziskave vpliva geometrije orodja in varilnih parametrov na statično trdnost, tip poškodbe in mikrostrukturo zvarov. Najprej so bili ocenjeni učinki dveh različnih parametrov, globine penetriranja in časa zadržanja orodja. Globina je variirala med 1,9 mm in 2,8 mm in zadrževalni čas med 8 s in 16 s. Natezna strižna trdnost se je s povečanjem globine penetracije najprej zvišala, nato pa znižala, medtem ko je čas zadrževanja orodja povečal natezno strižno trdnost zvarov. Izdelani so bili tudi zvari, na katerih se je določil vpliv geometrije orodja, klasičnega polkrožnega in trikotnega profila, na obliko, mikrostrukturo in trdnost zvarov. Statična trdnost zvarov, narejenih z orodjem trikotnega profila, je bila višja kot tista, pridobljena s polkrožno obliko.

Ključne besede: torno-vrtilno točkovno varjenje, geometrija orodja, statična trdnost, dvofazno jeklo, mikrostruktura

1 INTRODUCTION

Friction-stir welding (FSW) is a new solid-state joining technique, developed by TWI in 1991. This new welding method is usually used in the welding of plates and is different from conventional friction welding.[1] Friction-stir welding is commercially used for the welding of light metals such as aluminium alloys, e.g., standard-length Al extrusion panels for high-speed cruise ships, fuel tanks used in aerospace manufacturing and carriage manufacturing of high-speed trains.[2–4] Friction-stir spot welding (FSSW) is a derivative of friction-stir welding and is widely used for the welding of soft metals such as Al-, Cu- and Mg-alloys as well as different material combinations, particularly those with close melting temperatures. As a new solid-state joining process, FSSW, can avoid many problems associated with the fusion-welding processes. Therefore, in recent years, its applications have been extended to the welding of high-melting-temperature materials such as various types of steels, nickel and titanium alloys.[1–7] Following the success in the friction-stir spot welding of several steel alloys including hot-stamped boron steel,[8] DP600 and M190,[9] attempts to evaluate this process for the welding of more problematic steel alloys took place.

Dual-phase (DP) steels are an important class of high-strength low-alloy steels (HSLA) that have a unique combination of properties such as high tensile strength, high elongation, high ratio of strength to weight and continuous yielding. These properties stem from the microstructure of dual-phase steels, in which a soft and ductile matrix of ferrite provides good ductility while hard martensite islands provide high strength.[9–11] In the case of dual-phase steels, fusion-welding technique, such as resistance spot welding, are inadequate due to a dramatic softening in the heat-affected zone.[12] Therefore, the application of solid-state welding processes, such as friction-stir spot welding, for joining these steels has been extended.[3] Although the feasibility of joining advanced high-strength steels (AHSS) with friction-stir spot welding has been recently considered, it is shown that microstructural changes during FSSW dramatically affect mechanical properties by transforming the base-metal (BM) microstructure.[13] To date, the microstructures and failure

mechanisms of friction-stir spot-welded DP780 have not been examined in great detail. Thus, the increased utilization of advanced high-strength steel grades in the automotive architecture emphasized the need to examine how the FSSW joining works.

During friction-stir spot welding, a non-consumable rotating tool consisting of a pin and a shoulder is inserted into the upper sheet of a lap configuration while the backing tool beneath the lower sheet supports the downward force. Important process parameters of FSSW are the tool geometry, plunge depth, rotational speed, plunge rate, tilt angle and holding time. The tool plunge depth and the holding time determine the amount of heat generation, the material flow into the overlapped sheets, the weld geometry and, therefore, the mechanical properties of joints.[13–18]

It is reported[17] that the tool plunge depth strongly affects the strength of friction-stir spot-welded joints. However, it is shown that a deep tool penetration decreases the joint volume and the upper sheet thickness which, in turn, decreases the tensile shear strength.[14,15] The friction-stir spot welding of lap-configuration sheets is characterized by the formation of a partial metallurgical bond called the hook. The hook is a geometrical defect, formed in the weld region between the joining sheets. There is often a thin oxide film on the surface of the metallic materials. During the tool penetration into the bottom sheet, the oxide film is broken up into smaller particles. Distribution of the small oxide particles, because of the stirring of the tool, leads to the formation of the metallurgical bond between the two welded sheets. The tool-pin design significantly affects the hook geometry; thus, the failure mode and the static strength of the welds are influenced.[16,19–22]

Many efforts have been made to optimize the welding parameters and the tool design as well as modifying the friction-stir spot welding technique using a tool without a probe.[23,24] However, further investigation on the effect of the welding parameters and tool-pin geometry on the properties of the joints is required. Therefore, this study applies friction-stir spot welding to DP780 dual-phase steel sheets using a WC-Co alloy tool with two, tapered- and triangular-pin, geometries and a concave shoulder design with the following two goals. The first is to investigate the influence of the tool penetration depth and tool holding time on the mechanical shear strength and microstructure of the welded joints. The penetration depth and tool holding time were chosen because these two parameters have significant effects on the joint properties. The second goal of this work is to analyse the effect of the pin design on the hook geometry, weld strength and failure mode.

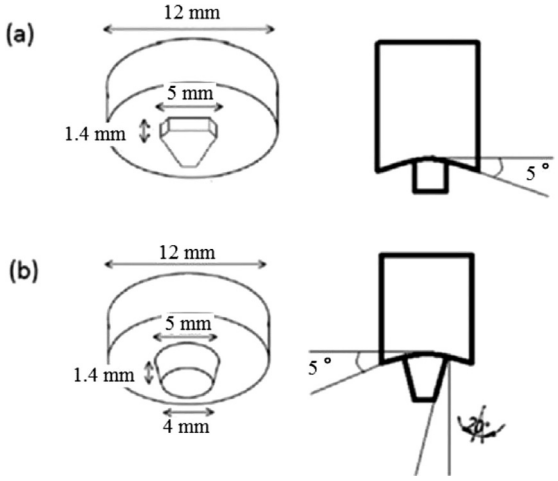

Figure 1: Schematic illustration of FSSW tool geometry: a) triangular pin shape, b) tapered pin shape

2 EXPERIMENTAL PART

1.5-mm-thick DP780 sheets were used in this study as the base metal whose chemical composition is summarized in **Table 1**. Individual sheet dimensions were 140 mm × 60 mm and the sheets were joined in the lap position with an overlap area of 45 mm × 60 mm. The friction-stir spot welding equipment provided rotational speeds from 1000 min^{-1} to 2500 min^{-1} and axial loads of up to 30 kN. The FSSW tools were made from the WC-Co alloy having a pin length of 1.4 mm and a shoulder with a diameter of 12 mm with a concave profile. As schematically shown in **Figure 1**, two different pin geometries were used: the tapered and triangular ones. All spot welds were made under the following processing conditions: the tool rotational speed and the plunge rate were kept constant at 1000 min^{-1} and 20 mm/min, respectively, while the tool holding time was (8, 12 or 16) s and the tool plunge depth was (1.9, 2.2, 2.5 or 2.8) mm.

Table 1: Material properties of DP780 (in mass fractions, *w*/%)

Element	C	Mn	Si	Ni	Cr	S	p
Content	0.1	0.44	0.13	0.04	0.08	0.02	0.14

Joint mechanical properties of the spot welds were evaluated with the hardness profile and tensile shear tests. A Vickers microhardness measurement was conducted at 0.3 mm above the interface of the overlapped sheets on the metallographic samples under a load of 500 g for 15 s. The tensile shear test was performed using an Instron 8502 machine with a constant crosshead speed of 1 mm/min. The lap shear strength was obtained by averaging the strength of five individual samples, welded using identical welding parameters. Macro- and micro-structure examinations were performed on the specimens. As-welded and tested samples were sectioned along the diameter of the weld keyhole. Metallographic observations were made with a light microscope and a scanning electron microscope (SEM, Hitachi S-2400) following the standard metallographic polishing and etching with a 2 % nital solution.

3 RESULTS AND DISCUSSION

3.1 Tensile shear strength

3.1.1 Effect of welding parameters on the tensile shear strength

The relationships between the tensile shear force (F_s), tool holding time (t) and plunge depth for both the triangular and tapered pin, for a constant 1000 min^{-1} tool rotational speed and a 20 mm/min tool plunge rate are indicated for individual data points in **Figure 2**. It is shown that the tensile shear force reaches its maximum at the 2.2 mm plunge depth and 16 s tool holding time. Thus, for both the plunge depth and the tool holding time, the tensile-shear-force trend was independent of the tool geometry.

Figures 3a and **3b** show examples of the size of the stir zone for the welding conditions consisting of the tool rotational speed of 1000 min^{-1}, tool plunge rate of 20 mm/min, tool holding time of 16 s and plunge depth of 1.9 mm and 2.2 mm, respectively, using the triangular pin. It can be seen that for the 2.2 mm tool plunge depth, the amount of the upward material flow of the lower sheet is higher than that of the weld with the 1.9 mm tool plunge depth. An increase in the upward material flow increases the faying surface between the upper and lower sheets, which, in turn, increases the tensile shear strength.[25–26]

Figure 4 shows views of macrosections taken at different plunge depths of (2.2, 2.5 and 2.8) mm at a constant 1000 min^{-1} tool rotational speed and 20

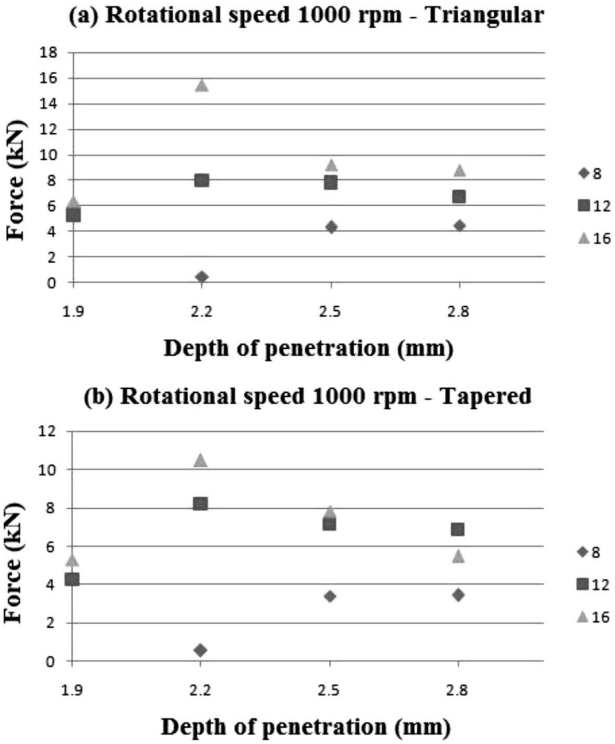

Figure 2: Tensile-shear force as a function of plunge depth and tool holding time at 1000 min^{-1} rotational speed for two different tool designs: a) triangular pin, b) tapered pin

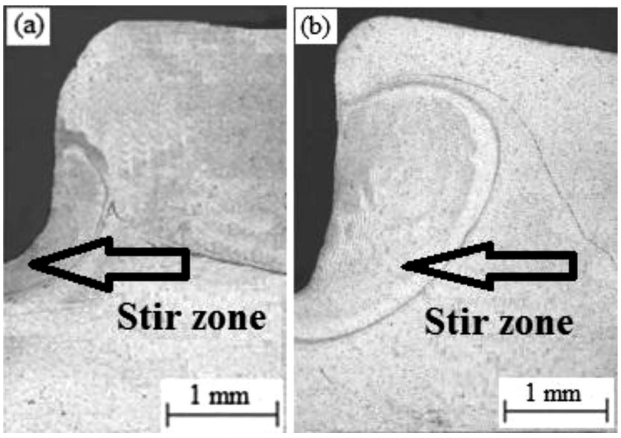

Figure 3: Microstructures of the stir zones of friction-stir spot welds for: a) 1.9 mm plunge depth and b) 2.2 mm plunge depth at a tool rotational speed of 1000 min^{-1} and dwell time of 12 s for the triangular pin

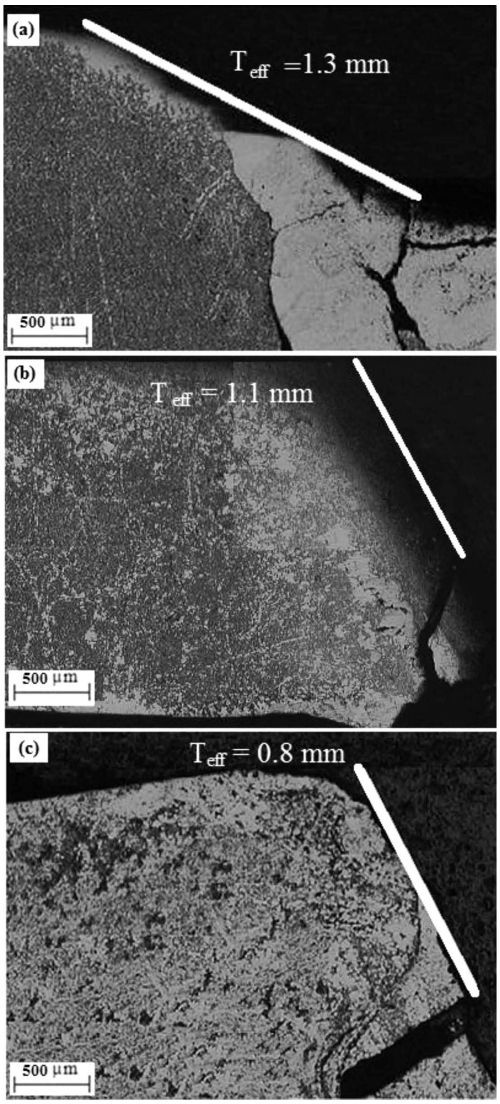

Figure 4: Typical cross-sectional macrostructures of friction-stir spot welds (a holding time of 16 s using a triangular pin) showing different upper-sheet thickness values: a) FSSW at 2.2 mm, b) FSSW at 2.5 mm and c) FSSW at 2.8 mm

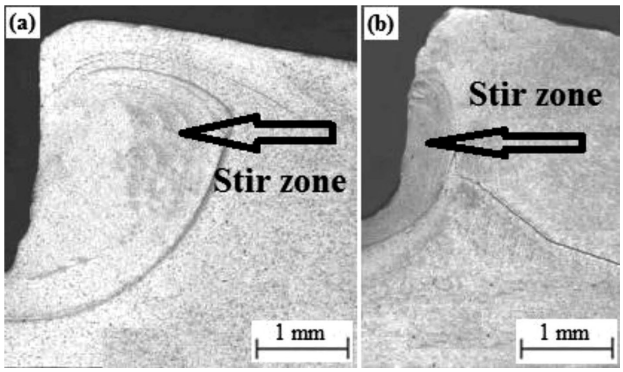

Figure 5: Typical cross-sectional macrostructures of friction-stir spot welds made with a triangular pin: a) plunge depth of 2.2 mm and tool holding time of 16 s, b) plunge depth of 2.2 mm and tool holding time of 8 s; rotational speed for both welds is 1000 min^{-1}

mm/min tool plunge rate, using the triangular pin. It is shown that an increasing tool plunge depth decreases the thickness of the upper sheet, which, in turn, decreases the tensile shear force of the welds made with the triangular pin from 15.46 kN to 8.81 kN. In fact, the thickness of the upper sheet is a function of the tool penetration depth; thus, a deep plunge depth can decrease the weld strength because the thickness of the upper sheet decreases with the increase in the plunge depth.[25,27] As can be seen in **Figure 4**, the final crack path in the fractured samples is through the effective thickness of the upper sheet. As a result, the thickness of the upper sheet provides resistance against external loading; therefore, to obtain a weld with high static strength, the thickness of the upper sheet should be as large as possible. According to the above reasons, the weld made with the 2.2 mm tool penetration depth has the highest tensile shear force for both the triangular and tapered pin.

Figure 2 also reveals that at the constant tool plunge depth of 2.2 mm, the increase in the tool holding time from 8 s up to 16 s increases the tensile shear force of the welds from 0.54 kN to 10.49 kN and from 0.42 kN to 15.46 kN for the tapered and triangular pin, respectively. In fact, by increasing the tool holding time at a constant plunge depth, the upward material flow of the lower sheet increases, which, in turn, increases the size of the stir zone, thus increasing the tensile shear force.[19] From **Figure 5,** it is evident that at the constant tool plunge depth of 2.2 mm, the longer tool holding time results in a larger stir zone. As a result, the tensile shear strength of a joint is maximum at the 16 s dwell time and the constant tool penetration depth.

3.1.2 Effect of the tool geometry on the tensile shear strength

Figure 2 shows that the maximum strength of the weld made with the triangular pin at the 2.2 mm plunge depth and 16 s tool holding time is about 50 % higher than that of the weld made with the tapered one at the same conditions. The existence of this difference between the tensile shear forces is due to the manner of the

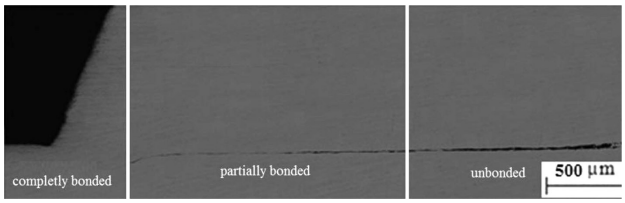

Figure 6: Macrostructure of a friction stir spot welds. Three characteristic regions: completely bonded region, partially bonded region and unbonded region

upward material flow during friction-stir spot welding using two different pin designs.[16,28] As it can be seen in the cross-sectional microstructure in **Figure 6**, there are three characteristic regions: a completely bonded region, a partially bonded region and an unbounded region, which are in sequence from the weld keyhole towards the base metal. These regions were fully described elsewhere.[16] As mentioned above, the hook is a partially metallurgically bonded area, which forms in the weld region between the welded sheets.

Figure 7 shows the pattern of the material flow and the formation of the hook in the weld region during friction-stir spot welding using tapered and triangular pins. As reported by H. Badarinarayan et al.,[16] the geometry of the pin significantly affects the hook geometry. In the case of the weld made with the tapered pin, the hook moves upward and then, near the stir-zone points, downward toward the weld bottom. When using this special shape of tool, the symmetrical rotation of the pin causes a shear deformation of the material around the pin surface. On the other hand, the hook direction in the weld

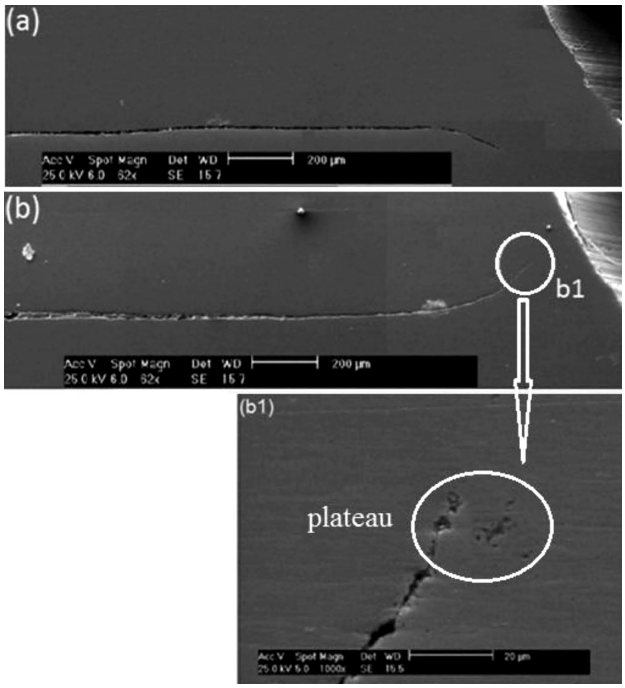

Figure 7: Views of the hook geometry of the welds made with: a) tapered pin, b) triangular pin; b1) magnified view of the plateau at the end of the hook in region b1 for the friction-stir spot weld made with the triangular pin

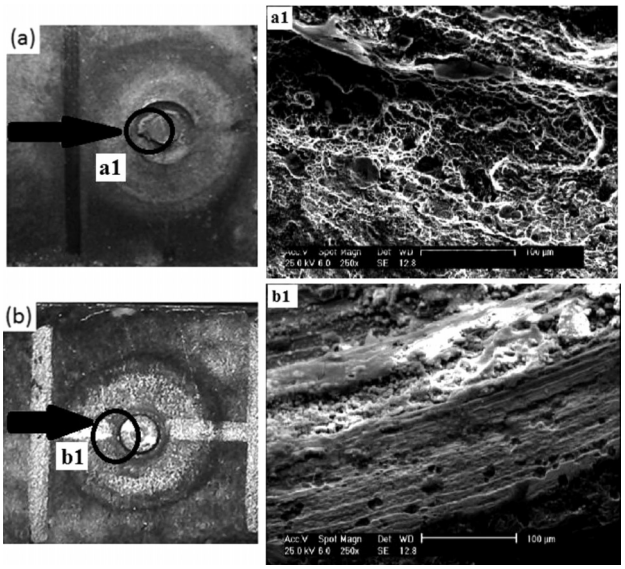

Figure 8: a) Appearance of the weld made with tapered pin after fracture, b) appearance of the weld made with triangular pin after fracture; a1) fractograph of selected location a1 on the friction-stir spot weld made with tapered pin, b1) fractograph of selected location b1 on the friction-stir spot weld made with triangular pin

made with the triangular pin is upward towards the stir zone and ends with a plateau, as can be seen in **Figure 7b**. The large difference in the shear tension strength between the welds made with the two different types of pin could be caused by the following factors: the finer-grain structure near the weld keyhole, the strength of the material in this region that is higher than that near the weld bottom. On the other hand, the crack propagation happens along the hook in both welds; on the weld made with the tapered pin, the crack initially passes around the stir zone and then moves down towards the weld bottom while on the weld made with the triangular pin, the crack moves upward towards the stir zone along the hook. For this reason, the failure load of the weld made with the triangular pin is about 50 % higher than that of the weld made with the tapered one at the same processing conditions (2.2 mm plunge depth, 16 s tool holding time) used in this study.

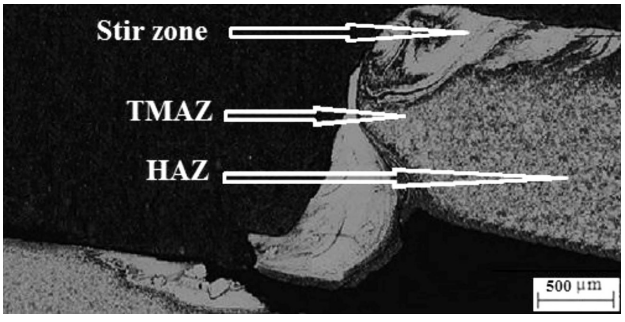

Figure 9: Cross-sectional microstructure of a friction-stir spot weld (the plunge depth of 2.2 mm and dwell time of 16 s) showing different regions of the weld: stir zone (SZ), heat-affected zone (HAZ), thermo-mechanically affected zone (TMAZ)

On the contrary, the fracture surface in **Figure 8** shows that the failure mode varies for the welds made with two different pin designs when they are subjected to shear-tension loading. The existence of dimples in the fracture surface of the weld made with the tapered pin shows that, during the final stage of failure, this weld experiences a plastic collapse near the weld bottom in the shear mode while, in the weld made with the triangular pin, fracture occurs due to the crack propagation through the stir zone under the tension. Therefore, a higher external load causing the failure of the weld made with the triangular pin might be related to the tensile failure mode where the tensile strength of the material is about 1.6 times the shear strength.

3.2 Microstructure characterization of the welds

The cross-sectional microstructure of the friction-stir spot weld in **Figure 9** shows that the microstructure of the weld consists of three distinct zones: the dynamically recrystallized zone or stir zone (SZ), which lies at the centre of the spot weld, bordering, on either side, on the remaining two constituent zones, the thermo-mechanically affected zone (TMAZ) and the heat-affected zone (HAZ). The microstructure of the stir zone includes very fine grains subjected to a high strain and also high thermal energies from the rotational pin. Due to the occurrence of phase transformation in this region, the micro-

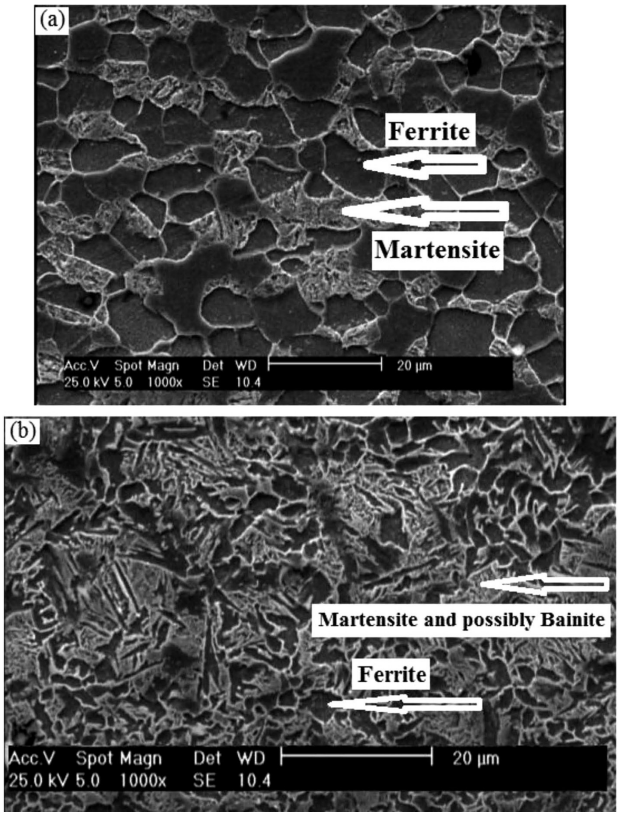

Figure 10: SEM micrographs of cross-sectional microstructures of a friction-stir spot weld (the plunge depth of 2.2 mm and dwell time of 16 s): a) base material, b) heat-affected zone (HAZ)

structure morphology of the stir zone is quite different from those of the other regions.[4,14] The thermo-mechanically affected zone (TMAZ), which is entirely unique to FSSW, is affected by both the deformation and the temperature during friction-stir spot welding. This region is the transition zone between the parent material and the nugget zone. The grains in the TMAZ are highly elongated due to high strain forces and the presence of an upward-flowing pattern around the stir zone.[14,29] Furthermore, the thermo-mechanically affected zone is the heat-affected zone (HAZ) that is not plastically deformed but undergoes a thermal cycle during the friction-stir welding process.[29]

A SEM micrograph of the DP780 steel as the base metal is shown in **Figure 10a**. It shows that the microstructure of the base metal is composed of martensite islands surrounded by a ferrite matrix. The hardness values of the base metal are in the range of 190–210 HV0.15, which can be an indication of the mainly ferritic nature of the base-metal microstructure. As can be seen in **Figure 10b**, the original grains in the HAZ are homogeneously distributed, and the microstructure of the HAZ consists of tempered martensite and possibly bainite along with some pre-existing martensite in the ferrite matrix. The peak temperature in the heat-affected zone (HAZ) is between the martensite tempering temperature and the liquidus. Coarsening of the martensite phase occurs in this region where the peak temperature is between AC_1 and AC_3. Increasing the temperature above AC_3 results in a complete austenitization, which, in turn, leads to the formation of fine ferrite grains and the banding nature of martensite and possibly bainite.[1] According to the above reason, the grain size and the volume fraction of the martensite in the heat-affected zone (HAZ) are increased. The hardness values in this region (250–270 HV0.15) indicate an increase in the martensite volume fraction in the microstructure.

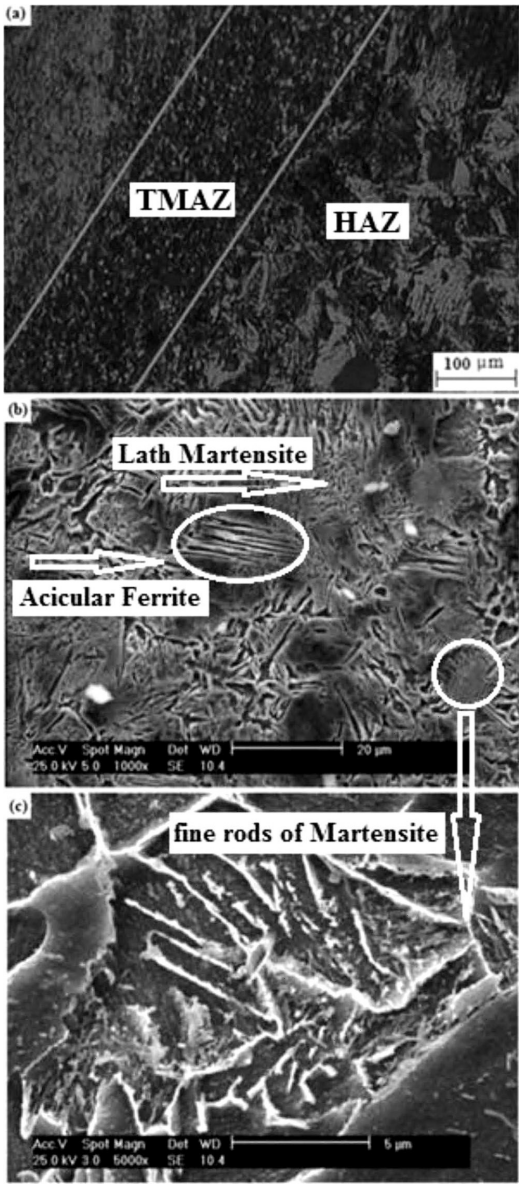

Figure 11: a) optical microscopy of the microstructure of the HAZ and TMAZ in friction-stir spot weld, b) scanning electron microscopy of the microstructure of the TMAZ in friction-stir spot weld (the plunge depth of 2.2 mm and dwell time of 16 s)

Figure 11 shows the cross-sectional microstructures of the heat-affected zone and thermo-mechanically affected zone. As it is shown, the grains in the HAZ tend to grow because of the significant amount of the heat generated during friction-stir spot welding. However, the fine-grained microstructure in the thermo-mechanically affected zone is due to the continuous dynamic recrystallization, induced by shear deformation and a high amount of the heat generated during welding.[1] The temperature of the TMAZ goes above AC_3 and this region undergoes a high strain leading to dynamic recrystallization.[12] As a result, the microstructure of the TMAZ is composed of a mixture of lath martensite and fine acicular ferrite (**Figure 11b**). In addition to the lath martensite, fine rods of martensite, which are less than 2 µm long, are observed in the microstructure. The average hardness in the TMAZ is about 310 HV0.15.

As mentioned above, the microstructure of the stir zone includes very fine grains and the morphology of this region is quite different from those of the other regions.[14] **Figure 12** shows a finer-grain microstructure of

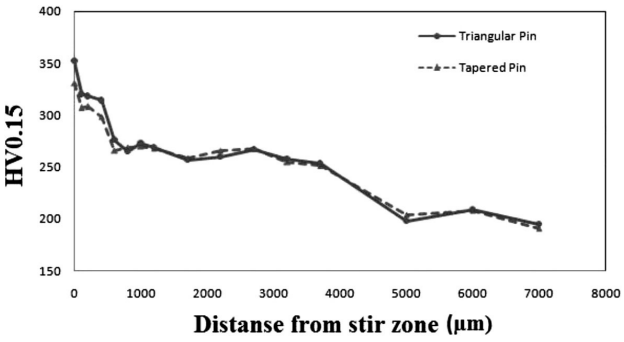

Figure 12: SEM images of the microstructure of the stir zone in a friction-stir spot weld (the plunge depth of 2.2 mm and dwell time of 16 s) and a magnified view of the martensitic microstructure in this region

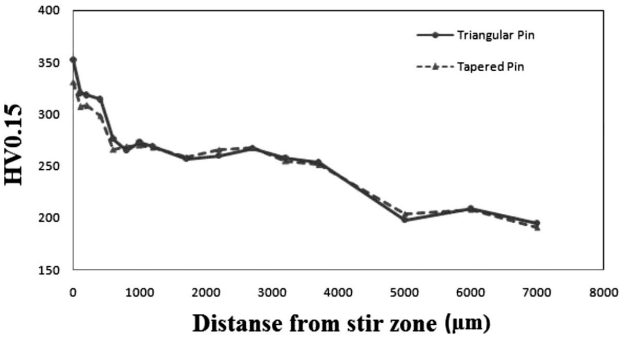

Figure 13: Microhardness profile for friction-stir spot welding using triangular and tapered pins

the stir zone of a friction-stir spot weld as compared to the other regions. As indicated in this figure and according to the high hardness values of the microhardness profile on **Figure 13**, the microstructure of the stir zone predominately consists of martensite.

3.3 Microhardness profiles

A microhardness profile is an excellent indicator of the changes in the properties occurring across the weld zone.[30] **Figure 13** shows the microhardness plot of different regions around the stir zone for the welds performed with the triangular and tapered pins. As can be seen in this figure, the stir zone and thermo-mechanically affected zone of the weld made with the triangular pin is, on average, a little harder than the weld made with the tapered one. SEM micrographs of the thermo-mechanically affected zone on **Figure 14** shows that the plastic deformation during the friction-stir spot welding using the triangular pin is more severe than that of the tapered pin; therefore, the grain size of the TMAZ in the weld made with the triangular pin is finer than that of the weld made with the tapered one. The mechanism of the material flow during the FSSW using different tool designs was fully described elsewhere.[16,31] As a result, the finer-grain structure in the stir zone and thermo-mechanically affected zone of the FSSW using the triangular pin led to a higher hardness than that of the weld made with the tapered pin.

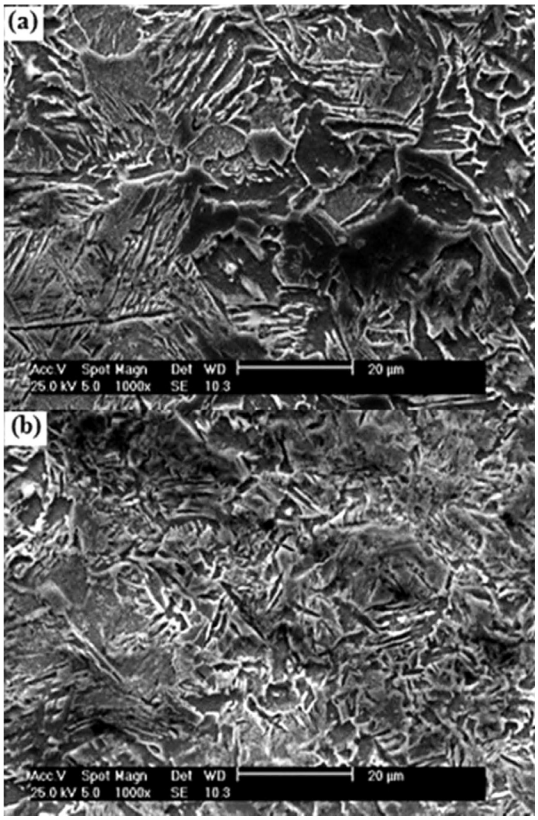

Figure 14: SEM micrographs of the microstructure of the TMAZ for friction-stir spot welds (the plunge depth of 2.2 mm and dwell time of 16 s) with two different tool geometries: a) tapered pin, b) triangular pin

4 CONCLUSIONS

1. The weld made with the 2.2 mm tool penetration depth has the highest tensile shear force. In fact, the amount of the upward material flow of the lower sheet is increased with the plunge depth, regardless of the tool holding time. Thus, the tensile shear strength is first increased with the plunge depth of up to 2.2 mm and then it starts to decrease with a further increase in the plunge depth to 2.8 mm.

2. At the constant tool plunge depth of 2.2 mm, by increasing the tool holding time from 8 s up to 16 s, the tensile shear force of the welds is increased from 0.54 kN to 10.49 kN and from 0.42 kN to 15.46 kN for the tapered and triangular pin, respectively.

3. For the weld made with a tapered pin, the crack initially passes around the stir zone and then moves down towards the weld bottom, while, for the weld made with a triangular pin, the crack moves upward towards the stir zone along the hook. Because of the finer-grain structure near the weld keyhole, the material is stronger in this region than near the weld bottom. Therefore, the maximum strength of the weld made with the triangular pin at the 2.2 mm plunge depth and 16 s tool holding time is about 50 % higher than that of the weld made with the tapered one.

4. The grain size and the volume fraction of the martensite in the heat-affected zone (HAZ) is increased as compared to the base metal. The hardness values in this region (230–270 HV0.15) indicate an increase in the martensite volume fraction in the microstructure.

5. The microstructure of the TMAZ is composed of a mixture of lath martensite and fine acicular ferrite. In addition to lath martensite, fine rods of martensite, which are less than 2 μm long, are observed in the microstructure. The average hardness in the TMAZ is about 310 HV0.15.

6. As the plastic deformation during friction-stir spot welding performed with the triangular pin is more severe

than what occurs when using the tapered pin, the grain size of the TMAZ in the weld made with the triangular pin is finer than that of the weld made with the tapered one. As a result, the hardness of the stir zone and thermo-mechanically affected zone of the weld made with the triangular pin is higher than that of the weld made with the tapered one.

5 REFERENCES

[1] H. H. Cho, H. N. Han, T. Hong, J. H. Park, Y. J. Kwon, S. H. Kim, R. J. Steel, Microstructural analysis of friction stir welded ferritic stainless steel, Materials Science & Engineering A, 528 (**2011**), 2889–2894, doi:10.1016/j.msea.2010.12.061

[2] G. Çam, S. Mıstıkoğlu, Recent Developments in Friction Stir Welding of Al-Alloys, Journal of Materials Engineering and Performance, 23 (**2014**), 1936–1953, doi:10.1007/s11665-014-0968-x

[3] G. Çam, Friction Stir Welded Structural Materials: Beyond Al-Alloys, International Materials Reviews, 56 (2011), 1–48, doi:10.1179/095066010X12777205875750

[4] W. B. Lee, Y. M. Yeon, S. B. Jung, Evaluation of the microstructure and mechanical properties of friction stir welded 6005 aluminum alloy, Materials Science and Technology, 19 (**2003**), 1513–1518, doi:10.1179/026708303225008068

[5] A. K. Lakshminarayanan, V. Balasubramanian, Assessment of fatigue life and crack growth resistance of friction stir welded AISI 409M ferritic stainless steel joints, Materials Science and Engineering A, 539 (**2012**), 143–153, doi:10.1016/j.msea.2012.01.071

[6] Y. F. Sun, H. Fujii, N. Takaki, Y. Okitsu, Microstructure and mechanical properties of mild steel joints prepared by a flat friction stir spot welding technique, Materials & Design, 37 (**2012**), 384–392, doi:10.1016/j.matdes.2012.01.027.

[7] M. Habibnia, M. Shakeri, S. Nourouzi, M. K. Besharati Givi, Microstructural and mechanical properties of friction stir welded 5050 Al alloy and 304 stainless steel plates, The International Journal of Advanced Manufacturing Technology, 76 (**2015**), 819–829, doi:10.1007/s00170-014-6306-5

[8] Y. Hovanski, M. L. Santella, G. J. Grant, Friction stir spot welding of hot-stamped boron steel, Scripta Materialia, 57 (**2007**), 873–876, doi:10.1016/j.scriptamat.2007.06.060

[9] Z. Feng, R. J. Steel, S. M. Packer, Friction Stir Spot Welding of Advanced High-Strength Steels – A Feasibility Study, SAE Tech. Papers, 1 (**2005**), 1248, doi:10.4271/2005-01-1248

[10] M. Azuma, S. Goutianos, N. Hansen, G. Winther, X. Huang, Effect of hardness of martensite and ferrite on void formation in dual phase steel, Materials Science and Technology, 28 (2012), 1092–1100, doi:10.1179/1743284712Y.0000000006

[11] B. C. Hwang, T. Y. Cao, S. Y. Shin, S. H. Kim, S. H. Lee, S. J. Kim, Effects of ferrite grain size and martensite volume fraction on dynamic deformation behaviour of 0·15C–2·0Mn–0·2Si dual phase steels, Materials Science and Technology, 21 (2005), 967–975, doi:10.1179/174328405X47609

[12] M. I. Khan, M. L. Kuntz, P. Su, A. Gerlich, Y. Zhou, Resistance and friction stir spot welding of DP600: a comparative study, Science and Technology of Welding and Joining, 12 (2007), 175–182, doi:10.1179/174329307X159801

[13] Y. Uematsu, K. Tokaji, T. Tozaki, Y. Nakashima, Fatigue behaviour of dissimilar friction stir spot weld between A6061 and SPCC welded by a scrolled groove shoulder tool, Procedia Engineering, 2 (**2010**), 193–201, doi:10.1016/j.proeng.2010.03.021

[14] R. S. Mishra, Z. Y. Ma, Friction stir welding and processing, Materials Science and Engineering R: Reports, 50 (**2005**), 1–78, doi:10.1016/j.mser.2005.07.001

[15] R. Karthikeyan, V. Balasubramanian, Predictions of the optimized friction stir spot welding process parameters for joining AA2024 aluminum alloy using RSM, The International Journal of Advanced Manufacturing Technology, 51 (**2010**), 173–183, doi:10.1007/s00170-010-2618-2

[16] H. Badarinarayan, Q. Yang, S. Zhu, Effect of tool geometry on static strength of friction stir spot-welded aluminum alloy, International Journal of Machine Tools and Manufacture, 49 (**2008**), 142–148, doi:10.1016/j.ijmachtools.2008.09.004

[17] Y. H. Yin, N. Sun, T. H. North, S. S. Hu, Influence of tool design on mechanical properties of AZ31 friction stir spot welds, Science and Technology of Welding and Joining, 15 (**2010**), 81–86, doi:10.1179/136217109X12489665059384

[18] D. Zhang, T. Shibayanagi, Material flow during friction stir spot welding of dissimilar Al2024/Al materials, Materials Science and Technology, 31 (2015), 1077–1087, doi:10.1179/1743284714Y.0000000674

[19] D. Mitlin, V. Radmilovic, T. Pan, J. Chen, Z. Feng, M. L. Santella, Structure-properties relations in spot friction welded (also known as friction stir spot welded) 6111 aluminum, Materials Science and Engineering A, 441 (**2006**), 79–96, doi: 10.1016/j.msea.2006.06.126

[20] H. Badarinarayan, Y. Shi, X. Li, K. Okamoto, Effect of tool geometry on hook formation and static strength of friction stir spot welded aluminum 5754-O sheets, International Journal of Machine Tools and Manufacture, 49 (**2009**), 814–823, doi:10.1016/j.ijmachtools.2009.06.001

[21] N. Sun, Y. H. Yin, A. P. Gerlich, T. H. North, Tool design and stir zone grain size in AZ31 friction stir spot welds, Science and Technology of Welding and Joining, 14 (2009), 747–752, doi:10.1179/136217109X12518083193559

[22] Y. H. Yin, N. Sun, T. H. North, S. S. Hu, Influence of tool design on mechanical properties of AZ31 friction stir spot welds, Science and Technology of Welding and Joining, 15 (**2010**), 81–86, doi:10.1179/136217109X12489665059384

[23] Y. Tozaki, Y. Uematsu, K. Tokaji, A newly developed tool without probe for friction stir spot welding and its performance, Journal of Materials Processing Technology, 210 (**2010**), 844–851, doi:10.1016/j.jmatprotec.2010.01.015

[24] N. Sun, T. H. North, D. R. Chen, Y. H. Yin, Influences of welding parameters on mechanical properties of AZ31 friction stir spot welds, Science and Technology of Welding and Joining, 17 (**2012**), 304–308, doi:10.1179/1362171812Y.0000000008

[25] Y. Tozaki, Y. Uematsu, K. Tokaji, Effect of tool geometry on microstructure and static strength in friction stir spot welded aluminium alloys, International Journal of Machine Tools and Manufacture, 47 (**2007**), 2230–2236, doi:10.1016/ j.ijmachtools.2007.07.005

[26] C. Jonckheere, B. de Meester, C. Cassiers, M. Delhaye, A. Simar, Fracture and mechanical properties of friction stir spot welds in 6063-T6 aluminum alloy, The International Journal of Advanced Manufacturing Technology, 62 (**2012**), 569–575, doi:10.1007/s00170-011-3795-3

[27] H. H. Cho, S. H. Kang, S. H. Kim, H. H. Oh, Microstructural evolution in friction stir welding of high-strength linepipe steel, Materials & Design, 34 (**2012**), 258–267, doi:10.1016/j.matdes.2011.08.010

[28] A. Emamikhah, A. Abbasi, A. Atefat, M. K. Besharati Givi, Effect of tool pin profile on friction stir butt welding of high-zinc brass (CuZn40), The International Journal of Advanced Manufacturing Technology, 71 (2014), 81–90, doi:10.1007/s00170-013-5480-1

[29] A. Biro, B. Chenelle, D. Lados, Processing, microstructure, and residual stress effects on strength and fatigue crack growth properties in friction stir welding: a review, Metallurgical and Materials Transactions B, 43 (**2012**), 1622–1637, doi:10.1007/s11663-012-9716-5

[30] D. Bakavos, H. Chen, L. Babout, P. Prangnell, Material interactions in a novel pinless tool approach to friction stir spot welding thin aluminum sheet, Metallurgical and Materials Transactions A, 42 (**2010**), 1266–1282, doi:10.1007/s11661-010-0514-x

[31] S. Hirasawa, T. Van-Xuan, Analysis of effect of tool geometry on plastic flow during friction stir spot welding using particle method, Journal of Materials Processing Technology, 210 (**2010**), 1455–1463, doi:10.1016/j.jmatprotec.2010.04.003

UDK 620.1:67.017:620.3
Original scientific article/Izvirni znanstveni članek

ISSN 1580-2949
MTAEC9, 51(4)695(2017)

CHARACTERIZATION OF STRUCTURAL MATERIALS BY SPHERICAL INDENTATION

KARAKTERIZACIJA STRUKTURNIH MATERIALOV PRI SFERIČNEM VTISKOVANJU

Jaroslav Čech, Petr Haušild, Ondřej Kovářík

Czech Technical University, Faculty of Nuclear Sciences and Physical Engineering, Department of Materials, Trojanova 13, 120 00, Prague 2, Czech Republic
jaroslav.cech@fjfi.cvut.cz

Prejem rokopisa – received: 2016-10-19; sprejem za objavo – accepted for publication: 2017-01-16

doi:10.17222/mit.2016.302

Nano-indentation with spherical indenters is a method of mechanical properties characterization that could be used for the determination of stress-strain curves. A necessary condition for an evaluation of the results is an exact knowledge of the indenter shape. In this study, the shapes of two spherical indenters with a nominal radius of 20 μm were investigated by atomic force microscopy and by indentation into materials with a known Young´s modulus. It was found that the actual indenter differs from the ideal shape and it is affected by the crystallographic orientation of the diamond crystal. The effective radius determined from the indentation measurements depends on the material deformation characteristics and it was lower than the actual radius. The computed representative stress vs. representative strain curves of steel samples were significantly affected by the actual radii of the investigated indenters.

Keywords: nano-indentation, spherical indenter, actual indenter shape, representative stress, representative strain curves

Nanoindentacija s sferičnimi vtiskovalci je metoda karakterizacije mehanskih lastnosti, ki se lahko uporablja za ugotovitev napetostno-deformacijske krivulje. Pogoj za oceno rezultatov je točno določeno poznavanje stanja vtiskovalca. V študiji sta bili raziskovana dva sferična vtiskovalca z nominalnim radijem 20 μm, ki sta bila raziskovana z AFM in z vtiskovanjem v material z Youngovim modulom. Ugotovljeno je bilo, da se dotični vtiskovalec razlikuje od idealne oblike in, da nanj vpliva kristalografska orientacija diamantnega kristala. Efektivni radij, ugotovljen z meritvami vtiskovanja je odvisen od deformacije karakteristik materiala in je bil nižji od dejanskega radija. Izračunane reprezentativne napetostne krivulje jeklenih vzorcev so bile občutno pod vplivom dejanskih radijev preiskovanih vtiskovalcev.

Ključne besede: nanoindentacija, sferični vtiskovalec, dejanska oblika vtiskovalca, reprezentativna napetost, reprezentativna napetostna krivulja

1 INTRODUCTION

Nano-indentation is an effective method for the characterization of mechanical properties for very small volumes of material. It is advantageously applied when standard tests (e.g., tensile, fracture toughness tests) cannot be used. It can be employed to characterize thin films, welds or individual phases of a multi-phase material.

Sharp indenters (such as the Berkovich three-sided pyramid) are the most frequently used due to the simplicity of the data interpretation. On the other hand, they do not provide any information about the evolution of the elastic and plastic stress-strain field under the indenter. In spherical indentation, the stress and strain progressively increase with the penetration depth and thus the stress-strain curves of the materials can be determined.

Several models are used for a description of the elastic-plastic stress-strain field under the indenter. At the beginning of the indentation process, only elastic deformation occurs and Hertz theory can be applied.[1] With increasing penetration depth, the plastic zone starts to evolve under the surface below the indenter and it spreads to the surface.[2] When the plastic zone is fully developed, the ratio of hardness to yield strength stabilizes at an approximate value $H/\sigma_y = 3$.[3] This ratio expresses the restriction of plastic deformation under the indenter compared to the tensile tests. Several models make it possible to evaluate stress-strain curves in whole range of deformations.[4] Methods determining the yield strength, strain hardening exponent and other mechanical characteristics do exist; however, several problems have to be considered when analyzing the experimental data.

The crucial factor is a knowledge of actual indenter shape.[5–9] The real indenter does not match its ideal shape. Imperfections are created already during the indenter's fabrication and the indenter is progressively worn with usage. The shape and properties of the indenter also depend on the crystallographic orientation of the diamond crystal.[10] The projected indenter area function A_p effectively corrects the imperfections of Berkovich, Vickers, or conical indenters. However, for the spherical indenters, the actual projected area is not frequently used as it cannot be directly related to the actual radius, giving a tangent at the contact. Instead, the effective radius of the indenter R_{eff} can be used.

In this study, two diamond spherical indenters with the nominal radius R = 20 μm were investigated. Their

actual shape was determined by direct (atomic force microscopy) and indirect (indentation into materials with a known Young's modulus) methods and its effect on the stress-strain curves of structural materials was evaluated.

2 MATERIALS AND METHODS

Indentation tests were carried out on Anton Paar CSM NHT nano-indentation instrument. Two steel samples (hardness etalon 487 HV from ball bearing carbon steel and bainitic JRQ steel used in the nuclear industry) were investigated by two spherical diamond indenters (denoted as indenter A and indenter B) with nominal radius R = 20 μm. Electrolytically polished samples were loaded in the regime with partial unloading (CMC mode) in the range of maximum force from 10 mN to 500 mN. The whole indentation test consisted of 20 cycles with progressively increasing maximum force. The increase to the maximum force in the cycle takes 10 s, holding at maximum force 5 s, and unloading to 20 % of maximum force 10 s. Every unloading was analyzed using the Oliver-Pharr procedure.[11]

Since the shape of the indenter is not supposed to be ideal, the calibration procedure was performed for both indenters. For a contact depth h_c given by Equation (1):[12]

$$h_c = h_{max} - 0.75\frac{P_{max}}{S} \tag{1}$$

the projected contact area A_p was determined according to Equation (2):[12]

$$A_p(h_c) = \frac{\pi S^2}{4E_r^2} \tag{2}$$

where the maximum penetration depth h_{max}, maximum applied force in the cycle P_{max}, and contact stiffness S are obtained from the force-displacement curve. E_r stands for the reduced modulus, comprising elastic properties of the indenter and the sample in Equation (3):[12]

$$\frac{1}{E_r} = \frac{1-\upsilon_s^2}{E_s} + \frac{1-\upsilon_i^2}{E_i} \tag{3}$$

The Young's modulus and Poisson's ratio of sample E_s and υ_s were determined by independent ultrasound pulse-echo measurement, and E_i and υ_i are the known Young's modulus and Poisson's ratio of the diamond indenter, respectively. The indenter effective radius can be obtained from the geometry of the system (relation between the projected contact area and the contact depth):

$$R_{eff} = \frac{\frac{A_p}{\pi} + h_c^2}{2h_c} \tag{4}$$

Representative stress σ_{repr} vs. representative strain ε_{repr} curves were determined using Tabor formulae in Equation (5):[3]

$$\sigma_{repr} = \frac{P_{max}}{C\pi a^2}, \qquad \varepsilon_{repr} = 0.2\frac{a}{R} \tag{5}$$

where C is a constraint factor (C = 3), a is the contact radius, and R is the radius of the indenter (nominal or effective).

The tips of the spherical indenters were also examined by atomic force microscope AFM Park XE-100 with closed-loop z-piezo in tapping mode. An area of 20×20 μm^2 was scanned with the resolution of 256×256 points. The data were corrected to the drift in slow scanning axis and the noise was filtered. The projected area A_p for the depths up to 2 μm was estimated from AFM measurements as a surface of a planar cut through the indenter perpendicular to the load axis. From the measured $A_p(h_c)$ dependency, the actual radius of the indenters was computed using Equation (4).

3 RESULTS AND DISCUSSION

3.1 Atomic force microscopy

The topology of the indenters A and B and the maps of their local radius of curvature obtained from the analysis of AFM data are shown in **Figure 1**. The local radius of curvature is defined as a radius of the sphere interpolated in the circular neighborhood (1 μm in radius) of the particular point on the indenter surface. Comparing the topology of both indenters, it can be seen that the indenter B is more irregular than the indenter A. The differences are also visible on the maps of local radius of curvature, where the local radius of curvature of indenter A at the apex is higher than for indenter B and it reaches a higher value than the stated 20 μm.

For the data analysis, and also for the fabrication of the diamond indenters, it is very important to know its crystallographic orientation. The investigated indenters were produced with the loading axis parallel to the direction [100] of the diamond crystal. The crystallographic orientation has a significant effect on the indenter actual

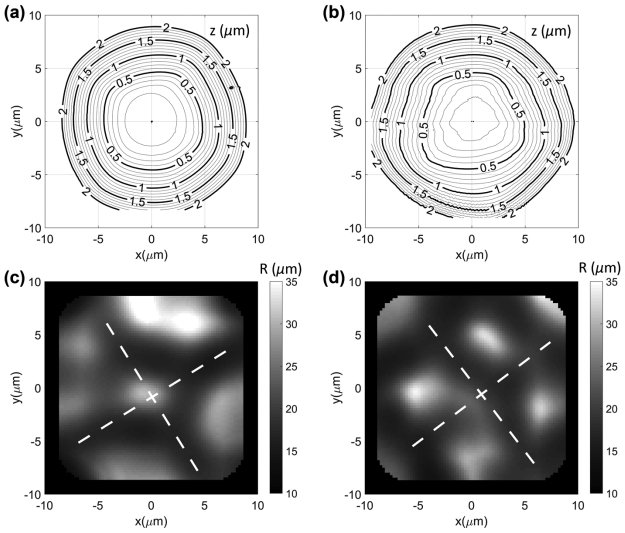

Figure 1: AFM images of: a) the topology of indenters A and b) indenter B, c) local radius of curvature of indenters A and d) B with shown axes of the four-fold symmetry (dashed lines)

shape and it can introduce deviation from its nominal spherical shape. As the diamond crystal is anisotropic, it is worn and grinded more easily in the softer directions. The four-fold symmetry of the diamond crystal is clearly visible in the figures of the local radius of curvature (**Figure 1c** and **1d**).

The actual radii estimated from Equation (4) are shown in **Figure 2**. The radius determined by AFM decreases with depth for both investigated indenters. The decrease is more abrupt for indenter A (from approximately R = 30 μm to R = 22 μm at a depth h = 100 nm and h = 500 nm, respectively). For greater depths, the radius of indenter A stabilizes at a nominal value of R = 20 μm. The radius of indenter B decreases only slightly from R = 24 μm at a depth 200 nm to R = 23 μm at a depth 500 nm. For depths h > 400 nm it is higher than the radius of indenter A and it reaches a constant value of nearly 23 μm, far more than the nominal value of 20 μm.

3.2 Indentation

Evolution of the effective radius determined from indentation measurements on steel samples at low penetration depths shows a different trend compared with AFM results. The effective radius increases from a very low value of about 10 μm and it reaches its maximum at a depth approximately h = 200 nm. These low values of effective radius result from the uneven contact between the indenter and the surface of the sample. After electrolytic polishing, the surface of steel sample is wavy, as schematically shown in **Figure 3**. The indenter touches the local surface asperities and thus the actual contact area for a given penetration depth is not spherical, but it is irregular and smaller than the theoretical one. According to Equation (4) the final effective radius is subsequently smaller than the actual radius of the indenter.

The maximum effective radius from the indentation measurements differs for both investigated indenters and materials. Higher values were obtained by indenter A than by indenter B, similar to the AFM measurements. For greater depths the evolution of the effective radius follows the trend of the AFM measurements. The radius

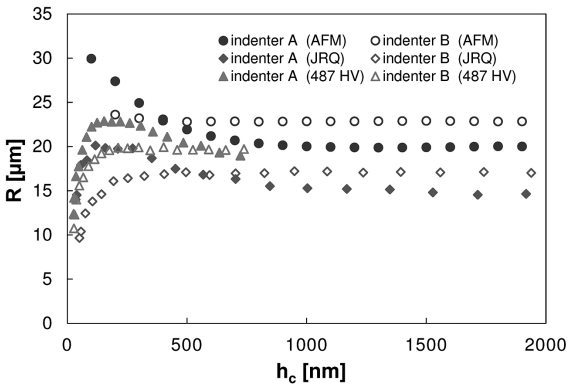

Figure 2: Radius of spherical indenters with nominal radius R = 20 μm obtained by AFM and indentation measurements

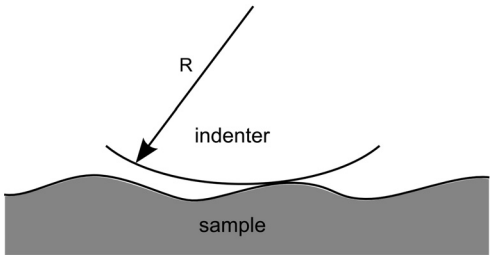

Figure 3: Schematic sketch of contact between spherical indenter and surface asperities[13]

of indenter A decreases with depth and it is lower than the radius of indenter B from depths of about 600 nm. The effective radius of indenter B is rather constant. However, the effective radii could not be compared for higher penetration depths since high hardness of etalon 487 HV and the maximum possible applied force (500 mN) limit the maximum penetration depth into the 487 HV sample to approximately 1 μm.

The differences in the effective radius estimated from indentation into JRQ steel and etalon 487 HV could be explained by the difference of their elastic-plastic properties. It is well known that the contact area (which is used for a determination of effective radius) depends on the actual indenter shape and the material deformation characteristics.[14] The effects of pile-up or sink-in can introduce the error in the determination of contact area by as much as 60 %.[15] The effective radii measured by indentations on investigated samples are lower than the radii from the AFM. More significant difference is for JRQ steel, which is probably caused by higher strain hardening exponent.

Representative stress vs. representative strain curves were evaluated according to Equation (5) and they are presented in **Figure 4**. Each material was investigated by both indenters. The results considering nominal radius R = 20 μm and effective radius R_{eff} obtained from the indentation into the corresponding material were compared. To avoid the problems with the transition from the elastic to the plastic region and the errors arising from the uncertainty of geometry of contact at low penetration depths, the cycles with low maximum load were excluded from the analysis.

As the nominal radius is higher than the effective radius, flow curves of JRQ steel using R = 20 μm are lower than the curves obtained with R_{eff} (**Figure 4a**). The curves based on nominal radius significantly differ for both indenters, especially for lower deformations (i.e., low penetration depths). Moreover, stress obtained with indenter A using nominal radius decreases with increasing deformation, which should not occur as the material is hardening. It is caused by an important difference between the nominal and the actual shape of indenter A at low depths (**Figure 2**). Using the effective radius, the flow curves obtained by both indenters are nearly equivalent. Small differences could result from using Equation (5) for evaluating representative deformation. The for-

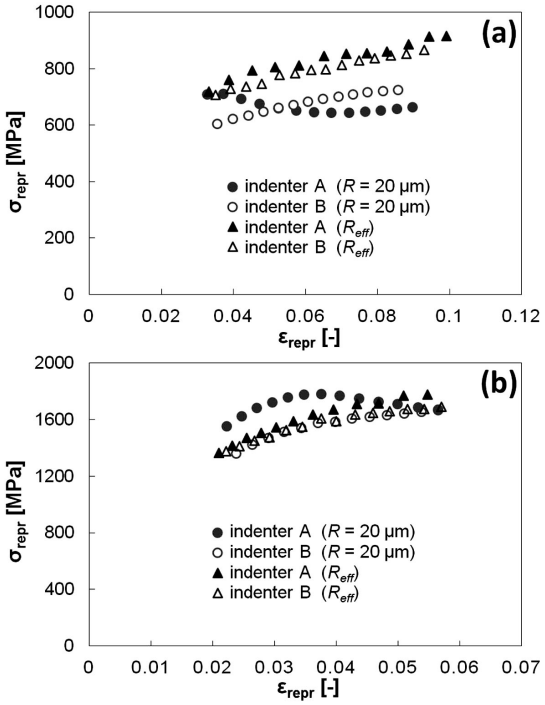

Figure 4: Representative stress vs. representative strain curves obtained using Tabor formulae: a) JRQ steel, b) hardness etalon 487 HV

mula for representative deformation is based on the ratio of contact and indenter radii a/R, which is valid for ideally spherical indenters. Actual deformation is given by the contact angle between the indenter and the sample surface. As the shape of the indenter is not ideally spherical, approximation of this angle by a/R is not exactly valid and it could introduce small errors into the values of the representative deformation.

The decrease of the stress with strain was also observed for hardness etalon 487 HV using indenter A and R = 20 μm. Nevertheless, the differences in flow curves, which results from using nominal and effective radius, are less significant than for JRQ steel. For indenter B, representative stress vs. representative strain curves are nearly identical as the effective radius for higher penetration depths reaches approximately its nominal value R = 20 μm.

4 CONCLUSIONS

The shapes of two diamond spherical indenters with nominal radius R = 20 μm were investigated in this study. Their actual and effective radius was determined by AFM measurements and indentation into materials with a known Young's modulus, respectively. It was found that the indenter shape is affected by the crystallographic orientation of the diamond crystal. For low depths, both investigated indenters are flatter (larger radius) than stated by the supplier. For greater depths, indenter A reaches the nominal value, and the indenter B has a slightly larger radius. The effective radius measured by indentation into JRQ steel and hardness etalon 487 HV is lower than the actual radii, which is caused by the surface irregularities (for lower depths) and materials deformation characteristics (for greater depths).

Determined representative stress vs. representative strain curves of JRQ steel and hardness etalon 487 HV are affected by the used radius (nominal or effective). To obtain indenter-independent results, effective radii determined for a given material should be used.

Acknowledgment

Support from Czech Science Foundation (project no. GB14-36566G) and Czech Technical University in Prague (project no. SGS16/172/OHK4/2T/14) is gratefully acknowledged.

5 REFERENCES

[1] K. L. Johnson, Contact mechanics, 1st ed., Cambridge University Press, Cambridge 1985, 452

[2] Y. J. Park, G. M. Pharr, Nanoindentation with spherical indenters: finite element studies of deformation in the elastic-plastic transition regime, Thin Solid Films, 447–448 (**2004**), doi:10.1016/S0040-6090(03)01102-7

[3] D. Tabor, The Hardness of Metals, 1st ed., Oxford University Press, London 1951, 175

[4] B. Taljat, T. Zacharia, F. Kosel, New analytical procedure to determine stress-strain curve from spherical indentation data, Int. J. Solids. Struct., 35 (**1998**) 33, doi:10.1016/S0020-7683(97)00249-7

[5] J. S. Field, M. V. Swain, A simple predictive model for spherical indentation, J. Mater. Res., 8 (**1993**) 2, doi:10.1557/JMR.1993.0297

[6] K. Herrmann, N. M. Jennett, W. Wegener, J. Meneve, K. Hasche, R. Seemann, Progress in determination of the area function of indenters used for nanoindentation, Thin Solid Films, 377–378 (**2000**), doi:10.1016/S0040-6090(00)01367-5

[7] P. Haušild, A. Materna, J. Nohava, On the identification of stress-strain relation by instrumented indentation with spherical indenter, Mater. Des., 37 (**2012**), doi:10.1016/j.matdes.2012.01.025

[8] S. Sagadevan, P. Murugasen, Novel analysis on the influence of tip radius and shape of the nanoindenter on the hardness of materials, Proc. Mat. Sci., 6 (**2014**), doi:10.1016/j.mspro.2014.07.218

[9] K.-D. Bouzakis, M. Pappa, G. Maliaris, N. Michailidis, Fast determination of parameters describing manufacturing imperfections and operation wear of nanoindenter tip, Surf. Coat. Technol., 215 (**2013**), doi:10.1016/j.surfcoat.2012.09.061

[10] W. J. Zong, D. Wu, Z. Q. Li, Strength dependent design method for the crystal orientation of diamond Berkovich indenter, Mater. Des. 89 (**2016**), doi:10.1016/j.matdes.2015.10.062

[11] W.C. Oliver, G.M. Pharr, An improved technique for determining hardness and elastic modulus using load and displacement sensing indentation experiments, J. Mater. Res., 7 (**1992**) 6, doi:10.1557/JMR.1992.1564

[12] ISO 14577:2002(E) – Metallic Materials - Instrumented indentation test for hardness and material parameters, Geneve

[13] J. Čech, P. Haušild, O. Kovářík, M. Škereň, Effect of actual indenter shape on the results of spherical nanoindentation, Def. Diff. Forum., 368 (**2016**), doi:10.4028/www.scientific.net/DDF.368.25

[14] K. R. Gadelrab, F. A. Bonilla, M. Chiesa, Densification of fused silica under nanoindentation, J. Non.-Cryst. Solids, 358 (**2012**) 2, doi:10.1016/j.jnoncrysol.2011.10.011

[15] A. Bolshakov, G. M. Pharr, Influences of pileup on the measurement of mechanical properties by load and depth sensing indentation techniques, J. Mater. Res., 13 (**1998**) 4, doi:10.1557/JMR.1998.0146

UDK 621.793.7:620.1:67.017
Original scientific article/Izvirni znanstveni članek

ISSN 1580-2949
MTAEC9, 51(4)699(2017)

ZrMoN FILMS ON 304 STAINLESS STEEL AS BIPOLAR PLATES FOR PEMFCs USING PHYSICAL-VAPOR-DEPOSITION (PVD) TECHNOLOGY

ZrMoN PREVLEKE NA NERJAVNEM JEKLU 304 KOT BIPOLARNE PLOŠČE ZA PEMFC-je Z UPORABO TEHNOLOGIJE NANAŠANJA IZ PARNE FAZE (PVD)

Chuan-Bo Zheng, Xi Chen

Jiangsu University of Science and Technology, School of Material Science and Engineering, Zhenjiang 212003, China
15952802516@139.com

Prejem rokopisa – received: ;2016-11-09 sprejem za objavo – accepted for publication: 2017-01-20

doi:10.17222/mit.2016.316

ZrMoN films were deposited on a 304 stainless-steel (SS304) substrate with a radio-frequency (RF) reactive magnetron-sputtering system and the properties were changed by adjusting the power of the Mo target. The corrosion behaviors of the ZrMoN films were investigated with potentiodynamic tests and electrochemical impedance spectroscopy (EIS) under the condition of an aerated 0.5M H_2SO_4 + 1,99 mg/L NaF solution at 70 °C. The results revealed that all samples with ZrMoN films have good hydrophobicity. The XRD test showed that the ZrMoN film is the substitutional solid solution of Mo atoms into ZrN films. As an overall evaluation, the power of the Mo target is 30W. A coated sample displays the best corrosion resistance in the cathode of the PEMFC environment when the power of the Mo target is considered, which indicates that with an increase of the power of the Mo target, the solid solubility also increases; but with a continuous increase of the Mo-target power, the solubility increases and a lattice distortion also occurs, leading to an increase in defects.

Keywords: ZrMoN, corrosion behavior, bipolar-plate material, physical-vapor-deposition technology (PVD)

ZrMoN prevleke so bile nanešene na substrat 304 nerjavnega jekla (SS 304) z radiofrekvenčnim reaktivnim (angl. RF) magnetronskim napršcvalnikom in lastnosti so bile spremenjene s prilagoditvijo moči Mo tarče. Korozijsko obnašanje prevlek ZrMoN smo raziskovali s potenciodinamskimi preizkusi in elektrokemijsko impedančno spektroskopijo (EIS) v raztopini 0,5 M H_2SO_4 + 1,99 mg/L NaF pri temperaturi 70 °C. Rezultati so pokazali, da imajo vsi vzorci z ZrMoN prevlekami dobro hidrofobnost. XRD-analiza kaže, da je prevleka ZrMoN nadomestna trdna raztopina atomov Mo v ZrN plasti. Rezultati kažejo najboljšo korozijsko odpornost na katodi v okolju PEMFC pri moči Mo tarče 30 W, kar kaže, da se s povečanjem moči Mo povečuje tudi trdna topnost. Vendar pa se s kontinuiranim povečevanjem moči Mo tarče neprestano povečuje tudi topnost, zato pride do popačenja kristalne mreže, kar povzroči povečanje napak.

Ključne besede: ZrMoN, korozijsko obnašanje, bipolarni material, tehnologija nanašanja iz parne faze (PVD)

1 INTRODUCTION

The whole world requires the pollution to be reduced due to the global warming, caused by greenhouse gases such as CO_2, NOx and Sox.[1,2] The proton-exchange-membrane fuel cell (PEMFC) is considered to be a competitive candidate as the next-generation power source for automotive, stationary and portable applications due to its prominent characteristics including a quick start-up, zero emission, high efficiency, etc.[3–5] It is a device that directly and efficiently converts chemical energy into electricity.[6] One of the most expensive and heaviest components in a PEMFC stack is the bipolar plate (BPP).[7] The BPP plays several important roles in the whole fuel-cell stack, affecting its total weight, volume and cost. In order to perform these functions, a BPP should feature high corrosion resistance in PEMFC environments, good electrical conductivity, high mechanical strength, high capability of gas separation, low cost and easily machining.[8] Metallic BPPs have been widely accepted due to their good electrical conductivity, good mechanical properties, processing performance and low production cost. However, during the fuel-cell operating condition, a sample exposed to a highly acidic medium (pH2–3) containing ions like F^-, SO_4^{2-} and HCO_3^-, undergoes severe corrosion on its surface, which results in a loss of the power output of the PEMFC.[9]

In general, transition-metal nitride films are chemically inert and thermally stable. However, an attack of the corrosive medium on the substrate is severe due to the defects within the film (such as micro-cracks, pores, pinholes, grain boundaries, etc.).[10] These defects create a direct path between the exposed substrate and the corrosive medium, thus affecting the electrochemical behavior of these films. Among the large refractory-metal carbonitrides, ZrCN is an attractive material because of its excellent chemical and physical properties, such as a relatively low electrical resistivity and high corrosion resistance.[11] Zr alloys undergo corrosion in high-temperature water and steam, with rapid initial corrosion forming an oxide layer which causes the oxidation rate to slow down. This is because the migration of charged species (oxygen ions and electrons) across the oxide thickness is inhibited. As corrosion progresses, a critical ox-

ide thickness is reached, at which the protection of the oxide layer breaks down and a rapid increase in the oxidation rate is observed. The breakdown is known as 'the transition' and it is followed by a reduction in the oxidation rate as a new protective oxide layer forms.[12] Molybdenum (Mo) is considered as one of the principal alloying elements for stainless steels and its beneficial effects on the corrosion resistance were most thoroughly investigated.[13–15] It is well known that Mo enhances the resistance to pitting corrosion and expands the passive region in sulfuric acid, making types 316 and 317 suitable for 90 % mass fractions of H_2SO_4 at ambient temperature. The corrosion behavior of single-layer films like TiN and CrN was widely reported;[16–18] however, very few studies reported on ZrMoN films.

In order to improve the corrosion resistance of metallic BPPs, many attempts were made by employing different surface-modification methods. The formation of a protective film on the BPPs with physical-vapor deposition (PVD) is proven to be an effective method and has been extensively studied.[19–24] Many researchers focused on the multilayer, while fewer on the composite film.

Thus, in this study, ZrMoN films were deposited on SS304 using an RF magnetron-sputtering system and the properties were changed by adjusting the power of the Mo target. The effects of the Mo-target power on the corrosion behavior were investigated by simulating the cathode environment of the PEMFC.

2 EXPERIMENTAL PART

2.1 ZrMoN films and electrode preparation

The substrate (a 15 mm diameter and 2 mm thickness) used was SS304 consisting of 0.08 % amount fraction of C, 1.00 % amount fraction of Si, 2.00 % amount fraction of Mn, 0.045 % amount fraction of P, 0.03 % amount fraction of S, 18–20.% amount fraction of Cr, 8.0–10.5 % amount fraction of Ni and Fe balance. ZrMoN films were deposited on the substrate surface using the PVD technology, and the properties were changed by adjusting the power of the Mo target. The film was deposited using an RF magnetron-sputtering system (JGP450, SKY Technology Development Co., Ltd, CAS, China), which consists of two RF sputtering guns, each of them mounted on water-cooled target holders. The distance between the substrate holder and the targets was 11 mm. The substrates were cleaned with successive rinsing in ultrasonic baths of deionized water, ethyl alcohol absolute (C_2H_6O = 99.7 %) and acetone and blown dry with dry air. The Zr target and the Mo target with the same purities of 99.9 % were positioned 11 mm from the substrate. Argon gas and nitrogen gas of very high purity (99.999 %) were introduced. The base pressure was less than 6.0×10^{-4} Pa. Prior to deposition, the targets were cleaned by pre-sputtering for 10 min, while the substrate was isolated from the plasma with a shutter. More parameters for the deposition of the ZrMoN films are listed in **Table 1**.

Table 1: Deposition parameters for ZrMoN films

ZrMoN films	Parameters
Base pressure	Less than 6.0×10^{-4} Pa
Total pressure	0.3 Pa
Flow rate of Ar and N_2	10:3
Zr-target power (RF)	150W
Mo-target power (RF)	20W, 30W, 50W, 90W
Deposition temperature	Room temperature
Deposition time	2 h

2.2 Contact-angle test

Wettability has a strong effect on the cell performance, particularly at high current densities. A high contact angle implies a high surface energy and low surface wettability of a material.[25] Water contact angles (WCA) were measured using a drop shape analyzer (DSA) (JC2000D, Powereach Corporation, Shanghai, China). The volume of a water droplet was ≈4 μL and the average values of 10 measurements were reported as the water contact angle.

2.3 Structural characterization

The samples were sealed in rubber mud; XRD data of the films were reordered with SHIMADZU XRD-6000 ray diffraction (XRD, Cu-K_α = 1). The working voltage and the current for the diffractometer were set at 40 kV and 30 mA, respectively. The scanning range (2θ) was 20°~80°.

The thickness and surface morphology of the films were observed using JSM-6480 scanning electron microscopy.

2.4 Electrochemical corrosion test

The corrosion behavior of ZrMoN-coated and uncoated samples under the cathode of PEMFC were studied; the electrolyte was a 0.5M H_2SO_4 + 2 mg/L NaF solution at 70 °C, and the air was bubbled through the test. A three-electrode electrochemical cell was used, together with a platinum counter electrode and an Hg/HgO saturated KCl electrode as the reference electrode. The sample to be tested was the working electrode. Samples were loaded in silicon rubber and the surface area exposed to the corrosive medium was approximately 0.25 cm^2. The samples were kept in the test solution for a period of time before the potentiodynamic polarization study in order to establish the open-circuit potential (E_{ocp}) or the steady-state potential.[26]

2.4.1 Potentiodynamic polarization

The sweep range was –0.4 V~1.5 V (relative to the E_{ocp}) and the sweep rate was 1mv/s. Tafel plots were obtained after the electrochemical measurements. The corrosion potential (E_{corr}) and the corrosion-current density (i_{corr}) were deduced from the Tafel plots (that is, log i vs. E plot). The polarization resistance (R_p) was measured

using linear sweep voltammetry and calculated from the Stern-Geary equation, with Equation (1):[27]

$$R_p^{-1} = 2.303 i_{corr}\left(\frac{1}{b_a}+\frac{1}{|b_c|}\right) \quad (1)$$

R_p in Equation (1) relates to the corrosion behavior of the test materials; the i_{corr} and the Tafel constants b_a and b_c can be measured from the experimental data. The Tafel constant b_c is negative; its absolute value was used in Equation (1).

2.4.2 Electrochemical impedance spectroscopy

The impedance measurements were made at the open-circuit potential and the applied alternating potential had an amplitude of 10 mV. The spectrum was recorded in a frequency range of 10 mHz~100 KH. After each experiment, the impedance data was displayed as Nyquist plots. The Nyquist plot is a plot of the real (Z') vs. imaginary impedance (Z''). From this plot at a high frequency, the value of the solution resistance (R_s) was obtained and at a low frequency, the charge transfer resistance (R_{ct}) was deduced. The data were analyzed using the Zview software.

3 RESULTS AND DISCUSSION

3.1 Contact-angle test

Table 2 shows the contact angles of the ZrMoN coated samples with water. Due to the liquid water, the battery cannot be discharged in time and the water enters the porous electrode blocking the reaction gas path and reducing the catalytic activity area. This results in a decreased cell performance, and the liquid water attached to the surfaces of the metallic bipolar plates accelerates the corrosion of the bipolar plates.[28] So, the bipolar-plate material should have low surface wettability. On **Table 2**, the contact angles are nearly 90°. It is obvious that the ZrMoN coated samples have high contact angles on the surfaces, which shows good hydrophobicity.

Table 2: Contact-angle-measurement results of ZrMoN films

Films	Contact angle	
ZrMoN films	P(Mo)=20W	96.11°
	P(Mo)=30W	94.45°
	P(Mo)=50W	97.61°
	P(Mo)=90W	93.83°

3.2 XRD test

Crystal phases of the ZrMoN coated samples were analyzed with XRD patterns and the results are presented in **Figure 1**. This figure shows that the films mainly include ZrN phases; there are no MoN and Mo phases in the films, and it is obvious that a ZrMoN film is the substitutional solid solution of Mo atoms into ZrN films. The XRD patterns show that there are two main diffraction peaks, a (1 1 1) peak and a (2 2 2) peak. The (1 1 1) peak is the strongest; therefore, the growth orientation of the ZrMoN film is mainly in the (1 1 1) direction.

3.3 SEM analysis

Figure 2 is a SEM micrograph of the ZrMoN film where the Mo-target power is 20 W. The formation of pinholes is nearly impossible to avoid. This is because the coated surfaces are always non-uniform and because the coating tends to grow in a non-uniform manner. Various growth models were developed to describe the growth process.[29] A general feature of these models is the fact that after the original nucleation stage, the growth takes place in isolated islands, which then grow together, leaving the voids between them. The general growth morphology of the coatings is typically columnar. Although various techniques can be used to minimize the number of pinholes, they usually cannot be totally eliminated. They occur commonly in all kinds of coatings on all kinds of substrates.[30]

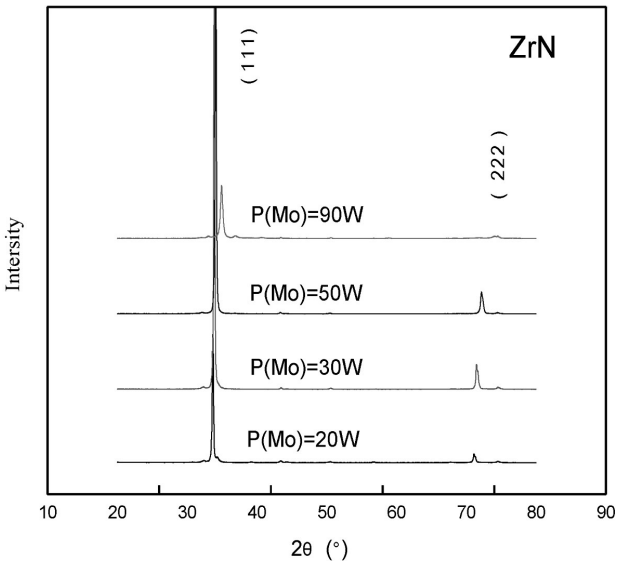

Figure 1: XRD test results for ZrMoN films

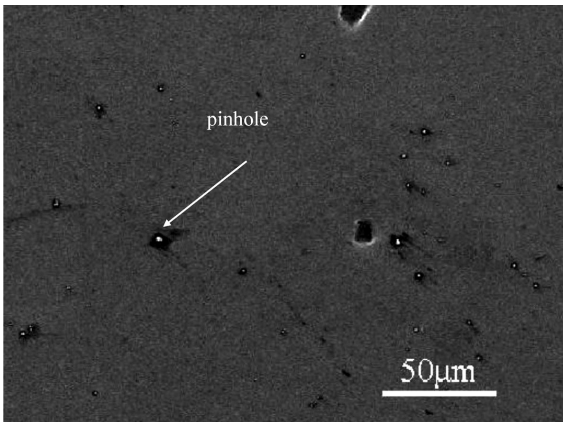

Figure 2: SEM micrograph of the ZrMoN film where the power of Mo target is 20 W

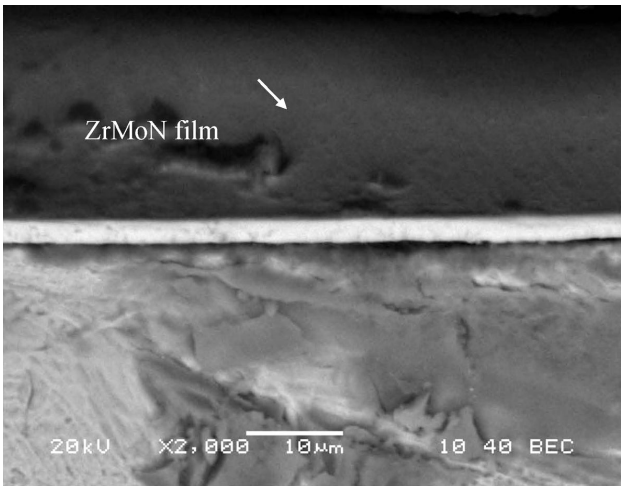

Figure 3: Cross-sectional view of the ZrMoN film where the power of Mo target is 50 W

In this study, the coating layers also had such defects, arising from the coating process or the substrate, although relatively dense coatings were obtained. A SEM micrograph of the defects in the coating layer of the ZrMoN film is given in **Figure 2**. It can be clearly seen from **Figure 2** that there is a pinhole in the film, shown as a black hole, due to the columnar growth during the coating process. It is indicated that the electrolyte may penetrate through the pores and the micro-pores in the film to the substrate, causing corrosion.[31–33] **Figure 3** presents a cross-sectional view of the ZrMoN film with the power of the Mo target of 50 W and a thickness of 2.3 μm.

3.4 Potentiodynamic tests

Table 3 shows the E_{ocp} values of the ZrMoN coated and uncoated samples. Except for the sample with 20 W, the E_{ocp} values for the samples with a higher Mo-target power are higher than that of the uncoated sample, showing a better corrosion resistance than the uncoated sample. **Figure 4** shows potentiodynamic polarization curves of the ZrMoN coated and uncoated samples in a simulated PEMFC working solution. **Table 4** lists polarization parameters of the ZrMoN coated and uncoated samples. It is clear from a comparison of the E_{corr}, i_{corr} and R_p values of the samples, with the power of the Mo target increasing from 20 W to 90 W, that there is a gradual shift in the E_{corr} values towards the positive side (from –0.395 to –0.0347), while the i_{corr} decreases gradually from 18.1 to 0.0169, and the R_p is gradually improved. The ZrMoN films exhibited much lower i_{corr} values and nobler E_{corr} under the simulated PEMFC working condition. These results revealed that the ZrMoN films markedly enhanced the corrosion resistance of SS304.

According to the technical index of DOE published in 2006[34], relating to a sample in the cathode of a PEMFC environment (about 0.6V vs. SCE), the passivation-current density must be less than 1.0 μA cm^{-2}; thus, a vertical line was set as the standard in **Figure 4**. **Table 5** shows the passive-current density of the samples in the PEMFC cathode. When the power of the Mo target is 30 W, the sample has a good corrosion resistance in the PEMFC environment, and it is also close to the technical index of DOE. However, a significant finding was that the other coated samples had a lower corrosion resistance. They even surprisingly exhibited higher corrosion-current densities than the uncoated sample, resulting in a need for further investigation. This finding indicates that with an increase in the power of the Mo target, the solid solubility also increases; when the power of the Mo target is 30 W, the solid solubility in the medium has good corrosion resistance. However, with a continuous increase of the Mo-target power, the solubility increases and a lattice distortion occurs, which will also lead to an increase in defects.

Table 3: E_{ocp} of ZrMoN coated and uncoated samples

ZrMoN films	P(Mo) = 20 W	P(Mo) = 30 W	P(Mo) = 50 W	P(Mo) = 90 W	uncoated
E_{ocp} /(V)	–0.377	–0.179	0.0428	0.152	–0.1986

Table 4: Polarization parameters of ZrMoN coated and uncoated samples

ZrMoN films	i_{corr} (μA/cm^2)	E_{corr} (V)	b_a (A/cm^2)	b_c (A/cm^2)	R_p (A/cm^2)
P(Mo) = 20 W	18.1	–0.395	0.4949	0.34343	0.00486
P(Mo) = 30 W	0.0923	–0.187	0.1319	0.1637	0.3436
P(Mo) = 50 W	0.0670	–0.0368	0.2132	0.2187	0.6997
P(Mo) = 90 W	0.0169	–0.0347	0.0636	0.0574	0.7752

Table 5: Passivation-current density regarding 0.6 V vs. SCE of ZrMoN coated and uncoated samples

ZrMoN films	P(Mo) = 20 W	P(Mo) = 30 W	P(Mo) = 50 W	P(Mo) = 90 W	uncoated
(lg *i*) *i*/(A/cm^2)	–3.943	–5.526	–4.936	–3.017	–5.281

As mentioned earlier, the formation of coating defects is almost impossible to avoid totally. Consequently,

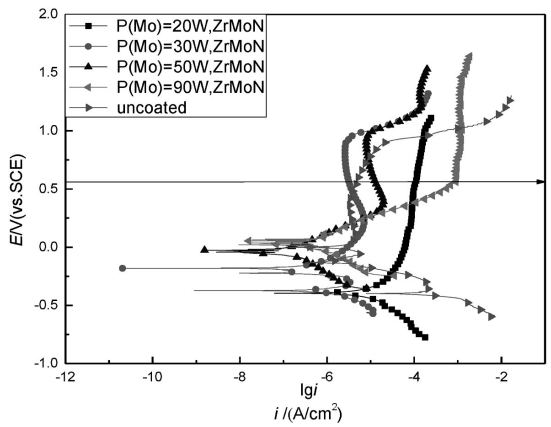

Figure 4: Potentiodynamic polarization curves of ZrMoN coated and uncoated samples (the cathode condition)

when subjected to a corrosive atmosphere, coated samples form galvanic cells at the defects near the interface due to an electrochemical difference between the ZrMoN film and the substrate. Once aggressive ions such as SO_4^{2-} penetrate the film through these small channels, driven by capillary forces, the area is exposed to anodic dissolution, which usually extends laterally along the interface between the film and the substrate. Finally, the formed pits link up with each other, causing a removal of the entire coating by flaking,[35] which causes the abovementioned corrosion process. As an overall evaluation, the power of the Mo target is 30 W. The coated sample displays the best corrosion resistance in the cathode of the PEMFC environment when the power of the Mo target is considered.

3.5 EIS tests

Figures 5 and **6** show the Nyquist and Bode plots for of the ZrMoN coated and uncoated samples. The EIS data are displayed in **Table 6**. The Nyquist plots (**Figure 5**) show the presence of a single semicircle for the ZrMoN coated samples, which may be attributed to the short exposure time in the corrosive medium. The Bode plots (**Figure 5a**) show that the absolute impedance increases in the same order. **Figure 5b** shows that the phase angles of all the samples are nearly 80°. In this study, the equivalent-circuit diagram used in the experiment is shown in **Figure 7**.[26] The equivalent circuit for the uncoated sample is shown in **Figure 7a**. It consists of a double layer capacitance (Q_{dl}), which is parallel to the charge transfer resistance (R_{ct}); both of them are associated with the solution resistance (R_s) between the working electrode (WE) and the tip of the Luggin capillary. Q stands for the constant phase element, which accounts for the deviations from the ideal dielectric behavior related to surface inhomogeneities. The value of n is obtained from the slope of the log $|Z|$ vs. log f plot. The phase angle (θ) can vary between 90° (for a perfect capacitor (n = 1)) and 0° (for a perfect resistor (n = 0)). In the present study, it represents a somewhat leaky capacitor with n = 0.85. The C_{dl} is, therefore, replaced with the constant phase element when $n < 1$.

The CDC for the equivalent circuit proposed for a mild steel substrate is $R(QR)$. The proposed equivalent circuit for the PVD coating on the steel substrate with defects is shown in **Figure 7b**. Due to the low film thickness, when the coated sample is immersed in the electrolyte, the corrosion is expected to initiate rapidly at the pores present in the film. This leads to the formation of localized galvanic cells, which dominate the galvanic corrosion process.[19] In such cases, the electrochemical interface can be divided into the sub-interface electrolyte/coating and the electrolyte/substrate. For the EIS data simulation, the equivalent-circuit model for the coated samples proposed by V. K. William Grips[26] is used in this study, describing the mechanism of an electrochemical reaction. Therefore, the electrolyte can penetrate through the coating and attack the steel substrate. As the experiments are bubbled with air, the corrosion rate is limited by the slow diffusion of the electrolyte and oxygen through the defects in the film. This behavior can be described using a finite-length diffusion process.

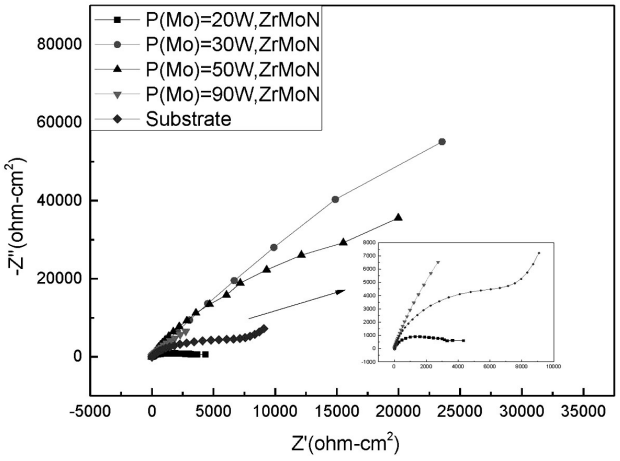

Figure 5: Impedance spectra of samples with ZrMoN films and substrate

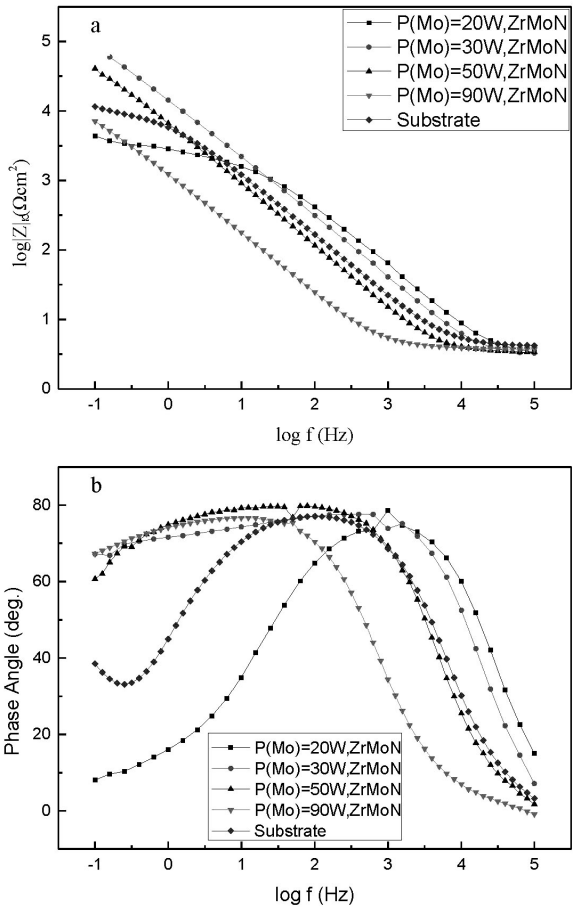

Figure 6: a) Bode plots (log |Z| vs. log f) of samples with ZrMoN films and substrate, b) Bode plots (phase angle vs. log f) of samples with ZrMoN films and substrate

Table 6: EIS data obtained with an equivalent-circuit simulation of ZrMoN coated and uncoated samples

ZrMoN films	R_s (Ω)	Q_{film}-Y_0 (s-sec^n)	n_{film} (0<n<1)	R_{pore} (Ω)	Q_{dl}-Y_0 (s-sec^n)	n_{dl} (0<n<1)	R_{ct} (Ω)	O-Y_0 (s-sec^.5)	B (sec^.5)
P(Mo) = 20 W	3.219	4.706 E-6	0.923	0.016	5.47 E-5	0.383	3.808	1.21 E-3	1.226
P(Mo) = 30 W	3.115	1.391 E-6	0.754	0.149	2.35 E-6	0.997	1.158 E6	2.909	1.844 E7
P(Mo) = 50 W	3.387	2.371 E-5	0.913	1.992	1.11 E-5	0.525	2.473 E5	3.46 E-13	2.125 E-11
P(Mo) = 90 W	3.760	2.907 E-5	1	1.666	1.355 E-4	0.809	8.367	4.539 E-5	1.799 E4
uncoated	4.031	-	-	-	2.514 E-5	0.856	1.224 E4	-	-

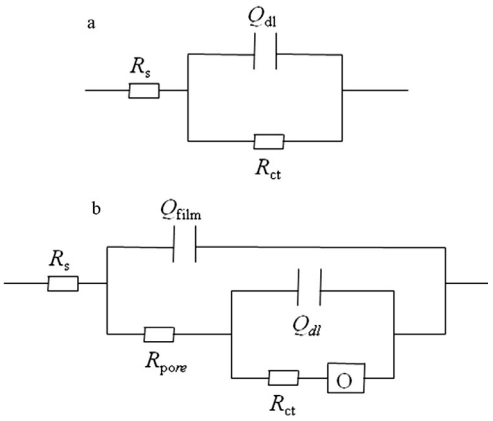

Figure 7: Equivalent-circuit diagram, used in the experiment

Therefore, the cotangent diffusion element (O) should be adopted in series with the charge-transfer resistance.

In **Figure 6b**, the CDC is $R(Q(R(Q(RO))))$. The capacitance (Q_{film}) and the charge-transfer resistance for the porosity of the film (R_{pore}) are included as additional elements to the equivalent circuit, as shown for the substrate in **Figure 7a**. From the EIS data given in **Table 6**, the R_{ct} increases in the following order: 20 W, 90 W, uncoated, 50 W, 30 W. This indicates that the samples with a higher Mo-target power show a better corrosion resistance. With the increase of the power of the Mo target, the solid solubility also increases. When the power of the Mo target is 30 W, the solid solubility in the medium has good corrosion resistance. But, with a continuous increase in the Mo-target power, the solubility increases and the lattice distortion occurs, leading also to an increase in defects. In the case of the sample with 50 W, the R_{pore} shows a gradual decrease with the increase in the Mo-target power.

4 CONCLUSIONS

ZrMoN films are deposited on SS304 with an RF magnetron-sputtering system. The total thickness of a film is 2.3 μm and the growth orientation of a ZrMoN film is mainly in the (1 1 1) direction. Static-water contact-angle results show that the ZrMoN films have a low surface wettability, which is beneficial to the water management of a PEMFC stack. As the Mo-target power increases from 20 W to 90 W, the E_{corr} shifts towards the positive side (from -0.395 to -0.0347), the i_{corr} decreases gradually from 18.1 to 0.0169, and the R_p gradually improves. As an overall evaluation, the power of the Mo target is 30W. A coated sample displays the best corrosion resistance in the cathode of the PEMFC environment when the power of the Mo target is considered, which indicates that with an increase of the power of the Mo target, the solid solubility also increases. However, with a continuous increase of the Mo-target power, the solubility increases and a lattice distortion also occurs, leading to an increase in defects. Through the study of PEMFC bipolar-plate materials, ZrMoN-coated stainless steel can be proven as a good candidate.

Acknowledgement

This work was financially supported by the Natural Science Foundation of the Jiangsu Province, China (No.BK20141292).

5 REFERENCES

[1] L. Carrette, K. A. Friedrich, U. Stimming, Fuel cells-fundamentals and applications, Fuel Cells, 1 (**2001**) 1, 5–39, doi:10.1002/1615-6854(200105)1:1 5

[2] G. O. Collantes, Incorporating stakeholders perspectives into models of new technologies diffusion: the case of fuel cell vehicles, Technol. Forecasting Soc. Change, 74 (**2007**) 3, 267–80, doi:10.1016/j.techfore.2006.02.001

[3] Y. Wang, K. S. Chen, J. Mishler, A review of polymer electrolyte membrane fuel cells: technology, applications, and needs on fundamental research, Appl. Energy, 88 (**2011**), 981–1007, doi:10.1016/j.apenergy.2010.09.030

[4] T. Sasabe, S. Tsushima, In-situ visualization of liquid water in an operating PEMFC by soft X-ray radiography, International Journal of Hydrogen Energy, 35 (**2010**) 20, 11119–11128, doi:10.1016/j.ijhydene.2010.06.050

[5] D. Q. Mei, M. Qian, B. H. Liu et al., A microreactor with micro-pin-fin arrays for hydrogen production via methanol steam reforming, J. Power Sources, 205 (**2012**), 367–76, doi:10.1016/j.jpowsour.2011.12.062

[6] Min Zhang, Kwang Ho Kim, Zhigang Shao et al., Effects of Mo content on microstructure and corrosion resistance of arc ion plated Ti-Mo-N films on 316L stainless steel as bipolar plates for polymer exchange membrane fuel cells, Journal of Power Sources, 253 (**2014**), 201–204, doi:10.1016/j.jpowsour.2013.12.075

[7] A. Kumar, R. G. Reddy, Materials and design development for bipolar/end plates in fuel cells, Journal of Power Sources, 129 (**2004**), 62–67, doi:10.1016/j.jpowsour.2003.11.011

[8] M. J. Kelly, G. Fa?lek, J. O. Besenhard et al., Contaminant absorption and conductivity in polymer electrolyte membranes, Journal of Power Sources, 145 (**2005**), 249–252, doi:10.1016/j.jpowsour. 2005.01.064

[9] S. P. Mani, A. Srinivasan, N. Rajendran, Effect of nitrides on the corrosion behaviour of 316L SS bipolar plates for Proton Exchange Membrane Fuel Cell (PEMFC), International Journal of Hydrogen Energy, 40 (**2015**) 8, 3359–3369, doi:10.1016/j.ijhydene.2014.12.108

[10] H. A. Jehn, Improvement of the corrosion resistance of PVD hard coating substrate systems, Surface and Coatings Technology, 125 (**2000**), 212, doi:10.1016/S0257-8972(99)00551-4

[11] S. H. Yao, Y. L. Su, W. H. Kao et al., Wear behavior of DC unbalanced magnetron sputter deposited ZrCN films, Materials Letters, 59 (**2005**) 26, 3230–3233, doi:10.1016/j.matlet.2005.04. 064

[12] B. D. C. Bell, S. T. Murphy, P. A. Burr et al, The influence of alloying elements on the corrosion of Zr alloys, Corrosion Science, 105 (**2016**), 36–43, doi:10.1016/j.corsci.2015.12.022

[13] A. Pardo, M. C. Merino, A. E. Coy et al, Effect of Mo and Mn additions on the corrosion behaviour of AISI 304 and 316 stainless steels in H_2SO_4, Corrosion Science, 50 (**2008**), 780–794, doi:10.1016/j.corsci.2007.11.004

[14] R. Qvarfort, Some observations regarding the influence of molybdenum on the pitting corrosion resistance of stainless steels, Corrosion Science, 40 (**1998**), 21–223, doi:10.1016/S0010-938X(97)00118-2

[15] M. Kaneko, H. S. Isaacs, Effects of molybdenum on the pitting of ferritic- and austenitic-stainless steels in bromide and chloride solutions, Corrosion Science, 44 (**2002**), 1825–1834, doi:10.1016/S0010-938X(02)00003-3

[16] J. Piippo, B. Elsener, H. Bohni, Electrochemical characterization of TiN coatings, Surface and Coatings Technology, 61 (**1993**), 43, doi:10.1016/0257-8972(93)90200-8

[17] C. Liu, Q. Bi, A. Matthews, EIS comparison on corrosion performance of PVD TiN and CrN coated mild steel in 0.5 N NaCl aqueous solution, Corrosion Science, 43 (**2001**), 1953–1961, doi:10.1016/S0010-938X(00)00188-8

[18] S. H. Ahn, Y. S. Choi, J. G. Kim et al., A study on corrosion resistance characteristics of PVD Cr-N coated steels by electrochemical method, Surface and Coatings Technology, 150 (**2002**), 319, doi:10.1016/S0257-8972(01)01529-8

[19] Y. Fu, G. Lin, M. Hou et al., Carbon-based films coated 316L stainless steel as bipolar plate for proton exchange membrane fuel cells, International Journal of Hydrogen Energy, 34 (**2009**), 453–458, doi:10.1016/j.ijhydene.2008.10.068

[20] B. Wu, G. Lin, Y. Fu, M. Hou, B. Yi, Chromium-containing carbon coating on stainless steel as bipolar plates for proton exchange membrane fuel cells, International Journal of Hydrogen Energy, 35 (**2010**), 13255–13261

[21] J. Barranco, F. Barreras, A. Lozano, M. Maza, Influence of CrN-coating thickness on the corrosion resistance behaviour of aluminium-based bipolar plates, Journal of Power Sources, 196 (**2011**), 4283–4289, doi:10.1016/j.jpowsour.2010.11.069

[22] B. C. Cha, Y. Z. You, S. T. Hong et al., Nitride films as protective layers for metallic bipolar plates of polymer electrolyte membrane fuel cell stacks, International Journal of Hydrogen Energy, 36 (**2011**), 4565–4572, doi:10.1016/j.ijhydene.2010.04.116

[23] H. S. Choi, D. H. Han, W. H. Hong et al., (Titanium, chromium) nitride coatings for bipolar plate of polymer electrolyte membrane fuel cell, Journal of Power Sources, 189 (**2009**), 966–971, doi:10.1016/j.jpowsour.2008.12.060

[24] L. Wang, D. O. Northwood, X. Nie et al., Corrosion properties and contact resistance of TiN, TiAlN and CrN coatings in simulated proton exchange membrane fuel cell environments, Journal of Power Sources, 195 (**2010**), 3814–3821, doi:10.1016/j.jpowsour.2009. 12.127

[25] P. Yi, L. Peng, L. Feng et al., Performance of a proton exchange membrane fuel cell stack using conductive amorphous carbon-coated 304 stainless steel bipolar plates, Journal of Power Sources, 195 (**2010**) 20, 7061–7066, doi:10.1016/j.jpowsour.2010.05.019

[26] V. K. W. Grips, H. C. Barshilia, V. E. Selvi et al., Electrochemical behavior of single layer CrN, TiN, TiAlN coatings and nanolayered Ti Al N/Cr N multilayer coatings prepared by reactive direct current magnetron sputtering, Thin Solid Coatings, 514 (**2006**), 204–211, doi:10. 1016/j.tsf.2006.03.008

[27] A. P. Yadav, F. Suzuki, A. Nishikata et al., Investigation of atmospheric corrosion of Zn using ac impedance and differential pressure meter, Electrochimica Acta, 49 (**2004**), 2725–2729, doi:10.1016/j.electacta.2004.01.033

[28] Y. Fu, G. Q. Lin, M. Hou et al., Carbon-based films coated 316L stainless steel as bipolar plate for proton exchange membrane fuel cells, International Journal of Hydrogen Energy, 34 (**2009**) 1, 405–409, doi:10.1016/j.ijhydene.2008.10.068

[29] H. Altun, S. Sen, The effect of PVD coatings on the corrosion behaviour of AZ91 magnesium alloy, Materials and Design, 27 (**2006**), 1174–1179, doi:10.1016/j.matdes.2005.02.004

[30] A. S. Korhonen, Corrosion of thin hard PVD coatings, Vacuum, 45 (**1994**) 10–11, 1031–1034, doi:10.1016/0042-207X(94)90015-9

[31] C. H. Hsu, M. L. Chen, K. L. Lai, Corrosion resistance of TiN/TiAlN-coated ADI by cathodic arc deposition, Materials Science and Engineering A, 421 (**2006**), 182–190, doi:10.1016/j.msea.2005. 12.014

[32] D. A. Jones, Principles and Prevention of Corrosion, 2nd Edition, Prentice-Hall, Upper Saddle River, NJ, 43 (**1992**) 4, 8–10, doi: 9780133599930

[33] F. Lang, Z. Yu, The corrosion resistance and wear resistance of thick TiN coatings deposited by arc ion plating, Surface & Coatings Technology, 145 (**2001**), 80–87, doi:10.1016/S0257-8972(01)01284-1

[34] DOE Hydrogen Program, FY 2006 Annual Progress Report, 2006, http://www.hydrogen.energy.gov/pdfs/progress06

[35] H. Dong, Y. Sun, T. Bell, Enhanced corrosion resistance of duplex coatings, Surface & Coatings Technology, 90 (**1997**) 1–2, 91–101, doi:10.1016/S0257-8972(96)03099-X

ELECTRONIC ACCESS

http://mit.imt.si

ISSN 1580-2949